Universitat
de les Illes Balears

DOCTORAL THESIS
2018

HEAT AND CHARGE TRANSPORT IN NANOSTRUCTURES: INTERFERENCE, AC-DRIVING, ENVIRONMENT, AND FEEDBACK

Guillem Rosselló Rosselló

DOCTORAL THESIS
2018

Doctoral Programme of Physics

HEAT AND CHARGE TRANSPORT IN NANOSTRUCTURES: INTERFERENCE, AC-DRIVING, ENVIRONMENT, AND FEEDBACK

Guillem Rosselló Rosselló

Directora: Rosa López
Tutor: Raúl Toral

Doctor by the Universitat de les Illes Balears

PUBLICATIONS

[1] G. Rosselló, F. Battista, M. Moskalets, and J. Splettstoesser, “Interference and multiparticle effects in a Mach-Zehnder interferometer with single-particle sources,” Phys. Rev. B **91**, 115438 (2015).

[2] G. Rosselló, R. López, and J. S. Lim, “Time-dependent heat flow in interacting quantum conductors,” Phys. Rev. B **92**, 115402 (2015).

[3] G. Rosselló, R. López, and G. Platero, “Chiral Maxwell demon in a quantum Hall system with a localized impurity,” Phys. Rev. B **96**, 075305 (2017).

[4] G. Rosselló, R. López, and R. Sánchez, “Dynamical Coulomb blockade of thermal transport,” Phys. Rev. B **95**, 235404 (2017).

AGRAÏMENTS

Vull començar agraint a la Rosa López tota la seva ajuda i dedicació en fer que aquesta tesi fos possible. El seu suport i la seva confiança en mi han estat imprescindibles per a poder dur a bon port el treball de tots aquests anys. Gràcies per la teva confiança, que m'ha permès superar moments difícils i que m'ha portat a completar aquesta tasca.

També vull agrair al Rafa Sánchez i al Jong-Soo Lim per la seva col·laboració en la investigació de resultats que finalment han format part d'aquesta tesi. Així mateix vull estendre l'agraïment a la resta de membres del grup de recerca en quàntica de l'IFISC.

Menció especial per a la Gloria Platero, que em va permetre fer i va finançar dues estades interessantíssimes al seu grup de recerca a l'ICMM de Madrid i que, amb el seu encoratjament i la seva forma de ser, em va fer sentir un privilegiat.

Agraeixo també a la Janine Splettstößer l'oportunitat de conèixer el món de la recerca a nivell internacional. Així mateix agraeixo a la RWTH d'Aachen i al ministeri de ciència NRW pel finançament rebut durant el meu temps allà que em permeteren desenvolupar part de la feina que ha format part d'aquesta tesi. No m'oblido dels meus fantàstics companys i amics d'allà que em permeteren gaudir de la meva estada allí.

Cal agrair a la UIB el finançament rebut en part d'aquesta tesi, primer en forma de beca de col·laboració i després en forma de contracte predoctoral. També cal mencionar a l'IFISC que m'ha ofert un lloc a on treballar i un bon ambient de treball, on es busca sempre fer ciència d'alt nivell.

Finalment, vull agrair a la meva família el seu suport incondicional, ja sabeu que sense vosaltres això no hauria estat possible. Des de sempre heu encoratjat la meva curiositat i el meu afany per saber i m'heu fet tenir la ment sempre atenta. Sense tot això no m'hauria estat possible arribar fins aquí. M'heu ajudat molt a superar situacions difícils i a treure el cap endavant quan no sempre era fàcil. Gràcies de tot cor, no sé què faria sense vosaltres! Gràcies Carme, gràcies Joan i gràcies Carmeta!

AGRADECIMIENTOS

Quiero empezar agradeciendo a Rosa López toda su ayuda y dedicación en hacer que esta tesis fuera posible. Su ayuda y su confianza en mi han sido imprescindibles para poder llevar a cabo el trabajo de todos estos años. Gracias por tu confianza, que me ha permitido superar momentos difíciles y que me ha llevado a completar esta tarea.

También quiero agradecer a Rafa Sánchez y a Jong-Soo Lim por su colaboración en la investigación de resultados que finalmente han formado parte de esta tesis. Así mismo quiero extender el agradecimiento al resto de miembros del grupo de investigación de cuántica del IFISC.

Mención especial para Gloria Platero, que me permitió hacer y financió dos estancias de investigación interesantísimas en su grupo de investigación en el ICMM de Madrid que, con su impulso y forma a de hacer me, hizo sentir un privilegiado.

Agradezco también a Janine Splettstößer la oportunidad de conocer el mundo de la investigación a nivel internacional. Así mismo agradezco a la RWTH de Aachen y al ministerio de ciencia de NRW por la financiación recibida durante mi tiempo allí, que me permitieron desarrollar parte del trabajo que ha formado parte de esta tesis. No me olvido de mis fantasticos compañeros y amigos de allí que me permitieron disfrutar de mi tiempo en Aachen.

Hay que agradecer a la UIB por la financiación recibida durante parte de esta tesis, primero en forma de beca de colaboración y luego en forma de contrato predoctoral. También debo mencionar al IFISC, que me ha ofrecido un lugar donde trabajar y un buen ambiente de trabajo, donde siempre se busca hacer ciencia de primer nivel.

Finalmente, quiero agradecer a mi familia por su apoyo incondicional, ya sabéis que sin vosotros esto no hubiera sido posible. Desde siempre habéis alentado mi curiosidad y mi afán por saber y me habéis hecho tener la mente siempre atenta. Sin todo esto, no me hubiera sido posible llegar hasta aquí. Me habéis ayudado mucho a superar situaciones difíciles y a sacarlo adelante aunque no siempre fuera fácil. Gracias de todo corazón, no sé que haría sin vosotros! Gracias Carme, gracias Joan y gracias Carmeta!

ACKNOWLEDGMENTS

I would like to start thanking Rosa López for all her help and dedication in making this thesis possible. Her support and her faith in me have been essential for the realization of all this year's work. Thank you for your trust, that allowed me to overcome difficult times and that brought me to finishing this great task.

I would also like to thank Jong-Soo Lim and Rafa Sánchez for their collaboration in the development of results that are part of this thesis. As well, thank the other members of the quantum research group at IFISC.

Special thanks to Gloria Platero for allowing and paying for my two very interesting research stays in her research group at ICMM in Madrid and as well to her encouragement and her way of being that made me feel privileged.

Thanks to Janine Splettstösser for giving me the chance of getting to know the research world in an international level. This extends to the RWTH university of Aachen and the science ministry of NRW for their funding during the time that I spent there that allowed me to develop part of the work presented in this thesis. I don't forget my great colleagues and friends that I had there, who made me enjoy my time there.

Thanks to the UIB for the financial support received during part of this thesis, first in a beca de col·laboració and then as a predoctoral contract. I'd like also to mention IFISC that gave me a place to develop my work as well as a good work environment where high-quality science is always the priority.

Finally, I'd like to thank my family for their unconditional support, you know that without you this would not have been possible. You have always encouraged my curiosity and my pursuit of knowledge and you've made me always keep a keen mind. Without all of this I could have made it this far. You've helped me overcome difficult situations and to make it work even when it was not easy. Thank you from the bottom of my heart, I don't know what I would do without you!

RESUM

L'augment del nombre de transistors en circuits integrats, seguint la llei de Moore, ha portat a la miniaturització dels xips fins a la nano-escala des dels transistors originals, de la mida de centímetres fins als xips d'avui en dia de fins a un nanòmetre. Gràcies a aquesta reducció en mida, avui en dia existeixen components més petits i més ràpids per a ordinadors i smartphones. Tot i els avantatges d'aquesta millora, tan en rendiment com en mida, aquesta també comporta problemes ja que el fet que aquests sistemes operin a major velocitat comporta un major encalentiment dels circuits. Per tant, quan s'estudien aquests sistemes cal tenir en compte no només la corrent elèctrica que un desitja controlar sinó també les corrents d'energia i calor, tot sabent com es dissipa aquesta, juntament amb la relació que guarden electricitat i calor. L'estudi d'aquestes magnituds no és una tasca fàcil, ja que en sistemes d'aquesta escala els efectes quàntics poden tenir un paper rellevant i cal tenir en compte nous fenòmens, propis de l'escala microscòpica. Llavors, l'objectiu d'aquesta tesi és donar llum en aquest camp mitjançant l'estudi de diversos sistemes de mida nanomètrica, caracteritzant la seva resposta, en termes de corrents elèctriques i de calor, a forces elèctriques i tèrmiques.

Per assolir dit objectiu, comencem al capítol 1 amb una introducció als tipus de sistemes que estudiarem en aquesta tesi. Majoritàriament tractarem sistemes confinats com punts quàntics i sistemes Hall quàntics i en descriurem les seves propietats més rellevants. Per altra banda, en el capítol 2, es descriuen breument les principals magnituds que usarem per descriure els sistemes mencionats, és a dir, els fluxos d'electricitat i de calor. Finalment, hi presentem els distints mètodes que emprarem per calcular-los.

Els resultats de la tesi comencen al capítol 3, on considerem la corrent més petita possible, un electró emès en cada període, i estudiem una de les propietats més intrigants de la física quàntica, la dualitat ona-partícula. Amb aquest objectiu en ment, usem un interferòmetre Mach-Zehnder construït en un sistema Hall quàntic on els electrons emesos per un o dos emissors d'electrons poden interferir i col·lisionar. D'aquesta manera, la interferència ens permet estudiar els comportaments com a ones i les col·lisions els comportaments de tipus partícula. Estudiant aquest sistema en termes de corrents de càrrega i de calor, els nostres resultats permeten afirmar que les dues corrents es comporten de manera molt diferent i que la interpretació en termes de partícules no serveix per explicar els resultats de la corrent de calor, mentre que la basada en ones sí que permet interpretar correctament els resultats d'ambdues quantitats.

En el capítol 4, estudiem en més profunditat l'aparell usat per emetre electrons d'un en un en el capítol 3: un condensador quàntic. Sometem el sistema a un voltatge que oscil·la ràpidament en el temps, fet que ens permet estudiar els efectes de processos assitits per fotons, així com els efectes de la interacció en la dinàmica de relaxació de l'equivalent quàntic del circuit RC. Els nostres resultats ens permeten comprovar que la definició típica de la corrent energètica no és del tot correcta, ja que s'ha de tenir en compte la calor que es guarda i que es relaxa en les barreres per poder tenir un resultat correcte.

A continuació, en el capítol 5 investiguem com el circuit que hi ha al voltant del sistema afecta el transport de calor i de càrrega a través d'un transistor d'un sol electró (un punt quàntic connectat a dos contactes). Per això, estudiem els fluxos de càrrega i de calor en el règim lineal i mostrem que l'efecte ambiental pot causar una rectificació de calor, fins i tot en el règim lineal. A més, mostrem que quan s'usa el transitor com a motor termoelèctric, l'energia ambiental pot ajudar a millorar-ne l'eficiència.

Al capítol 6 seguim amb la idea d'usar un transistor d'un sol electró com a motor termoelèctric. Així, dissenyem un sistema format per un punt quàntic connectat a dos estats de vorera d'un sistema Hall quàntic. En aquest sistema, implementem un protocol de *feedback* en el que un ens extern, un *dimoni*, és capaç de controlar la quiralitat dels estats de vora mitjançant la mesura de l'estat del punt quàntic. Això permet a l'ens obtenir informació del sistema que llavors és usada per extreure treball del sistema sense necessitat d'un gradient tèrmic.

Finalment, les conclusions generals de la tesi es troben al capítol 7.

RESUMEN

El aumento del número de transistores en circuitos integrados, siguiendo la ley de Moore, ha llevado a la miniaturización de los chips hasta la nanoescala desde los transistores originales, que medían unos pocos centímetros hasta los chips de hoy de hasta un nanómetro. Gracias a esta reducción en tamaño, hoy en día existen componentes más pequeños y más rápidos para ordenadores y smartphones. Aún con las ventajas de esta mejora, tanto en rendimiento como en tamaño, esto también comporta problemas ya que el hecho de hacer funcionar estos dispositivos a mayor velocidad implica que se calientan más. Por tanto, al estudiar estos sistemas, no sólo hay que tener en cuenta la corriente de carga sino también las corrientes de energía y de calor, estudiando cómo se disipa ésta, junto con la relación entre electricidad y calor. El estudio de estas cantidades no es una tarea fácil, ya que en sistemas de esta escala los efectos cuánticos pueden tener un papel relevante y hay que tomar en consideración nuevos fenómenos, propios de la escala microscópica. Por eso, el objetivo de esta tesis es aportar a esta cuestión, mediante el estudio de diversos sistemas de tamaño nanométrico, describiendo su respuesta en términos de corrientes eléctricas y de calor, a fuerzas eléctricas y térmicas.

Para conseguir dicho objetivo, empezamos con una introducción a los tipos de sistemas que estudiaremos en esta tesis en el capítulo 1. Trataremos mayoritariamente con sistemas confinados como puntos cuánticos y sistemas Hall cuánticos y describimos sus propiedades más relevantes. Por otro lado, en el capítulo 2, se detallan brevemente las principales magnitudes que utilizaremos para describir los sistemas mencionados, es decir, los flujos de electricidad y de calor. Finalmente, presentamos los diferentes métodos que utilizaremos para calcularlos.

Los resultados de la tesis empiezan en el capítulo 3, dónde consideramos la corriente más pequeña posible, un electrón emitido en cada período, y estudiamos una de las propiedades más intrigantes de la física cuántica, la dualidad onda-partícula. Con este objetivo en mente, usamos un interferómetro Mach-Zehnder construido en un sistema Hall cuántico donde los electrones emitidos por uno o dos emisores de electrones pueden interferir y colisionar. Así, la interferencia nos permite estudiar los comportamientos cómo ondas y las colisiones los comportamientos tipo partícula. Estudiando este sistema a través de las corrientes de carga y de energía, nuestros resultados permiten afirmar que ambas corrientes tienen comportamientos muy diferentes y que la interpretación de partículas no permite explicar los resultados, mientras que la basada en ondas sí que permite interpretar correctamente los resultados de ambas cantidades.

En el capítulo 4, estudiamos en más profundidad el aparato utilizado para emitir electrones de uno en uno en el capítulo 3: un condensador cuántico. Sometemos el sistema a un voltaje que oscila rápidamente en el tiempo, hecho que nos permite estudiar los efectos de los procesos asistidos por fotones, así como los efectos de la interacción en la dinámica de relajación del equivalente cuántico del circuito RC. Con nuestros resultados comprobamos que la definición típica de la corriente energética no es del todo correcta, ya que hay que tener en cuenta el calor que se guarda y que se relaja en las barreras para poder tener el resultado correcto.

A continuación, en el capítulo 5, investigamos cómo el circuito que hay alrededor del sistema afecta al transporte de calor y de carga a través de un transistor de electrón único (un punto cuántico conectado a dos contactos). Para eso, estudiamos los flujos de carga y de calor en el régimen lineal y mostramos que cuando se usa el transistor cómo motor termoeléctrico, la energía ambiental puede ayudar a mejorar la eficiencia.

En el capítulo 6 seguimos con la idea de utilizar un transistor de electrón único cómo motor termoeléctrico. Así, diseñamos un sistema formado por un punto cuantico conectado a dos estados de borde de un sistema Hall cuántico. En este sistema implementamos un protocolo de *feedback* en el que un ente externo, un *demon*, es capaz de controlar la quiralidad de los estados de borde mediante la medición del estado del punto cuántico. Eso permite al ente obtener información del sistema que entonces es usada para extraer trabajo del sistema sin necesidad de un gradiente térmico.

Finalmente, las conclusiones generales de la tesis son presentadas en el capítulo 7.

OVERVIEW

The fulfillment of Moore's law, the doubling of number of transistors in integrated circuits every two years [1], has led to the miniaturization of chips to the nanoscale from the initially centimeter size transistors [2] to nowadays, with transistors down to 1 nm [3]. As a consequence, faster and smaller components for computers and smartphones are available nowadays. As good as this sounds, this improvement in performance and size comes with some associated problems since rapid operation means a stronger heat dissipation in the system. To overcome these problems one needs to characterize not only the charge current that is used in these systems but also to study its relation to heat currents and how they are dissipated. The investigation of these currents is not an easy task since in such small systems quantum effects start to play a crucial role and many new phenomena emerge. The aim of this thesis is to shed some light in this field by studying various nanoscale systems and characterizing their response to electrical and thermal forces in terms of charge and energy flows.

To this end, in Chapter 1, we start with an introduction of the systems that we analyze in this thesis. In most of the cases we deal with confined systems in the nanoscale such as quantum dots and quantum Hall systems. In this chapter we describe some of their most relevant peculiarities. In Chapter 2, we briefly discuss the main magnitudes that we are going to use to describe those systems, namely the charge and energy flows, and we present the different approaches and formalisms of quantum transport theory used to calculate charge and energy currents.

We start, in Chapter 3, by considering the smallest possible current, i.e. one single electron emitted in one period and we study one of the most intriguing properties of the quantum world, the particle-wave duality. With this purpose, we use a Mach-Zehnder interferometer built in a quantum Hall setup where electrons emitted by one or two single-particle sources can interfere and collide. Interference allows us to address the wave-like properties of electrons, and collisions allow us to address the particle-like features. By studying the charge and energy currents of these systems we are able to show that charge and energy flows have different behaviors and that the particle-like picture is only suited to explain the charge current whereas the wave-like picture allows us to interpret correctly the results of both quantities.

In Chapter 4 we study in more detail the setup used to emit single particles in Chapter 3, the quantum capacitor. By subjecting this system to a fast AC-driving we can study the effects of photo-assisted events and of electron-electron interaction on the relaxation dynamics of the quantum equivalent to the RC-circuit. We check that the usual definition for energy currents is flawed and that one needs to take the energy relaxed in the barriers for a proper result, in terms of symmetry.

In Chapter 5 we study the effect of the surrounding circuit, an environment, on the transport properties of heat and charge through a single electron transistor, a gated quantum dot connected to two reservoirs. We study the charge and heat currents in the linear regime and we show that the environment is able to produce heat rectification even in the linear regime and that it can help improve the efficiency of the single electron transistor when it is used as a thermoelectric engine.

In Chapter 6 we follow the idea of Chapter 5 of using a single electron transistor as a thermoelectric engine. We devise a setup consisting of a quantum dot connected to two quantum Hall edge states. We implement a feedback scheme in which an external entity, a "demon", is able to control the chirality of the edge states by reading the state of the quantum dot. The demon does work on the system thanks to the information that extracts by reading the charge dot state.

Finally, we present the general conclusions of this thesis in Chapter 7.

CONTENTS

Part I

INTRODUCTION

1

NANO-STRUCTURES

Nanoscale devices appeared as a consequence of the miniaturization of electrical components, mainly used in computation. The search for faster and more powerful devices lead to a search for increasingly small systems where the usual electrical components of computer circuits could be implemented. The performance of these components is measured basically in terms of electrical currents, but faster electrical currents mean that a greater amount of heat is dissipated in these type of systems. Hence, in nanoscale systems, the heat dissipated (or flowing) becomes a relevant quantity that needs to be characterized alongside the electrical current. Furthermore, a good characterization of heat flows in nanostructures leads to the possibility of controlling such flows.

With this in mind, we define a nanoscale device as a structure of dimensions in the nanometers which performs a useful task [4]. Many examples of this are available nowadays, from nanoscale transistors to graphene, all the way to quantum wires and carbon nanotubes. These kind of devices are usually built using semiconductor materials.

Since the discovery of the solid-state transistor [2], a lot of progress has been made, leading to the field of mesoscopics and nanoscale systems where many relevant applications and effects have been described. Examples of this are: the quantum Hall effect, graphene, electrical and optical applications for quantum dots.

In this chapter we introduce the basic notions about nano-structures needed for the understanding of this thesis. We start by a short overview of different types of nano-structures and their definition in Section 1.1. Once we have introduced the nano-structures in general, we focus on the main example which is the most prominent system that we are going to study throughout this thesis, i.e. quantum dots, in Section 1.2. Finally, in Section 1.3, we discuss the quantum Hall effect and the ballistic and chiral nature of its edge states that we use as building blocks for the systems studied in Chapters 3 and 6.

1.1 FROM TWO TO ZERO DIMENSIONS: CONFINED SYSTEMS

Of particular interest to this thesis are the nano-systems in which the motion of carriers is restricted in some of the spatial directions, known as confined systems. In the field of mesoscopic devices, any system in which the motion of the electrons is forbidden in any direction is considered a confined system. Examples of this type of systems, classified according to the number of restricted dimensions of movement from two to zero dimensions, are: two-dimensional electron gases, quantum wires and quantum dots.

Two-dimensional systems

The motion of electrons in condensed matter can be restricted so that electrons can move only in a two-dimensional plane. This can be achieved either by forming a very narrow interface between two different semiconductors (e.g. GaAs and AlGaAs) or by construction of the material, as in mono-layer materials such as graphene [5].

The electrons in the interface between two semiconductors are said to be confined to a two-dimensional electron gas (2DEG). The 2DEG is one of the most widely used setups in condensed matter studies concerning transport properties of mesoscopic systems. Two dimensional electron gases are the base to many applications, form the creation of Fabry-Perot interferometers using quantum point contacts (QPC) [6], the creation of quantum dots and quantum dot arrays to the possibility of implementing systems using the quantum Hall effect, which was first observed in a 2DEG [7].

One-dimensional systems

One can further reduce the dimensionality of condensed matter systems to one dimension by confining the motion of electrons in two dimensions, allowing for movement in just one dimension. The reduction of dimensionality to one dimension (or quasi-one) is usually achieved by construction of the system and thus the most relevant examples of one-dimensional systems are nanowires and nanotubes (especially carbon nanotubes). These type of systems have been used for many applications, e.g. nanowires are used to create Majorana fermions [8], and carbon nanotubes can be used as supercapacitors [9].

In this thesis, our interest in one-dimensional systems is reduced to the fact that they can be used to build zero-dimensional structures with properties different to those created in two-dimensional systems. Quantum dots created in carbon nanotubes can exhibit spin-orbit and valley couplings which are hard to achieve in quantum dots implemented in 2-DEG.

Zero-dimensional systems

Finally, when movement of charges is constricted in all three directions we obtain zero-dimensional systems. It is to be noted that they are not true zero dimensional but rather quasi zero-dimensional. In a 2DEG one can further confine the electrons in the two available dimensions or in a quantum wire by using constrictions or gate voltages in order to achieve zero-dimensional structures. It is also possible to directly grow such structures in the form of nano-pillars directly on a substrate in a process known as self-assembly. Being zero-dimensional, these systems receive the name of quantum dots. In the next section we give a more detailed overview of quantum dots, since they are the most prominent nanostructure in this thesis.

1.2 CONFINED SYSTEMS: QUANTUM DOTS

A quantum dot is a quasi-zero-dimensional nanostructure whose electronic states are totally quantized. They are built by constricting the motion of electrons in all three dimensions which results in a discrete spectrum of energy levels similar to what happens in atoms. Therefore quantum dots can be thought of as artificial atoms with a controllable energy spectrum. Firstly introduced as such due to their discrete spectrum in the optics field, quantum dots have evolved to be one of the most active fields of research in condensed matter physics [4, 5, 10–15]. The great advantage of studying physics in 0-D artificial atoms is that the system can be modified in a control-

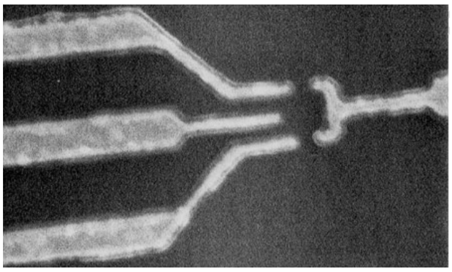

Figure 1.1: Scanning microscopy image of a quantum dot defined in a 2DEG via gate depletion. Image taken from [16].

lable way and out-of-equilibrium states can be induced either by electrical AC and DC potentials or thermals biases.

On top of that, quantum dots are of special relevance to this thesis since they are the only nano-structure appearing in all chapters of this thesis. They appear as single-particle emitters in Chapter 3, as quantum capacitors in Chapter 4, as single electron transistors in Chapter 5 and as a localized state in the bulk of a quantum Hall system in Chapter 6.

Many types of quantum dots are available nowadays, depending on the method of fabrication or the type of system in which they are found: vertical quantum dots are obtained by etching techniques through which metallic islands are obtained, effectively trapping electrons, quantum dots can also be obtained by confining electrons in two-dimensional electron gas through gate depletion and quantum point contacts (QPC), see Fig. 1.1, recently quantum dots have also been created in carbon nanotubes [4].

1.2.1 *Applications*

Our main focus on quantum dots is their use in transport of charge and energy in condensed matter systems and their behavior when they are part of a nano-scale circuit. Transport in quantum dots is a wide-ranging field where all types of configurations using quantum dots have been envisioned, from quantum capacitors (connected to one reservoir) and single electron transistors (one quantum dot connected to two reservoirs) to double quantum dots both in series and parallel, and quantum dot arrays. In each of these configurations, different properties of the quantum dots emerge and thus they all present their own interest and potential applications. In this thesis we focus on two of these configurations, the quantum capacitors and the single electron transistors.

1.2.1.1 *Quantum capacitors*

One of the most prominent applications of quantum dots is their use as quantum capacitors which are the quantum equivalent of RC circuits [17]. In a typical application, the quantum dot plays the role of one of the "plates" of the capacitor being the macroscopic back-gate the other plate of the capacitor. The quantum point contact defining the dot plays the role of a resistor. In this type of application, quantum dots can be used to store charge. Quantum capacitors subjected to AC voltages present a quantization of their charge relaxation resistance [18], even in the presence of interactions [19]. We investigate the response of the heat current in such a device in Chapter 4.

The quantum capacitor is a type of quantum circuit that can be implemented using a 2DEG and a QD defined via a QPC. This type of circuit not only can store charge (as a capacitor) but it can also be used to emit charge one by one, in other words, it can be used as an on-demand single-electron emitter [20]. By driving the voltage gate, $V_G(t)$, controlling the energy levels of the dots above and below the Fermi energy with an amplitude similar to the level spacing of the energy levels of the dot, the capacitor acts as a single particle emitter, emitting an electron in one half of the period and a hole in the other half of the period, see Fig. 1.2. This implementation of the quantum capacitor is known as a single-electron source (SES).

These type of sources, implemented in a QH setup where no backscattering is possible serve as the equivalent of single-photon sources of quantum optics, allowing for the reproduction of optics experiments using electrons [21, 22].

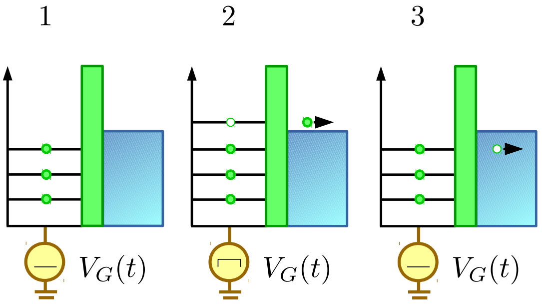

Figure 1.2: Driving sequence on a quantum capacitor used as a single electron source by moving the gate voltage $V_G(t)$. Reproduced from Ref.[20]

1.2.1.2 *Single-electron transistors*

The single electron transistor configuration is widely used for transport studies in quantum dots [16, 23–25]. This setup consists of a quantum dot attached to two leads, acting as source and drain for the charge current, as the systems studied in Chapters 5 and 6. A prototypical example of such setup is shown in Fig. 1.1 where an experimental image of such setup is presented. We model such a setup as two metallic contacts acting as electronic reservoirs with a continuum of states connected via tunneling junctions to the quantum dot, characterized by discrete states as shown in Fig. 1.3. The discrete energy levels of the quantum dot can be controlled via a gate voltage V_G and transport of electrons is triggered by the application of a voltage bias between source and drain $V_S > V_D$. Single-electron transistors can be used as thermoelectric engines when the application of a thermal gradient between source and drain induces a current against the applied voltage bias, effectively being able to extract power from the system.

In this setup it is possible to observe how the discreteness of the energy levels of the quantum dots affects transport and it is possible to observe how the Coulomb repulsion between charges can block transport in what is known as Coulomb blockade of transport which we introduce in the next Section 1.2.2. Coulomb blockade peaks obtained from conductance measurement in the SET of Fig. 1.1 are shown in Fig. 1.4.

We investigate how the environment (the surrounding circuit) affects transport in a SET in Chapter 5.

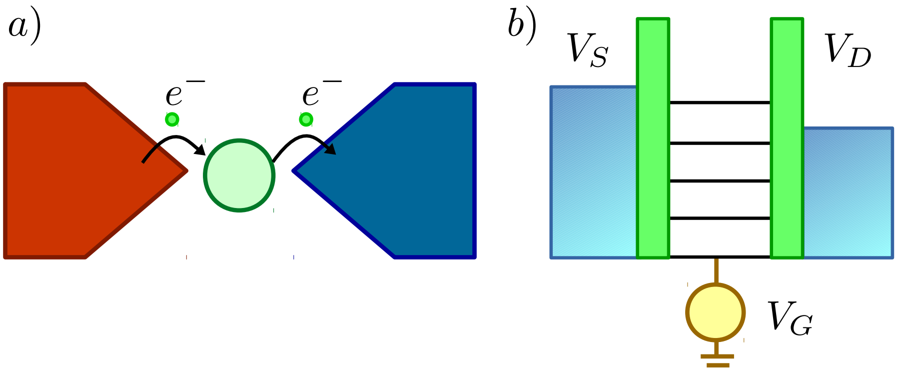

Figure 1.3: a) Sketch of a typical setup of a SET, two electronic reservoirs (in red (source) and blue(drain)) in contact with a quantum dot (in green). b) Energy representation of the SET, two reservoirs at different voltages represented as a continuum and the quantum dot (delimited by tunneling barriers) represented as the discrete energy levels.

1.2.2 *Charging energy: Coulomb Blockade*

Due to their nature, electronic states in quantum dots are very sensitive to the presence of multiple electrons due to the Coulomb interaction [4] resulting in frozen dynamics inside the dot and the appearance of charging effects [12]. As a consequence transport through quantum dots has a rich variety of phenomena, e.g. Coulomb blockade, Kondo resonances or Fano interference. In this section we describe the Coulomb blockade effect, the blocking of transport through a quantum dot due to electron-electron interactions. This repulsion between charges, also known as charging effects, can become of importance in small quantum dots when they are weakly coupled to the leads through which transport happens.

As shown in Fig. 1.4, charging effects can be of importance, but it is not ensured that this will be the case, some requirements must be met. Taking the SET setup and removing the contacts, we would have a metallic island occupied by N electrons, i.e. with a quantized charge eN. If then we add the contacts and allow for particle exchange, the number of particles in the island will adjust itself to minimize circuit energy. When particle exchange occurs, the charge of the island changes by e and thus the electrostatic potential is modified by the charging energy $E_C = \frac{e^2}{2C}$, related to the total capacitance of the dot, C. The charging energy will be of relevance if it is greater than the thermal energy $k_B T$. Another condition must be fulfilled in order for the charge to be well quantized and that is electrons must be well-localized which imposes a lower boundary in the tunneling resistance of the dot R_t which defines the typical discharge time of the island $\Delta t = R_t C$. It is also needed for charge quantization that energy uncertainty ΔE is smaller than the charging energy. By means of Heisenberg uncertainty relation we have then: $\Delta E \Delta t = R_t C e^2/C > h$ implying that the tunneling resistance ought to be larger than the resistance quantum,i.e $R_t \gg \frac{h}{e^2}$. Summarizing, charging effects (quantization of the charge) will only be important if the following conditions are fulfilled:

$$R_t \gg \frac{h}{e^2}; \tag{1.1}$$

$$\frac{e^2}{2C} \gg k_B T. \tag{1.2}$$

These conditions can be achieved by a weak coupling of the dot to the reservoirs and by making a sufficiently small dot respectively. If charging effects become strong enough, transport may be blocked and then the dot is said to be in the Coulomb Blockade (CB) regime. Therefore Coulomb blockade can be seen as a suppression of electrical current at low biases. If the bias is smaller than the charging energy, current is strongly suppressed. Coulomb blockade regime can also be seen by the appearance of very strong peaks in the conductance of the system, see Fig. 1.4.

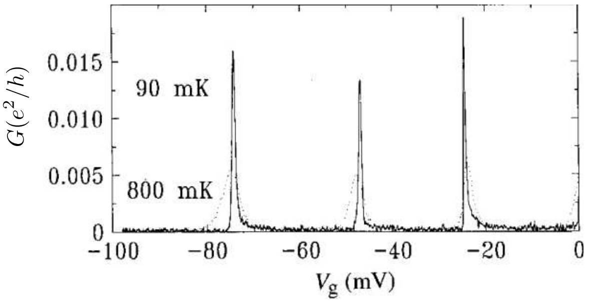

Figure 1.4: Characteristic Coulomb blockade peaks in the electrical conductance G of a quantum dot. Image taken from [16].

1.3 TOPOLOGICAL SYSTEMS: QUANTUM HALL

The quantum Hall effect is the quantum mechanical version of the Hall effect and is characterized by the quantisation of the Hall conductivity [7]. It is observed in two-dimensional electron gases, see Section 1.1, at low temperatures subjected to strong perpendicular magnetic fields. When a 2DEG is subjected to a strong magnetic field, the electrons in the bulk of the sample describe cyclotron orbits whereas the electrons near the boundaries describe skipping orbits that follow the edges, creating chiral edge channels for transport, see Fig. 1.5 a). From a thoretical point of view this is understood since, in this strong magnetic field regime, the Landau levels describing the quantized cyclotronic orbits of the electrons are extremely degenerate which allows all the electrons to be in just a few Landau levels. Deep within the interior of 2DEG with well delimited boundaries, the conduction band edge is essentially flat, independent of position, and the corresponding Landau-level energies are similarly constant. The boundaries of the sample correspond to those regions, however, where the conduction band edge rises well above the Fermi level, to confine the electron system to a finite area, see Fig. 1.5 b). Each Landau level that is occupied in the interior of the 2DEG therefore intersects the Fermi level at two different points, located near the opposite edges of the sample, and therefore yields two counter-propagating edge states that function as one-dimensional channels. Under this conditions current flow is carried by these ballistic edge states [4].

These edge states are ballistic since back-scattering is suppressed in the edge channels through which this states travel. The suppression of backscattering can be easily understood using a classical picture of skipping orbits, since the Lorentz force pushes the electron back to the boundary and makes it maintain its skipping motion [4], see Fig. 1.5 a). Therefore it is possible to create one-dimensional channels where no back-scattering is present. This

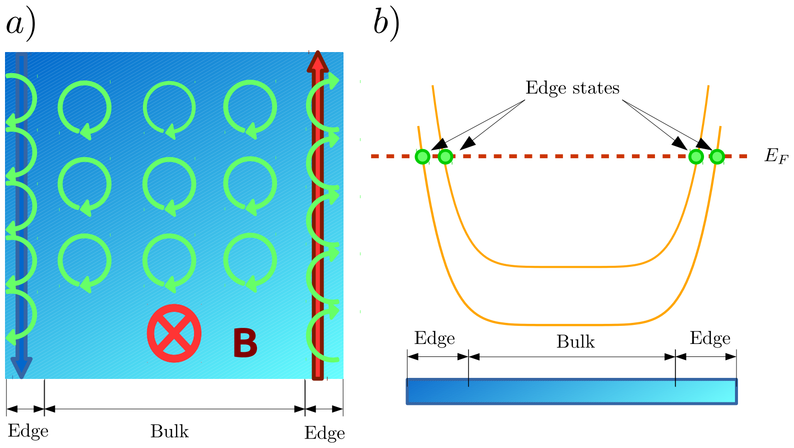

Figure 1.5: Quantum Hall effect. a)Top view of a 2DEG subjected to a strong magnetic field B. Electrons in the bulk follow circular orbits whereas those in the outer part follow skipping orbits, forming chiral edge channels. b) Landau levels in real space. The levels are essentially flat in the bulk of the 2DEG but they rise up near the edges of the sample.

technique has proven to be very useful for the implementation of electronic equivalents to the quantum optical experiments.

1.3.1 *Quantum Hall bar*

The quantum Hall effect was detected via the quantization of the Hall conductivity. Measurements of this quantity are obtained by measuring the conductance perpendicular to the applied current in a sample in the quantum Hall regime, see Fig. 1.6. This kind of device, consisting of a 2DEG in a strong magnetic field with contacts that allow the application of a current in one axis and the measurement of conductances in the other is known as a quantum Hall bar. The presence of edge states is clearly visible in a quantum Hall bar from the measurement of the Hall conductivity.

If an impurity is present in the bulk of the 2DEG in the bar, it forms a localized state that acts as a quantum dot. In Chapter 6 we explore such device and its applicability to implement a Maxwell demon.

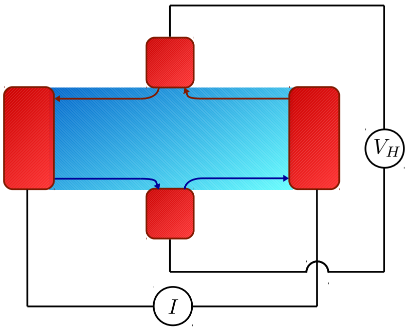

Figure 1.6: Prototypical example of a quantum Hall bar, where the Hall conductance can be measured.

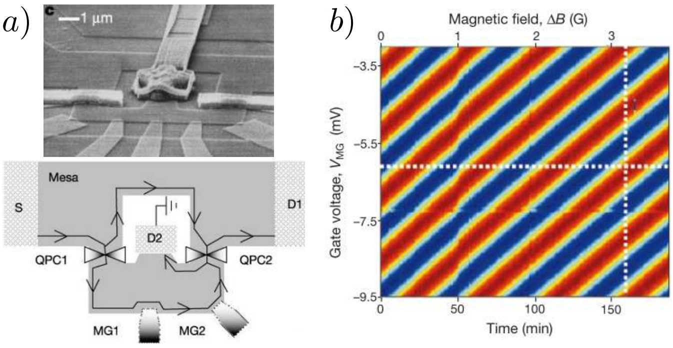

Figure 1.7: An electronic Mach-Zehnder interferometer. In the left side of the picture, a microscopic image of the experimental device and a corresponding sketch of the interferometer. On the right side, the current measured experimentally as a function of the magnetic field and the voltage measuring the detuning of the arms of the interferometer. Images extracted from Ref.[26].

1.3.2 *Mach-Zehnder interferometer*

The chirality and lack of backscattering of the edge states of the quantum Hall effect can be used to realize optics experiments using electrons in condensed matter systems. An example of such setup is the electronic equivalent of the Mach-Zehnder interferometer (MZI), experimentally implemented using the edge states of a quantum Hall system with two QPC acting as beam-splitters [26]. The experimental setup and the results for the electrical current are shown in Fig. 1.7.

In this setup, electrons are injected from S, which acts as a source of electrons due to an applied voltage. Then, electrons are scattered at QPC 1 to either of the arms of the interferometer and they are recombined at QPC 2, being finally scattered to leads D1 and D2, where they are detected. The length of one of the arms can be controlled via a gate voltage V_G applied to MG1 and MG2. Due to the magnetic flux enclosed by the two arms of the interferometer, electrons are subjected to the Aharonov-Bohm effect when traversing the interferometer, which results in a magnetic-dependent interference pattern at the output of the interferometer [27, 28]. The interference pattern, in the form of oscillations with the magnetic field in the charge current, is clearly shown in Fig. 1.7 b).

An example of a MZI fed by SES is investigated in Chapter 3 where we show the interference patterns of single electrons and how they can be affected by two-particle effects.

2

THERMOLECTRIC TRANSPORT IN NANO-STRUCTURES

Transport in nano-strucutres is understood as the movement of carriers, carrying charge and/or energy, in systems with nano-scale dimensions. A nano-device is a functional structure with nano-scale dimensions which performs some useful operation, for example a nano-scale transistor (e.g. the single-electron transistor of Section 1.2.1.2). We consider the prototypical setup for studying transport as an active region connected to reservoirs, see Fig. 2.1. There we show the system as a region (in green), possibly gate-controlled via capacitive coupling, connected to two metallic-like electronic reservoirs, acting as contacts. These two contacts act as a source and a drain for electrons and transport is achieved by applying a voltage or temperature difference between the two contacts. This triggers the flow of carriers which can be measured as a current which depends on the properties of the system under study. These properties and hence the current can be controlled by changing the gate voltage V_G.

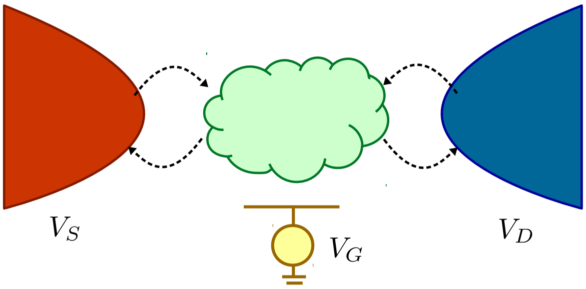

Figure 2.1: Prototypical example of a transport setup for a nano-device. The active region is represented by a green contour and is connected to two reservoirs: source (in red) at voltage V_S and drain (in blue) at voltage V_D. Additionally, there is a back gate (in yellow) that allows to control the energy levels inside the region via the voltage V_G.

The vision of the setup to study transport built using ideal separated regions is a common and useful way of visualizing such systems. Even so, the idea of having contacts acting as ideal injectors or extractors of carriers and an active region that limits transport is limited to the cases where the coupling between system and contacts is not too strong, since when the coupling is strong the separation between regions might not be clear.

If inelastic scattering events are frequent as carriers traverse the active region of the device, carrier transport is diffusive in nature, and is reasonably approximated by the semiclassical Boltzmann transport equation. Energy dissipation occurs throughout the device, and the contacts are simply injectors and extractors of carriers near equilibrium. In contrast, if little or no scattering occurs from source to drain, transport is said to be ballistic, and the wave nature of charge carriers becomes important in terms of quantum mechanical reflection and interference from the structure itself, and the overall description of transport is in terms of quantum mechanical fluxes and transmission. Energy is no longer dissipated in the active region of the device, rather, it is dissipated in the contacts themselves [4].

It becomes clear then that when studying transport through nanostructures one needs to characterize the charge current in order to know how the particles traversing the systems behave and also to study the energy currents to investigate how heat is dissipated in the system. As a consequence, it is also of relevance to study the interplay between the two, that is, the thermoelectric effects.

Therefore, thermoelectric effects have generated an immense interest for quite some time already because they offer the possibility to convert heat into electrical work [29–35]. Hence, they can be used for energy harvesting in electric circuits in computers, to achieve both active cooling and energy recovery. This harvested energy can then be used to recharge batteries. Unfortunately, even after decades of material research current thermoelectric materials still have a very low efficiency in converting heat into electrical work and deliver only moderate powers [36]. Due to this low efficiency, thermoelectric energy recovery is restricted to very few applications.

Thermoelectricity, in short, can be understood from the base of two effects, the Seebeck and Peltier effects. The Seebeck effect describes the flow of an electrical current in response to an applied temperature gradient whereas the Peltier is the thermal counterpart, the flow of energy caused by an electrical voltage bias [37]. Both effects can be understood from the fact that carriers carry both charge and energy, then a thermal gradient causes a flow of carriers from hot to cold, causing both an energy and charge flows, similarly, a voltage bias causes a flow of carriers from high to low voltage with the corresponding energy flow.

Since usually materials with good electrical conductivity are also good thermals conductors, it is difficult to create efficient thermoelectric devices. Hence, the need for ways to create systems with high electrical conductance and low thermal conductance remains one of the main challenges of the study of thermoelectrics [36].

Quantum dots, or more generally confined systems, have been demonstrated to exhibit large Seebeck coefficients due to the discrete nature of their energy spectrum [30]. To properly characterize thermoelectric effects in those systems, we study transport of electrons through confined systems [4, 10, 11].

In this chapter we review the main concepts about transport of charge and energy in nano-structures that are going to be used in this thesis. Firstly, in Section 2.1, we present a brief overview of some basic concepts of transport in nano-structures, including a short introduction to the concepts of charge and energy currents and their relation through the Onsager matrix. Next we introduce the formalisms used to describe the aforementioned quantities in the time-dependent regime, in Sections 2.2 and 2.3 we review the microscopic Landauer or Landauer–Büttiker scattering theory for systems of non-interacting electrons and the Green's functions approach for systems with electron-electron interaction. Finally, in Section 2.4, we introduce our description for transport in time-independent (time-dependent systems in the steady-state regime) systems based on the master equation approach, which is well adapted to describe simple quantum systems with strong electron–electron interactions.

2.1 BRIEF OVERVIEW

2.1.1 *Charge currents*

Nano- and meso- devices were invented with the purpose of manipulating and controlling electrical currents. Still nowadays, the main purpose that they serve is the control of electrical currents (in the form of transistors in chips). Hence, electrical currents are the quantity most widely used in the characterization of such devices. The work presented in this thesis is no exception to that rule and one of the focuses of this work is to study electrical currents in nano-devices.

Charge currents are usually induced by creating an electrical bias between a source and a drain contacts, thus creating an energy imbalance between the two contacts which favors the movement of charges from one side to the other. A similar result can be obtained by applying a temperature difference between the source and the drain, which is known as a thermoelectric effect (more specifically it is the aforementioned Seebeck effect).

By virtue of continuity laws, the charge flowing out of all sources is the same as the charge flowing into the drains. This means that charge is conserved.

2.1.2 *Energy and heat currents*

As is known from thermodynamics, a temperature difference between two contacts generates a flux of energy from the hot contact to the cold contact which tends to equal both temperatures. Under such circumstances, particles with high energy flow from the hot lead to the cold lead, generating an energy current. Similarly, an electrical bias can also be used to generate an energy current, since particles with high energy flow from source to drain, this phenomenon is known as electrothermal effect (also known as Peltier effect).

This energy flow is not to be confused by the heating caused by the dissipation of heat in a resistive circuit, known as Joule heating. When the heat dissipated is taken into account with the flow of energy we talk about heat currents instead of energy currents.

As a consequence of energy conservation, the sum of energy currents is zero (there is no creation of energy). Therefore, the sum of heat currents equals the Joule heating.

2.1.3 *Conductances: Thermoelectrics*

For the characterization of thermoelectric effects in nanostructures we investigate the conductances. They provide the system response, i.e., electrical and energy currents, to the application of electrical and thermal biases. Hence, these conductances can be obtained from the expansion of the currents $\{I_i, J_i\}$ in terms of the applied forces $\{V_i, \theta_i\}$.

Firstly, we start from the well-known fact that applying a voltage bias ΔV to a system drives a charge current I. The relation between the applied voltage in contact j, V_j, and the electrical current at contact i, I_i, is given (at first order) by the electrical conductance $G_{ij} = \frac{\partial I_i}{\partial V_j}\Big|_{V_j=0}$.

Similarly, applying a temperature bias $\Delta\theta$ to a system will drive a heat current J and so a heat conductance can also be defined: $K_{ij} = \frac{\partial J_i}{\partial \theta_j}\Big|_{\theta_j=0}$. In the linear regime the electrical and thermal conductances follow Ohm's and Fourier's laws respectively.

On the other hand there are the thermoelectric effects, i.e. driving a charge current with a temperature difference (Seebeck effect) and creating a heat current by applying a voltage bias (Peltier effect). These effects also allow us to define conductances, the thermoelectric conductance $L_{ij} = \frac{\partial I_i}{\partial \theta_j}\Big|_{\theta_j=0}$ and the electrothermal conductance $M_{ij} = \frac{\partial J_i}{\partial V_j}\Big|_{V_j=0}$.

2.1.3.1 *Onsager relations*

In the linear regime, these relations between currents and biases or fluxes and forces with the four conductances can be conveniently expressed in a matrix, formed by the conductances, known as the Onsager matrix:

$$\begin{pmatrix} I \\ J \end{pmatrix} = \begin{pmatrix} \mathcal{G} & \mathcal{L} \\ \mathcal{M} & \mathcal{K} \end{pmatrix} \begin{pmatrix} V \\ \theta \end{pmatrix}. \tag{2.1}$$

When the system through which transport is studied has more than one terminal, the Onsager matrix elements are in turn also matrices for all the conductances between different reservoirs.

$$\begin{pmatrix} I_i \\ J_i \end{pmatrix} = \begin{pmatrix} G_{ij} & L_{ij} \\ M_{ij} & K_{ij} \end{pmatrix} \begin{pmatrix} V_j \\ \theta_j \end{pmatrix}. \tag{2.2}$$

Onsager reciprocity relations state that thermoelectric (Peltier and Seebeck) conductances, i.e. the off-diagonal terms of the Onsager matrix, are not independent quantities[38]. As in many physical systems, reciprocal relations occur between pairs of forces (V, θ) and flows (I, J). In this case:

$$M_{ij} = \Theta_o L_{ji}. \tag{2.3}$$

Where Θ_o is the base temperature. Onsager's relations are a direct consequence of the principle of reciprocity or microreversibility, resulting from the time-reversal symmetry. Thus, they are only valid in a situation of local equilibrium, i.e. in the linear regime [38]. Later on, H.B.G. Casimir [39] enunciated the Casimir-Onsager relations, generalizing such relations to the case where time-reversal symmetry is broken due to the presence of a magnetic field. In such case Eq. (2.3) is generalized to

$$M_{ij}(B) = \Theta_o L_{ji}(-B), \tag{2.4}$$

or quite generally

$$\hat{O}(B) = \hat{O}^T(-B), \tag{2.5}$$

where $\hat{O}$ is the Onsager matrix appearing in Eq. (2.2) where the temperature has been changed to the "normalized" temperature $\theta \to \theta/\theta_o$.

Once we introduced the magnitudes that we want to describe and some relations among them, we move on to describe the theoretical formalisms to describe these transport properties. Firstly, we start by considering two ways of describing time-dependent systems. The Landauer-Büttiker or scattering formalism is well-suited for systems with non-interacting electrons and will be used in Chapter 3 to describe transport through a Mach-Zehnder interferometer. On the other hand, the Green's functions formalism allows us to describe interacting systems.

2.2 SCATTERING MATRIX APPROACH

In this section we introduce the Landauer-Büttiker approach to transport in non-interacting systems. A generalization to include electronic interactions based on generalized internal potentials is possible [40], however the systems investigated along this thesis treated with this technique can be safely considered as non-interacting.

2.2.1 *Scattering theory: from operators to currents*

In this section we present a general overview on how the charge current (and equivalently the energy current) is calculated from quantum mechanical wave-functions using the scattering theory developed by Landauer and Büttiker [41].

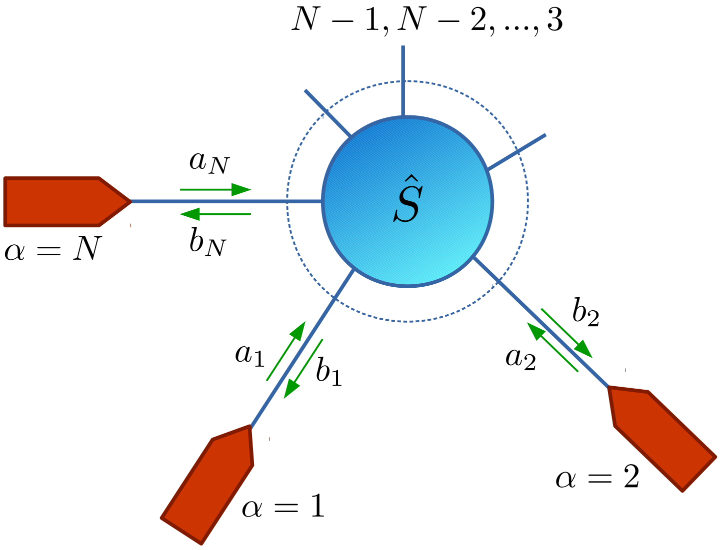

Figure 2.2: Sketch of a mesoscopic sample connected to N reservoirs acting as a scatterer. The greek letter α denotes the reservoir number. The arrows to and from the scatterer represent flows of incident and scattered electrons. Extracted from Ref[41].

In this section we derive the charge operator following closely the work by M. Moskalets, see Ref.[41].

We start expressing the current flowing to lead α in terms of the eigen-wave-functions of the propagating electrons. We assume without loss of generality that the current flows in the z direction which is different for each lead since it is the direction connecting the sample and the reservoir. Then the current at lead α is given by the expression:

$$\hat{I}_\alpha(z_\alpha, t) = -i\frac{\hbar e}{2m}\int dr_\perp \left[\hat{\psi}^\dagger(\vec{r},t)\frac{\partial}{\partial z_\alpha}\hat{\psi}(\vec{r},t) - \left(\frac{\partial}{\partial z_\alpha}\hat{\psi}^\dagger(\vec{r},t)\right)\hat{\psi}(\vec{r},t)\right]. \quad (2.6)$$

In this equation m is the effective mass of the electron. The wave-functions $\hat{\psi}(\vec{r},t)$ describe electrons in leads. We assume that the wave-functions can be separated in two parts, one in the direction z of motion (plane waves) and a transverse one $r_\perp$ ($\chi_E(r_\perp)$):

$$\hat{\psi}(\vec{r},t) = \int_{-\infty}^{\infty} dE e^{-iEt/\hbar}\frac{\chi_E(r_\perp)}{(2\pi\hbar v_\alpha(E))^{1/2}}\left[a_\alpha(E)e^{-ik_\alpha(E)z} + b_\alpha(E)e^{ik_\alpha(E)z}\right].$$

$$(2.7)$$

The electron velocity in reservoir α is $v_\alpha(E) = \hbar k_\alpha(E)/m$, $a_\alpha(E)$ and $b_\alpha(E)$ are amplitudes for incident and scattered particles respectively and $k_\alpha(E)$ is the wave number at energy E, defined by:

$$k_\alpha(E) = \frac{\sqrt{2mE}}{\hbar}. \tag{2.8}$$

From the normalization condition for the wave-function it follows that the transverse part of the wave-function has to be normalized:

$$\int dr_\perp \left|\chi_{E,\alpha}(r_\perp)\right|^2 = 1. \tag{2.9}$$

We are interested in the regime of small bias compared to the Fermi energy. Under this condition, we can approximate $v_\alpha(E) \approx v_\alpha(E')$. Since we consider leads with only one sub-band we can also approximate: $\chi_{E,\alpha}(r_\perp) = \chi_{E',\alpha}(r_\perp)$. This yields to a great simplification of the expression for the current operator. In order to obtain the current operator in second quantization we approximate in this way the wave-function expression, Eq.(2.7) and we substitute the wave-functions with field operators expressed in terms of creation and annihilation operators $a(E), b(E)$. Finally, taking a fixed z point we obtain:

$$\hat{I}_\alpha(t) = \frac{e}{h}\int_{-\infty}^{\infty} dE \int_{-\infty}^{\infty} dE' e^{i(E-E')t/\hbar} \left(b^\dagger_\alpha(E) b_\alpha(E') - a^\dagger_\alpha(E) a_\alpha(E')\right). \tag{2.10}$$

We have expressed the current in terms of the creation and annihilation operators for incoming and outgoing electrons from the scatterer. In this notation we consider the current to be positive when directed to the reservoir.

2.2.2 *Landauer-Büttiker formalism: Scattering matrix approach*

The Landauer-Büttiker formalism for transport phenomena in mesoscopic conducting systems treats the propagation of electrons as a quantum-mechanical scattering problem. We consider a mesoscopic system connected to N reservoirs as shown in Fig. 2.2. The reservoirs are macroscopic and at equilibrium, characterized by a given temperature T_α and a chemical potential μ_α. The flux of particles does not change their equilibrium condition. A particle is injected from one reservoir and it will scatter elastically at the central area (the scatterer). It will be transmitted to the other reservoirs or reflected back.

All the transport properties of the system are described by its scattering matrix [41] which stores the amplitudes for all the possible single-particle scattering events. The matrix element $S_{\alpha\beta}(E)$ is the amplitude of being reflected $\alpha = \beta$ or transmitted $\alpha \neq \beta$ from reservoir α to reservoir β at energy E.

In second quantization thus, the scattering matrix couples the operators for particles incoming to lead α ($b^\dagger_\alpha(E), b_\alpha(E)$), with the operators for the particles leaving lead β $a^\dagger_\beta(E), a_\beta(E)$ as follows:

$$b_\alpha(E) = \sum_\beta S_{\alpha\beta}(E) a_\beta(E), \tag{2.11a}$$

$$b^\dagger_\alpha(E) = \sum_\beta S^\dagger_{\alpha\beta}(E) a^\dagger_\beta(E). \tag{2.11b}$$

Due to conservation in the number of particles (current conservation) the scattering matrix must be unitary:

$$\sum_{\beta} S^{\dagger}_{\alpha\beta}(E) S_{\beta\gamma}(E) = \delta_{\alpha\gamma}. \tag{2.12}$$

Here $\delta_{\alpha\gamma}$ is the Kronecker delta.

2.2.2.1 *Current for a stationary system*

We start by characterizing the current through a stationary system to get familiar with the formalism so that it is simpler to understand the time-dependent case. The current is calculated from the quantum mechanical and statistical average of Eq.(2.10) which can be interpreted as the difference in spectral particle densities coming in and out of the contact α:

$$I_{\alpha} = \langle \hat{I}_{\alpha} \rangle = \frac{e}{h} \int_{-\infty}^{\infty} dE \int_{-\infty}^{\infty} dE' e^{i(E-E')t/\hbar} (\langle a^{\dagger}_{\alpha}(E) a_{\alpha}(E') \rangle - \langle b^{\dagger}_{\alpha}(E) b_{\alpha}(E') \rangle). \tag{2.13}$$

The creation (annihilation) operators of the electrons coming out of the scatterer $b^{\dagger}_{\alpha}(b_{\alpha})$, are related to the creation (annihilation) operators for the electrons going to the scatterer $a^{\dagger}_{\alpha}(a_{\alpha})$ through the scattering matrix of the system as shown in Eqs.(2.11a,2.11b).

Since the operators $a^{\dagger}_{\alpha}(a_{\alpha})$ describe particles coming from the reservoir at equilibrium, their quantum and statistical average is

$$\langle a^{\dagger}_{\alpha}(E) a_{\alpha}(E') \rangle = \delta(E - E') f_{\alpha}(E), \tag{2.14}$$

where $f_{\alpha}(E)$ is the Fermi function of the lead α:

$$f_{\alpha}(E) = \frac{1}{1 + e^{\beta_{\alpha}(E - \mu_{\alpha})}}. \tag{2.15}$$

Here: $\beta_{\alpha} = \frac{1}{k_B T_{\alpha}}$, T_{α} is the temperature of the lead, k_B is the Boltzmann constant and μ_{α} is the electro-chemical potential of the lead α, i.e. $\mu_{\alpha} = \mu_0 - eV_{\alpha}$, μ_0 is the Fermi energy and V_{α} the voltage applied to the reservoir.

With this relations and taking into account the unitarity of the scattering matrix one obtains from Eq.(2.13):

$$I_{\alpha} = \frac{e}{h} \int_{-\infty}^{\infty} \sum_{\beta} |S_{\alpha\beta}|^2 \left[f_{\beta}(E) - f_{\alpha}(E) \right] dE. \tag{2.16}$$

This result shows that the current can be calculated just by knowing the electron states in the reservoirs and the scattering properties of the system.

2.2.3 *Time dependence: Floquet Matrices*

Periodic, time-dependent systems can be described via a scattering matrix approach which is based on the Floquet theorem [41]. The Floquet theorem assures that the solutions to a linear differential equation with periodic time dependent coefficient are also periodic and with the same period.

As opposed to stationary elastic scatterers, dynamical elastic scatterers can change the energy of the incident particles.

The effect of the interaction of electrons with incoming energy E with a periodic potential, with period $\mathcal{T} = 2\pi/\Omega$, is the gain or loss of multiple energy quanta $\hbar\Omega$. Therefore, the energy of scattered electrons is characterised by the energies:

$$E_n = E + n\hbar\Omega, \tag{2.17}$$

with n an integer number. The Floquet theorem assures that this set of energies, composed by the incoming energy plus the absorbed Floquet quanta, is the full set of energies for the outgoing particles. Thus the scattering through dynamical scatterers can be described via the Floquet scattering matrix $\hat{S}_F$, with elements $S_{\alpha\beta}(E_n, E)$ [42]. The amplitude $S_{\alpha\beta}(E_n, E)$ for a carrier with incident energy E, which absorbs an energy $n\hbar\Omega = E_n - E$, describes the scattering of electrons by a time-dependent system. One must redefine the unitarity condition for this kind of matrices, since current conservation is only ensured if one considers all possible outgoing energies [42]. Then the unitarity conditions for the Floquet matrices are:

$$\sum_\beta \sum_n S_{\gamma\beta}(E_m, E_n) S^\dagger_{\alpha\beta}(E, E_n) = \delta_{m0}\delta_{\alpha\gamma}. \tag{2.18}$$

Notice that compared to the unitarity of the stationary scattering matrix, in this case a sum over energy states is needed.

The element $S_{\alpha\beta}(E_n, E)$ can be obtained as the Fourier transform of the dynamical scattering matrix $S(t, E)$:

$$S_{\alpha\beta}(E_n, E) = \int \frac{dt'}{\mathcal{T}} e^{in\Omega t'} S_{\alpha\beta}(t', E). \tag{2.19}$$

Here $\mathcal{T}$ is the period of the dynamical scatterer which, as previously mentioned, is related to the frequency Ω via the relation: $\mathcal{T} = 2\pi/\Omega$. The matrix $S_{\alpha\beta}(t', E)$ describes the scattering of an incident particle with energy E exiting the scatterer at a later time t'. Expressing quantities in terms of this dynamical scattering matrix makes it easier to understand and analyse the time dependent features of transport. Thus, in what follows we will write currents in terms of Floquet scattering matrices and dynamical scattering matrices since the two equivalent expressions highlight different aspects. We will show how this matrix is calculated for certain devices in Chapter 3.

2.2.3.1 *Time-dependent current*

The creation (annihilation) operators of the electrons coming out of the scatterer $b^\dagger_\alpha(b_\alpha)$, can be related to the creation (annihilation) operators for the electrons going to the scatterer $a^\dagger_\alpha(a_\alpha)$ via the Floquet amplitude:

$$\hat{b}_\alpha(E) = \sum_\beta \sum_n S_{\alpha\beta}(E, E_n) \hat{a}_\beta(E_n) \tag{2.20a}$$

$$\hat{b}^\dagger_\alpha(E) = \sum_\beta \sum_n S^\dagger_{\alpha\beta}(E, E_n) \hat{a}^\dagger_\beta(E_n) \tag{2.20b}$$

Using the relations from Eq.(2.20a) and Eq.(2.20b) in the expression of the current, Eq.(2.13) as well as taking into account that the quantum mechanical average of the equilibrium operators is described by a Fermi function (Eq.(2.14)), one obtains:

$$I_\alpha(t) = \frac{e}{h}\int_{-\infty}^{\infty} dE \sum_{\beta}\sum_{l,m} e^{-il\Omega t} S^\dagger_{\alpha\beta}(E_m, E) S_{\alpha\beta}(E_{l+m}, E)\{(f_\beta(E) - f_\alpha(E_m)\}. \tag{2.21}$$

Substituting Eq.(2.19) into Eq.(2.21) we obtain the current in terms of the dynamical scattering matrix:

$$I_\alpha(t) = \frac{e}{h}\int dE \int \frac{dt'}{\mathcal{T}} \sum_{\beta,n} e^{in\Omega(t-t')} S^\dagger_{\alpha\beta}(t', E) S_{\alpha\beta}(t, E)\{f_\beta(E) - f_\alpha(E_n)\}. \tag{2.22}$$

This is the current corresponding to electrons coming from all leads β with energy E exiting the scatterer at time t through the lead α. Eqs. (2.21) and (2.22) are equivalent and define the time-dependent current arriving to reservoir α after exiting a dynamical scatterer which is defined by a time-dependent matrix.

In this expression we can see that one of the consequences of having a time-dependent scatterer is that there can be current flow even in the absence of bias ($V_\beta = V_\alpha \to f_\beta = f_\alpha$) due to the energy difference of the Fermi functions:

$$I_\alpha(t) = \frac{e}{h}\int dE \int \frac{dt'}{\mathcal{T}} \sum_{\beta,n} e^{in\Omega(t-t')} S^\dagger_{\alpha\beta}(t', E) S_{\alpha\beta}(t, E)\{f(E) - f(E_n)\}. \tag{2.23}$$

In contrast, in a stationary system current is always null whenever all the Fermi functions of the contacts are equal. Once we have obtained the time-resolved charge current we can easily obtain the time-averaged charge current, which is the quantity that we study in Chapter 3 from:

$$\bar{I}_\alpha = \int \frac{dt}{\mathcal{T}} I_\alpha(t). \tag{2.24}$$

This results in a compact expression for the charge current, similar to that for the stationary case:

$$\bar{I}_\alpha = \frac{e}{h}\int_{-\infty}^{\infty} dE \sum_{n}\sum_{\beta} |S_{\alpha\beta}(E_n, E)|^2 \big(f_\beta(E) - f_\alpha(E_n)\big). \tag{2.25}$$

In this case, the time-dependence is included in this expression through the Floquet quanta $E_n - E = n\hbar\Omega$, which change the energy of incoming particles even in the absence of inelasticities.

2.2.3.2 *Energy current*

Important information on the transport features can be extracted from the energy flow, as already stated in the introduction. As for the charge current, we write the energy current as a function of the field operators:

$$\begin{aligned}\hat{J}_\alpha(z_\alpha,t) = -i\frac{\hbar^2}{4m}\int dr_\perp\Big[\hat{\psi}^\dagger(\vec{r},t)\frac{\partial^2\hat{\psi}(\vec{r},t)}{\partial z_\alpha \partial t} - \frac{\partial\hat{\psi}^\dagger(\vec{r},t)}{\partial z_\alpha}\frac{\partial\hat{\psi}(\vec{r},t)}{\partial t} \\ + \hat{\psi}(\vec{r},t)\frac{\partial^2\hat{\psi}^\dagger(\vec{r},t)}{\partial z_\alpha \partial t} - \frac{\partial\hat{\psi}(\vec{r},t)}{\partial z_\alpha}\frac{\partial\hat{\psi}^\dagger(\vec{r},t)}{\partial t}\Big].\end{aligned} \tag{2.26}$$

Then, inserting the operators, given by Eq. (2.7), into Eq. (2.26) we obtain the expression of the energy current as usually employed [41–43], in terms of creation and annihilation operators:

$$\hat{J}_\alpha(t) = \frac{1}{h}\int_{-\infty}^{\infty} dE \int_{-\infty}^{\infty} dE' \frac{E+E'}{2} e^{i(E-E')t/\hbar}\left(b_\alpha^\dagger(E)b_\alpha(E') - a_\alpha^\dagger(E)a_\alpha(E')\right). \tag{2.27}$$

Again, our interest lies in the time-averaged current since this is the quantity studied in Chapter 3. The average energy current is obtained from

$$\bar{J}_\alpha = \int \frac{dt}{\mathcal{T}}\langle \hat{J}_\alpha(t)\rangle, \tag{2.28}$$

yielding an expression similar to that of the charge current but weighted by an energy E factor

$$\bar{J}_\alpha = \frac{1}{h}\int_{-\infty}^{\infty} dE E\left(\langle a_\alpha^\dagger(E)a_\alpha(E)\rangle - \langle b_\alpha^\dagger(E)b_\alpha(E)\rangle\right). \tag{2.29}$$

The energy is carried by the particles to the reservoirs. We assume the reservoirs to be big enough to absorb this energy and stay in thermal equilibrium. Substituting Eqs.(2.20a),(2.20b) and proceeding as done for the charge current, we obtain:

$$\bar{J}_\alpha = \frac{1}{h}\int_{-\infty}^{\infty} dE \sum_n \sum_\beta E_n |S_{\alpha\beta}(E_n,E)|^2\big(f_\beta(E) - f_\alpha(E_n)\big). \tag{2.30}$$

This expression corresponds to the energy flow to the reservoir α carried by scattered particles with energy E_n coming from reservoirs β with initial energy E. This expression can be rewritten in terms of the dynamical scattering matrices via the Fourier transform in Eq.(2.19). One finally obtains:

$$\begin{aligned}\bar{J}_\alpha = \frac{1}{h}\int_{-\infty}^{\infty} dE \sum_n \sum_\beta E_n \int \frac{dt}{\mathcal{T}} \int \frac{dt'}{\mathcal{T}} \\ e^{in\Omega(t-t')} S_{\alpha\beta}(t,E) S_{\alpha\beta}^\dagger(t',E)\{f_\beta(E) - f_\alpha(E_n)\}.\end{aligned} \tag{2.31}$$

We see from this expression, similarly to the case of the charge current, that the dynamical scatterer can cause energy flows even between reservoirs at the same chemical potential, i.e. there can be energy flow even if the Fermi functions are equal ($f_\alpha = f_\beta$).

2.2.3.3 *Spectral current*

A quantity that is not usually studied but that is going to be useful for us in Chapter 3 is the spectral current, or energy resolved particle current. This current is defined from the operator

$$\hat{\imath}_\alpha(E,E') = [\hat{b}_\alpha^\dagger(E)\hat{b}_\alpha(E') - \hat{a}_\alpha^\dagger(E)\hat{a}_\alpha(E')] \tag{2.32}$$

that quantifies the difference between incident and emitted particles in reservoir α at possibly different energies E, E'. It is related to the electrical current through the following relation

$$\hat{I}_\alpha(t) = \frac{-e}{h}\int_{-\infty}^{\infty} dE \int_{-\infty}^{\infty} dE' e^{i(E-E')t/\hbar}\, \hat{i}_\alpha(E,E'). \tag{2.33}$$

Then, the excess-energy distribution function $i_\alpha(E)$, which we also refer to as the spectral current, entering the two current expressions is given by [43, 44]

$$\begin{aligned} i_\alpha(E) &= \int_0^{\mathcal{T}} \frac{dt}{\mathcal{T}} \int_{-\infty}^{\infty} dE' e^{i(E-E')t/\hbar}\, \langle \hat{i}_\alpha(E,E')\rangle \\ &= \sum_\beta \sum_{n=-\infty}^{\infty} |S_{\alpha\beta}(E,E_n)|^2 [f(E_n) - f(E)] \ . \end{aligned} \tag{2.34}$$

It describes the distribution of incident electron and hole excitations with respect to the Fermi sea in reservoir α. The excess-energy distribution is related to the time-averaged charge current via an energy integral

$$\bar{I}_\alpha = \frac{e}{h}\int_{-\infty}^{\infty} dE i_\alpha(E). \tag{2.35}$$

The energy current can also be related to the spectral current via a relation similar to that of the charge current which takes into account a weight factor given by the energy E:

$$\bar{J}_\alpha = \frac{1}{h}\int_{-\infty}^{\infty} dE E i_\alpha(E) \tag{2.36}$$

By studying this quantity thus we have access to the energy-resolved properties of both charge and energy currents.

2.2.3.4 *Noise for the charge current*

More information on charge and energy transport can be inferred from the study of their fluctuations. There are two main sources of noise [45]: thermal noise, due to finite temperature effects causing only fluctuations of the occupation number at the reservoir and shot noise due to the discreteness of the charge combined with transmission probabilities at the scatterer smaller than 1. The quantum noise power in the time domain of the current is calculated from its correlation function [41, 46]:

$$P_{\alpha\beta}(t,t') = \frac{1}{2}\langle \Delta\hat{I}_\alpha(t)\Delta\hat{I}_\beta(t') + \Delta\hat{I}_\beta(t')\Delta\hat{I}_\alpha(t)\rangle. \tag{2.37}$$

Here $\Delta\hat{I} = \hat{I} - \langle\hat{I}\rangle$ is the operator of the current fluctuations. The $1/2$ factor is used so that the autocorrelator $P_{\alpha\alpha}$ is properly normalized. In this thesis we are interested in the zero-frequency noise, which is defined by:

$$P_{\alpha\beta} = \int_{-\infty}^{\infty} d(t-t') \int_0^{\Omega/2} \frac{dt}{\mathcal{T}} P_{\alpha\beta}(t,t') \tag{2.38}$$

Now, we aim to express this zero-frequency shot noise in terms of scattering matrices. We substitute the expression for the current in terms of operators, given by Eq.(2.10). Once we have the expression in terms of incoming and outgoing operators, one relates the incoming operators with the outgoing ones via the Floquet scattering matrices, see Eqs.(2.20a),(2.20b). Then using Eq.(2.14) to evaluate the quantum statistical average we finally obtain:

$$\begin{aligned}P_{\alpha\beta} =&\frac{e^2}{h}\int_{-\infty}^{\infty} dE\Big[F_{\alpha\alpha}(E,E) - \sum_n S^{\dagger}_{\beta\alpha}(E,E_n)S_{\beta\alpha}(E_n,E)F_{\alpha\alpha}(E,E) \\ &- \sum_n S^{\dagger}_{\alpha\beta}(E,E_n)S_{\alpha\beta}(E_n,E)F_{\beta\beta}(E,E) \\ &+ \sum_{p,n,m}\sum_{\gamma\delta} S^{\dagger}_{\alpha\gamma}(E_n,E)S_{\alpha\delta}(E,E_m)S^{\dagger}_{\beta\delta}(E_m,E_p)S_{\beta\delta}(E_p,E_n)F_{\gamma\delta}(E_n,E_m)\Big].\end{aligned} \tag{2.39}$$

Here for notation simplicity we have introduced the function $F_{\gamma\delta}(E_n,E_m) = \frac{1}{2}(f_\gamma(E_n)(1-f_\delta(E_m)+f_\delta(E_m)(1-f_\gamma(E_n))$.
In this work we are interested in the noise for a system at zero temperature and with no applied bias to it. Then, under these conditions, the noise power is reduced to pure shot noise:

$$P_{\alpha\beta} = \frac{e^2}{h}\int_{-\infty}^{\infty} dE \sum_{p,n,m}\sum_{\gamma\delta} F(E_n,E_m)S^{\dagger}_{\alpha\gamma}(E_n,E)S_{\alpha\delta}(E,E_m)S^{\dagger}_{\beta\delta}(E_m,E_p)S_{\beta\delta}(E_p,E_n). \tag{2.40}$$

Then, substituting the Floquet matrices by the corresponding Fourier transform of the dynamical scattering matrices, Eq.(2.19), we obtain:

$$\begin{aligned}P_{\alpha\beta} =&\frac{e^2}{h}\sum_q \mathrm{sign}(q)\int_{\mu_o - q\hbar\Omega}^{\mu_o} dE\int\frac{dt}{\mathcal{T}}\int\frac{dt'}{\mathcal{T}}e^{iq\Omega(t-t')} \\ &\sum_{\gamma,\delta} S^{\dagger}_{\alpha\gamma}(t,E_q)S_{\alpha\delta}(t,E)S^{\dagger}_{\beta\delta}(t',E)S_{\beta\delta}(t',E_q).\end{aligned} \tag{2.41}$$

2.3 GREEN'S FUNCTIONS APPROACH

When interactions such as electron-electron interactions (known as Coulomb interactions) have to be taken into account, one has to resort to a different approach than for the scattering matrix. A very powerful and useful tool to consider interacting systems subjected to time-dependent driving such as those addressed in Chapter 4 is the use Green's functions (GF's) formalism. In classical physics, Green's functions are a powerful tool for solving inhomogeneous differential equations. Similarly, when applied to quantum many-body problems, one can introduce Green's functions that obey a wave equation with a single inhomogeneity. These Green's functions are suited to study both equilibrium and non-equilibrium in many-body physics problems [47, 48].

For illustration, we first consider equilibrium GF's, using the second quantization formalism. We start by considering generic Hamiltonian $\mathcal{H}$ for an interacting system

$$\mathcal{H} = \mathcal{H}_0 + V \tag{2.42}$$

where $\mathcal{H}_0$ contains the non-interacting part and V is the interacting part of the Hamiltonian. We start by defining a time-ordered (also called causal) zero-temperature single-particle Green function

$$G(x,t;x',t') = \frac{i}{\hbar}\frac{\langle\Psi_o|\hat{T}\{\psi_H(x,t)\psi^{\dagger}_H(x',t')\}|\Psi_o\rangle}{\langle\Psi_o|\Psi_o\rangle} \tag{2.43}$$

Where $\mathcal{H}|\Psi_o\rangle = E_o|\Psi_o\rangle$ is the ground state of the Hamiltonian $\mathcal{H}$ and $\hat{T}\{\}$ is the time ordering operator. The time-ordering operator pushes the operator with the earlier time to the right:

$$\hat{T}\{A(x,t)B(x',t')\} = \theta(t-t')A(t)B(t') - \theta(t'-t)B(t')A(t) \tag{2.44}$$

The negative sign in front of the second term appears because of the interchange of fermionic operators caused by the time ordering.

The operators $\psi_H(x,t)$ are time dependent and evolve according to:

$$\psi_H(x,t) = e^{iHt/\hbar}\psi_H(x,0)e^{-iHt/\hbar} \tag{2.45}$$

Although in equilibrium, in principle, one Green's function is enough to describe the system, we define other GF's that are useful when dealing with non-equilibrium situations:

$$G^r(x,t;x',t') = -i\theta(t-t')\langle\{\Psi(x,t),\Psi^\dagger(x',t')\}\rangle \tag{2.46}$$

$$G^a(x,t;x',t') = i\theta(t'-t)\langle\{\Psi(x,t),\Psi^\dagger(x',t')\}\rangle \tag{2.47}$$

$$G^<(x,t;x',t') = i\langle\Psi^\dagger(x,t)\Psi(x',t')\rangle \tag{2.48}$$

$$G^>(x,t;x',t') = -i\langle\Psi(x,t)\Psi^\dagger(x',t')\rangle \tag{2.49}$$

These four functions are known respectively as retarded, advanced, lesser (than) and greater (than) Green's functions. The retarded function is only different from zero if $t > t'$ (it describes the response at time t to an event at time t') and the advanced function is the opposite, i.e. is only different from zero if $t < t'$. Their inhomogeneous differential equation is as the one for the time-ordered function $G(x,t;x',t')$. Furthermore, they are good tools to calculate physical responses and they have a nice analytic structure. The "lesser than" Green function is also called the particle propagator, while the "greater than" Green function, in which the order of the creation and annihilation operators are reversed, is called the hole propagator. Importantly, their differential equations do not have the singular inhomogeneous terms. They are directly linked to observables and kinetic properties, such as particle densities or currents [49]. In fact the lesser Green function is directly related to the occupation number $n(x)$:

$$\langle n(x)\rangle = -iG^<(x,t;x,t) \tag{2.50}$$

One of the most important properties of equilibrium theory is that all four functions $G, G^{r,a}, G^{>,<}$ are linked via the fluctuation-dissipation theorem [49].

The advantage of the time-ordered Green's function is the fact that it has a systematic perturbation expansion, as we show next. To realize the perturbation expansion of the time-ordered Green's function, we resort tot the interaction picture where the time evolution of operators is governed by the non-interacting part of the Hamiltonian whereas the evolution of the wavefunctions evolves following the full Hamiltonian. Then, we have that the wavefunctions evolve from time t' to t according to

$$\Psi(t) = S(t,t')\Psi(t') \tag{2.51}$$

where we dropped the position x for compactness. The time evolution is then governed by the S-matrix

$$S(t,t') = \hat{T}\exp\left(\frac{-i}{\hbar}\int_{t'}^{t}\hat{V}(\tau)d\tau\right) \tag{2.52}$$

The S-matrix is a time-ordered operator that depends on the interacting part of the Hamiltonian, written here as $\hat{V}(\tau)$. To obtain the ground state for the interacting wave-function we resort to the wave function of the non-interacting system ϕ_o and we evolve the system from time $-\infty$, when the system was in the absolute ground state, to t_0, when the system is in the ground state of the interacting Hamiltonian Ψ_o. That is, we evolve the system from $-\infty$ to t_0

$$|\Psi_o\rangle = S(t_0, -\infty)|\phi_o\rangle. \tag{2.53}$$

Equivalently we find

$$\langle\Psi_o| = \langle\phi_o|S(\infty, t_0). \tag{2.54}$$

With this in mind we are now able to rewrite the time-ordered Green's function in terms of the non-interacting ground state and the S-matrix

$$G(x,t;x',t') = \frac{i}{\hbar}\frac{\langle\phi_o|\hat{T}\{S(\infty,-\infty)\psi(x,t)\psi^\dagger(x',t')\}|\phi_o\rangle}{\langle\phi_o|S(\infty,-\infty)|\phi_o\rangle} \tag{2.55}$$

This expression is relevant because it allows for a systematic perturbation expansion of the Green's functions which leads to the Dyson equations. The calculation now proceeds by expanding $S(-\infty,\infty)$ in powers of $\hat{V}(t)$. By using Wick's theorem we are able to get rid of the terms in the denominator [49] which leads to

$$G(x,t;x',t') = -i\sum_{n=0}^{\infty}(-i)^n\int_{-\infty}^{+\infty} dt_1 ... dt_n \langle\phi_o|\hat{T}\psi(x,t)\psi^\dagger(x',t')\hat{V}(t_1)...\hat{V}(t_n)|\phi_o\rangle, \tag{2.56}$$

where we sum over connected Feynman diagrams. This equation is the starting point of many calculations involving Green's functions.

2.3.1 *Non-equilibrium Green's functions*

When dealing with non-equilibrium situations, that is, when the system is subjected to a time-dependent perturbation, one needs to consider an extra term in the Hamiltonian to account for this perturbation. Fortunately this term can be treated in a similar fashion to what we did for the interaction part of the Hamiltonian and the procedure to obtain the perturbation expansion for the Green's function in the non-equilibrium case resembles that of the equilibrium case.

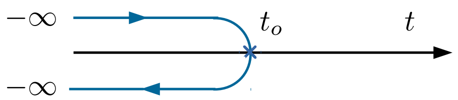

Figure 2.3: The time contour for the GF's is modified in a non-equilibrium situation.

In the case of non-equilibrium situation, the contour has to be modified and it does not run from $-\infty$ to $+\infty$ but rather from $-\infty$ to $-\infty$ so that it is assured that the final state is the same state as the initial state [48]. Hence, the time evolution now occurs in two directions, first from $-\infty$ to t_o and then from t_o to $-\infty$, see Fig. 2.3, being t_o an arbitrary time after the perturbation of the system and thus is governed by $S_+(t_o,-\infty)$ and $S_-(-\infty,t_o)$ for the forward and backward in time, respectively. To this end one has to change from time-ordered quantities to contour ordered quantities so that the order is not given by the time but rather the branch in the contour (an earlier time can come later in the contour since it goes forward, in one branch, and back in time in the other branch). With this transformation, one obtains that the contour-ordered GF has the same Dyson equation than the equilibrium GF. Then, the equilibrium and nonequilibrium theories are structurally equivalent. The only difference is the replacement of real axis integrals by contour integrals [49] that run on the (complex) Keldysh contour, see Fig. 2.3.

This has as a consequence that the Green's functions that we need to calculate are now defined over a contour and thus expressed in terms of contour integrals. One must then apply Langreth's rules, which are used to convert contour integrals into real time integrals, in what is called analytic continuation. Langreth theorem is used to solve the Dyson equation which contains integrals over the contour of products of GFs. The Langreth rules lead to the fact that we have to use the retarded, advanced, lesser and greater Green's functions in order to solve the Dyson equation and therefore to solve whichever problem we study.

Taking all of this into account we finally reach the Dyson equation for the contour-ordered Green's function in terms of the unperturbed Green's function G_0 and contour integrals:

$$\begin{aligned} G(x_1,t_1;x_1',t_1') &= G_0(x_1,t_1;x_1',t_1') \\ &+ \int d^3x_2 \int d^3x_3 \int_C d\tau_2 \int_C d\tau_3 G_0(x_1,t_1;x_2,\tau_2)\Sigma(\tau_2,\tau_3)G(x_3,\tau_3;x_1',t_1'), \end{aligned} \tag{2.57}$$

where Σ accounts for the effects of interactions. On top of that, we observe that the time integrals run over the contour C.

We now apply Langreth's continuation rules to convert the contour integrals into time integrals and we obtain the equation for the lesser GF. Using a compact notation, where the product of functions means an integration over time we obtain:

$$G^< = G_0^< + G_0^r \Sigma^r G^< + G_0^r \Sigma^< G^a + G_0^< \Sigma^a G^a. \tag{2.58}$$

We observe that the lesser GF is expressed in terms of itself, so we re-iterate for $G^<$ and we finally obtain

$$G^< = (1 + G^r \Sigma^r) G_0^< (1 + \Sigma^a G^a) + G^r \Sigma^< G^a \tag{2.59}$$

Which is an equivalent to what one obtains following Keldysh's method [49]. This equation is the time (not contour) defined Dyson equation for non-equilibrium Green's functions. One can go one step further by assuming that the term with $G_0^<$ vanishes since in the initial state, the system is not subjected to anything, it is totally in equilibrium, so its propagator must be zero:

$$G^< = G^r \Sigma^< G^a \tag{2.60}$$

2.3.2 *Illustrative example: non-interacting resonant levels*

To illustrate how the Green's functions are used, we take a simple model of a non-interacting resonant model and study how to obtain the different Green's functions in order to be able to characterize the charge current. In

Chapter 4 we expand this by studying the energy current in a resonant level model with interactions and a time-dependent driving. The following example serves to get familiar with the techniques that we are going to use later in the thesis, since the logical order is similar.

We start this example by writing the Hamiltonian of the system, which we split in three parts, one for the leads $\mathcal{H}_L$, one for the tunneling $\mathcal{H}_T$ and, one for the central region $\mathcal{H}_C$, similar to the division in Fig. 2.1. Therefore we have

$$\mathcal{H} = \mathcal{H}_L + \mathcal{H}_T + \mathcal{H}_C. \tag{2.61}$$

Considering that the leads are big reservoirs of electrons, the part corresponding to the leads describes a continuum of electrons which we take to be in equilibrium

$$\mathcal{H}_L = \sum_{k,\alpha} \epsilon_{k\alpha} c^\dagger_{k\alpha} c_{k\alpha}, \tag{2.62}$$

hence, the operators $c_{k\alpha}, c^\dagger_{k\alpha}$ describe the creation/annihilation of electrons of momentum k in reservoir α with the corresponding energy $\epsilon_{k\alpha}$. The central region, the resonant levels, is described by

$$\mathcal{H}_C = \sum_{m} \epsilon_m d^\dagger_m d_m, \tag{2.63}$$

with $d_m, d^\dagger_m$, the creation/annihilation operators for an electron in level m. Finally the tunneling processes between leads and the resonant levels are described by

$$\mathcal{H}_T = \sum_{k,\alpha,m} \left(V_{k\alpha,m} c^\dagger_{k\alpha} d_m + \text{h.c.} \right), \tag{2.64}$$

where the coupling constants between regions are given by $V_{k\alpha,m}$. We assume that this constants are known.

We are able now to calculate the currents in the leads, with the charge current given by the change in occupation at the leads [48]:

$$I_s = -e \frac{\partial}{\partial t} \langle N_s \rangle = -i \frac{e}{\hbar} [\mathcal{H}, N_s], \tag{2.65}$$

being N_s the occupation in lead s, given by

$$N_s = \sum_{k,\alpha \in s} c^\dagger_{k\alpha} c_{k\alpha}. \tag{2.66}$$

We evaluate the derivative of the occupation by taking the commutator of the Hamiltonian and we obtain

$$I_s = i \frac{e}{\hbar} \sum_{k,\alpha \in s, m} \left(V_{k\alpha,m} \langle c^\dagger_{k\alpha} d_m \rangle + V^*_{k\alpha,m} \langle d^\dagger_m c_{k\alpha} \rangle \right) \tag{2.67}$$

We see that this expression for the current can be cast in terms of the hybrid dot-reservoir GFs which are defined as:

$$G^<_{n,k\alpha}(t-t') \equiv i \langle c^\dagger_{k\alpha}(t') d_m(t) \rangle \tag{2.68}$$

$$G^<_{k\alpha,n}(t-t') \equiv i \langle d^\dagger_m(t') c_{k\alpha}(t) \rangle \tag{2.69}$$

Once we have written the expressions for these GFs we notice that they fulfill the following relation $G^<_{n,k\alpha}(t-t') = -\left[G^<_{k\alpha,n}(t-t')\right]^*$. Thus, we can re-express the charge current in lead s as

$$I_s = \frac{2e}{\hbar}\text{Re}\left(\sum_{k,\alpha\in s,m} V_{k\alpha,m}G^<_{n,k\alpha}(t,t)\right). \tag{2.70}$$

In order to obtain the charge current, we need to be able to obtain $G^<_{n,k\alpha}(t,t)$. To this end we use the equation-of-motion technique. This technique allows us to obtain an equation for the contour ordered GF $G_{n,k\alpha}(\tau,\tau')$. We start by considering the equation of motion for the time ordered Green's function $G^t_{n,k\alpha}(t-t')$:

$$-i\frac{\partial}{\partial t}G^t_{n,k\alpha}(t-t') = \frac{1}{\hbar}[\mathcal{H}, G^t_{n,k\alpha}(t-t')] \tag{2.71}$$

which is cast in terms of the time-ordered GF of the central region $G^t_{nm}(t-t') = -i\langle Td^\dagger_m(t')d_n(t)\rangle$:

$$\left(-i\frac{\partial}{\partial t} - \epsilon_{k\alpha}\right)G^t_{n,k\alpha}(t-t') = \sum_m G^t_{nm}(t-t')V^*_{k\alpha,m} \tag{2.72}$$

We notice that the factor $(\epsilon_{k\alpha} - i\frac{\partial}{\partial t})$ is equivalent to the inverse of the contact Green function operator $(g^t_{k\alpha})^{-1}$, acting from the right hand side. Then, by multiplying by the corresponding Green function $(g^t_{k\alpha})$ we find an expression for the time-ordered hybrid GF:

$$G^t_{n,k\alpha}(t-t') = \sum_m \int dt_1\, G^t_{nm}(t-t_1)V^*_{k\alpha,m}g^t_{k\alpha}(t_1-t'). \tag{2.73}$$

From the previous deduction on Green's functions, we know that in non-equilibrium, the expression is the same but defined in the contour and therefore

$$G_{n,k\alpha}(\tau,\tau') = \sum_m \int d\tau_1\, G_{nm}(\tau,\tau_1)V^*_{k\alpha,m}g_{k\alpha}(\tau_1,\tau'), \tag{2.74}$$

where we substituted all time-ordered GFs for contour-ordered GFs (τ, τ', τ_1 run on the contour). From this expression, by applying the continuation rules, we are able to obtain an expression for the desired GF:

$$G^<_{n,k\alpha}(t-t') = \sum_m \int dt_1\, V^*_{k\alpha,m}(G^r_{nm}(t-t_1)g^<_{k\alpha}(t_1-t') + G^<_{nm}(t-t_1)g^a_{k\alpha}(t_1-t')). \tag{2.75}$$

With this expression we are able to express the hybrid GF in terms of the central site Green function and the non-interacting lead Green functions that are known. In this manner the current calculation is reduced to the computation of the central part Green function (lesser and retarded) within some approximation since interactions prevent the possibility of an exact expression for it.

How to calculate these functions depends on the system details and we do not cover it here. The corresponding details on how this is carried about and how to proceed with the calculations when a driving is applied are given in Chapter 4 where we also calculate the energy current.

2.4 MASTER EQUATION APPROACH

We have studied how the scattering matrix and Green's functions approaches are used to characterize transport. Finally we expose the last formalism that we employ in this thesis, the master equation approach. The main idea behind this formalism is that one can characterize the system and its evolution through the occupation probabilities of the different states of the system. Then the rate equation describes the change in these probabilities through transition rates between the states.

We have discussed how the quantities characterizing thermoelectric transport are represented in the time-dependent case. Now, we change the focus to systems in the stationary regime and describe stationary quantum transport of charge and heat for a interacting quantum dot in Chapters 5 and 6.

When studying interacting systems in the Coulomb blockade regime, we resort to the master equation (or rate equation) approach to transport. The appeal of Coulomb blockade systems is that the electrons, under most general circumstances, are transferred one-by-one. This follows from the fact that the charge states are well defined, and most of the time the system is in a well defined charge state. This state, however, may change as a result of electron tunneling either to or from the leads from or to the quantum dot. Most probable changes are those involving only one tunneling electron, i.e. single-electron transfers [4].

When electron transport occurs as single-electron transfers, it is called sequential transport. The range of applicability is then determined by two scales: Γ which is the level broadening due to the fact that the dot is tunnel-coupled to the leads, and the temperature. Transport is then well described by sequential tunneling when only tunneling events of order lower than Γ^2 matter, that is when $h\Gamma \ll k_B T$.

2.4.1 *General formulation*

Let us consider a quantum dot with N electrons, coupled to (two) contacts. When transport occurs sequentially, as in the case of the Coulomb blockade regime, it is very useful to use the master equation approach. Since in this regime the charge states of the system are well-defined, one can fully characterize the system by using the charge states. Then, transitions between states happen as electron transfers. These (random) transitions happen with a certain probability, characterized by a rate $\Gamma^{\pm}(N)$ with the $\pm$ denoting whether the electron jumped out of or into the quantum dot and N the number of charges in the dot before the transition. This causes the dynamics of Coulomb blockade systems to be random and thus they need to be described by using a probabilistic approach, i.e. using probabilities of the system to be in a state with N charges at time t: $p_N(t)$. The time-evolution of this probabilities can then be obtained through a master equation [11] and since we are in the sequential regime, only terms that change the charge by one electron are present in the equation:

$$\frac{\partial p_N(t)}{\partial t} = \Gamma^{+}(N+1)p_{N+1}(t) + \Gamma^{-}(N-1)p_{N-1}(t) - (\Gamma^{-}(N) + \Gamma^{+}(N))p_N(t). \tag{2.76}$$

Here, rates $\Gamma^{\pm}$ are the total tunneling of one electron out of(+)/into(-) the dot, taking account transitions to the right (R) and to the left (L) reservoirs:

$$\Gamma^{\pm} = \Gamma_R^{\pm} + \Gamma_L^{\pm}. \tag{2.77}$$

If the parameters defining the system do not vary in time, neither do the rates defining the transitions. Then one is able to obtain a stationary solution to the equations (taking $\dot{p}_N(t) = 0$). This implies that the sum of probabilities must be unity: $\sum_N p_N = 1$, which can also be interpreted as particle conservation.

In this stationary regime one can obtain the current flowing through the system by simply "counting" electrons so that the current is just the difference between electrons flowing in one direction and the electrons flowing in the opposite:

$$I_L = e\sum_N (\Gamma_L^{+}(N) - \Gamma_L^{-}(N))p_N(t), \tag{2.78}$$

$$I_R = e\sum_N (\Gamma_R^{+}(N) - \Gamma_R^{-}(N))p_N(t). \tag{2.79}$$

By this definition, currents are positive when flowing out of the system and negative otherwise. In the stationary case it is automatically fulfilled that $I_L + I_R = 0$ so that the current is conserved.

Heat currents can also be calculated using this method:

$$J_L = \sum_N (\gamma_L^{+}(N) - \gamma_L^{-}(N))p_N(t), \tag{2.80}$$

$$J_R = \sum_N (\gamma_R^{+}(N) - \gamma_R^{-}(N))p_N(t). \tag{2.81}$$

One needs only substitute the corresponding transition rates for the charge Γ by transition rates for the heat γ [35].

2.4.1.1 *Tunneling rates*

To fully characterize the system, once we have the occupation probabilities and the current we are left only with calculating the transfer rates, which we call tunneling rates since all electron transfer events are tunneling events. Since the transitions considered here are between a discrete state of the dot and a continuum of states in the reservoir α, Fermi's Golden rule can be applied to calculate the tunneling rates. Since Fermi's golden rule attains transitions between states rather than simply electron transfers, we changed the notation (from $\Gamma^{\pm}(N)$ to $\Gamma^{\alpha}_{i\to j}$) to accommodate that fact but the rates describe the same processes [1]. Then the transition rates are:

$$\Gamma^{\alpha}_{i\to j} = \Gamma_\alpha \int_{-\infty}^{\infty} d\epsilon \rho_i(\epsilon - \mu_i)\bar{\rho}_j(\epsilon - \mu_j). \tag{2.82}$$

In this notation then, $\rho_i(\epsilon), \bar{\rho}_i(\epsilon)$ represent the electron and hole density of states. If they represent a state of the dot, $\rho_i(\epsilon) = \bar{\rho}_i(\epsilon) = \delta(\epsilon)$. When they describe electronic states in the reservoirs the densities are $\rho_i(\epsilon) = f_\alpha(\epsilon)$, $\bar{\rho}_i(\epsilon) = 1 - f_\alpha(\epsilon)$, with $f_\alpha(\epsilon)$ the Fermi function. That is: $f_\alpha(\epsilon) =$

---

[1] E.g. if i denoted a state of the dot and j a state of the reservoir, the rate that we are calculating describes a tunneling out of the dot and is therefore a Γ^{+}

$\frac{1}{1+e^{\epsilon/k_B(T_\alpha)}}$ where k_B is Boltzmann's constant and T_α is the temperature of the reservoir.

Similarly, we calculate the tunneling rate for the heat current:

$$\gamma^{\alpha}_{i\to j} = -\Gamma_\alpha \int_{-\infty}^{\infty} d\epsilon(\epsilon-\mu_\alpha)\rho_i(\epsilon-\mu_i)\bar{\rho}_j(\epsilon-\mu_j). \tag{2.83}$$

In the case of the tunneling rate for the heat current we need to weigh the integral with the corresponding energy $\epsilon - \mu_\alpha$, being μ_α the electrochemical potential of the reservoir [35].

2.4.2 *Master equation with an environment: P(E)-theory*

Tunneling events are frequently affected by fluctuations of the electromagnetic environment [50]. To fully account for such quantum fluctuations we adopt the $P(E)$ theory [50, 51] of dynamical Coulomb blockade, recently revisited to consider heat fluxes [31, 52]. The spirit of the $P(E)$ theory relies on the fact that individual tunneling events involve energy exchange processes. The Dirac-delta accounting for energy conservation in the (Fermi golden rule) tunneling rates is relaxed into a broadened distribution $P(E)$. In the context of this theory the environment of the systems is considered to be a group of harmonic oscillators describing bosonic modes.

The function $P(E)$ that gives name to the theory describes the influence of the environment on the system. It can be interpreted as the probability that a tunneling particle absorbs ($E < 0$) or emits ($E > 0$) an energy E from/to the external circuit (i.e. the environment). Since $P(E)$ is a probability function, it has to fulfill some conditions:

$$\int_{-\infty}^{\infty} P(E)dE = 1, \tag{2.84}$$

$$P(E) \geqslant 0. \tag{2.85}$$

The function $P(E)$ can be obtained from a circuit theory analysis of the system. The system that we take into account, see Chapter 5, is a single quantum dot, i.e. a double junction defining a Coulomb island, where each of the junctions j has a specific capacitance C_j. The role of the environment is modeled as a circuit that has its own impedance. More specifically for each junction j in a double junction the $P(E)$ function reads

$$P_j(E) = \frac{1}{2\pi\hbar}\int dt \exp\left(\kappa_j^2 J(t) + \frac{i}{\hbar}Et\right). \tag{2.86}$$

where $\kappa_j = 1 - C_j/C$ is a measure of the asymmetry of the two junctions with $C = \sum_j C_j$. We introduced the (phase-phase) correlation function

$$J(t) = \frac{2h}{e^2}\int_0^{\infty} \frac{d\omega}{\omega} \mathrm{Re}[\tilde{Z}(\omega)]c(\omega, T_0), \tag{2.87}$$

that contains all the information of the environment fluctuations, with[51]:

$$c(\omega, T_0) = \coth\left(\frac{\hbar\omega}{2k_BT_0}\right)[\cos(\omega t - 1) - i\sin\omega t]. \tag{2.88}$$

For a realistic environment one usually has to evaluate P(E) numerically. In Chapter 5 we restrict ourselves to a high impedance ohmic environment for which the P(E) can be calculated analytically.

To apply $P(E)$ theory it is assumed that coupling between the different electron systems is weak and that the temperature of the electrons of the environment is high enough so that transport can be described by the lowest order Fermi golden rule, i.e. in the sequential tunneling regime. Also, it is assumed that environment relaxation is much faster than the tunneling rate. Then, the effect of the environment modifies the tunneling rates (Eqs. (2.82) and (2.83)) as follows:

$$\Gamma^{\alpha}_{i\to j} = \Gamma_{\alpha} \int_{-\infty}^{\infty} d\epsilon_i \int_{-\infty}^{\infty} d\epsilon_j \rho_i(\epsilon_i - \mu_i)\bar{\rho}_j(\epsilon_j - \mu_j) P_{\alpha}(\epsilon_i - \epsilon_j). \qquad (2.89)$$

Again, in the case of the tunneling rate for the heat current we need to weigh the integral with the corresponding energy $\epsilon_{i/j} - \mu_{\alpha}$, so that $\epsilon_{i/j}$ is always the integrated energy and μ_{α} the electrochemical potential of the reservoir.

$$\gamma^{\alpha}_{i\to j} = -\gamma_{\alpha} \int_{-\infty}^{\infty} d\epsilon_i \int_{-\infty}^{\infty} d\epsilon_j (\epsilon_{i,j} - \mu_{\alpha}) \rho_i(\epsilon_i - \mu_i)\bar{\rho}_j(\epsilon_j - \mu_j) P_{\alpha}(\epsilon_i - \epsilon_j). \qquad (2.90)$$

Here the weighing energy factor $(\epsilon_{i,j} - \mu_{\alpha})$ should be taken so that $\epsilon_{i,j}$ is always the integrating energy corresponding to the reservoir, so that if we take e.g. i to represent the reservoir, then $\epsilon_{i,j} = \epsilon_i$. In this way, we are able to model environmental effects by modifying the tunneling rates for charge (Eq. (2.82)) and heat (Eq. (2.83)).

Part II

THE CONTENT

3

TWO-PARTICLE EFFECTS IN AN INTERFEROMETER FED BY SINGLE-PARTICLE SOURCES

3.1 INTRODUCTION

In this chapter we investigate the quantum interference effects detected as a result of the injection of particles from a single particle source (SPS) into a Mach-Zehnder interferometer (MZI). The signal detected at the output shows intriguing features due to the energy-dependent transmission of the MZI. Additionally, a second SPS is introduced injecting particles into one of the interferometer arms only. The setup is chosen such that two-particle effects, namely the collision and absorption of particles [53], can happen in different parts of the interferometer.

Single particle sources are devices that coherently emit single particles into a nano-electronic circuit. This coherent emission of single particles can be achieved via a time-dependent modulation of mesoscopic structures. Recent developments such as the creation of Lorentzian current pulses carrying exactly one electron charge [54–56], the realization of periodically driven mesoscopic capacitors as single-particle sources by time-dependent gating [20, 22, 57], the emission of particles from quantum dots with surface-acoustic waves [58–60], as well as particle emission from dynamical quantum dots [61–63] are prime examples of this type of sources. Nano-electronic devices fed by these single-particle sources allow for the observation of controlled and tunable quantum-interference and multiple-particle effects and even for the combination of both [21, 22, 53, 64–75].

To observe quantum-interference effects we use the electronic equivalent of a Mach-Zehnder interferometer (MZI), [26–28, 76] as sketched in Fig. 3.1 a), which can be realized by edge states in Quantum Hall systems with the help of quantum point contacts (QPCs). It has been shown that the investigation of the output current of an MZI, when fed by a single-particle source (SPS), such as the one realized by Fève *et al.* [20], see also Fig. 3.1 b), allows for the extraction of an electronic single-particle coherence time. More generally, it carries interesting new features of coherence properties of the traveling particles. [77–81] The combination of several of these sources makes it possible to study controlled two-particle effects, for example the electronic analogue of the Hong-Ou-Mandel effect [21, 66], which was realized experimentally by Bocquillon *et al.* [22] and Dubois *et al.* [56] The combination of several MZIs and SPSs is a possibility to create and detect time-bin entanglement [67, 82, 83]. However, the impact of controlled multiple-particle effects on the interference pattern detected in electronic interferometers was studied only sparsely [70, 84] and leaves a number of open questions concerning the interplay of the two effects.

We use the setup shown in Fig. 3.1 a) to investigate the effect of particle emission (and absorption) from the second source and find that it has a tunable impact on the interference effects obtained from the signal of the first SPS. In order to visualize this impact, we study the spectral properties of the detected signal, the charge and energy currents, [85] as well as the charge-current noise, [86] based on a Floquet scattering-matrix approach [43]. This means that we neglect Coulomb interaction, which can lead to

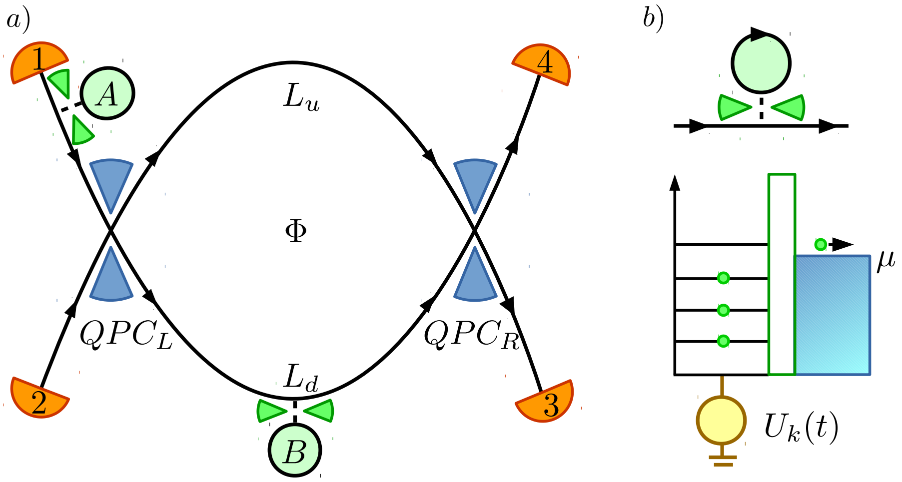

Figure 3.1: a) Schematic of an electronic MZI. Transport takes place along edge states (black lines; arrows indicate their chirality). Quantum point contacts, $\mathrm{QPC_L}$ and $\mathrm{QPC_R}$, act as beam splitters. All the reservoirs are grounded and particles are injected into the system by two single-particle sources $\mathrm{SPS_A}$ and $\mathrm{SPS_B}$. Charge and energy currents are measured at reservoir 4. b) Schematic of an SPS, which is realized by a mesoscopic capacitor. It is implemented as a circular edge state and periodically driven by a potential $U_k(t)$, emitting one electron and one hole per period.

relaxation and decoherence [87] of the injected single particles and which is expected to modify our results at most on a quantitative level [88].

This chapter is organized as follows. We introduce the system and the investigated observables, as well as the scattering matrix approach employed by us in Sec. 3.2. The presentation of results starts with the spectral current, the charge and the energy currents, and the charge noise for the case of an interferometer fed by one SPS only, in Sec. 3.3. In Sec. 3.4, this is followed by a study of the same quantities in an MZI where particles from two SPSs can collide or where particles can get absorbed. Finally conclusions for this chapter are given in Section 3.5. In Appendix A, all relevant analytic results which are not presented explicitly in the main text are summarized.

3.2 MODEL AND TECHNIQUE

3.2.1 *Mach-Zehnder interferometer with two single-particle sources*

The electronic analogue of an MZI can be realized in a two-dimensional electron gas in the quantum Hall regime [26–28] using the chiral edge states for transport, as sketched in Fig.3.1 a), see also Section 1.3.2. Edge states are represented as black lines with arrows indicating the chirality. Two quantum point contacts, QPC_ℓ, $\ell = L, R$, with energy-independent transmission (reflection) amplitudes t_ℓ (r_ℓ) and the related transmission (reflection) probabilities $T_\ell = |t_\ell|^2$ ($R_\ell = |r_\ell|^2 = 1 - T_\ell$) act as beam splitters. The incoming electronic signal is reflected or transmitted at $\mathrm{QPC_L}$, into the upper arm (u) or the lower arm (d) of the interferometer, with the respective length L_u and L_d. At $\mathrm{QPC_R}$ the signal from both arms is recombined and is finally reflected or transmitted into reservoir 3 or 4. Assuming a linear dispersion with the drift velocity v_D, the traversal time of the interferometer arms is given by $\tau_u = L_u/v_D$ and $\tau_d = L_d/v_D$.

The phase acquired by the electronic wave function due to the propagation along the upper and the lower arm is given by $\phi_{u/d} = \Phi_{u/d} + E\tau_{u/d}/\hbar$ with the energy-dependent dynamical phase $E\tau_{u/d}/\hbar$ and the energy-independent part, $\Phi_{u/d}$, including the magnetic-flux contribution Φ_0, i.e. the magnetic flux penetrating the interferometer. The energy and charge currents observed at the detector are known to depend on the difference between the two phases, $\Delta\phi(E,\Phi) = \Phi + E\Delta\tau/\hbar$ with $\Phi = \Phi_u - \Phi_d$ and the detuning, $\Delta\tau = \tau_u - \tau_d$ of the traversal times of the interferometer, which is a measure of the imbalance of the interferometer. We assume the extensions of the MZI to be smaller than the dephasing length, which can be limited due to environment- and interaction-induced effects. [89–93] The electronic reservoirs, $\alpha = 1, 2, 3, 4$, are at temperature θ and they are grounded at the equilibrium chemical potential μ, which we take as the zero of energy from here on.

Particles - electrons and holes - are injected into the MZI by means of a controllable single-particle source, SPS_A, situated at the channel incoming from reservoir 1. A second single-particle emitter, SPS_B, is placed at the lower arm at $L_d/2$. Inspired by the experimental realization by Fève *et* al. [20], we take the SPSs to be mesoscopic capacitors Section 1.2.1.1 subjected to a time-dependent periodic driving as sketched in Fig. 3.1 b). These SPS_k, with k =A,B, consist of a quantum dot (acting as a capacitor) with a discrete spectrum, weakly coupled to an edge state through a QPC_k. The energy levels of the quantum dot are controlled by a periodically oscillating time-dependent gate voltage $U_k(t)$, with period $\mathcal{T} = 2\pi/\Omega$ and frequency Ω, such that one of the levels is sequentially driven above and below the electro-chemical potential μ. This triggers the emission of an electron from source k = A,B at time t_k^e, during one half of the driving period, and the emission of a hole (which is equivalent to the absorption of an electron) at a time t_k^h during the other half of the period.

The current pulses injected from SPS_A result in an interference pattern in the detected observables at the output of the interferometer [72, 74]. Oppositely, those emitted from SPS_B do not create an interference pattern on their own since they only travel along the lower arm.

The synchronization of the two sources, obtained by tuning the emission times $t_k^{e/h}$, results in absorption processes (i.e. the overlap of a current pulse carrying an electron with a current pulse carrying a hole) at SPS_B or in collisions of particles (i.e. the overlap of current pulses carrying an electron (or hole) each) at SPS_B or QPC_R. It has been shown in Ref. [70] that these collisions and absorptions add a non-trivial phase to the interference pattern in the time-resolved current at the detector at the output of the MZI, which can even lead to the full suppression of interference in the detected average charge current.

3.2.2 *Scattering matrix formalism*

We describe the transport properties of the above introduced system with the help of a Floquet scattering matrix formalism Section 2.2. Due to the time-periodic modulation of the SPSs, coherent inelastic scattering can take place. Thus the scattering matrix elements $S_{\alpha\beta}(E_n, E_m)$, connect the incoming currents from reservoir β at energy $E_m = E + m\hbar\Omega$ to the outgoing currents at reservoir α at energy $E_n = E + n\hbar\Omega$ differing from the incoming energy by an integer multiple $n - m$ of the energy quantum $\hbar\Omega$ given by the driving frequency (Floquet quanta) [43].

These Floquet scattering matrices thus relate the creation and annihilation operators, $\hat{b}^{\dagger}_{\alpha}(E)$ and $\hat{b}_{\alpha}(E)$, of particles incident in reservoir α to the respective operators for particles emitted from reservoir β onto the scattering region, $\hat{a}^{\dagger}_{\beta}(E)$ and $\hat{a}_{\beta}(E)$ via

$$\hat{b}^{\dagger}_{\alpha}(E) = \sum_{\beta} \sum_{n=-\infty}^{\infty} S^{*}_{\alpha\beta}(E, E_n)\hat{a}^{\dagger}_{\beta}(E_n), \tag{3.1}$$

(and equivalently for the annihilation operators).

Furthermore, the Floquet scattering matrices can be conveniently written in terms of the partial Fourier transforms,

$$S_{\alpha\beta}(E_n, E_m) = \int_0^{\mathcal{T}} \frac{dt}{\mathcal{T}} e^{i(n-m)\Omega t} S_{\text{in},\alpha\beta}(t, E_m), \tag{3.2a}$$

$$S_{\alpha\beta}(E_n, E_m) = \int_0^{\mathcal{T}} \frac{dt}{\mathcal{T}} e^{-i(n-m)\Omega t} S_{\text{out},\alpha\beta}(E_n, t). \tag{3.2b}$$

Here, $S_{\text{in},\alpha\beta}(t, E_m)$ is the dynamical scattering amplitude for a current signal incoming from reservoir β at energy E_m to be detected at a time t at reservoir α, while $S_{\text{out},\alpha\beta}(E_n, t)$ is the dynamical scattering matrix for a current signal incoming from reservoir β at time t to be found at energy E_n at reservoir α. [57]

In this chapter, we are interested in the regime of adiabatic driving, namely where the dwell time of a particle in the mesoscopic capacitor constituting the SPS is much smaller than the modulation period $\mathcal{T}$ of the driving potential. [53] Note that this is an assumption on the time-scales describing the SPSs and their driving only, and does not concern the time-scales describing the traversal of the interferometer which can be of arbitrary magnitude. The result is that time-dependent current pulses of Lorentzian shape are emitted into the MZI. This is similar to the recently realized "levitons", [56] which are of Lorentzian shape as well. In the adiabatic regime, the dynamical scattering matrices describing the subsystem of an SPS, $S_k(t)$ for $k = $ A,B, are energy independent on the scale of the driving frequency and $S_{\text{in},k}(t, E) = S_{\text{in},k}(t, \mu) = S_{\text{out},k}(E, t) = S_{\text{out},k}(\mu, t) \equiv S_k(t)$. For weak coupling and slow driving of the sources, these scattering matrices are given by, [66]

$$S_k(t) = n^e_k \frac{t - t^e_k + i\sigma_k}{t - t^e_k - i\sigma_k} + n^h_k \frac{t - t^h_k - i\sigma_k}{t - t^h_k + i\sigma_k} \,. \tag{3.3}$$

The emission times of electrons and holes, t^i_k, and the width of the emitted current pulses, σ_k, are directly related to the properties of the sources and are thus tunable [53]. We introduced the variables n^i_k in order to distinguish whether the emission of an electron or of a hole is treated. This variable takes the value $n^{e/h}_k = 1$ if a time-interval where an electron/hole is emitted from source k is considered, and $n^{e/h}_k = 0$ otherwise. We assume that electron and hole emission happen at times which differ from each other by much more than the pulse width σ_k, $|t^e_k - t^h_k| \gg \sigma_k$, meaning that the different current pulses emitted from the same source are well separated. The full system, comprising the sources and the MZI, is described by a scattering matrix that contains the following elements:

$$S_{\text{in},41}(t,E) = S_A(t-\tau_u) r_L e^{i\phi_u(E)} r_R + S_A(t-\tau_d) t_L S_B(t-\frac{\tau_d}{2}) e^{i\phi_d(E)} t_R, \tag{3.4a}$$

$$S_{\text{in},42}(t,E) = t_L e^{i\phi_u(E)} r_R + r_L S_B(t-\frac{\tau_d}{2}) e^{i\phi_d(E)} t_R, \tag{3.4b}$$

$$S_{\text{in},31}(t,E) = S_A(t-\tau_u) r_L e^{i\phi_u(E)} t_R + S_A(t-\tau_d) t_L S_B(t-\frac{\tau_d}{2}) e^{i\phi_d(E)} r_R, \tag{3.4c}$$

$$S_{\text{in},32}(t,E) = t_L e^{i\phi_u(E)} t_R + r_L S_B(t-\frac{\tau_d}{2}) e^{i\phi_d(E)} r_R. \tag{3.4d}$$

All other matrix elements have no relevance for the quantities studied in this chapter. Similar expressions are found for the corresponding elements of the matrix $S_{\text{out},\alpha\beta}(E,t)$, which are calculated following the same logic and are not needed for the final results obtained here.

3.2.3 *Observables*

The charge current, the energy current, and their spectral functions, as well as the zero-frequency charge-current noise are the observables that we use to study our system. In this section we introduce their definitions.

We start from the time-resolved charge [45] and energy [94–96] current operators in lead α, $\hat{I}_\alpha(t)$ and $\hat{J}_\alpha(t)$, defined as

$$\hat{I}_\alpha(t) = \frac{-e}{h}\int_{-\infty}^{\infty} dE \int_{-\infty}^{\infty} dE' e^{i(E-E')t/\hbar}\, \hat{\imath}_\alpha(E,E'), \tag{3.5}$$

$$\hat{J}_\alpha(t) = \frac{1}{h}\int_{-\infty}^{\infty} dE \int_{-\infty}^{\infty} dE' e^{i(E-E')t/\hbar} \left[\frac{(E+E')}{2}\right] \hat{\imath}_\alpha(E,E') \tag{3.6}$$

with the electron charge $-e$, considering $e>0$. Both quantities are defined by the operator $\hat{\imath}_\alpha(E,E') = [\hat{b}^\dagger_\alpha(E)\hat{b}_\alpha(E') - \hat{a}^\dagger_\alpha(E)\hat{a}_\alpha(E')]$, that quantifies the difference between incident and emitted particles in reservoir α. In turn, the operators for incident particles in α are related to particles emitted from β, see Eq. (3.1).

We are interested in the time-averaged charge and energy currents, $\bar{I}_\alpha$ and $\bar{J}_\alpha$, which are given by the time integral over the expectation values of Eqs. (3.5) and (3.6),

$$\bar{I}_\alpha = \int_0^{\mathcal{T}} \frac{dt}{\mathcal{T}} \langle \hat{I}_\alpha(t)\rangle, \tag{3.7}$$

$$\bar{J}_\alpha = \int_0^{\mathcal{T}} \frac{dt}{\mathcal{T}} \langle \hat{J}_\alpha(t)\rangle\ . \tag{3.8}$$

Here, $\langle\dots\rangle$ indicates a quantum-statistical average. The quantum-statistical average of particles incoming from the reservoirs is given by the Fermi function $f_\alpha(E) = [1+\exp(E/k_B\theta_\alpha)]^{-1}$, namely the equilibrium distribution function of the reservoirs, $\langle\hat{a}^\dagger_\alpha(E)\hat{a}_\alpha(E')\rangle = f_\alpha(E)\delta(E-E')$. Substituting Eq. (3.1) into Eqs. (3.5) and (3.6) and taking the time-average of the expectation values as given in Eqs. (3.7) and (3.8), we find

$$\bar{I}_\alpha = \frac{-e}{h}\int_{-\infty}^{\infty} dE\ i_\alpha(E), \tag{3.9}$$

$$\bar{J}_\alpha = \frac{1}{h}\int_{-\infty}^{\infty} dE\ E\ i_\alpha(E). \tag{3.10}$$

The excess-energy distribution function $i_\alpha(E)$, which we also refer to as the spectral current, entering the two current expressions is given by [43, 44]

$$\begin{aligned} i_\alpha(E) &= \int_0^{\mathcal{T}} \frac{dt}{\mathcal{T}} \int_{-\infty}^{\infty} dE' e^{i(E-E')t/\hbar} \langle \hat{i}_\alpha(E,E') \rangle \\ &= \sum_\beta \sum_{n=-\infty}^{\infty} |S_{\alpha\beta}(E,E_n)|^2 [f(E_n) - f(E)] \, . \end{aligned} \tag{3.11}$$

It describes the distribution of incident electron and hole excitations with respect to the Fermi sea in reservoir α. [1]

Finally, we are interested in the zero-frequency charge-current noise [86], which is known to be sensitive to two-particle effects,

$$\mathcal{P}_{\alpha\beta} = \frac{1}{2} \int_0^{\mathcal{T}} \frac{dt'}{\mathcal{T}} \int_{-\infty}^{\infty} d(t-t') \left[\langle \hat{I}_\alpha(t) \hat{I}_\beta(t') + \hat{I}_\beta(t') \hat{I}_\alpha(t) \rangle - 2 \langle \hat{I}_\alpha(t) \rangle \langle \hat{I}_\beta(t') \rangle \right]. \tag{3.12}$$

In the following, we focus on the zero-temperature regime. The Fermi functions are therefore replaced by sharp step functions, $[f(E_n) - f(E)] \to [\Theta(-E_n) - \Theta(-E)]$. Then, the expression for the zero-frequency noise power assumes a rather compact form. Substituting Eqs. (3.1), (3.2) and (3.5) into Eq. (3.12), we find

$$\begin{aligned} \mathcal{P}_{\alpha\beta} = \frac{e^2}{2h} \sum_{m=-\infty}^{\infty} \text{sign}(m) \int_{-m\hbar\Omega}^{0} dE \int_0^{\mathcal{T}} \frac{dt}{\mathcal{T}} \int_0^{\mathcal{T}} \frac{dt'}{\mathcal{T}} e^{im\Omega(t'-t)} \\ \sum_{\gamma,\delta} \left[S^*_{\alpha\gamma}(t,E) S_{\alpha\delta}(t,E_m) S^*_{\beta\delta}(t',E_m) S_{\beta\gamma}(t',E) \right]. \end{aligned} \tag{3.13}$$

In what follows all currents are evaluated at the detector situated at reservoir $\alpha = 4$. We thus suppress the reservoir index, taking $i_4(E) \equiv i(E)$, $\bar{I}_4 \equiv \bar{I}$, $\bar{J}_4 \equiv \bar{J}$. Furthermore, we are interested in the cross-correlation function of charge currents, for which we have $\mathcal{P}_{34} = \mathcal{P}_{43} \equiv \mathcal{P}$. Note that the time average over one period will always include electron as well as hole contributions from the different time-dependently driven SPSs. In the next sections we will separate the contributions by adding superscripts e and h to the considered quantities and by using the variables $n_k^{e/h}$, previously introduced in the context of Eq. (3.3), to highlight the origin of the different terms stemming from electron and hole contributions.

3.3 SINGLE-PARTICLE INTERFERENCE - WAVE PACKET PICTURE

In order to get a better grasp on the physics and the behavior of the studied quantities, we start by considering the case where only source SPS_A is active, see Fig. 3.2. In this case, the injection of particles from A leads to an interference pattern at the output of the MZI (measured in reservoir 4). The excess-energy distribution function (or spectral current) at the detector reads

$$i_{\text{MZI},A}(E,\Phi) = i^{\text{cl}}_{\text{MZI},A}(E) + i^{\text{int}}_{\text{MZI},A}(E,\Phi) \tag{3.14a}$$

---

[1] The energy-resolved spectral current should not be confused with the time-resolved current pulses studied e.g. in Ref. [70].

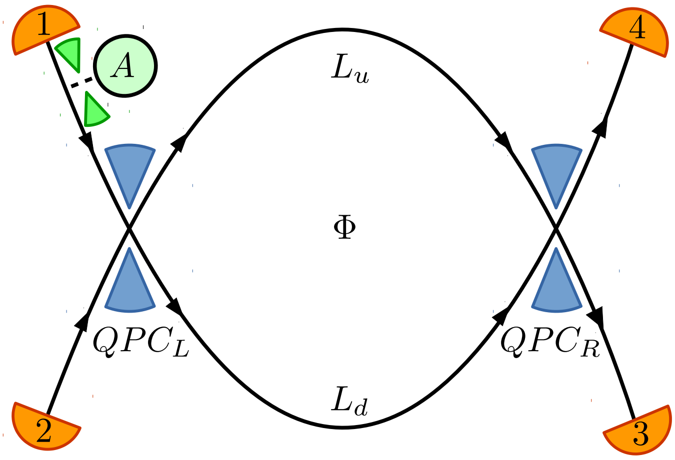

Figure 3.2: Schematic of an electronic MZI. Transport takes place along edge states (black lines; arrows indicate their chirality). Quantum point contacts, QPC_L and QPC_R, act as beam splitters. All the reservoirs are grounded and particles are injected into the system by the single-particle source SPS_A. Charge and energy currents are measured at reservoir 4.

where the classical part and the interference part, which oscillates as a function of the magnetic-flux dependent phase $\phi(E, \Phi)$, are given by

$$i^{cl}_{MZI,A}(E) = (R_L R_R + T_L T_R)\left[i^e_A(E) + i^h_A(E)\right], \tag{3.14b}$$

$$i^{int}_{MZI,A}(E,\Phi) = -2\gamma \cos\Delta\phi(E,\Phi)\left[i^e_A(E) + i^h_A(E)\right]. \tag{3.14c}$$

Here, we have defined $\gamma = t^*_L r_L t_R r^*_R = \sqrt{T_L T_R R_L R_R}$. The excess-energy distribution function contains both electron- and hole-like contributions from the emission of the different types of particles from SPS_A. The particles injected by SPS_A into the edge states are described by the excess-energy distribution functions [65]

$$i^e_A(E) = \Theta(E) n^e_A 2\Omega\sigma_A e^{-2E\sigma_A/\hbar}, \tag{3.15}$$

$$i^h_A(E) = -\Theta(-E) n^h_A 2\Omega\sigma_A e^{2E\sigma_A/\hbar} \tag{3.16}$$

of electron-like and hole-like excitations, with contributions in the positive, respectively the negative, energy range only. Note that, according to the definition given in Eq. (3.11), the excess-energy distribution function of the hole-like excitations, $i^h_\alpha(E)$, is always negative, which is consistent with the interpretation of a “hole" as a missing electron in the Fermi sea. [2]

The term $i^{cl}_{MZI,A}(E)$, see Eq. (3.14b), is of classical nature and it is given by the sum of contributions from particles reaching the detector after traveling the upper or the lower arm with a probability $R_L R_R$, respectively $T_L T_R$. In contrast, $i^{int}_{MZI,A}(E,\Phi)$, see Eq. (3.14c), shows the wave nature of the emitted signals. It is due to the interference between waves propagating along the upper and the lower arms.

The interference effects on the electronic contribution to the excess-energy distribution function, $i^e_{MZI,A}(E,\Phi)$, is shown in Fig. 3.3 a) as a flux dependence for the almost perfectly balanced case, $\Delta\tau \leqslant \sigma_A$. The excess-energy

---

[2] When introducing the magnetic field, which determines the direction of propagation of the chiral edge states, as an additional variable to the excess-energy distribution function, the equality $i^e_\alpha(E, \mathbf{B}) = -i^h_\alpha(-E, -\mathbf{B})$ relates the excess-energy distribution function of electrons, i^e_α, to the one of holes, i^h_α.

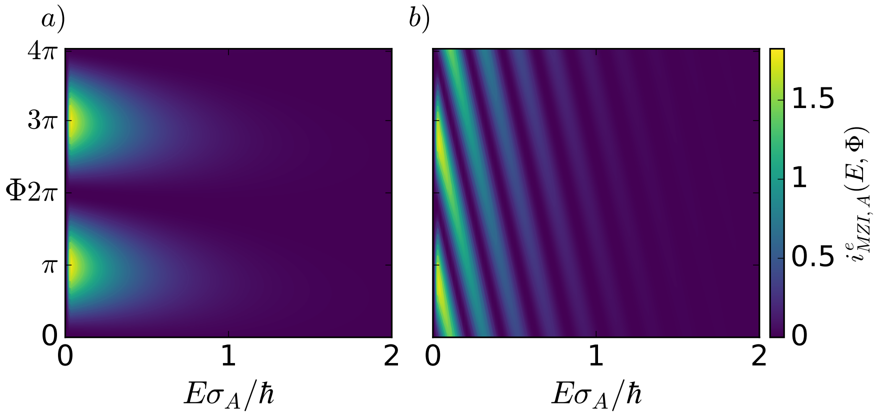

Figure 3.3: Electronic part of the excess-energy distribution function, $i^e_{MZI,A}(E,\Phi)$ as a function of the energy E in units of $\hbar/\sigma_A$ and the magnetic-flux-dependent phase Φ. a) Almost perfectly balanced interferometer, with $\Delta\tau = 0.01\sigma_A$. b) Unbalanced interferometer, with $\Delta\tau = 20\sigma_A$. In all plots, the transmission probabilities are given by $T_L = T_R = 0.5$.

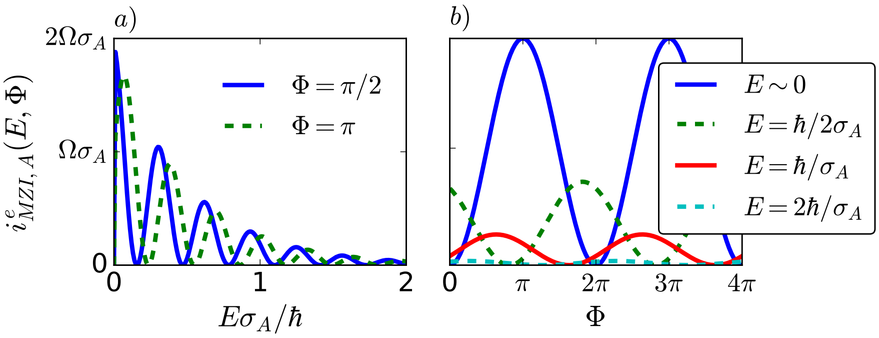

Figure 3.4: Cuts through the 3D plot of Fig. 3.3 b) at different energies, E, and phases, Φ. In all plots, the transmission probabilities are given by $T_L = T_R = 0.5$.

distribution is exponentially suppressed for increasing energies on the energy scale given by the inverse of the pulse width $\hbar/\sigma_A$. In contrast, for a strongly unbalanced interferometer, $\Delta\tau \gg \sigma_A$, as shown in Fig. 3.3 b), also the energy-dependent part $E\Delta\tau/\hbar$ of the phase $\Delta\phi(E,\Phi)$ starts to play an important role leading to exponentially damped, fast energy-dependent oscillations in the spectral current. This goes along with a phase shift between the different energy contributions. In Fig. 3.4, where we show phase- and energy-dependent cuts through the plot in Fig. 3.3 b), this behavior is clearly visible.

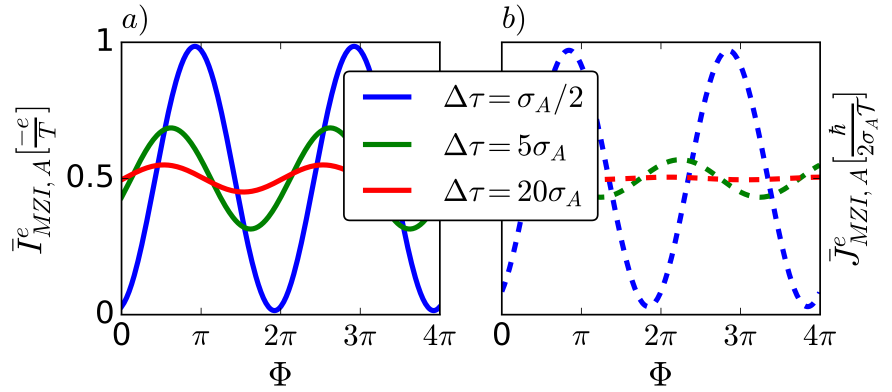

Figure 3.5: Electronic part of the average charge current, $\bar{I}^e_{MZI,A}$, (full lines) and of the average energy current, $\bar{J}^e_{MZI,A}$, (dashed lines) as a function of the phase Φ for different values of the detuning $\Delta\tau$. The transmission probabilities are $T_L = T_R = 0.5$.

The energy dependence of the interference part of the excess-energy distribution function is the electron analogue of the so-called channelled spectrum known from optics [75]. This energy dependence leads to dramatic differences for the charge and energy currents – namely the energy-integrated quantities – between the case of a balanced and a strongly unbalanced interferometer. The analytic results for the time-averaged charge and energy currents, obtained from the energy integrals of the spectral current as shown in Eqs. (3.9) and (3.10), are given by

$$\begin{aligned}\frac{\bar{I}_{MZI,A}}{-e/\mathcal{T}} &= (R_L R_R + T_L T_R)\left(n^e_A - n^h_A\right) \qquad (3.17)\\ &- 2\gamma\mathrm{Re}\left\{e^{-i\Phi}\left(n^e_A\frac{-2i\sigma_A}{\Delta\tau - 2i\sigma_A} - n^h_A\frac{2i\sigma_A}{\Delta\tau + 2i\sigma_A}\right)\right\},\\ \frac{\bar{J}_{MZI,A}}{\hbar/(2\sigma_A\mathcal{T})} &= (R_L R_R + T_L T_R)\left(n^e_A + n^h_A\right) \qquad (3.18)\\ &- 2\gamma\mathrm{Re}\left\{e^{-i\Phi}\left(n^e_A\left(\frac{-2i\sigma_A}{\Delta\tau - 2i\sigma_A}\right)^2 + n^h_A\left(\frac{2i\sigma_A}{\Delta\tau + 2i\sigma_A}\right)^2\right)\right\}.\end{aligned}$$

The equations show the sum of the electron and hole contributions, which are indicated by factors n^e_A and n^h_A stemming from different parts of the driving cycle. When considering a full period, both n^e_A and n^h_A are equal to one. By considering half-cycle we obtain the electronic part only, as shown in Fig. 3.5. A full 3D plot as function of $\Delta\tau$ and Φ is shown in Figs. 3.10 a) and b), equivalent results are found for the hole-like contributions.

Here we observe that the interference pattern observed in the excess-energy distribution function is clearly visible also in the charge and energy currents. The amplitude of the oscillations is maximal when $\Delta\tau \leqslant \sigma_A$ and it gets strongly suppressed for $\Delta\tau \gg \sigma_A$. This suppression of the flux dependence can be understood as an averaging effect of the phase-shifted contributions of the excess-energy distribution function at different energies (clearly visible in Fig. 3.3 b)).

On the other hand, this suppression of interference is also a manifestation of the particle nature of the injected signal, made of a sequence of well-separated Lorentzian current pulses carrying exactly one electron or one hole. The width in time of these current pulses, σ_A, is directly related to the single-particle coherence time of electrons and holes, as shown in Refs. [72, 74]. The latter can be read out by measuring the visibility of the current signal detected at the output of an MZI: whenever the detuning of the interferometer, characterized by $\Delta\tau$, is much larger than the single-particle coherence time σ_A, the interference in the charge (and energy) current is suppressed. In this case the current pulses traveling along the upper arm and the lower arm arrive at the detector in well separated time intervals and the signals from the two different paths are thus distinguishable.

The coexistence of these two interpretations is consistent with the idea that, in quantum mechanics, a particle is described by a wave packet, composed of a superposition of plane waves at different energies.

Due to the energy-filtering properties of the MZI and to the different energies at which and electrons are emitted, we see from Eqs. (3.17) and (3.18), that the contributions for electrons and holes have different weights for finite detuning $\Delta\tau$. Then, although the total injected current is zero, the DC charge current at each output is finite for finite detuning.

As an additional result of the finite detuning, a phase shift with respect to the $\cos(\Phi)$-dependence is introduced. The energy dependence of the excess-energy distribution function, namely the channelled spectrum, hence leads to charge and energy currents which are in general out of phase. Therefore, it is possible to tune the magnetic flux such that an electron is detected with a higher probability in reservoir 4, while the energy detected in reservoir 3 is on average larger than the one detected in reservoir 4 (and vice versa).

The extra factor E in the integrand of $\bar{J} = h^{-1}\int_{-\infty}^{\infty} dE\ E\ i(E)$ with respect to the charge current makes it more sensitive to the energy dependence of the distribution function $i(E)$. Thus, it is also more sensitive than the charge current to the variation of the interferometer imbalance, showing interference suppression at smaller $\Delta\tau$ values, see Fig. 3.5 for the electronic contributions to charge and energy currents. The visibility extracted from Eq. (3.17) for the charge current in the case of symmetric transmission of the QPCs, namely $|I^{i,int}_{MZI,A}/I^{i,cl}_{MZI,A}| = 2\sigma_A/\sqrt{\Delta\tau^2 + 4\sigma_A^2}$ indeed decays slower with $\Delta\tau$ than the visibility extracted from Eq. (3.18) for the energy current, namely $|J^{i,int}_{MZI,A}/J^{i,cl}_{MZI,A}| = 4\sigma_A^2/(\Delta\tau^2 + 4\sigma_A^2)$.

It is to be noted that the results presented in this section are not entirely new since works dealing with the same system have already been presented, indeed an MZI fed by a non-adiabatically driven SPS has been studied by Ferraro *et al.* [75] in the framework of Wigner functions. In that case the excess-energy distribution function of emitted particles, $i_A^{e/h}(E)$, is approximated by a Lorentzian function. The system shows a qualitatively similar behavior to the one described here. A closely related work by Hofer and Flindt [84] focuses on the propagation of multi-electron pulses through a Mach-Zehnder interferometer.

3.3.1 *Noise of an MZI with one source*

As a final step for the characterization of the MZI fed only by $\mathrm{SPS_A}$, we study the zero-frequency current noise as described by Eq. (3.13). The current noise, for the half period in which an electron emitted from $\mathrm{SPS_A}$ arrives at the MZI outputs, can then be written as

$$\begin{aligned}\frac{\mathcal{P}^{e}_{\mathrm{MZI,A}}}{-e^2/\mathcal{T}} &= T_R R_R + T_L R_L - 4\gamma^2 \\ &+ 2\gamma\,(T_L - R_L)\,(T_R - R_R)\,\mathbb{R}\mathrm{e}\left\{e^{-i\Phi}\frac{-2i\sigma_A}{\Delta\tau - 2i\sigma_A}\right\} \\ &- \left(2\gamma\mathbb{R}\mathrm{e}\left\{e^{-i\Phi}\frac{-2i\sigma_A}{\Delta\tau - 2i\sigma_A}\right\}\right)^2 .\end{aligned} \tag{3.19}$$

A similar expression is found for the hole contribution; see the full expression in Appendix A.4.

Since the noise comes from a product of current operators, it has contributions both from the first and second harmonics in the magnetic flux. Given that only single particles are emitted into the interferometer per half period it is quite intuitive that we should be able to understand the noise as a simple product of currents. More precisely, it should be proportional to a product of transmission probabilities to the contacts at which the two currents are detected.

In order to show that, we consider the charge current in the detector, see Eq. (3.17), and rewrite it in terms of effective transmission probabilities, $T_{41}^{\mathrm{eff,e}}$ and $T_{41}^{\mathrm{eff,h}}$, for electrons and holes respectively, $\bar{I}_{\mathrm{MZI,A}} = -e\left(n_A^e T_{41}^{\mathrm{eff,e}} + n_A^h T_{41}^{\mathrm{eff,h}}\right)/\mathcal{T}$, with

$$T_{41}^{\mathrm{eff,e}} = R_L R_R + T_L T_R - 2\gamma\mathbb{R}\mathrm{e}\left\{e^{-i\Phi}\frac{-2i\sigma_A}{\Delta\tau - 2i\sigma_A}\right\} \tag{3.20}$$

$$T_{41}^{\mathrm{eff,h}} = -R_L R_R - T_L T_R + 2\gamma\mathbb{R}\mathrm{e}\left\{e^{-i\Phi}\frac{2i\sigma_A}{\Delta\tau + 2i\sigma_A}\right\} . \tag{3.21}$$

Extracting in an equivalent manner effective transmission probabilities, $T_{31}^{\mathrm{eff,e}}$ and $T_{31}^{\mathrm{eff,h}}$, from the current in contact 3, we are indeed able to show that the noise of the MZI with a single source can simply be written as

$$\mathcal{P}_{\mathrm{MZI,A}} = -\frac{e^2}{\mathcal{T}}\left[n_A^e T_{41}^{\mathrm{eff,e}} T_{31}^{\mathrm{eff,e}} + n_A^h T_{41}^{\mathrm{eff,h}} T_{31}^{\mathrm{eff,h}}\right] . \tag{3.22}$$

This product form of the noise, shown in Eq. (3.22), is clearly not expected to hold in the case where two particles are injected into the interferometer from different sources and thus two-particle effects will contribute to the noise. For a better understanding of the impact of two-particle effects, as discussed in Sec. 3.4.4, the following interpretation of the classical part of the noise, given in Eq. (3.19), turns out to be useful. The classical part $T_R R_R + T_L R_L - 4\gamma^2 = (R_L R_R + T_L T_R)(R_L T_R + T_L R_R)$, stemming from the product of the classical parts of the effective transmission probabilities, results in the partition noise of the left and the right QPC, $T_L R_L$ and $T_R R_R$, and a mixed contribution, $-4\gamma^2$. Furthermore this can be rewritten as $T_R R_R + T_L R_L - 4\gamma^2 = T_R R_R + T_L R_L\,(T_R - R_R)^2$. It means that the classical part of the noise is given by the partition noise of $\mathrm{QPC_R}$, $T_R R_R$, on one hand, and the partition noise of $\mathrm{QPC_L}$ in the presence of $\mathrm{QPC_R}$, $T_L R_L\,(T_R - R_R)^2$, on the other hand. The latter shows that, in the absence of interference, $\mathrm{QPC_L}$ only produces partition noise if QPC_R is not symmetric. Indeed, if QPC_R was symmetric, the probability of particles from SPS_A to be scattered into the reservoirs 3 and 4 would be one half each, independently of the transmission probability of QPC_L, and the partition noise of QPC_L would thus be invisible.

3.4 SYNCHRONIZED PARTICLE EMISSION FROM TWO SOURCES

The influence of the particle emission from SPS_B on the interference pattern of the currents at the output of the MZI is studied in this section, using the setup shown in Fig. 3.1. It has been shown in Ref. [70] that the interference pattern in the time-resolved current, $\langle \hat{I}(t) \rangle$, detected at the output of the MZI is subject to a phase-shift, which can take values between 0 and 2π, depending on the emission time of electrons or holes from source B. This has as a consequence that the interference effects in the time-averaged current, $\bar{I}$, detected at the output of the interferometer in every half period, get strongly suppressed when the emission of the particles is synchronized such that either particles emitted from SPS_A can be absorbed at SPS_B or that particles of the same kind can collide at QPC_R. This synchronization of particles occurs as a perfect overlap of the time-resolved wave packets emitted from the two sources.

The two time-differences Δt_d^{ij}, Δt_u^{ij} are of particular relevance for these synchronized two-particle events. The first one is the difference between the time at which a particle i =e,h emitted from SPS_A traveling the lower arm arrives at SPS_B and the emission time of a particle j =e,h at SPS_B, $\Delta t_d^{ij} \equiv t_A^i - t_B^j + \tau_d/2$. The second one is the difference between the time at which a particle i emitted from SPS_A traveling the upper arm arrives at QPC_R and the time at which a particle j emitted from SPS_B arrives at QPC_R, $\Delta t_u^{ij} \equiv t_A^i - t_B^j + \tau_u - \tau_d/2$. A full absorption thus can occur when $t_A^e + \tau_d/2 = t_B^h$ (or $t_A^h + \tau_d/2 = t_B^e$), which corresponds to $\Delta t_d^{eh} = 0$ (or $\Delta t_d^{he} = 0$), together with $\sigma_A = \sigma_B$. A full collision of electrons (or holes) can occur when $t_A^e + \tau_u = t_B^e + \tau_d/2$ (or $t_A^h + \tau_u = t_B^h + \tau_d/2$), which corresponds to $\Delta t_u^{ee} = 0$ (or $\Delta t_u^{hh} = 0$), together with $\sigma_A = \sigma_B$.

Interestingly, the conditions for the averaging of the time-resolved currents, leading to a full suppression of the interference effects in the detected charge, allow for a particularly interesting interpretation, which has been put forward in Ref. [70]. This interpretation is based on which-path information which can be acquired in the case that particle collisions or absorptions occur due to an appropriate synchronization of the two SPSs. In order to introduce this interpretation in a nutshell, let us for the moment assume for simplicity that the QPCs defining the MZI are both semi-transparent.

We first consider the situation where SPS_A emits an electron and SPS_B a hole. Whenever the condition $\Delta t_d^{eh} = 0$ is fulfilled, no particle arrives at any of the outputs when the electron emitted from source A takes the lower arm of the MZI and gets absorbed. When the particle emitted from A takes the upper arm, the average charge remains to be equal to zero, however; fluctuations occur. This leads to which-path information suppressing the interference effect: whenever an electron or a hole is detected in one of the detectors, we can conclude that the electron emitted from SPS_A took the upper arm.

Equally, when both SPSs emit electrons and the condition $\Delta t_u^{ee} = 0$ is fulfilled, these two electrons could collide at QPC_R. When the electron emitted from source A travels along the upper arm of the MZI, the two electrons

- being in the same state - would have to be scattered to the two opposite outputs of the MZI at QPC_R; [66] in the case that the particle emitted from A takes the lower arm of the MZI both particles can go to both outputs randomly. This means that the average charge in each detector is always $-e$ independently of the traversed path, however only when the electron from SPS_A took the lower arm, fluctuations can occur. This again leads to which-path information leading to an interference suppression: whenever 0 or 2 electrons arrive in one of the detectors, we can conclude that the electron from SPS_A took the lower arm.

Note that this setup is very different from MZIs where an interference suppression is reached by placing a voltage probe [97] in one of the interferometer arms [92, 98, 99]. A voltage probe acts as a which-path detector itself and leads to dephasing. However, the presence of SPS_B leads to a coherent suppression of interference and which-path information can be acquired only at the detectors at the outputs of the MZI, thanks to the synchronized emission of particles from SPS_B.

In the following, in addition to the charge current we will investigate also the spectral current and the energy current of the emitted signals as well as the charge-current noise with the aim to extend the understanding of the impact of the above described multi-particle effects on the MZI signal.

3.4.1 *Spectral properties*

As we did for the case with only one source, we start by considering the spectral current. We study the case where one source emits an electron and one source emits a hole in the same half period, allowing for the absorption of particles at SPS_B, as well as the case where both sources, SPS_A and SPS_B, emit the same kind of particles, allowing for possible collisions between particles in one half period.

The synchronized emission from the two sources goes along with inelastic scattering processes. More specifically, scattering at the time-dependently driven SPS_B results in an energy increase or decrease in the scattering process [68]. This leads to a deformation of the spectral distribution of the current as will be shown in the following.

Absorption of particles

In the case where particles of opposite type emitted from the two sources are detected in the same half period, absorptions can occur at source B and the spectral current is given by

$$\begin{aligned} i^{eh}(E,\Phi) &= R_L R_R i^e_A(E) + R_L T_R i^h_B(E) \\ &+ T_L T_R \left(i^h_B(E) + i^e_A(E)\right)\left(1 - \frac{4\sigma_A\sigma_B}{{\Delta t^{eh}_d}^2 + (\sigma_A+\sigma_B)^2}\right) \\ &- 2\gamma i^e_A(E)\mathbb{R}\mathrm{e}\left\{e^{-i\Phi}e^{-iE\Delta\tau/\hbar}\left(1 - \frac{2i\sigma_B}{\Delta t^{eh}_d + i\left(\sigma_A+\sigma_B\right)}\right)\right\}. \end{aligned} \tag{3.23}$$

From now on, for observables calculated for the MZI with two sources, we drop the subscript indicating the presence of the MZI and the number of working sources, the latter being evident from the superscript ij for the type of particle $i = e,h$ emitted from SPS_A and the type of particle $j = e,h$ emitted from SPS_B. Here, we show the case where SPS_A emits an electron and SPS_B a hole ($n^e_A = n^h_B = 1$ and $n^h_A = n^e_B = 0$); the opposite case is shown in Appendix A.1.

When the two particles are emitted independently, such that the electron emitted from SPS_A is not in the vicinity of SPS_B when a hole emission occurs at the latter. Then, far away from the condition, $\Delta t^{eh}_d = 0$ and $\sigma_A = \sigma_B$, the expression given in Eq. (3.23) reduces to the sum of the separate contributions of the two sources, namely for the hole emitted from SPS_B and transmitted at QPC_R, $T_R i^h_B(E)$, and the electron term containing interference effects, as the one in the previous section, given in Eq. (3.14a).

The absorption of electrons emitted from SPS_A at SPS_B can occur when the time difference Δt^{eh}_d is of the order of the width of the associated time-resolved current pulses σ_A, σ_B. It leads to a cancellation of the contribution of the current traveling along the lower arm in an energy-independent manner, depending only on how accurately the absorption conditions, $\Delta t^{eh}_d = 0$ and $\sigma_A = \sigma_B$, are fulfilled. Equally, the suppression of the interference part of the current takes place in a way which is independent of the energy E. It becomes evident also from Fig. 3.6, where the electronic (positive energy) part of this spectral current is shown as a function of energy and of the magnetic-flux dependent phase. Indeed, the amplitude of the flux-dependent oscillations is suppressed with respect to the case where $\Delta t^{eh}_d \gg \sigma_{A/B}$ – the latter being equivalent to the case of an emission from A only, while source B is switched off, as in Fig. 3.3 a).

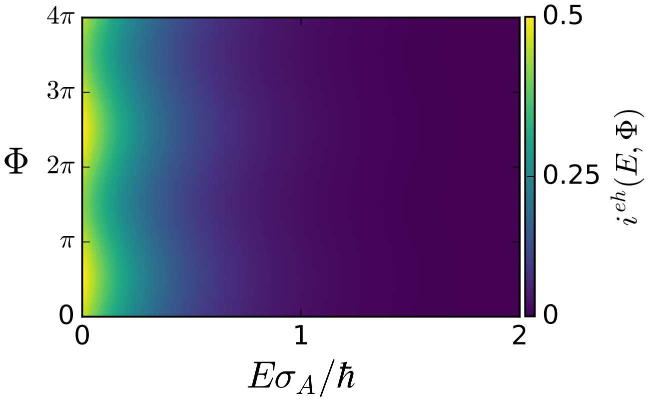

Figure 3.6: Energy-distribution function, $i^{eh}(E, \Phi)$, shown for positive values of the energy E only, in the regime where absorptions of electrons emitted by A are possible through the emission of holes from B depending on the time difference Δt^{eh}_d. Here we take $\Delta t^{eh}_d = 0.1\sigma_A$ and show $i^{eh}(E, \Phi)$ as a function of the energy E in units of $\hbar/\sigma_A$ and the magnetic-flux-dependent phase Φ. The interferometer is almost perfectly balanced, $\Delta\tau = 0.01\sigma_A$, the pulse widths are assumed to be equal, $\sigma_A = \sigma_B$, and the transmission probabilities are given by $T_L = T_R = 0.5$.

Collision of particles of the same kind

In the case where particles of the same type emitted from both sources are detected in one half period, we find for the electron part of the spectral current

$$\begin{aligned}
i^{ee}(E,\Phi) &= R_L R_R i^e_A(E) + T_L T_R i^e_A(E)\times \qquad (3.24)\\
&\mathbb{R}\mathrm{e}\left\{1+\frac{4\sigma_A\sigma_B}{\Delta t_d^{ee\,2}+(\sigma_A-\sigma_B)^2}-2i\sigma_B\frac{\Delta t_d^{ee}-i(\sigma_A+\sigma_B)}{\Delta t_d^{ee\,2}+(\sigma_A-\sigma_B)^2}e^{-iE\left(\Delta t_d^{ee}+i(\sigma_A-\sigma_B)\right)/\hbar}\right\}\\
&+R_L T_R i^e_B(E) + T_L T_R i^e_B(E)\times\\
&\mathbb{R}\mathrm{e}\left\{1+\frac{4\sigma_A\sigma_B}{\Delta t_d^{ee\,2}+(\sigma_A-\sigma_B)^2}-2i\sigma_A\frac{\Delta t_d^{ee}-i(\sigma_A+\sigma_B)}{\Delta t_d^{ee\,2}+(\sigma_A-\sigma_B)^2}e^{-iE\left(\Delta t_d^{ee}+i(\sigma_B-\sigma_A)\right)/\hbar}\right\}\\
&-2\gamma i^e_A(E)\mathbb{R}\mathrm{e}\left\{e^{-i\Phi}e^{-iE\Delta\tau}\left[1+\frac{2i\sigma_B}{\Delta t_d^{ee}+i\,(\sigma_A-\sigma_B)}\left(1-e^{-iE\left(\Delta t_d^{ee}+i(\sigma_A-\sigma_B)\right)/\hbar}\right)\right]\right\},
\end{aligned}$$

the hole contribution is given in Appendix A.1.

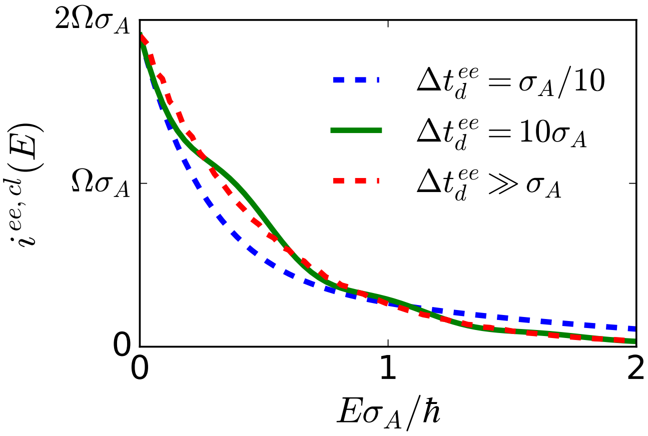

Figure 3.7: Classical part of the excess-energy distribution function, $i^{ee,cl}(E)$, in the regime where collisions between particles of the same kind are possible depending on the time difference Δt_d^{ee}. We show the electronic contribution as a function of the energy E in units of $\hbar/\sigma_A$. We take $\sigma_A = \sigma_B$ and the transmission probabilities are given by $T_L = T_R = 0.5$.

The classical part, $i^{ee,cl}(E)$, is given by the expression in the first two lines of Eq. (3.24). Again, when $\Delta t_d^{ee} \gg \sigma_A, \sigma_B$, it reduces to the sum of the single-particle contributions, namely the sum of $T_R i^e_B$ and of the expression in Eq. (3.14b). The resulting exponential behavior of the spectral current is represented by the red (dashed line) in Fig. 3.7. However, if the tuning of the emission times from SPS_A and SPS_B is such that particles could collide at SPS_B, in other words, if there is an overlap of the time-resolved current pulses emitted from the two sources and the difference of the emission times, Δt_d^{ee}, is of the order of the width of the current pulses, then energy-dependent oscillations occur in the classical part of the spectral current on a scale given by the inverse of the time difference, $\hbar/\Delta t_d^{ee}$. This oscillation on top of the energy-dependent exponential decay of the spectral current is a result of the complex exponential factor in the last term of the first two lines of Eq. (3.24). Importantly, its amplitude gets suppressed for large time differences. Therefore the amplitude of the oscillations is largest close to the collision condition $\Delta t_d^{ee} = 0$, while the frequency of the oscillations is reduced.

This behavior becomes apparent from the green (full) line in the plot shown in Fig. 3.7 where damped oscillations are visible. The oscillations of the blue (dashed) line are hardly visible due to the small oscillation frequency. It is this complex energy dependence at the scale $\hbar/\Delta t_d^{ee}$, which leads to the fact that the classical part of the energy-integrated, average charge current is insensitive to collisions of particles at $\mathrm{SPS_B}$, while an increase of the classical part of the energy current is observed when two particles are emitted on top of each other at $\mathrm{SPS_B}$. [68]

This behavior is very different from the energy-independent suppression of parts of the spectral current in the regime of possible particle absorptions.

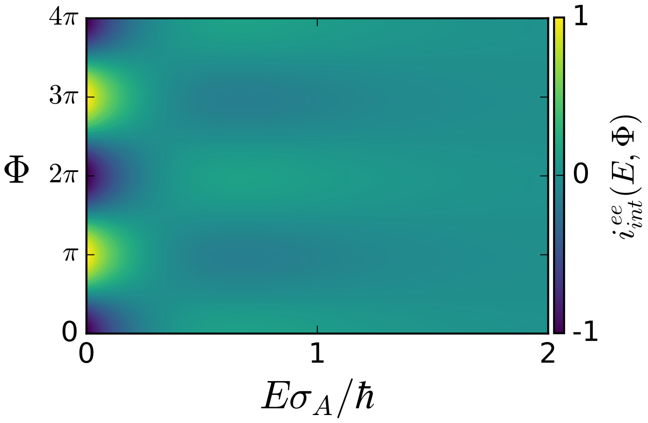

Figure 3.8: Interference part of the excess-energy distribution function, $i^{ee,int}(E,\Phi)$, in the regime where collisions between particles of the same kind are possible depending on the time difference Δt_d^{ee}. We show the electron contribution as a function of the energy E in units of $\hbar/\sigma_A$ and the magnetic-flux-dependent phase Φ close to collision $\Delta t_d^{ee} = 0.1\sigma_A$. The interferometer is almost perfectly balanced, $\Delta\tau = 0.01\sigma_A$, the pulse widths are assumed to be equal, $\sigma_A = \sigma_B$, and the transmission probabilities are given by $T_L = T_R = 0.5$.

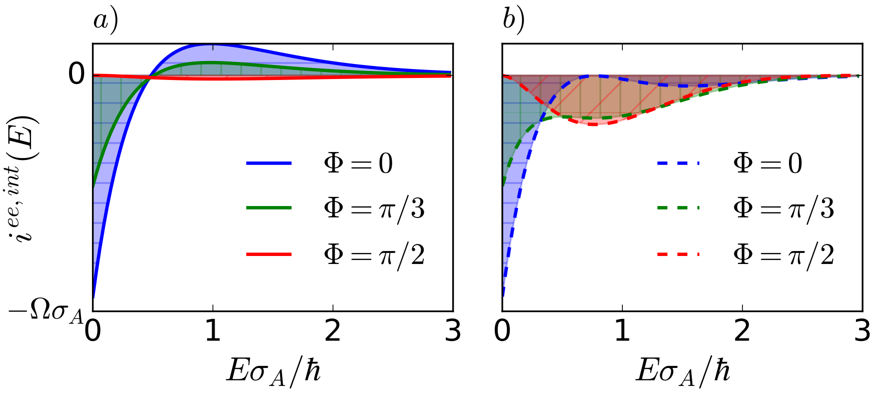

Figure 3.9: Interference part of the excess-energy distribution function, $i^{ee,int}(E,\Phi)$, in the regime where collisions between particles of the same kind are possible depending on the time difference Δt_d^{ee}. We show the electron contribution as a function of the energy E for three different flux values and for $\Delta t_d^{ee} = 0.1\sigma_A$ (full lines) and $\Delta t_d^{ee} = 2\sigma_A$ (dashed lines). The parameters are the same as in Fig. 3.8

The interference contribution, $i^{\mathrm{ee,int}}(E)$, is given by the third line of Eq. (3.24) and it is shown in Fig. 3.8. Far from the collision condition, this contribution stems from the signal emitted from source A only where it equals Eq. (3.14c). When the particles from $\mathrm{SPS_A}$ and $\mathrm{SPS_B}$ are emitted such that collisions between them are possible at $\mathrm{SPS_B}$, oscillations with two competing time-scales appear, namely the time-scale of the collision condition, Δt_d^{ee}, and the time-scale related to the detuning of the interferometer, $\Delta\tau$. Again, oscillations on the energy scale given by $\hbar/\Delta t_d^{ee}$ are suppressed for large time differences Δt_d^{ee}. Note once more, that this is however very different from the absorption case where the time-scale of the absorption condition enters in a fully energy-independent manner. For an almost perfectly balanced interferometer, $\Delta\tau \ll \sigma_A$, the interference contribution to the spectral current is shown as a function of the energy and the flux-dependent phase in Fig. 3.8, exhibiting slow oscillations on the scale $\hbar/\Delta t_d^{ee}$, where we here chose the case close to the collision condition, $\Delta t_d^{ee} = 0.1\sigma_A$. In Fig. 3.9 cuts through the density plot of Fig. 3.8 are shown as a function of energy for different values of the phase, Φ. We compare these curves with the case slightly farther away from the collision condition, where the modulation on the energy scale given by $\hbar/\Delta t_d^{ee}$ becomes more obvious. Interestingly, the areas enclosed by the curves below and above the energy-axis (indicated by the shaded areas in Fig. 3.9) close to the collision condition, $\Delta t_d^{ee} = 0.1\sigma_A$, sum up to a value close to zero independently of the value of the magnetic flux entering the phase Φ. We will see in the following section, Section 3.4.2, that this leads to a suppression of the interference in the (energy-integrated) charge current, when the two sources are adequately synchronized. However, as soon as the time difference Δt_d^{ee} is increased while keeping the interferometer balanced, $\Delta\tau \approx 0$, the sum of the enclosed areas becomes flux dependent, as can be seen from the dashed lines in Fig. 3.9.

3.4.2 *Charge current*

The energy-dependent interference occurring in the previously studied spectral currents is equivalent to what is known as a channelled spectrum from optics. The behavior of the charge end energy currents, which are given by the energy averages of the spectral currents multiplied by the charge, respectively the energy, see Eqs. (3.9) and (3.10), can therefore be understood based on the previous investigations.

Absorption of particles

We start with the presentation of the charge current found in one half period in which an electron emitted from $\mathrm{SPS_A}$ and a hole emitted from $\mathrm{SPS_B}$ are detected in reservoir 4 (namely taking $n_A^e = n_B^h = 1$ and $n_A^h = n_B^e = 0$), allowing for the absorption of particles if $\Delta t_d^{eh} \approx 0$. The charge current is then given by

$$\begin{aligned}\frac{\bar{I}^{eh}}{-e/\mathcal{T}} &= R_L R_R + T_L T_R - T_R \\ &- 2\gamma \mathbb{R}\mathrm{e}\left\{ e^{-i\Phi} \frac{-2i\sigma_A}{\Delta\tau - 2i\sigma_A} \left(1 - \frac{2i\sigma_B}{\Delta t_d^{eh} + i(\sigma_A + \sigma_B)} \right) \right\} .\end{aligned} \tag{3.25}$$

We find that only the interference part of the charge current (second line) is affected by the synchronization of the particle emission from the two sources. The dependence of the spectral current on the time-difference $\Delta t_{\mathrm{d}}^{\mathrm{eh}}$, see Eq. (3.23), thus cancels out in the classical part.

The factor leading to the maximum of interference for the balanced case, $\frac{-2i\sigma_A}{\Delta\tau - 2i\sigma_A}$, in the absence of absorptions, and the factor suppressing the interference in case of absorptions, $\frac{2i\sigma_B}{\Delta t_{\mathrm{d}}^{\mathrm{eh}} + i(\sigma_A + \sigma_B)}$, are of very similar nature, both leading to a Lorentzian-type structure together with a phase shift at the maximum/minimum of their contribution. This similarity becomes also obvious when comparing Figs. 3.10 a) and 3.11 a) which bring out the two effects.

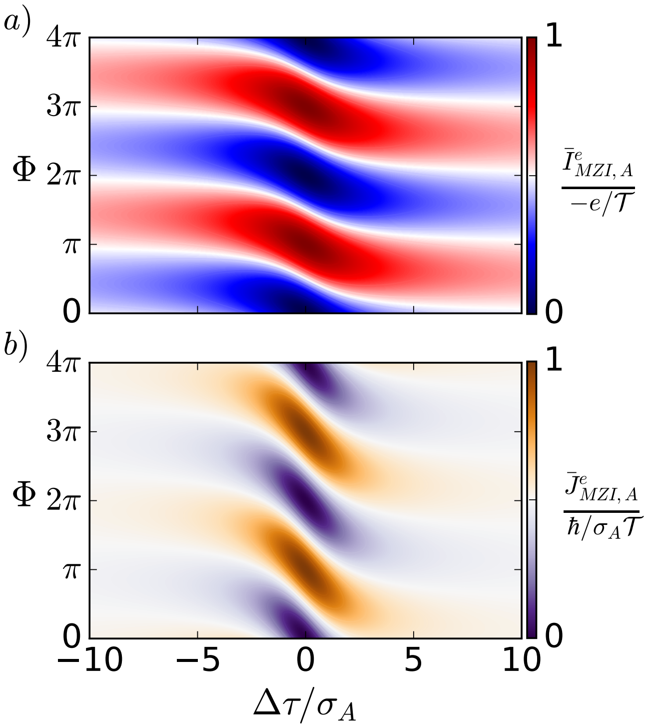

Figure 3.10: Charge and energy current detected at reservoir 4 (output of the interferometer), with symmetric transmission of $\mathrm{QPC_L}$ and $\mathrm{QPC_R}$. a) Charge current of an MZI fed by $\mathrm{SPS_A}$ only, as a function of the MZI detuning $\Delta\tau$ in units of the current-pulse width σ_A and as a function of the magnetic flux Φ. b) Energy currents for the same situation shown in a).

As for the case of the MZI fed by one source and as mentioned in the beginning of this section, two interpretations can be given for our results, based on the wave or particle nature of the particles emitted by the sources, see also Ref. [70]. On one hand the insensitivity of the classical part of the current to absorptions as well as the suppression of interference can be interpreted as the result of an energy average of the spectral current given in Eq. (3.23). On the other hand, a physically more insightful interpretation can be given based on a particle picture of the injected signals.

The average charge current of each classical path is not affected by an absorption - in other words, an electron and a hole carry in total no charge independently of whether they recombine in an absorption process or not.

Even so, the absorption of an electron by a hole suppresses the fluctuation in the charge current. Hence, there are fluctuations at the output depending on whether the particle from $\mathrm{SPS_A}$ took the upper or lower arm which leads

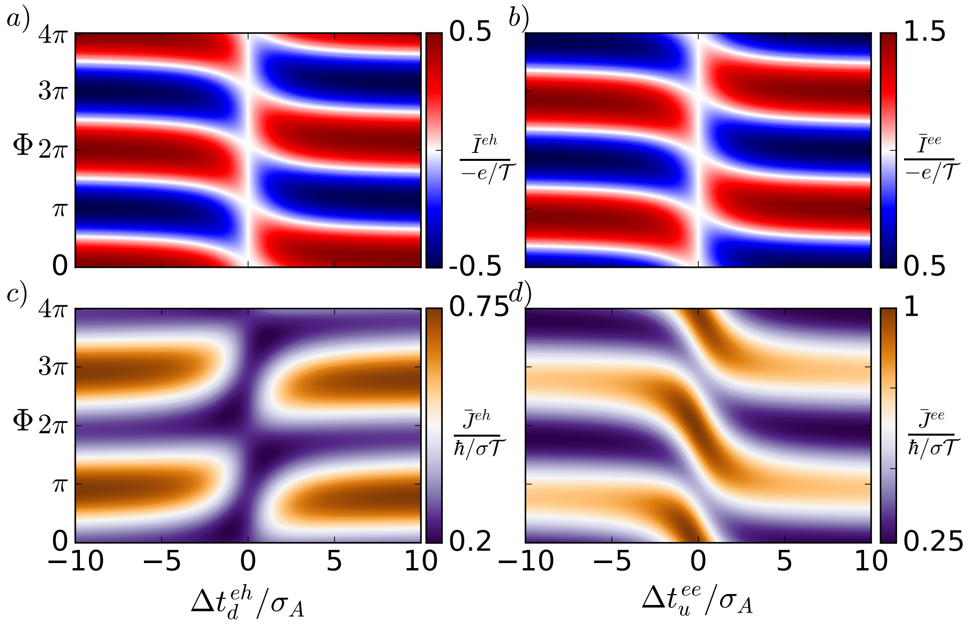

Figure 3.11: Charge and energy current detected at reservoir 4 (output of the interferometer), with symmetric transmission of $\mathrm{QPC_L}$ and $\mathrm{QPC_R}$. a) Charge current of a slightly detuned MZI, $\Delta\tau = 0.5\sigma_A$ fed by an electron from $\mathrm{SPS_A}$ and a hole from $\mathrm{SPS_B}$ as a function of the time difference Δt_d^{eh} in units of the pulse width $\sigma_A = \sigma_B$ and the magnetic flux-dependent phase Φ. b) Charge current of a slightly detuned MZI, $\Delta\tau = 0.5\sigma_A$ fed by an electron both from $\mathrm{SPS_A}$ and $\mathrm{SPS_B}$ as a function of the time difference Δt_u^{ee} in units of the pulse width $\sigma_A = \sigma_B$ and the magnetic flux-dependent phase Φ. c)-d) Energy currents for the same situations shown in a)-b).

to which-path information thus suppressing the interference. This suppression of fluctuations in the case of absorptions is shown in a detailed study of the noise in Sec. 3.4.4.

For completeness we report the case in which holes emitted from $\mathrm{SPS_A}$ can be absorbed at $\mathrm{SPS_B}$. The charge current detected in this half period behaves similarly as the one for the previous case, described in Eq. (3.25), and it is given by

$$\begin{aligned}\frac{\bar{I}^{he}}{-e/\mathcal{T}} &= -R_L R_R - T_L T_R + T_R \\ &+ 2\gamma \mathbb{R}\mathrm{e}\left\{ e^{-i\Phi} \frac{2i\sigma_A}{\Delta\tau + 2i\sigma_A} \left(1 - \frac{-2i\sigma_B}{\Delta t_d^{he} - i(\sigma_A + \sigma_B)} \right) \right\}.\end{aligned} \tag{3.26}$$

The difference with respect to Eq. (3.25), is given by a sign difference due to the contribution of oppositely charged particles and by a different phase which enters both through the factor stemming from the detuning properties of the MZI as well as from the factor describing the synchronization of particles. As a consequence of this phase shift between hole and electron contribution, the charge current detected at reservoir 4 during a whole period, does not vanish (even though the total current injected by the sources is zero) and it is given by

$$\begin{aligned}\frac{\bar{I}^{eh+he}}{-e/\mathcal{T}} &= 2\gamma\sin(\Phi)\frac{4\sigma_A\Delta\tau}{\Delta\tau^2+4\sigma_A^2}\frac{\Delta t_d^2+\sigma_A^2-\sigma_B^2}{\Delta t_d^2+(\sigma_A+\sigma_B)^2}\\ &+2\gamma\sin(\Phi)\frac{4\sigma_A^2}{\Delta\tau^2+4\sigma_A^2}\frac{4\sigma_B\Delta t_d}{\Delta t_d^2+(\sigma_A+\sigma_B)^2}\,. \qquad (3.27)\end{aligned}$$

Here we assume that $\Delta t_d^{eh} = \Delta t_d^{he} \equiv \Delta t_d$ for simplicity. Both contributing terms depend on the energy-filtering properties of the MZI due to finite detuning $\Delta\tau$ and on the synchronized emission of multiple particles leading to a modification of the channelled spectrum of the device. The first of these terms is finite only for finite detuning, the other one occurs only when the emission of the two particles of opposite type is slightly off, $\Delta t_d \neq 0$. Interestingly, the latter term is finite also when the detuning is zero: in this case the total charge current at the output of the MZI both due to SPS_A alone and due to SPS_B alone would vanish. However, when the sources are synchronized such that $\Delta t_d \approx \sigma_A, \sigma_B$, the term survives showing features due to two-particle effects in the DC charge current.

Collision of particles of the same kind

We now consider the case where an electron from each SPSs arrives at the detector in the same half period. The average charge current in this case is

$$\begin{aligned}\frac{\bar{I}^{ee}}{-e/\mathcal{T}} &= R_LR_R+T_LT_R+T_R \qquad (3.28)\\ &-2\gamma\mathbb{R}\mathrm{e}\left\{e^{-i\Phi}\frac{-2i\sigma_A}{\Delta\tau-2i\sigma_A}\left(1-\frac{-2i\sigma_B}{\Delta t_u^{ee}-i\left(\sigma_A+\sigma_B\right)}\right)\right\}\,.\end{aligned}$$

Again, the classical contribution is independent of the synchronization of the two sources; in contrast, the interference part of the time-averaged charge current is sensitive to the collision of particles at QPC_R, see Fig. 3.11 b). This can again be understood as an energy-average of the synchronization-dependent spectral current. Note however, that while the structure of the expression given in Eq. (3.28) is very similar to the one for the absorption case (see Eq. (3.25)), the corresponding spectral currents have very different behaviors. In particular, the fact that the time-scale Δt_d^{ee} (for the emission of an electron at SPS_B on top of the one from SPS_A) introduces an energy-dependent oscillation into the spectral current is important here: together with the energy-dependent oscillation governed by the time-scale of the detuning $\Delta\tau$ it leads to features at the collision condition $\Delta t_u^{ee} \approx 0$, when the energy integration of the spectral current is performed to obtain the average charge current.

The interpretation of these facts is again more intuitive when resorting to an explanation based on a particle picture. As in the previous case, fluctuations on the charge occur or not depending on the path traversed by the electron from A under the collision condition $\Delta t_u^{ee} = 0$ (with $\sigma_A = \sigma_B$). Then, if the electron emitted from SPS_A travels along the upper arm, it collides with the electron emitted from SPS_B leading to the transmission of exactly one electron to each MZI output. But if the electron emitted from SPS_A takes the lower arm, the charge in the two MZI outputs fluctuates due to the probabilistic transmission at QPC_R. Despite not having an impact on the average charge transmitted along each of the classical paths, this allows to extract which-path information from the fluctuations in the transmitted charge. The question whether one particle arrives in each reservoir on average or whether it is indeed exactly one particle in each period, can ultimately be clarified by considering the noise, which we present in Sec. 3.4.4.

The full general expressions for the charge current in the case of collision and absorption are given in Appendix A.2.

3.4.3 *Energy current*

As we did in Section 3.3 we study not only the charge current but also the energy current. There, we have shown, see Figs. 3.5 and 3.10, that charge and energy both have oscillations due to the interference but their behaviors are different. On top of that, the results of the last section show the impact of absorptions and collisions on the charge current and how they can be explained either based on the structure of the spectral current or on the occurrence of two-particle effects. Both interpretations are clearly related to the energetic properties of the contributing current pulses, further motivating the following discussion of the energy currents detected at the output of the MZI.

Absorption of particles

In the case where a particle emitted by SPS_A can possibly be absorbed at SPS_B, the energy current in reservoir 4 is given by

$$\begin{aligned}\bar{J}^{eh} = {} & \frac{\hbar}{2\sigma_A\mathcal{T}}\left(R_L R_R + T_L T_R\right) + \frac{\hbar}{2\sigma_B\mathcal{T}} T_R \\ & - T_L T_R \left(\frac{\hbar}{2\sigma_A\mathcal{T}} + \frac{\hbar}{2\sigma_B\mathcal{T}}\right) \frac{4\sigma_A\sigma_B}{\Delta t_d^{eh\,2} + (\sigma_A+\sigma_B)^2} \\ & - 2\gamma \frac{\hbar}{2\sigma_A\mathcal{T}} \mathbb{R}\mathrm{e}\left\{ e^{-i\Phi} \left(\frac{-2i\sigma_A}{\Delta\tau - 2i\sigma_A}\right)^2 \left(1 - \frac{2i\sigma_B}{\Delta t_d^{eh} + i(\sigma_A+\sigma_B)}\right)\right\}.\end{aligned} \tag{3.29}$$

We see that the synchronization of the two particle sources affects both the classical and the interference part of the energy current. Let us start by considering the classical contribution: in contrast with the charge which has opposite sign for electrons and holes, independent electrons and holes carry the same amount of energy related to the width of the current pulse, $\hbar/2\sigma_{A/B}$. Therefore the absorption of a particle (which can occur when the particle emitted from SPS_A takes the lower MZI path) leads to an annihilation of the energy current. The classical part of the energy current thus reduces to $R_L R_R \hbar/2\sigma_A + R_L T_R \hbar/2\sigma_B$ in the case of full absorption in the lower arm, namely when $\Delta t_d^{eh} = 0$ and $\sigma_A = \sigma_B$.

Similarly, we see that the interference is suppressed under the condition, $\Delta t_d^{eh} = 0$ and $\sigma_A = \sigma_B$. If the particle from SPS_B is absorbed along the lower path, the energy going along with it does not fluctuate any more at the output and the same coexisting interpretations as for the charge current can be employed, based on the wave and the particle nature of the injected signal. Indeed, we find that the effect of the absorption is the suppression of the factor $(-2i\sigma_A)^2/(\Delta\tau - 2i\sigma_A)^2$, which was found to be typical of the oscillations on the energy current in the interferometer, see Eq. (3.18). The energy current in the case of absorption is shown in Fig. 3.11 c) as compared to the case of an MZI with a single working source shown in Fig. 3.10 b).

Results for the absorption of a hole, namely the synchronized emission of a hole from SPS_A and an electron from SPS_B are given in Appendix A.3.

Collision of particles of the same kind

The energy current in the regime where particles of the same type are injected from the two SPSs such that they arrive in the detector in the same half period is given by

$$\begin{aligned}
\bar{J}^{ee} = {} & \frac{\hbar}{2\sigma_A \mathcal{T}} \left(R_L R_R + T_L T_R\right) + \frac{\hbar}{2\sigma_B \mathcal{T}} T_R \\
& + T_L T_R \left(\frac{\hbar}{2\sigma_A \mathcal{T}} + \frac{\hbar}{2\sigma_B \mathcal{T}}\right) \frac{4\sigma_A \sigma_B}{\Delta t_d^{ee\,2} + \left(\sigma_A + \sigma_B\right)^2} \\
& - 2\gamma \frac{\hbar}{2\sigma_A \mathcal{T}} \mathbb{R}\mathrm{e}\left\{ e^{-i\Phi} \left(\frac{-2i\sigma_A}{\Delta\tau - 2i\sigma_A}\right)^2 \left(1 - \frac{-2i\sigma_B}{\Delta t_u^{ee} - i\left(\sigma_A + \sigma_B\right)}\right) \right\} \\
& + 2\gamma \frac{\hbar}{2\sigma_B \mathcal{T}} \mathbb{R}\mathrm{e}\left\{ e^{-i\Phi} \frac{-2i\sigma_A}{\Delta\tau - 2i\sigma_A} \left(\frac{-2i\sigma_B}{\Delta t_u^{ee} - i\left(\sigma_A + \sigma_B\right)}\right)^2 \right\} .
\end{aligned} \tag{3.30}$$

As for the charge, here we show the electronic contribution only; the general expression is given in Appendix A.3. The classical part of the energy current shows an enhancement when a particle from SPS_B is emitted on top of a particle emitted from SPS_A traveling along the lower arm, since the two particles can not occupy the same energy state. This enhancement occurs hence under the condition $\Delta t_d^{ee} = 0$ and $\sigma_A = \sigma_B \equiv \sigma$ and leads to the classical energy current $(R_L + 4T_L T_R)\,\hbar/2\sigma$. In contrast, the interference part of the energy current is not affected by this event.

However, like in the case of the charge current, the interference contribution to the energy current is sensitive to possible collisions at the interferometer output (at QPC_R) taking place if $\Delta t_u^{ee} \approx 0$. The interference term contains two contributions: the first is suppressed when the two emitted particles can collide at QPC_R and one could be tempted to say that is a suppression as the one in the charge current with the corresponding amount of energy of the colliding particles

However, there is an additional term which appears in the vicinity of the collision condition, which stems from the additional oscillations of the spectral current related to the energy scale associated to the time-scale Δt_d^{ee}, see the last term of Eq. (3.24).

Intriguingly, the energy current for two particles of the same kind hence behaves rather differently from the charge current: it has features both at the condition $\Delta t_d^{ee} = 0$ (classical part) and at the condition $\Delta t_u^{ee} = 0$ (interference part) and the interference effects in the energy current do not get suppressed under the collision condition (neither at QPC_R nor at SPS_B). The collision at QPC_R rather introduces a phase shift only, which can be seen in Fig. 3.11 d). This behavior has the following important implications.

The continued existence of the interference in the energy current in the case of possible collisions at QPC_R can obviously not be explained within one consistent particle picture, as it was done for the suppression of interference due to collisions in the charge current. Indeed, when particles can collide at QPC_R, fluctuations in the charge are suppressed while they persist in the energy. Hence, if a particle picture could be used then it would lead to an apparent separation of energy and charge of the particles, namely interference occurring in the energy current while the charge current is flux-independent. This “paradox" in the particle-interpretation of the energy-charge separation as well as its alternative description by quantum interference has recently been debated for spin-particle [100] and polarisation-particle [101] separation under the name “quantum Cheshire cat" [102, 103].

Finally, we notice that the enhancement of the energy current when collisions at $\mathrm{SPS_B}$ can occur could be considered as a which-path information. It however turns out that this does not influence the interference pattern neither in the charge current nor in the energy current. Consequently, we find that the coexistence of the interpretations of interference suppression due to phase averages and due to multi-particle effects is to be questioned when energy currents are taken into account.

Even so, the interpretation based on the wave picture is still valid in this case. We saw that in the case of the charge current, the suppression of interference was caused by the averaging of the spectral current (as shown in Fig. 3.9). This averaging is not expected to hold for the energy since the integral to obtain the energy current from spectral current is weighted by an E factor.

3.4.4 *Noise of an MZI with two sources*

In the following, we will consider the impact of two-particle effects on the charge-current noise. Since the interpretation of our results is not clear from one-particle quantities such as the charge and energy currents, we resort to a quantity where two-particle effects can be clearly seen, the noise.

Absorption of particles

Let us again start to consider the case where possible absorptions might occur. In this situation, the two explanations based either on an averaging effect of the spectral current or on the absorption of particles, carrying charge and energy, could coexist to explain the occurrence or absence of interference effects even when considering energy currents. In that case the charge-current noise is given by

$$\begin{aligned}\frac{\mathcal{P}^{eh}}{-e^2/\mathcal{T}} &= R_L T_L - 4\gamma^2 + 2R_L T_R R_R + 2T_L T_R R_R\left(1-\frac{4\sigma_A\sigma_B}{{\Delta t_d^{eh}}^2+(\sigma_A+\sigma_B)^2}\right)\\ &+2\gamma\,(T_L-R_L)\,(T_R-R_R)\,\mathrm{Re}\left\{e^{-i\Phi}\frac{-2i\sigma_A}{\Delta\tau-2i\sigma_A}\left(1-\frac{2i\sigma_B}{\Delta t_d^{eh}+i\,(\sigma_A+\sigma_B)}\right)\right\}\\ &-\left(2\gamma\mathrm{Re}\left\{e^{-i\Phi}\frac{-2i\sigma_A}{\Delta\tau-2i\sigma_A}\left(1-\frac{2i\sigma_B}{\Delta t_d^{eh}+i\,(\sigma_A+\sigma_B)}\right)\right\}\right)^2 . \qquad (3.31)\end{aligned}$$

The classical part of the noise, shown in the first line of Eq. (3.31), is partly suppressed by the absorptions. In particular, if the particle from $\mathrm{SPS_A}$ took the lower arm of the interferometer with probability T_L and could hence get absorbed, the partition noise at the right barrier created by particles coming from $\mathrm{SPS_A}$ and the opposite type of particle coming from $\mathrm{SPS_B}$, $2T_R R_R$, is fully suppressed. What is then left from the classical part of the noise is given by $R_L T_L - 4\gamma^2 + 2R_L T_R R_R = 2R_L T_R R_R + T_L R_L\,(T_R - R_R)^2$. It equals the partition noise of the two particles at $\mathrm{QPC_R}$ if the particle from $\mathrm{SPS_A}$ took the upper arm, $2R_L T_R R_R$, and the additional noise of the particle from $\mathrm{SPS_A}$ at

$\mathrm{QPC_L}$ in the presence of $\mathrm{QPC_R}$, which can obviously not get affected by the absorptions happening behind $\mathrm{QPC_L}$, $T_L R_L (T_R - R_R)^2$. Also the interference part of the noise gets fully suppressed by the factor $\left(1 - \frac{2i\sigma_B}{\Delta t_d^{eh} + i(\sigma_A+\sigma_B)}\right)$, in the case of absorptions. The result for the noise thus fully confirms that the absorption condition leads to a suppression of fluctuations at $\mathrm{QPC_R}$, yielding information on the path that a particle emitted from $\mathrm{SPS_A}$ took in the MZI.

Collision of particles of the same kind

Finally, we consider the case where an electron emitted each from $\mathrm{SPS_A}$ and $\mathrm{SPS_B}$ can reach the reservoirs in the same half period of the source operation. The charge-current noise takes the form

$$\begin{aligned}\frac{\mathcal{P}^{ee}}{-e^2/\mathcal{T}} &= R_L T_L - 4\gamma^2 + 2T_L T_R R_R + 2R_L T_R R_R \left(1 - \frac{4\sigma_A\sigma_B}{\Delta t_u^{ee\,2} + (\sigma_A+\sigma_B)^2}\right) \\ &+ 2\gamma\,(T_L - R_L)(T_R - R_R)\,\mathbb{R}\mathrm{e}\left\{e^{-i\Phi}\frac{-2i\sigma_A}{\Delta\tau - 2i\sigma_A}\left(1 - \frac{-2i\sigma_B}{\Delta t_u^{ee} - i(\sigma_A+\sigma_B)}\right)\right\} \\ &- \left(2\gamma\mathbb{R}\mathrm{e}\left\{e^{-i\Phi}\frac{-2i\sigma_A}{\Delta\tau - 2i\sigma_A}\left(1 - \frac{-2i\sigma_B}{\Delta t_u^{ee} - i(\sigma_A+\sigma_B)}\right)\right\}\right)^2 . \qquad (3.32)\end{aligned}$$

Equivalently to the absorption case, the behavior of the charge-current noise corroborates the interpretation of the suppression of interference effects in the charge current based on two-particle collisions. Indeed, only when the collision condition at $\mathrm{QPC_R}$ is fulfilled, the classical part of the noise gets suppressed by the contributions stemming from the partition at $\mathrm{QPC_R}$, when the particle took the upper arm, allowing for collisions at the output of the MZI. The remaining classical noise is then given by $2T_L T_R R_R + T_L R_L (T_R - R_R)^2$. At the same time also a full suppression of the interference part of the charge-current noise is found.

Again, the results for the absorption of holes by electrons emitted from $\mathrm{SPS_B}$ and the collision of holes at $\mathrm{QPC_R}$ are shown in the Appendix A.4.

3.5 CONCLUSIONS

In this chapter we have studied interference effects on the charge, energy, and spectral currents as well as on the charge current noise at the output of a MZI fed by one or two single particle sources.

We have shown that when the MZI is fed only by source $\mathrm{SPS_A}$, all quantities show dependence on the flux through the interferometer, i.e. interference effects. The interference effects, visible as oscillations with respect to the magnetic flux, are strongly affected by the detuning of the MZI, given by $\Delta\tau$, due to the energy-dependence of the transmission through the interferometer. This results in a phase shift between the oscillations in the charge and energy currents and in a finite DC current at both outputs despite the fact that the injected DC current is zero. We have also shown that two interpretations can be given for the suppression of the interference for large detuning, based either on the wave-like properties of the injected signal (averaging effect of the interference features occurring in the spectral currents which represent the plane wave contributions of the injected signals) or on the particle-like properties of the same (the limited single-particle coherence length).

We continued our study by adding a second SPS in the middle of the lower arm of the interferometer to investigate how the synchronization of the two sources affects the interference effects in the MZI. The synchronization of the sources, manifesting as collisions and absorptions of particles introduces new relevant time scales. These new time-scales lead to a suppression of the interference in the spectral current when the sources are tuned to allow for absorptions of particles, or even to the occurrence of additional energy-dependent oscillations when the possibility of collisions of particles of the same type is given. As a result of the occurrence of these new time-scales manifestations of two-particle effects are already visible in the DC charge current.

The absorption of particles at $\mathrm{SPS_B}$, as well as the collision of particles at $\mathrm{QPC_R}$ lead to a suppression of interference in the charge current. We demonstrated that this can be interpreted in two different manners: (1) the suppression of interference can be understood as the result of an averaging of the magnetic-flux dependent contributions of the spectral current. It can on the other hand (2) be explained by the possibility of extracting which-path information from reduced fluctuations due to two-particle effects. Our investigation of the noise properties corroborates the possibility of a particle-interpretation of the interference suppression by showing that the absorption and collision of particles indeed leads to a specific reduction of fluctuations. However, this work also shows that the particle-interpretation does not hold in the case of collisions, whenever the behavior of the energy current is considered. We show that the energy current behaves fundamentally different from the charge current of electrons and holes displaying signatures of interference when the charge current does not.

It is to be noted that the theoretical quantities that we studied here are experimentally accessible. Indeed, the charge current and charge-current noise of SPSs in Quantum Hall devices have been measured [22, 69, 73, 104]. Interference effects in energy or heat currents were detected in a stationary superconducting interferometer [105]. Also, measurements of the spectral current in the stationary regime in edge states out of equilibrium have been presented in Ref [44].

In this chapter we have used the single particle sources, implemented using quantum capacitors, as mere tools, that is, as particle emitters. We focused on the possibility of emitting and absorbing electrons from quantum dots acting as quantum capacitors when subjected to low frequency (adiabatic), strong, periodic driving gate potentials. In the next chapter we explore a different regime of operation of quantum capacitors where they are subjected to small-amplitude periodic driving gate potentials and we study their thermoelectric transport properties.

4

TIME-DEPENDENT HEAT FLOW IN INTERACTING QUANTUM CONDUCTORS

4.1 INTRODUCTION

Our previous findings show clearly that charge and energy currents have very different behaviors in nanoscale systems, therefore a thorough study of both electrical and heat properties is needed for a good characterization of this kind of systems. The expeditious advance of circuit miniaturization thus requires the knowledge of heat flow in quantum devices in response to electrical fields [106–108]. Due to this necessity, thermoelectrical transport in quantum devices is a research field that has vigorously relaunched nowadays [109–115]. Nevertheless, so far, the activity has focused on driving electrical currents by oscillatory forces [18, 116] for charge qubit manipulation [117, 118], quantum emitter generation [20, 119–121] or quantum tomography purposes [122].

One of the most widely used quantum devices are quantum capacitors (quantum RC circuits). In fact, the single particle emitters used in the previous chapter, Chapter 3, are quantum capacitors that emit and absorb electrons due to an applied AC signal [20]. Low frequency measurements of the electrical admittance in quantum RC circuits provide information about the spectroscopic (C_q quantum capacitance) and resistive (R_q relaxation resistance) properties of coherent conductors [17, 123, 124] in which $R_q = h/2e^2$ takes an universal value [125–129] for zero temperature. Interactions, such as charging effects [19] or Kondo correlations [130, 131] do not alter the universality of R_q, measured experimentally, in quantum capacitors [17, 123, 124, 132, 133], carbon nanotubes [134], superconducting junctions [135] and quantum dots [136].

In contrast, time-resolved heat transport has been poorly investigated [68, 96, 137, 138]. Only stationary or time-averaged heat flows have been analyzed in more detail [105, 139, 140]. The understanding of time dependent heat currents opens an avenue of creating circuit architectures where heat absorption or emission events are finely tunable via electrical and thermal time-dependent signals. Recently, the linear response for the charge and heat fluxes to electrical and thermal AC signals was attained for a quantum capacitor showing that heat flows can be delayed or elapsed with respect to the AC pulse depending on the dot gate position [138]. Later on, Ludovico, *et al.*, [96] showed, for a slow AC modulation and for noninteracting conductors, that time-dependent heat flow $J(t)$ needs to explicitly consider the energy stored and relaxed at the tunnel coupling region when a tunnel Hamiltonian description is employed.

Our aim in this chapter is to improve the understanding of quantum RC circuits by treating them from a perspective different from the previous chapter where we consider interactions and we do not restrict ourselves to the adiabatic regime but we restrict the amplitude of the driving. By including interactions, we complement the work from Ref.[96] where electrical and heat properties of non-interacting quantum capacitors in the non-adiabatic regime were studied. Furthermore, by studying the heat properties of an RC circuit, we expand the results of Ref.[19] where only the electrical properties of an interacting quantum capacitor were considered.

To this end we derive the time dependent heat flow for *interacting* multi-level conductors and *arbitrary AC frequencies*. Since our heat formula holds for arbitrary high frequencies, it is able to describe photon-assisted tunneling processes occurring in the heat transport. Our only limitation is that we are restricted to the linear response regime, i.e., low AC driving amplitudes. We confine our interests to the Coulomb blockade regime, see Section 1.2.2 of the introduction, and do not consider higher-order correlations like Kondo effect, we implicitly assume a temperature higher than the Kondo scale (T_K), i.e., $T \gg T_K$. For our calculations, we employ the non-equilibrium (Keldysh) Green's function formalism, see Section 2.3,which allows us to include electron-electron interactions, charging effects, in a feasible way within the so-called Hartree-Fock regime.

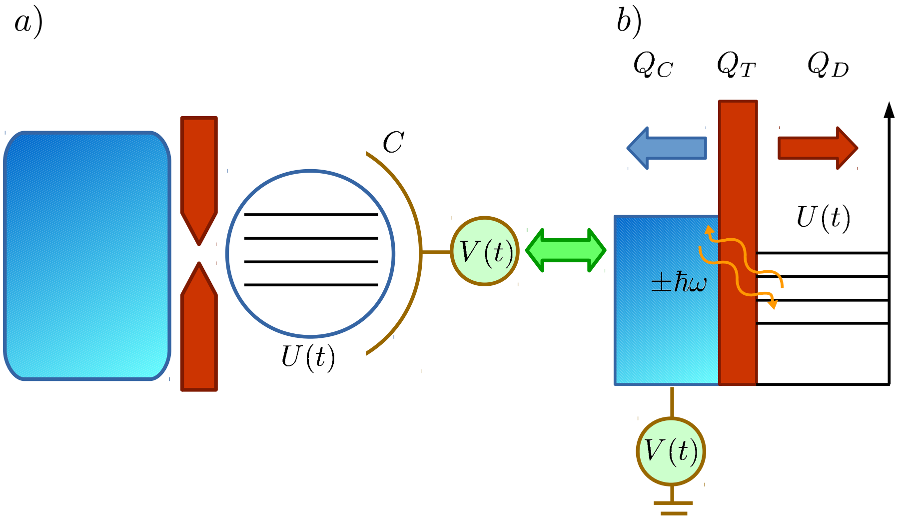

Figure 4.1: Schematic of the multi-orbital interacting quantum capacitor. It is shown two situations where the AC voltage is applied either a) to the dot or b) to the reservoir. Both cases are equivalent by means of a gauge transformation. $U(t)$ denotes the time-dependent internal potential of the dot as response of the charge injected by the AC driving field $V(t)$. We model such response with a capacitance C. We illustrate in b) the induced photon-assisted emission and absorption processes (shown by wiggle lines) in the heat by the action of $V(t)$. $\mathcal{Q}_R$, $\mathcal{Q}_D$, and $\mathcal{Q}_T$ are the energy change rates in time at the reservoir, quantum dot, and tunneling barriers.

The obtained expression for the heat flow is applied to a prototypical *interacting multi-orbital quantum circuit*– a quantum capacitor– formed by a carbon nanotube quantum dot that is coupled to a single terminal being modulated by an AC voltage, as shown in Fig. 4.1. Carbon nanotubes exhibit charging effects due to the formation of quantum dots inside the tube [141]. The valley degrees of freedom, corresponding to the K and K' Dirac points in graphene in addition to the spin indices, lead to a four-fold energy level degeneracy. Such degeneracy can be lifted by the presence of an external magnetic field B [142]. Furthermore, the nanotube curvature yields a spin-orbit interaction resulting in split time-reversal dot level pairs. Therefore, carbon nanotube quantum dots act as multi-orbital interacting conductors where Coulomb interactions give rise to Coulomb blockade phenomena. Even more importantly, carbon nanotube quantum dots have been demonstrated to be perfect platforms to investigate the frequency-resolved transport when they are embedded in electromagnetic cavities, [134] precisely the issue that our work addresses.

The chapter is structured as follows, in Sec. 4.2, we describe the theoretical model for an interacting multi-orbital quantum capacitor and the Hartree-Fock decomposition of electron-electron interaction. We derive the time-dependent heat flux for the reservoir in the linear response regime and obtain the electrothermal admittance. For completeness we also discuss the electrical admittance. In Sec. 4.3, we start by proving that our formalism can exhibit Coulomb blockade phenomena. The observations for a single orbital quantum dot are briefly discussed and then results for a multi-orbital one are presented. Here, we consider a four level degenerated carbon nanotube quantum dot which splits due to the presence of magnetic field and spin-orbit interaction. For this system, we show the RC parameters and investigate the electrical and electrothermal admittances. Our findings are summarized in Sec. 4.4.

4.2 TIME-DEPENDENT TRANSPORT FORMULATION

The purpose is to derive the linear response heat current for an interacting conductor coupled to a reservoir that oscillates with an AC voltage signal in the Coulomb blockade regime. We first propose a model Hamiltonian describing a multi-orbital quantum capacitor which is attached to a single reservoir. Using the Keldysh formalism for nonequilibrium Green's functions, see Section 2.3; we have the linear response heat flux at the reservoir subject to an oscillating electrical signal. Remarkably, the heat flux can be cast in terms of the conductor Green's function as it happens for its electrical counterpart [19].

4.2.1 *Model of Hamiltonian*

The starting point of our derivation is the tunnel Hamiltonian description of a quantum capacitor. The quantum capacitor Hamiltonian $\mathcal{H}$ is split into three parts, namely the reservoir part ($\mathcal{H}_R$), the dot contribution ($\mathcal{H}_D$), and the tunneling term ($\mathcal{H}_T$), i.e.,

$$\mathcal{H} = \mathcal{H}_R + \mathcal{H}_D + \mathcal{H}_T \,. \tag{4.1}$$

More concretely, the reservoir part reads

$$\mathcal{H}_R = \sum_{k,\sigma} \left[\epsilon_{k\sigma} - (\mu + eV(t))\right] c^{\dagger}_{k\sigma} c_{k\sigma} \,, \tag{4.2}$$

where $\mu = E_F + eV_{DC}$ is the chemical potential with E_F the fermi energy, V_{DC} the bias offset, $e > 0$ the unit charge, and $V(t)$ the electrical voltage modulation [see Fig. 4.1 b)]. As shown in Fig. 4.1, notice that this description is equivalent to the situation where the AC voltage is applied to the dot since a gauge transformation connects both situations and we thus employ two situations interchangeably [47]. Without loss of generality, we set $V_{DC} = 0$. The operator $c^{\dagger}_{k\sigma}(c_{k\sigma})$ creates (annihilates) an electron with wavevector k and spin σ in the reservoir. For the dot contribution describing an interacting system with n levels, we have

$$\mathcal{H}_D = \sum_{n,\sigma} \epsilon_{n\sigma} d^{\dagger}_{n\sigma} d_{n\sigma} + E_C \left[N_d + \mathcal{N}(t)\right]^2 \,, \tag{4.3}$$

where $d^\dagger_{n\sigma}(d_{n\sigma})$ corresponds to the creation (annihilation) operator for a dot electron in the nth level with spin σ, $\epsilon_{n\sigma}$ denotes the single-particle energies, and $E_C = e^2/2C$ is the electrostatic charging energy (C is the dot geometrical capacitance). Here, the dot occupation operator reads $N_d = \sum_{n,\sigma} d^\dagger_{n\sigma}d_{n\sigma}$ and the polarization charge is given by $\mathcal{N}(t)$. Finally, the tunneling term hybridizes the reservoir and the dot subsystems according to

$$\mathcal{H}_T = \sum_{n,k,\sigma}\left(t_{nk\sigma}c^\dagger_{k\sigma}d_{n\sigma} + \text{H.c.}\right). \tag{4.4}$$

where $t_{nk\sigma}$ denotes the tunneling amplitude.

When charge is injected in the dot by an external source $V(t)$, a polarization charge is created to keep the dot as a neutral charge object. In a simple electrostatic picture, we model such polarization charge with a capacitance C leading to [143]

$$e\mathcal{N}(t) = CU(t)\,, \tag{4.5}$$

in which $U(t)$ is the internal potential of the dot giving rise to a time-dependent potential inside the dot. Then, the dot Hamiltonian in Eq. (4.3), up to linear order in $U(t)$, can be written as

$$\mathcal{H}_D = \sum_{n,\sigma}\left[\epsilon_{n\sigma} + eU(t)\right] d^\dagger_{n\sigma}d_{n\sigma} + E_C N_d^2\,. \tag{4.6}$$

Since $N_d^2 = \sum_{m,\sigma}\sum_{n,\sigma'} d^\dagger_{m\sigma}d_{m\sigma}d^\dagger_{n\sigma'}d_{n\sigma'}$ is a quartic operator, the Hamiltonian cannot be solved without introducing some proper approximation.

4.2.2 *Hartree Fock approximation*

We thus perform the Hartree-Fock approximation [47] in the dot Hamiltonian. For the Hartree approximation, N_d^2 is decoupled in the form

$$[N_d^2]_{\text{Hartree}} = 2\sum_{m,\sigma}\sum_{n,\sigma'} d^\dagger_{m\sigma}d_{m\sigma}\langle d^\dagger_{n\sigma'}d_{n\sigma'}\rangle\,, \tag{4.7}$$

The problem with the Hartree approximation is that it does not take into account possible spin effects and thus we need the Fock approximation for which one has

$$[N_d^2]_{\text{Fock}} = -2\sum_{m,\sigma}\sum_{n,\sigma'} d^\dagger_{m\sigma}d_{n\sigma'}\langle d^\dagger_{m\sigma}d_{n\sigma'}\rangle\,. \tag{4.8}$$

Considering Hartree and Fock approximations (HF) together, the dot Hamiltonian then becomes

$$\mathcal{H}_D = \sum_{m,n,\sigma}\widetilde{\epsilon}_{mn\sigma}(t)d^\dagger_{m\sigma}d_{n\sigma}\,, \tag{4.9}$$

where

$$\widetilde{\epsilon}_{mn\sigma}(t) = \delta_{m,n}\Bigg(\epsilon_{m\sigma} + eU(t) + 2E_C\sum_{\substack{l,s\\(\neq m,\sigma)}}\langle d^\dagger_{ls}d_{ls}\rangle\Bigg) - 2E_C\langle d^\dagger_{m\sigma}d_{n\sigma}\rangle, \tag{4.10}$$

with $\sigma = \uparrow / \downarrow$. An important observation is in order when Eq. (4.9) is considered. We check that interactions are well described by our model by calculating the static occupation $\langle N_d \rangle$ and observing that it does not change continuously but shows plateaus and discontinuous jumps, see Appendix B. These jumps, or rather the fact that charge is frozen for a given value of ϵ_d, are clear evidence of Coulomb blockade, confirming that interactions are well captured by our approximations.

4.2.3 *Heat current*

Our main interest is focused on the rate of heat at the reservoir. For such purpose, we evaluate the time derivative of each component of the Hamiltonian which is given by

$$\mathcal{Q}_S(t) = \frac{d}{dt}\langle \mathcal{H}_S \rangle = \frac{i}{\hbar}\langle [\mathcal{H}, \mathcal{H}_S] \rangle + \left\langle \frac{\partial \mathcal{H}_S}{\partial t} \right\rangle , \tag{4.11}$$

where $S = \{R, D, T\}$ is referred to R reservoir, D dot, and T tunneling term. Notice that in Eq. (4.11) the last term is the power supplied by an external source and must be subtracted from the definition of the heat rate $\mathcal{Q}_S(t)$. Besides, since the Hamiltonian operator $\mathcal{H}$ commutes with itself it is fulfilled

$$\frac{i}{\hbar}\langle [\mathcal{H}, \mathcal{H}] \rangle = \mathcal{Q}_R(t) + \mathcal{Q}_D(t) + \mathcal{Q}_T(t) = 0 . \tag{4.12}$$

As mentioned, our goal is to compute $\mathcal{Q}_R(t)$. When Coulomb interaction is taken into account, we obtain the rate of heat at the reservoir, $\mathcal{Q}_R(t)$, in terms of interacting dot Green's functions. Since the direct calculation of $\mathcal{Q}_R(t)$ is cumbersome, our strategy is first to compute the energy change rates at the dot and tunnel barrier using Eq. (4.12)

$$\mathcal{Q}_R(t) = -(\mathcal{Q}_D(t) + \mathcal{Q}_T(t)) . \tag{4.13}$$

We recall that our calculation applies only for the linear response regime and thus we keep only the leading order contributions in the fields $V(t)$ and $U(t)$. We employ the non-equilibrium Keldysh Green's function formalism for the calculation of the energy change rates in time [48]. We start with the time derivative of $\mathcal{H}_D$ first,

$$\begin{aligned}\frac{d}{dt}\langle \mathcal{H}_D(t) \rangle = &\sum_{m,n,\sigma} [\partial_t \tilde{\epsilon}_{mn\sigma}(t)] \langle d^\dagger_{m\sigma}(t) d_{n\sigma}(t) \rangle \\ &+ \sum_{m,n,\sigma} \tilde{\epsilon}_{mn\sigma}(t) \partial_t \langle d^\dagger_{m\sigma}(t) d_{n\sigma}(t) \rangle . \end{aligned} \tag{4.14}$$

The first term on the right hand side denotes the power developed by the AC source and does not contribute to the heat flow. The second term represents the energy flux going into the dot which can be written in terms of the dot Green's function

$$\mathcal{Q}_D(t) = -i\mathrm{Tr}\left[\tilde{\boldsymbol{\epsilon}}_{d\sigma}(t) \partial_t \mathbf{G}^<_{d\sigma,d\sigma}(t,t) \right] . \tag{4.15}$$

Hereafter, **bold face symbols** denote matrices such that their (m, n) components are

$$\begin{aligned} [\tilde{\boldsymbol{\epsilon}}_{d\sigma}(t)]_{m,n} &= \tilde{\epsilon}_{mn\sigma}(t) , \\ [\mathbf{G}^<_{d\sigma,d\sigma}(t,t')]_{m,n} &= i\langle d^\dagger_{n\sigma}(t') d_{m\sigma}(t) \rangle . \end{aligned} \tag{4.16}$$

The trace means summations over energy levels and spin indices, i.e., $\mathrm{Tr} = \sum_{m,n}\sum_{\sigma}$. Secondly, from the definition of $\mathcal{H}_T$, it can be shown that

$$\langle \mathcal{H}_T \rangle = -i\mathrm{Tr}\left[\mathbf{G}^{<}_{d\sigma,c\sigma}(t,t)\mathbf{t}_{\sigma} + \mathbf{t}^{*}_{\sigma}\mathbf{G}^{<}_{c\sigma,d\sigma}(t,t)\right], \tag{4.17}$$

and thus the time variation of energy stored or relaxed at tunneling barrier $\mathcal{Q}_T(t) = \partial_t \langle \mathcal{H}_T \rangle$ is given by

$$\mathcal{Q}_T(t) = -i\partial_t \mathrm{Tr}\left[\mathbf{t}^{*}_{\sigma}\mathbf{G}^{<}_{c\sigma,d\sigma}(t,t) + \mathbf{G}^{<}_{d\sigma,c\sigma}(t,t)\mathbf{t}_{\sigma}\right]. \tag{4.18}$$

Here, the reservoir-dot and dot-reservoir Green's functions are given, respectively, by

$$[\mathbf{G}^{<}_{c\sigma,d\sigma}(t,t')]_{k,n} = i\langle d^{\dagger}_{n\sigma}(t')c_{k\sigma}(t)\rangle, \tag{4.19}$$

$$[\mathbf{G}^{<}_{d\sigma,c\sigma}(t,t')]_{n,k} = i\langle c^{\dagger}_{k\sigma}(t')d_{n\sigma}(t)\rangle, \tag{4.20}$$

with $[\mathbf{t}^{*}_{\sigma}]_{n,k} = t^{*}_{nk\sigma}$ and $\mathrm{Tr} = \sum_{k,n,\sigma}$.

Using the standard technique of equation of motion as explained in Section 2.3, shown in Eq. (2.75) , the reservoir-dot Green's function $\mathbf{G}^{<}_{c\sigma,d\sigma}(t,t)$ can now be recast in terms of solely the dot Green's functions as follows,

$$\mathbf{t}^{*}_{\sigma}\mathbf{G}^{<}_{c\sigma,d\sigma}(t,t) = \int \frac{dt_1}{\hbar}\,[\mathbf{\Sigma}^{r}_{\sigma}(t,t_1)\mathbf{G}^{<}_{d\sigma,d\sigma}(t_1,t) + \mathbf{\Sigma}^{<}_{\sigma}(t,t_1)\mathbf{G}^{a}_{d\sigma,d\sigma}(t_1,t)]. \tag{4.21}$$

Here, we have defined

$$\mathbf{\Sigma}^{a/r}_{\sigma}(t_1,t_2) = \pm\frac{i}{2}\hbar\mathbf{\Gamma}\delta(t_1-t_2), \tag{4.22}$$

$$\mathbf{\Sigma}^{<}_{\sigma}(t_1,t_2) = i\mathbf{\Gamma}e^{-i\phi_V(t_1,t_2)}f(t_1-t_2) \tag{4.23}$$

as the advanced/retarded and lesser self-energies [19] that contain the time-dependent fields. We have assumed a momentum-independent tunneling amplitude $t_{nk\sigma} = t_{n\sigma}$ leading to hybridization strength given by $[\mathbf{\Gamma}]_{m,n} = 2\pi\rho_0 t^{*}_{m\sigma}t_{n\sigma}$ with $\rho_0 = 1/2D$ the density of states of the reservoir and D the reservoir bandwidth. In such self-energies,

$$\phi_V(t_1,t_2) = \int_{t_2}^{t_1}\frac{dt}{\hbar}\,eV(t), \tag{4.24}$$

is defined as the time-dependent phase due to the AC external potential and

$$f(t_1-t_2) = \int\frac{d\epsilon}{2\pi}e^{-i\epsilon(t_1-t_2)/\hbar}f(\epsilon), \tag{4.25}$$

where $f(t_1-t_2)$ the Fermi-Dirac distribution function in the time domain. Similarly, the dot-reservoir Green's function $\mathbf{G}^{<}_{d\sigma,c\sigma}(t,t)\mathbf{t}_{\sigma}$ is given by

$$\mathbf{G}^{<}_{d\sigma,c\sigma}(t,t)\mathbf{t}_{\sigma} = \int\frac{dt_1}{\hbar}\,[\mathbf{G}^{r}_{d\sigma,d\sigma}(t,t_1)\mathbf{\Sigma}^{<}_{\sigma}(t_1,t) + \mathbf{G}^{<}_{d\sigma,d\sigma}(t,t_1)\mathbf{\Sigma}^{a}_{\sigma}(t_1,t)]. \tag{4.26}$$

Employing Eqs. (4.21) and (4.26), we find $\mathcal{Q}_T$ is also expressed only in terms of the dot Green's functions.

Once the heat energy rates for the dot and the tunneling parts ($\mathcal{Q}_D$, and $\mathcal{Q}_T$) are expressed in terms of the dot Green's function, the next step consists of computing such Green's functions in the presence of the time-dependent AC signal. For the dot's retarded/advanced Green's function, we have that in the H-F approximation [19]

$$\mathbf{G}^{r/a}_{d\sigma,d\sigma}(t,t') = e^{-i\phi_U(t,t')}\mathbf{G}^{r/a,eq}_{d\sigma,d\sigma}(t-t'), \tag{4.27}$$

where $\phi_U(t,t') = \int_{t'}^{t}(dt_1/\hbar)\, eU(t_1)$, and $\mathbf{G}^{r/a,eq}_{d\sigma,d\sigma}(t_1-t_2)$ denotes the dot's retarded/advanced Green's function in equilibrium, i.e., in the absence of AC signal. Finally, the dot's lesser Green's function is obtained, from the Keldysh equation Eq. (2.60), by means of

$$\mathbf{G}^{<}_{d\sigma,d\sigma}(t,t') = \int \frac{dt_1}{\hbar} \int \frac{dt_2}{\hbar}\, \mathbf{G}^{r}_{d\sigma,d\sigma}(t,t_1)\boldsymbol{\Sigma}^{<}_{\sigma}(t_1,t_2)\mathbf{G}^{a}_{d\sigma,d\sigma}(t_2,t'). \tag{4.28}$$

We proceed now inserting Eqs. (4.21)-(4.28) into Eqs. (4.15) and (4.18). After some cumbersome algebra, involving an expansion to linear order in V and U and a convenient Fourier transform into the frequency domain, the energy change rates become

$$\mathcal{Q}_D(\omega) = ie\omega\mathrm{Tr}\left\{\int \frac{d\epsilon}{2\pi}\, \widetilde{\boldsymbol{\epsilon}}_{d\sigma}\mathcal{A}(\epsilon,\hbar\omega)[V(\hbar\omega)-U(\hbar\omega)]\right\}, \tag{4.29a}$$

$$\mathcal{Q}_T(\omega) = ie\omega\mathrm{Tr}\left\{\int \frac{d\epsilon}{2\pi}\, (\hbar\omega + 2\epsilon - 2\widetilde{\boldsymbol{\epsilon}}_{d\sigma})\mathcal{A}(\epsilon,\hbar\omega)[V(\hbar\omega)-U(\hbar\omega)]\right\}, \tag{4.29b}$$

where $V(\hbar\omega)$, and $U(\hbar\omega)$ are the Fourier transforms of $V(t)$, and $U(t)$ respectively. Here,

$$\mathcal{A}(\epsilon,\hbar\omega) = \Upsilon(\hbar\omega,\epsilon)\mathcal{F}(\epsilon,\hbar\omega) \tag{4.30}$$

with

$$\begin{aligned} \Upsilon(\hbar\omega,\epsilon) &= \left[\mathbf{G}^{r,eq}_{d\sigma,d\sigma}(\epsilon+\hbar\omega)\boldsymbol{\Gamma}\mathbf{G}^{a,eq}_{d\sigma,d\sigma}(\epsilon)\right], \\ \mathcal{F}(\epsilon,\hbar\omega) &= \frac{f(\epsilon+\hbar\omega)-f(\epsilon)}{\hbar\omega}. \end{aligned} \tag{4.31}$$

The dot's retarded/advanced Green's function in equilibrium and in frequency domain is given by

$$\mathbf{G}^{r/a,eq}_{d\sigma,d\sigma}(\epsilon) = \frac{1}{\epsilon - \widetilde{\boldsymbol{\epsilon}}_{d\sigma} \pm i\boldsymbol{\Gamma}/2}, \tag{4.32}$$

with

$$[\widetilde{\boldsymbol{\epsilon}}_{d\sigma}]_{m,n} = \delta_{m,n}\left(\epsilon_{m\sigma} + 2E_C \sum_{\substack{l,s \\ (\neq m,\sigma)}} \langle d^\dagger_{ls} d_{ls}\rangle\right) - 2E_C\langle d^\dagger_{m\sigma} d_{n\sigma}\rangle. \tag{4.33}$$

Although Eq. (4.32) has the same structure with its noninteracting retarded/advanced Green's function, the charging energy is included in the denominator such that it can describe the Coulomb blockade effect as mentioned above [49]. To completely determine the dot Green's function, the diagonal and off-diagonal dot occupations need to be self-consistently calculated using

$$\langle d^\dagger_{ns} d_{ms}\rangle = \frac{1}{2\pi i}\int d\epsilon [\mathbf{G}^{<}_{d\sigma,d\sigma}(\epsilon)]_{n,m}. \tag{4.34}$$

Finally, from Eqs. (4.29) and (4.13), we obtain the expression for the energy change rate at the reservoir

$$\begin{aligned}&\mathcal{Q}_R(\omega) = -(\mathcal{Q}_D(\omega)+\mathcal{Q}_T(\omega)) = \\ &= -ie\omega\mathrm{Tr}\Big\{\int \frac{d\epsilon}{2\pi}(\hbar\omega + 2\epsilon - \widetilde{\epsilon}_{d\sigma})\mathcal{A}(\epsilon,\hbar\omega)[V(\hbar\omega)-U(\hbar\omega)]\Big\}. \quad (4.35)\end{aligned}$$

Importantly, neither $\mathcal{Q}_R(\omega)$ nor $\mathcal{Q}_D(\omega)$ have a well defined parity when the AC frequency is reversed, and therefore, within linear response theory, these two magnitudes do not represent physical quantities [47] (see Sec. 4.3). Based on these observations, the reservoir and dot frequency-dependent heat current expressions must be thus modified to exhibit a proper parity property when the AC frequency is reversed. We find that the expressions

$$J_R = \mathcal{Q}_R(\omega) + \frac{1}{2}\mathcal{Q}_T(\omega), \quad J_D = \mathcal{Q}_D(\omega) + \frac{1}{2}\mathcal{Q}_T(\omega) \quad (4.36)$$

satisfy the parity property. Remarkably, the choice of the factor $\frac{1}{2}\mathcal{Q}_T(\omega)$ is unique in order to ensure a well defined parity property in both J_R, and J_D.

After these considerations, the formulations for the the dot and reservoir frequency dependent heat currents in the linear response regime read

$$\begin{aligned}J_D = -J_R = ie\omega\mathrm{Tr}\Big\{\int \frac{d\epsilon}{2\pi}\left(\frac{\hbar\omega}{2}+\epsilon\right)\mathcal{A}(\epsilon,\hbar\omega) \\ \times [V(\hbar\omega)-U(\hbar\omega)]\Big\}. \quad (4.37)\end{aligned}$$

Therefore we have found the expressions for the heat currents in an interacting quantum capacitor at arbitrary AC frequencies. This is the central finding of our work.

Formally, these expressions agree with their noninteracting counterpart for the time dependent heat currents [96]. However, it should be noted that our theoretical analysis *(i)* goes beyond low AC frequencies in contrast with Ref. [96] in which the heat rate was obtained up to second order in the AC frequency using the Floquet theory, *(ii)* includes the effect of Coulomb blockade, and *(iii)* is applicable to multi-orbital conductors in contrast to previous time heat formulations.

Remarkably, our AC heat formula contains photon-assisted tunneling events only possible for sufficiently high AC frequencies. Note that a similar definition for the time-dependent heat, but applicable to a spin chain model (using a tight-binding model), was proposed in Ref. [144]. In such work, the heat flux connecting two sites, n and $n \pm 1$, was incorporated to the general heat flow expression with a $1/2$ factor in close analogy to Eq. (4.36). However, caution is needed when this comparison is made. The results for a chain of sites are not immediately generalized to our continuum model by just keeping the factor one-half in front of the tunneling energy flow.

4.2.4 *Electrothermal admittance*

In the presence of a time-dependent driving force, it is quite general to characterize the transport using the concept of admittance. The complex electrothermal admittance is defined as

$$\mathcal{M}(\omega) = \frac{J_R(\omega)}{V(\hbar\omega)}. \quad (4.38)$$

Notice that Eq. (4.38) which can be obtained from Eq. (4.37) contains the unknown function $U(\hbar\omega)$. Therefore, for a complete characterization of the complex electrothermal admittance, we need first to determine the internal potential $U(\hbar\omega)$. For such purpose, we note that the displacement current I_D can be featured by a capacitance C in a simple model (here, we consider the situation shown in Fig. 4.1 a))

$$I_D(\omega) = -i\omega C U(\hbar\omega). \tag{4.39}$$

Due to current conservation, the displacement current is equal to the tunneling current I_T [19] for a quantum capacitor, i.e. $I_T = I_D$. The tunneling current in the linear regime is

$$I_T(\omega) = g(\omega)[V(\hbar\omega) - U(\hbar\omega)], \tag{4.40}$$

where (see Ref. [19] for its explicit derivation)

$$g(\omega) = ie^2\omega \mathrm{Tr}\left\{\int \frac{d\epsilon}{2\pi}\mathcal{A}(\epsilon,\hbar\omega)\right\}. \tag{4.41}$$

The internal potential is obtained when we impose current conservation $I_D = I_T$, then $U(\hbar\omega)$ reads

$$U(\hbar\omega) = \frac{g(\omega)V(\hbar\omega)}{-i\omega C + g(\omega)}. \tag{4.42}$$

Inserting Eq. (4.42) into Eq. (4.37) completely characterizes the linear response of the heat current to a time dependent voltage, i.e., the electrothermal admittance

$$\mathcal{M}(\omega) = m(\omega)\frac{-i\omega C}{[-i\omega C + g(\omega)]}, \tag{4.43}$$

with

$$m(\omega) = ie\omega \mathrm{Tr}\left\{\int \frac{d\epsilon}{2\pi}\left(\frac{\hbar\omega}{2} + \epsilon\right)\mathcal{A}(\epsilon,\hbar\omega)\right\}. \tag{4.44}$$

Similarly, the thermoelectrical admittance is defined as

$$\mathcal{L}(\omega) = \frac{I_T(\omega)}{T(\omega)}, \tag{4.45}$$

with $T(\omega)$ being the Fourier transform of a time modulated temperature $T(t)$. Remarkably, the thermoelectrical and the electrothermal admittances are reciprocally related due to the microreversibility principle [38, 145]

$$\mathcal{M}(\omega) = T\mathcal{L}(\omega). \tag{4.46}$$

Notice that microreversibility principle only holds at linear order in $V(t)$, and $U(t)$. Hence, all results obtained for $\mathcal{M}(\omega)$ should be valid for $\mathcal{L}(\omega)$ Finally, a second order expansion in the AC frequency for $m(\omega)$

$$m(\omega) = -i\omega C_{\mathcal{M}} + \omega^2 C_{\mathcal{M}}^2 R_{\mathcal{M}}, \tag{4.47}$$

allows us to obtain the RC electrothermal parameters, see Appendix C for the full expression of $C_{\mathcal{M}}$ and $R_{\mathcal{M}}$. For comparison, we also calculate the electrical admittance defined by

$$\mathcal{G}(\omega) = \frac{I_T}{V(\hbar\omega)} = g(\omega)\frac{-i\omega C}{[-i\omega C + g(\omega)]}. \tag{4.48}$$

The corresponding second order expansion of $g(\omega)$ in frequency

$$g(\omega) = -i\omega C_{\mathcal{G}} + \omega^2 C_{\mathcal{G}}^2 R_{\mathcal{G}}, \tag{4.49}$$

always yields positive RC parameters, i.e., I_T is always delayed with respect to $V(\omega)$, see Appendix C.1. This is in clear contrast to the electrothermal admittance case in which both $C_{\mathcal{M}}$ and $R_{\mathcal{M}}$ can be either positive or negative as shown in Appendix C.2. The heat flow response is elapsed or delayed with respect to the electrical signal depending on the system parameters. Note however that the product of both quantities, the RC time, is kept always positive as expected. Similar results were obtained in Ref. [138] for the non-interacting case.

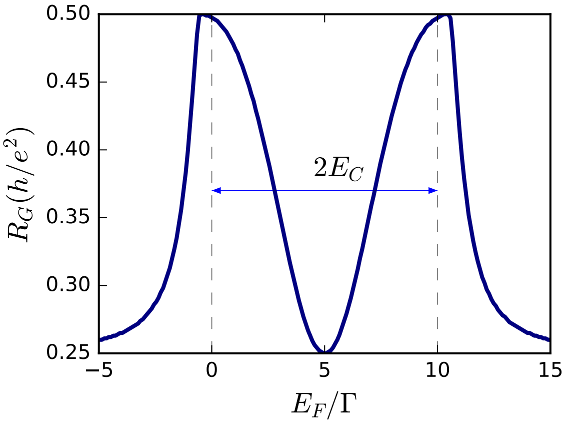

Figure 4.2: Charge relaxation resistance for a single orbital quantum capacitor versus the Fermi energy. Parameters: $\epsilon_d = 0$, $\Delta_Z = 0.5\Gamma$, $2E_C = 10\Gamma$, and $k_B T = 0.04\Gamma$.

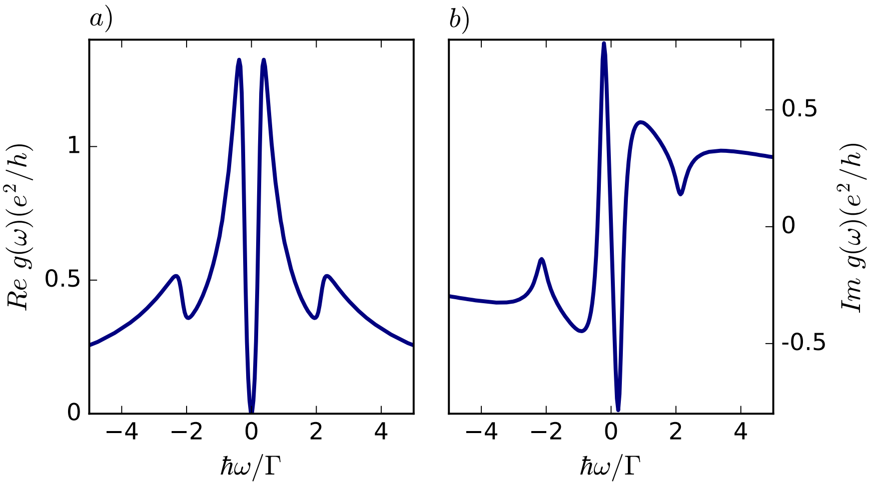

Figure 4.3: a) Real and b) imaginary parts of $g(\omega)$ for a single orbital quantum capacitor as a function of the AC frequency. Photon-assisted excitations occur at the transition rate energies $\pm\hbar\omega = |E_F - \epsilon_{d\sigma}|$ when $k_B T \ll \Gamma$. Parameters: $\epsilon_d = 0$, $\Delta_Z = 0.625\Gamma$, $2E_C = 10\Gamma$, $E_F = 0$, and $k_B T = 0.04\Gamma$.

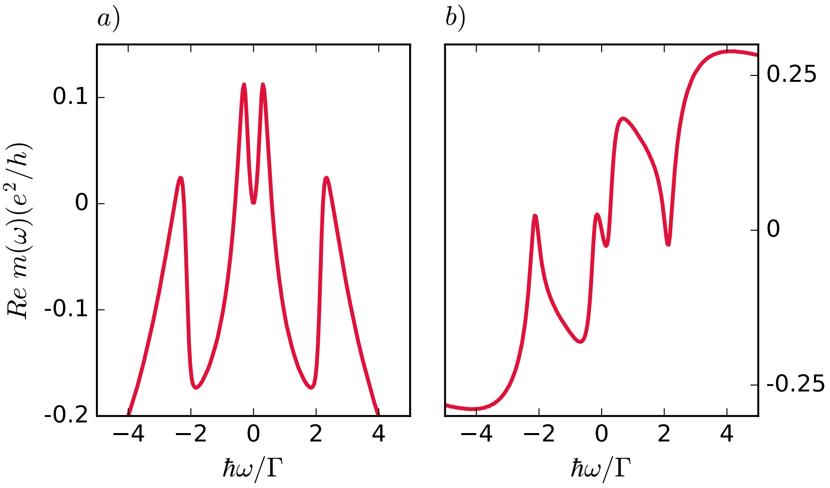

Figure 4.4: a) Real and b) imaginary parts of $m(\omega)$ for a single orbital quantum capacitor versus the AC frequency. Photon-assisted excitations occur at the resonant conditions. Parameters: $\epsilon_d = 0$, $\Delta_Z = 0.625\Gamma$, $2E_C = 10\Gamma$, $E_F = 0$, and $k_B T = 0.04\Gamma$.

4.3 APPLICATION: ILLUSTRATIVE EXAMPLES

Previously, we have derived the formal expressions for the reservoir heat flow and the corresponding electrothermal admittance. Now, we apply these formulas to the case of an interacting multi-orbital conductor. However, before addressing the multi-orbital case, for illustration purposes we first investigate a single orbital interacting quantum capacitor under the influence of an AC potential. Later on, we will analyze a prototype of multi-orbital conductor, a carbon nanotube quantum dot attached to a single reservoir. In both cases, we show results for the electrical and electrothermal transport.

4.3.1 *Single orbital quantum capacitor*

We consider an interacting quantum dot with just one orbital contacted to a single reservoir. The reservoir has an electrical potential that oscillates in time. In accordance with our previous theoretical considerations, the prefactor $g(\omega)$ of the electrical admittance $\mathcal{G}(\omega)$ can be expanded in powers of the AC frequency up to second order as shown in Eq. (4.49). A very well known result establishes that $R_\mathcal{G} = h/(2qe^2)$ becomes universal being q the number of transport channels. Our example as shown in Fig. 4.2 considers the presence of a Zeeman field to explicitly break spin degeneracy. $R_\mathcal{G}$ takes the value of $h/2e^2$ when just one of the two spin-resolved levels ($\epsilon_{d\uparrow/\downarrow} = E_F \pm \Delta_Z/2$) participates in transport, whereas it becomes $h/4e^2$ when the opposite spin channel also contributes. Clearly, the two main peaks observed in $R_\mathcal{G}$ are separated roughly by $2E_C$ the charging energy ($2E_C \gg \Delta_Z$). Our results for $R_\mathcal{G}$ indicate the presence of charging effects and the Coulomb blockade phenomenon.

More importantly, our major interest resides in the behavior of the electrical and electrothermal admittances at arbitrary AC frequencies. Figure 4.3 shows the real [Fig. 4.3 a)] and imaginary [Fig. 4.3 b)] parts of the prefactor $g(\omega)$ in the expression for the electrical admittance $\mathcal{G}(\omega)$ [see Eq. (4.48)]. We observe that $\Re\mathrm{e}g(\omega) = \Re\mathrm{e}g(-\omega)$ and $\Im\mathrm{m}g(\omega) = -\Im\mathrm{m}g(-\omega)$. The factor $-i\omega C/(-i\omega C + g(\omega))$ in Eq. (4.48) then does not change the parity property of $\mathcal{G}(\omega)$ with respect to ω, hence for simplicity we consider only $g(\omega)$. Excitations occur when the AC frequency matches with the resonant condition $\pm\hbar\omega \approx |\widetilde{\epsilon}_{d\sigma} - E_F|$. We recall that $\widetilde{\epsilon}_{d\sigma}$ is the spin-dependent dot energy level renormalized by electron-electron interactions according to

$$\widetilde{\epsilon}_{d\sigma} = \epsilon_d + \sigma\Delta_Z + 2E_C\langle d^\dagger_{\bar{\sigma}} d_{\bar{\sigma}}\rangle\,. \tag{4.50}$$

For the parameters used in Fig. 4.3, we obtain $\widetilde{\epsilon}_{d\sigma} \approx 0.3\Gamma$, 2.1Γ which agrees with the resonant behavior found in $g(\omega)$ with peaks at $\pm\hbar\omega \approx 0.3\Gamma$, and $\pm\hbar\omega \approx 2.1\Gamma$.

Similar features are observed in the electrothermal admittance shown in Fig. 4.4. Interestingly, the imaginary part of $m(\omega)$ for $\omega > 0$ takes either positive or negative values by tunning the AC frequency, which indicates that time heat current can be either delayed or elapsed with respect to the AC electrical time-dependent signal.

Now, we discuss the parity property of the response functions $g(\omega)$ and $m(\omega)$ [thus $\mathcal{G}(\omega)$ and $\mathcal{M}(\omega)$]. We write $g(\omega)$ in the form

$$g(\omega) = \Re\mathrm{e}g(\omega) + i\Im\mathrm{m}g(\omega)\,, \tag{4.51}$$

and express the real/imaginary part as

$$\Re\mathrm{e}g(\omega) = \frac{1}{2}\left[g(\omega) + g^*(\omega)\right] = \frac{1}{2}\int_{-\infty}^{\infty} dt\, e^{i\omega t}\left[g(t) + g(-t)\right]\,, \tag{4.52}$$

$$\Im\mathrm{m}g(\omega) = \frac{1}{2i}\left[g(\omega) - g^*(\omega)\right] = \frac{1}{2i}\int_{-\infty}^{\infty} dt\, e^{i\omega t}\left[g(t) - g(-t)\right]\,. \tag{4.53}$$

Here, we used the fact that the response function $g(t)$ must be real to have a real expectation value for the current $I_T(t)$. From Eq. (4.53), it is quite easy to show that

$$\Im\mathrm{m}g(-\omega) = \frac{1}{2i}\int_{-\infty}^{\infty} dt\, e^{i\omega t}\left[g(-t) - g(t)\right]\,, \tag{4.54}$$

which implies $\Im\mathrm{m}g(\omega) = -\Im\mathrm{m}g(-\omega)$. Using a similar line of reasoning, we can also prove that $\Re\mathrm{e}g(\omega) = \Re\mathrm{e}g(-\omega)$. This argument also works for $m(\omega)$. It is worth noting that this parity property comes from the fact that we have included the contribution due to the tunnel Hamiltonian in our definition for the heat flow as shown in Eq. (4.36). Furthermore, this parity argument goes beyond the simple site partitioning scheme explained in Ref. [144].

4.3.2 *Multi-orbital quantum capacitor*

We now investigate a single reservoir carbon nanotube quantum dot as an example of a *multi-orbital interacting* conductor. We regard the nanotube quantum dot as a localized single particle level described by two quantum numbers, the orbital quantum number τ associated to clockwise ($\tau = +1$) and anti-clockwise ($\tau = -1$) semi-classical orbits along the nanowire circumference (related with the K-valley degeneracy in graphene) and the spin degree of freedom σ. In the presence of magnetic field along the nanotube axis, the dot energy level splits in the spin sector by the Zeeman field Δ_Z

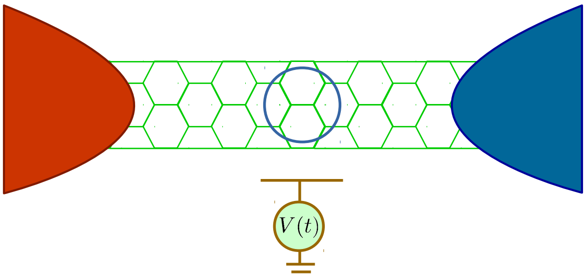

Figure 4.5: Schematic representation of a quantum dot (blue circle) created in a carbon nanotube.

and in the orbital sector by an amount Δ_{orb} that depends on the nanotube radius [142]. Besides, due to the nanowire curvature a non-negligible spin-orbit interaction is present, yielding a Kramers splitting of magnitude Δ_{so}. All together yields the following carbon nanotube dot energy level:

$$\epsilon_{d\sigma\tau} = \epsilon_d + \sigma\Delta_Z + \tau\Delta_{orb} + \sigma\tau\Delta_{so}. \tag{4.55}$$

In the following, we show results that correspond to the realistic parameters: [142] $\epsilon_d = 0$, $\Delta_Z = 0.625\Gamma$, $\Delta_{orb} = 5\Delta_Z$ (orbital magnetic moments can be $5 - 20$ times larger than its spin counterpart [142]), and $\Delta_{so} = 0.5\Delta_Z$. The charging energy is $2E_C = 2\Gamma$ which lies in the strong interacting regime. We restrict ourselves to the low temperature regime $k_B T = 0.05\Gamma$.

First, we show our results for the electrical and electrothermal RC parameters in Fig. 4.6. In the low temperature limit ($k_B T \ll \Gamma$) the RC parameters exhibit universal values [125–127]. We recall that in the low frequency regime the RC parameters characterize the electrical and electrothermal admittances (see Eqs. (4.47) and (4.49)). $C_{\mathcal{G}}$ and $R_{\mathcal{G}}$ are displayed in Fig. 4.6 a) and c) when E_F is varied. The electrical capacitance $C_{\mathcal{G}}$ shows oscillations which peaks at the positions located roughly at the CNT resonances

$$\epsilon_d - \Delta_Z - \Delta_{orb} + \Delta_{so} \approx -3.4\Gamma, \tag{4.56}$$

$$\epsilon_d + \Delta_Z - \Delta_{orb} - \Delta_{so} + 2E_C \approx -0.8\Gamma, \tag{4.57}$$

$$\epsilon_d - \Delta_Z + \Delta_{orb} - \Delta_{so} + 2(2E_C) \approx 6.2\Gamma, \tag{4.58}$$

$$\epsilon_d + \Delta_Z + \Delta_{orb} + \Delta_{so} + 3(2E_C) \approx 10\Gamma. \tag{4.59}$$

As expected, at each nanotube level position, $R_{\mathcal{G}}$ takes the value of $h/2e^2$, while in the middle of two consecutive resonances (when two resonances contribute to $R_{\mathcal{G}}$) it diminishes to half of this value. Whereas $R_{\mathcal{G}}$ and $C_{\mathcal{G}}$ display always positive values, the electrothermal capacitance $C_{\mathcal{M}}$ and resistance $R_{\mathcal{M}}$ can become positive or negative when E_F is tuned, see Appendix C for further details. This is shown in Fig. 4.6 b) and d). Indeed, $C_{\mathcal{M}}$ changes sign whenever the Fermi energy matches with any of the nanotube resonances. Heat current becomes delayed or elapsed with respect to the AC signal depending on the Fermi energy position. The electrothermal resistance $R_{\mathcal{M}}$ modifies its sign not only at the points when E_F coincides with the nanotube resonances [see Eq. (4.56)] but also when the electron-hole symmetry point occurs, just at the midpoint between two consecutive resonance points. The sign inversion in $R_{\mathcal{M}}$ happens when the derivative of the carbon nanotube quantum dot density of states vanishes[138]. Remarkably, both $C_{\mathcal{M}}$ and $R_{\mathcal{M}}$ diverge around the resonance points, behavior that is washed out by enhancing temperature. (Similar results were obtained for the weak interacting limit, when $E_C \ll \Gamma$ see Ref. [138] for details).

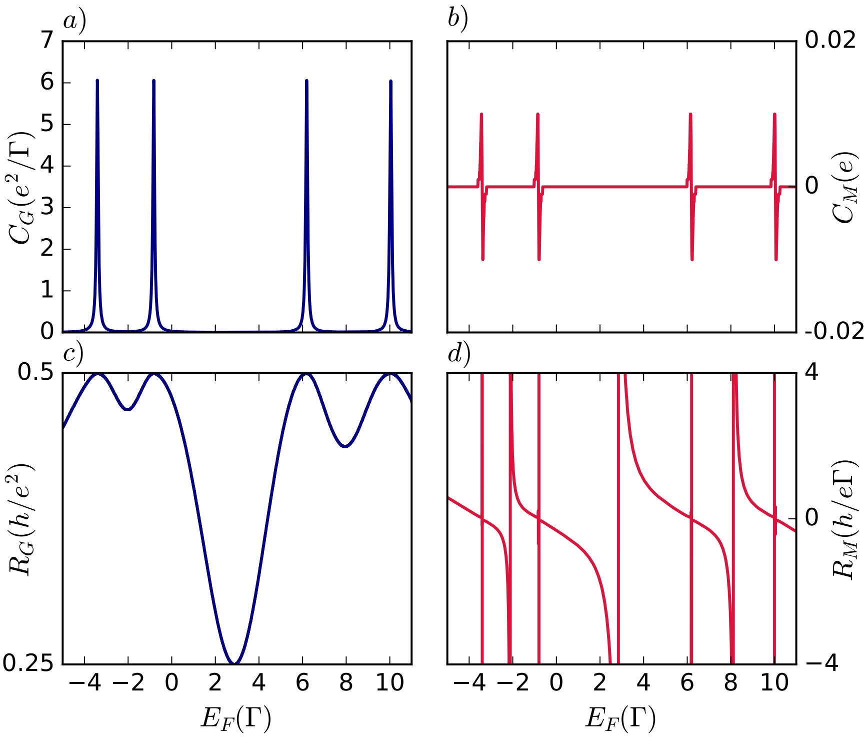

Figure 4.6: a) Electrical capacitance $C_{\mathcal{G}}$ and c) electrical relaxation resistance $R_{\mathcal{G}}$ versus the Fermi energy E_F. b) Electrothermal capacitance $C_{\mathcal{M}}$ and d) electrothermal relaxation resistance $R_{\mathcal{M}}$ versus the Fermi energy E_F. Nanotube parameters: $\epsilon_d = 0$, $\Delta_Z = 0.625\Gamma$, $\Delta_{orb} = 5\Delta_Z$, $\Delta_{so} = 0.5\Delta_Z$, $2E_C = 2\Gamma$, and $k_B T = 0.05\Gamma$.

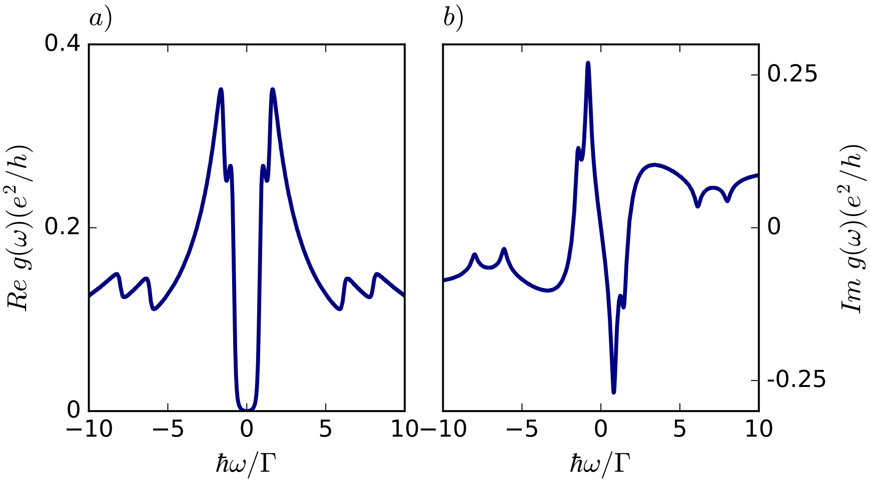

Figure 4.7: a) Real and b) imaginary parts of $g(\omega)$ versus the AC frequency ω. Parameters: $\epsilon_d = 0$, $\Delta_Z = 0.625\Gamma$, $\Delta_{orb} = 5\Delta_Z$, $\Delta_{so} = 0.5\Delta_Z$, $2E_C = 2\Gamma$, $E_F = 0$, and $k_B T = 0.05\Gamma$.

We now discuss the case of arbitrary AC frequencies and analyze the prefactor $g(\omega)$ of the electrical admittance in Fig. 4.7. The real and imaginary parts of $g(\omega)$ versus the AC frequency are depicted in Fig. 4.7 a) and b). As in the single orbital quantum capacitor, we observe that $\Im mg(\omega)$ has odd parity with respect to ω, while $\Re eg(\omega)$ is an even function of ω as a consequence of being response functions of a real perturbating force. $\Im mg(\omega)$ accounts for the dissipative part of the electrical conduction with resonances roughly located at $\pm\hbar\omega \approx |E_F - \widetilde{\epsilon}_{d\sigma\tau}|$. For the HF approximation, these resonances coincide with the dot level positions that are renormalized by interactions according to Eq. (4.10). These renormalized level positions (when $E_F = 0$) are at $\widetilde{\epsilon}_{d\sigma\tau} \approx -1.4\Gamma, -0.8\Gamma, 6.1\Gamma, 8.0\Gamma$ leading to the observed resonances in $g(\omega)$. The resonant behavior of $g(\omega)$ reflects the photon-assisted tunneling processes in which transport through the nanotube occurs by absorpting or emitting single photons. Furthermore, these resonances are broadened mainly by Γ at very low temperatures. The $\Re eg(\omega)$ corresponds to the reactive part of the electrical conduction and has also a similar resonant structure.

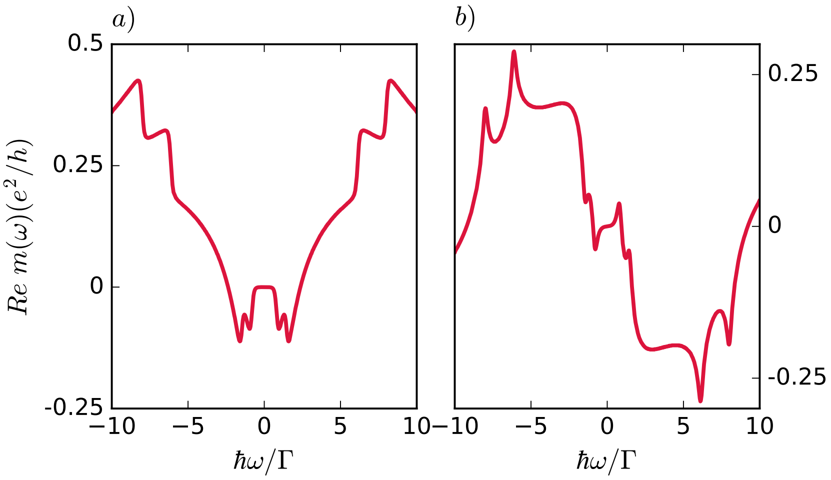

Figure 4.8: a) Real and b) imaginary parts of $m(\omega)$ versus the AC frequency ω. Parameters: $\epsilon_d = 0$, $\Delta_Z = 0.625\Gamma$, $\Delta_{orb} = 5\Delta_Z$, $\Delta_{so} = 0.5\Delta_Z$, $2E_C = 2\Gamma$, $E_F = 0$, and $k_BT = 0.05\Gamma$.

We turn to the analysis of the electrothermal admittance $\mathcal{M}(\omega)$ which is given in Eq. (4.43). As before, it is convenient to examine $m(\omega)$ defined in Eq. (4.44) and we thus plot it as a function of the AC frequency in Fig. 4.8. First, we observe $m(\omega)$ displays the same parity property as $g(\omega)$ which can be explained in the same way. Furthermore, the real and imaginary parts of $m(\omega)$ are also characterized by features located at $\pm\hbar\omega \approx |E_F - \widetilde{\epsilon}_{d\sigma\tau}|$. Remarkably, the observed peaks indicate single photon absorption and emission processes for the transport of heat. It is worthy to emphasize that our approach is able to capture such photon-assisted processes in contrast with other calculations restricted to AC frequencies smaller or similar to the tunnel coupling Γ: the other calculations assume the AC frequency is small such that only a second order expansion of $m(\omega)$ in powers of ω (characterized by the pairs $C_{\mathcal{M}}$, $R_{\mathcal{M}}$) can be justified. However, since we do not have such a restriction for the applied AC frequency, our results clearly exhibit photon-assisted processes for the heat transport.

Remarkably, $m(\omega)$ (either its real or imaginary part) takes positive or negative values depending on the AC frequency regime. We observe $\Re em(\omega) <$

0 for low and moderate ω, whereas for large AC frequencies its sign is reversed. We stress the importance of such result for the functionality of quantum circuits, in which one could manipulate the sign of the heat flow spectrum by properly tuning the AC frequency.

4.4 CONCLUSIONS

In closing, we have investigated the heat current spectrum in the linear response regime for an interacting conductor coupled to a single reservoir and modulated by an electrical AC signal. Our results, valid for arbitrary AC frequencies, show that the heat current expression for the reservoir needs to consider the heat stored or relaxed at the barrier. We illustrate our findings with two prototype of interacting conductors, namely, a single orbital quantum dot and a multi-orbital conductor, a carbon nanotube quantum dot coupled to a single reservoir. We deal with the strong interacting limit where Coulomb blockade phenomena applies. We highlight that *(i)* electrical and heat transport displays photon-assisted transport features, and *(ii)* the electrothermal admittance can be positive or negative and the sign can be chosen by adjusting properly the AC frequency. This is an important issue for engineering nanoelectronic circuits with optimal heat dissipation performances.

We have thus seen that photon-assisted events caused by an AC-driving have an impact both on the charge and on the heat currents in an interacting conductor. In the next chapter we study the effect of photon absorption and emission on transport through an interacting quantum conductor attached to two reservoirs. We do so by taking into account the circuit in which the conductor is embedded. The circuit acts as an electromagnetic environment emitting and absorbing photons. Oppositely to what we studied here, the environment in the next chapter is only of low frequency whereas here we studied all possible frequencies.

5

DYNAMICAL COULOMB BLOCKADE OF THERMAL TRANSPORT

5.1 INTRODUCTION

An external time-dependent driving can cause the emission (or absorption) of photons (in the form of energy quanta) into the system, as we have seen in the previous Chapter 4. There we have also seen that the presence of photons affects transport through photo-assisted events. In this chapter we present a different approach were an electromagnetic environment exchanges photons with the system and we study how these photons (rather than those emitted by a time-dependent source) affect the transport properties of the system.

As mentioned before, the properties of electronic and heat transport in nanostructures have recently attracted the attention of the scientific community for different reasons [112, 146, 147]. On one hand, the onset of quantum effects in the mesoscopic regime opens the way to the investigation of the impact of quantum mechanics on thermodynamics [148]. In particular, heat engines based on purely quantum mechanical effects have been recently proposed [149–154]. Complementary to this, there has been a spectacular progress in the field of quantum thermoelectrics, both from the theoretical and experimental sides. Exciting proposals like nanoprobe thermometers [146, 155], energy harvesting devices [36, 156–159], refrigerators [160–164], heat diodes [165], rectifiers [166–169], transistors [170, 171], multi-terminal heat engines [34, 172–174] among others have come up in the last years.

In this respect, quantum dots [30, 175–184] have a prominent role for being good energy filters that improve the thermoelectric efficiency [185, 186] due to the sharpness of their energy levels. The presence of strong interactions introduces the Coulomb blockade regime where transport can be controlled at the level of single-electron tunneling events [187, 188]. Different functionalities such as heat engines [36], pumps [189–191] and diodes [165] can be defined that use these properties.

Currents are small in nanostructures, and are hence sensible to external fluctuations. The question arises of how the system behavior is influenced by a noisy environment. On one hand, it leads to dephasing and decoherence which are detrimental to quantum coherent processes. This is however not necessarily a drawback [192, 193]. On the other hand, they may lead to inelastic transitions which can contribute to the engine performance by injecting or releasing energy in the conductor [194–196]. Indeed, non-local thermoelectric engines exist that use an environment as a heat source in an otherwise equilibrated conductor. The nature of the environment can either be fermionic [34, 197] or bosonic [172, 198]. It can also consist of transport induced fluctuations in a Coulomb coupled conductor [199–204] or be due to quantum fluctuations in an electromagnetic environment [31, 205]. This last effect has been observed in the form of the dynamical Coulomb blockade of charge currents [50, 206–209].

The linear response of a two terminal nanodevice is defined on the grounds of the Onsager-Casimir relations [39, 210, 211], as seen in the introduction, Section 2.1.3.1. The Onsager coefficients $\mathcal{O}_{ij} = \partial\mathcal{I}_i/\partial\mathcal{A}_j$ relate the charge and heat fluxes $\mathcal{I}_i \equiv \{I_i^e, I_i^h\}$ in terminal i to the applied voltages and temperatures $\mathcal{A}_j \equiv \{V_j, \Delta T_j\}$ in terminal j. Shortly, the coefficients $\mathcal{O}_{ij}$ can be collected into the so-called Onsager conductance matrix which is a symmetric and positively semi-defined matrix. [38, 145] Derived from the principle of microreversibility, Onsager reciprocity relations relate non diagonal coefficients, e.g. Seebeck and Peltier responses. Notoriously, such relations are also satisfied for quantum systems independently of the presence of interactions. For quantum systems in which phase coherence is preserved, additional relations for the Onsager coefficients are obtained from the unitarity of the electron dynamics [85, 97] giving rise to highly symmetric Onsager matrices. However, the interaction with an environment introduces energy dissipation which prevents the dynamics from being unitary. In particular some relations among the thermoelectric coefficients are no longer satisfied [32, 33]. The microscopic origin of such asymmetries has so far not been discussed. Although a phenomenological approach based on voltage probes has already been studied. Even so, studies based on voltage probes are limited since they lack an structure, which the environment does have [212].

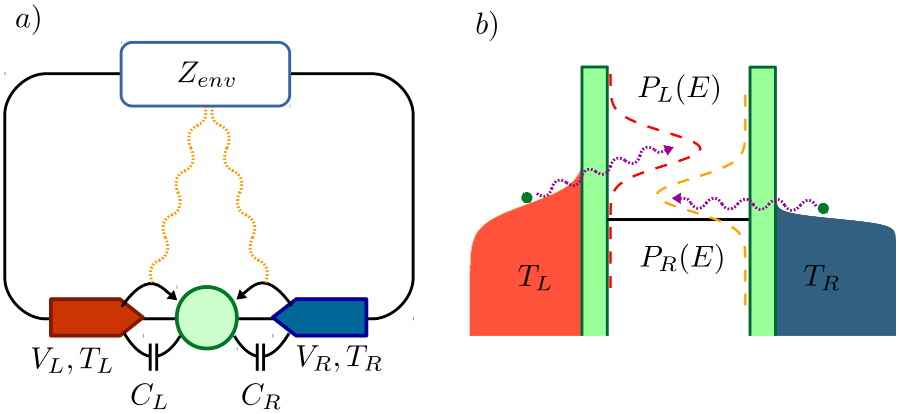

Figure 5.1: a) Schematic of a two terminal single-level quantum dot device in the presence of an electromagnetic environment described by an external impedance $Z_{env}(\omega)$. Each terminal is electrically and thermally biased with V_L, $T_L = T_0 + \Delta T_L$ (left contact) and V_R, $T_R = T_0 + \Delta T_R$ (right contact). The capacitance of each junction, C_i with $i = L, R$, determines the dynamical coupling to the environment. b) Inelastic tunneling into the quantum dot is then described by a distribution $P_i(E)$ which is different for each barrier.

In this work we explore this issue by using a microscopic model for the coupling of a mesoscopic system to a dynamical environment introduced as a circuit impedance [51]. We consider the simplest situation of a single-level quantum dot tunnel-coupled to two terminals, L and R, via tunneling barriers, cf. Fig. 5.1. Electrons tunneling through each of the barriers perceive a different environment. This results in photon-assisted tunneling events which on top of becoming inelastic, introduce left-right asymmetric rates. As we show below, the occurrence of Onsager matrix asymmetries is due to combination of these two effects. It leads to responses that do not only depend on the global temperature gradient $\Delta T = T_L - T_R$ but rather on how it is distributed with respect to some reference temperature T_0 in the two leads, $\Delta T_l = T_l - T_0$. It affects the thermoelectric response and most particularly, it introduces an apparent thermal rectification in the linear regime.

The remaining of this chapter is organized as follows: in Sec. 5.2 our model is described. Results for the single and double occupation regimes are presented in Secs. 5.3 and 5.4, respectively, with conclusions discussed in Sec. 5.5.

5.2 THEORETICAL MODEL

We consider a two terminal interacting conductor as illustrated in Fig. 5.1. We use a spinful single level quantum dot described by four states $|0\rangle$, $|u\rangle$, $|d\rangle$ and $|2\rangle$. They correspond to an empty dot ($|0\rangle$), a singly occupied dot with either spin up ($|u\rangle$) or down ($|d\rangle$) polarization, and the doubly occupied dot state ($|2\rangle$). Our transport description is restricted to the sequential tunneling regime for which $h\Gamma \ll k_B T_0$ (T_0 is the temperature). In this regime, transport events are predominantly of the first order in the tunneling coupling Γ. To properly account for Coulomb interactions we employ the electrostatic model schematically illustrated in Fig. 5.1. In such model, the electrostatic charging energy is described with two capacitances C_L and C_R. The dynamics of the system is modeled by the time evolution of the occupation probabilities $p \equiv \{p_0, p_u, p_d, p_2\}$ described by the following master equation

$$\begin{aligned}
\frac{dp_0}{dt} &= \sum_j \left[-2\Gamma_{j,0}^{+} p_0 + \Gamma_{j,0}^{-}(p_u + p_d)\right] \\
\frac{dp_\sigma}{dt} &= \sum_j \left[-\left(\Gamma_{j,0}^{-} + \Gamma_{j,1}^{+}\right) p_\sigma + \Gamma_{j,0}^{+} p_0 + \Gamma_{j,1}^{-} p_2\right] \\
\frac{dp_2}{dt} &= \sum_j \left[-2\Gamma_{j,1}^{-} p_2 + \Gamma_{j,1}^{+}(p_u + p_d)\right].
\end{aligned} \tag{5.1}$$

To which we have to add the normalization condition $p_0 + p_u + p_d + p_2 = 1$. The transition rates $\Gamma_{j,s}^{\pm}$ for electrons tunneling *in* (+) or *out* (-) of the dot through contact j=L,R are given below. We do not consider a magnetic field, so they do not depend on spin. They depend on the electrochemical potential μ_s when the dot is empty $s = 0$ or singly occupied $s = 1$. A simple electrostatic electrostatic model [12] yields

$$\mu_s = \epsilon_d + \frac{e^2(1+2s)}{2C} + e(\kappa_L V_L + \kappa_R V_R), \tag{5.2}$$

where e is the electron charge, ϵ_d is the bare energy level of the quantum dot, $C = C_L + C_R$ is its total capacitance, and $\kappa_j = 1 - C_j/C$, with $j = L, R$, see Fig. 5.1.

5.2.1 *Tunneling rates*

Tunneling events are frequently affected by fluctuations of the electromagnetic environment [50]. To fully account for such quantum fluctuations we adopt the $P(E)$ theory [50, 51] of dynamical Coulomb blockade, recently revisited to consider heat fluxes [31, 52]. The spirit of the $P(E)$ theory relies on the fact that individual tunneling events involve energy exchange processes. The Dirac-delta accounting for energy conservation in the (Fermi golden rule) tunneling rates is relaxed into a broadened distribution $P(E)$. More specifically for each junction j in a double junction it reads

$$P_j(E) = \frac{1}{2\pi\hbar}\int dt \exp\left(\kappa_j^2 J(t) + \frac{i}{\hbar}Et\right). \tag{5.3}$$

where the function

$$J(t) = \frac{2h}{e^2}\int_0^\infty \frac{d\omega}{\omega}\mathrm{Re}[\tilde{Z}(\omega)]c(\omega, T_0), \tag{5.4}$$

contains all the information of the environment fluctuations, with[51]:

$$c(\omega, T_0) = \coth\left(\frac{\hbar\omega}{2k_B T_0}\right)[\cos(\omega t - 1) - i\sin\omega t]. \tag{5.5}$$

If we consider a pure resistive or ohmic environment, i.e. we have

$$Z_{env}(\omega) = R \gg R_q = h/2e^2. \tag{5.6}$$

This situation corresponds to the case where the tunneling electron may easily excite many electromagnetic modes. Thus, the total impedance seen by the external circuit is

$$\tilde{Z}(\omega) = [i\omega C_{eff} + Z_{env}(\omega)]^{-1}, \tag{5.7}$$

with the effective capacitance of the quantum dot $C_{eff}^{-1} = C_L^{-1} + C_R^{-1}$. Semiconductor quantum dots in the sequential tunneling regime are typically affected by a high impedance environment [213, 214]. Under these considerations one obtains a Gaussian distribution:

$$P_j(E) = \frac{1}{\left(4\pi\kappa_j^2 E_C k_B T_0\right)^{1/2}} e^{-\frac{\left(E-\kappa_j^2 E_C\right)^2}{4\kappa_j^2 E_C k_B T_0}}, \tag{5.8}$$

where $E_C = e^2\kappa_L\kappa_R/2C$. Remarkably, asymmetries in the system capacitances translate in the $P_j(E)$ functions having different mean, $\kappa_j^2 E_C$, and variance, $2\kappa_j^2 E_C k_B T_0$. They modify the transition rates expressions according to

$$\Gamma_{j,s}^{\pm} = \Gamma_j \int dE f^{\pm}(E - eV_j, T_j)P_j(\pm(E - \mu_s)). \tag{5.9}$$

where $f^+(E, T) = 1/[1 + e^{E/(k_B T)}]$ is the Fermi function, and $f^- = 1 - f^+$. The tunneling rates can be left-right asymmetric either for having barriers with different transparencies, $\Gamma_L \neq \Gamma_R$, or for $P_L(E) \neq P_R(E)$, stemming from different capacitances $C_L \neq C_R$. We emphasize that having different $P_j(E)$ introduces an implicit asymmetry in the energy exchanged by the electrons with the environment in the tunneling processes. As we discuss below, the impact in the system response shows up in the thermal transport coefficients.

Finally, the charge and heat currents through contact j are calculated through

$$I_j^e = e\left[\sum_{\sigma=u,d}\left(\Gamma_{j,0}^{-} - \Gamma_{j,1}^{+}\right)p_\sigma - 2\Gamma_{j,0}^{+}p_0 + 2\Gamma_{j,1}^{-}p_2\right], \tag{5.10}$$

$$I_j^h = \sum_{\sigma=u,d}\left(\gamma_{j,0}^{-} - \gamma_{j,1}^{+}\right)p_\sigma - 2\gamma_{j,0}^{+}p_0 + 2\gamma_{j,1}^{-}p_2, \tag{5.11}$$

where the transition rates for the heat current in Eq. (5.11) are given by:

$$\gamma^{\pm}_{j,s} = \Gamma_j \int dE(E - eV_j) f^{\pm}(E - eV_j, T_j) P_j(\pm(E - \mu_s)). \tag{5.12}$$

These rates take into account the heat transported in each particle transition. In our setup, the tunneling rates in Eqs. (5.9) and (5.12) describe inelastic processes. Hence, they introduce energy exchange with the environment. The energy of the two terminal system is hence not conserved, $I^h_L + I^h_R \neq I_L(V_L - V_R)$. To obtain the energy conservation relation one needs to take into account the energy exchanged with the environment: $I^h_L + I^h_R + I^h_E = I_L(V_L - V_R)$, with the energy current to the environment I^h_E given by an expression like in Eq. (5.11) with $\gamma^{\pm}_{j,s}$ substituted by

$$\gamma^{E,\pm}_{j,s} = \Gamma_j \int dE(\pm(E - \mu_s)) f^{\pm}(E - eV_j, T_j) P_j(\pm(E - \mu_s)). \tag{5.13}$$

On top of that, charge conservation ensures $I^e_R = -I^e_L$.

5.2.2 *Linear regime*

By linearizing the electrical I^e_i and heat I^h_i currents at the i-th reservoir in response to the applied thermodynamical forces $\{V_j, \Delta T_j\}$

$$I^e_i = \sum_j (G_{ij} V_j + L_{ij} \Delta T_j), \tag{5.14}$$

$$I^h_i = \sum_j (M_{ij} V_j + K_{ij} \Delta T_j), \tag{5.15}$$

we obtain the four conductance matrices for each reservoir i that compose the Onsager matrix. Onsager-Casimir reciprocity relations dictate $G_{ij} = G_{ji}$, $K_{ij} = K_{ji}$, and $L_{ij} = eM_{ji}/T_0$. Additional relations imposed to the cross-conductances ($L_{ij} = L_{ji}$) arise in the case where transport occurs elastically [85, 97].

In the following we analyze the effect of inelasticity on the thermal coefficients, namely L_{ij} (or M_{ji}) and K_{ij}.

5.2.3 *Thermal coefficients*

Thermal rectification in an isoelectric ($V = V_R - V_L = 0$) two terminal conductor occurs when the heat current becomes asymmetric on the reversal of the temperature gradient. It has been discussed that this is not possible in the linear regime for the heat current across the system, even in the presence of an environment or a thermal bath [195]. One has to take into account that energy is dissipated into the environment at the nanostructure. However in an experiment this quantity is not easy to detect. One would rather measure the heat current at each terminal.

In this case, the measured heat current might be L-R asymmetric with the reversal of ΔT, i.e.

$$\delta I^h_{LR} = I^h_L(V{=}0, \Delta T) - I^h_R(V{=}0, -\Delta T) \neq 0. \tag{5.16}$$

It hence might lead to an apparent rectification of the measured heat currents. If we assume that the gradient is distributed between the two terminals, i.e. $\Delta T = \Delta T_R - \Delta T_L$, we get after linearizing the currents:

$$\delta I^h_{LR} = (K_{LL} - K_{RR}) \Delta T_L + (K_{LR} - K_{RL}) \Delta T_R. \tag{5.17}$$

The second term of the right-hand side of Eq. (5.17) vanishes due to the fulfillment of the Onsager relations. This however does not apply to the diagonal coefficients, K_{LL} and K_{RR} in the first term. We will discuss below in which conditions these two coefficients become unequal in the presence of an environment, thus leading to asymmetric heat conduction.

In that case, we can define a rectification coefficient

$$R = \left| \frac{I^h_L(\Delta T) - I^h_R(-\Delta T)}{I^h_L(\Delta T) + I^h_R(-\Delta T)} \right| = \left| \frac{(K_{LL} - K_{RR})\,\Delta T_L}{(K_{LL} + K_{RR})\,\Delta T_L + 2K_{LR}\Delta T_R} \right| \tag{5.18}$$

which reflects a thermal diode behavior for $R \approx 1$. In the particular case $\Delta T_R = 0$, it becomes:

$$R_L = \left| \frac{K_{LL} - K_{RR}}{K_{LL} + K_{RR}} \right|, \tag{5.19}$$

independently of the thermal gradient.

5.2.4 *Thermoelectric coefficients*

Our system can act as an engine by using a thermal gradient opposed to a voltage bias, in this case, our system acts as an engine which generates a finite power when the thermally activated current flows against a voltage gradient.

It has been discussed that asymmetries of the L_{ij} coefficients might improve the thermoelectric efficiency [215]. This is the case for instance for broken time reversal symmetry in the presence of a magnetic field. Then, the efficiency at maximum power depends on the ratio $L_{ij}b)/L_{ji}(-B)$. In our device L becomes asymmetric under "contact" inversion even in the absence of magnetic field.

Important coefficients of performance are the maximum generated power and the efficiency at maximum power. Let us specify, without loss of generality, a configuration where $T_L > T_R$. The extracted power

$$P = -I^e_L(V)V \tag{5.20}$$

is maximized for some drop voltage $V = V_m$, giving:

$$V_m = -(L_{LR}\Delta T_R + L_{LL}\Delta T_L)/(2G_{LR}), \tag{5.21}$$

which results in a maximum power:

$$P_{max} = \frac{(L_{LR}\Delta T_R + L_{LL}\Delta T_L)^2}{4G_{LR}}. \tag{5.22}$$

Finally the efficiency at maximum power η_{max} is easily computable from

$$\eta_{max} = \frac{P_{max}}{I^h_R(V_m) + P_{max}}, \tag{5.23}$$

where one has to take into account that heat is injected from the left reservoir, I^h_L, and from the environment, I^h_E. The total injected heat is hence $-[I^h_L(V_m) + I^h_E(V_m)] = I^h_R(V_m) + P_{max}$.

In order to carry a more meaningful study of the setup efficiency, we also study the Carnot efficiency for this setup. In our case we need to take into account that heat is being injected by the environment and thus the Carnot efficiency is not simply $\eta_C = 1 - T_R/T_L$. We define the Carnot efficiency at the reversible point where $\frac{I_L^h}{T_L} + \frac{I_R^h}{T_R} + \frac{I_E^h}{T_0} = 0$ (zero entropy production), which results in:

$$\eta_C = 1 + \left(\frac{I_L^h}{I_R^h} \frac{1 - T_0}{T_R} - \frac{T_0}{T_L} \right)^{-1} . \tag{5.24}$$

This efficiency is a benchmark for the performance of our setup.

5.3 SINGLE OCCUPANCY

We can make some analytical progress by considering a simplified situation. Let us assume the limit $E_C \gg k_B T_0$, such that the quantum dot can be occupied by a single electron at a time. It will later help to understand the numerical results for the general configuration presented in Sec. 5.4. In this case we only have two possible states for the quantum dot: empty $|0\rangle$ or occupied $|1\rangle$. This simplifies greatly the master equation which in the steady state read:

$$p_1(\Gamma_{L,0}^- + \Gamma_{R,0}^-) - p_0(\Gamma_{L,0}^+ + \Gamma_{R,0}^+) = 0 \tag{5.25}$$

$$p_0 + p_1 = 1 \tag{5.26}$$

These can be easily solved and one obtains:

$$p_0 = \frac{\Gamma_{L,0}^- + \Gamma_{R,0}^-}{\Gamma_{L,0}^+ + \Gamma_{R,0}^- + \Gamma_{L,0}^- + \Gamma_{R,0}^+}, \tag{5.27}$$

$$p_1 = \frac{\Gamma_{L,0}^+ + \Gamma_{R,0}^+}{\Gamma_{L,0}^+ + \Gamma_{R,0}^- + \Gamma_{L,0}^- + \Gamma_{R,0}^+}. \tag{5.28}$$

In this case, the charge current simply reads:

$$I_L^e = e\frac{\Gamma_{L,0}^-\Gamma_{R,0}^+ - \Gamma_{L,0}^+\Gamma_{R,0}^-}{\Gamma_{L,0}^+ + \Gamma_{R,0}^- + \Gamma_{L,0}^- + \Gamma_{R,0}^+}. \tag{5.29}$$

We consider the isoelectric case (with $V_L = V_R = 0$ and $\mu_0 = \epsilon_d + e^2/2C$) and compute the linearized charge current in contact l by linearizing the tunneling rates as follows

$$\Gamma_{l,0}^+ = \Gamma_l \left(g_l^{(0)} + \frac{\Delta T_l}{T_0} g_l' \right) \tag{5.30}$$

$$\Gamma_{l,0}^- = e^{\mu_0/k_B T_0} \left(\Gamma_l^+ - \frac{\Delta T_l}{T_0} \Gamma_l g_l^{(1)} \right), \tag{5.31}$$

where we have introduced the following integrals:

$$g_l^{(n)} = \int dE \left(\frac{E+\mu_0}{k_B T_0} \right)^n f^+(E + \mu_0) P_l(E), \tag{5.32}$$

$$g_l'^{n} = \int dE \left(\frac{E+\mu_0}{k_B T_0} \right)^n f^+(E+\mu_0) f^-(E+\mu_0) P_l(E). \tag{5.33}$$

Note that they only depend on the corresponding terminal through the $P_l(E)$ function, $l = L, R$. In the following, we write $f^\pm(E)$ for $f^\pm(E, T)$.

5.3.1 *Seebeck asymmetry*

Replacing them into Eq. (5.29) we obtain the Seebeck coefficients:

$$L_{ij} = \frac{e\Gamma_L\Gamma_R}{T_0\sum_l \Gamma_l g_l^{(0)}} f^-(\mu_0) g_i^{(0)} g_j^{(1)}. \tag{5.34}$$

The asymmetry in the thermoelectric coefficients, $\delta L = L_{LR} - L_{RL}$, is hence:

$$\delta L \propto g_L^{(0)} g_R^{(1)} - g_R^{(0)} g_L^{(1)} = X_{RL}^{(1)}, \tag{5.35}$$

with

$$X_{ll'}^{(n)} = \int dE dE' \left(\frac{E+\mu_0}{k_B T_0}\right)^n f^+(E+\mu_0) f^+(E'+\mu_0)[P_l(E)P_{l'}(E') - P_l(E')P_{l'}(E)]. \tag{5.36}$$

We can then explicitly relate the asymmetry of the Seebeck coefficients Eq. (5.35) to the inhomogeneous influence of the environment on the tunneling processes through each barrier, $P_l(E)$. This occurs when $C_L \neq C_R$: both the mean and variance of the distributions become different, cf. Eq. (5.8). Hereafter, we parametrize the asymmetry of the tunnel barrier capacitances with

$$\kappa = \frac{C_L - C_R}{C}. \tag{5.37}$$

Then, for a finite κ it follows that $P_L(E) \neq P_R(E)$. Note that $X_{ll'}^{(n)}$ is independent of the tunneling rates Γ_L, Γ_R.

The functions $X_{ll'}^{(n)}$ (and therefore the asymmetry) depend on the overlapping of the Gaussian distributions $P_L(E)$ and $P_R(E)$, whose mean and width are in principle different and depend on C_j and C. For very small capacitances, $C \to 0$, the two distributions are narrow and they do not overlap. In the opposite limit, they are so wide that their difference is tiny. Optimal values of C for which the effect of the environment is maximal are found int the intermediate regime.

These observations are reflected in Fig. 5.2. There we have represented δL for two different values of the total capacitance $C = C_0$ [Fig. 5.2a)] and $2C_0$ [Fig. 5.2b)], with $C_0 = e^2/10h\Gamma$, as a function of the energy level of the dot ϵ_d and κ. We vary the symmetry of the capacitances described by κ but not the total capacitance C which is kept constant. As seen in Fig. 5.2 δL is zero for $\kappa = 0$. This means that an environment coupled symmetrically to both barriers is not able to break this symmetry and therefore, inelastic scattering is not a sufficient condition for breaking this symmetry in the Onsager matrix. However, we observe that L_{LR} and L_{RL} differ for finite κ, see Fig. 5.2c) and d). Both have the expected saw-tooth lineshape [188]. Remarkably, δL changes sign when the asymmetry is inverted (i.e. when κ changes sign) and at the particle-hole symmetry point $\epsilon_d + E_C = 0$, where also $L_{ij} = 0$, see Fig. 5.2.

The maximal value of δL (at a finite value of κ) depends strongly on the total capacitance C. A plausible argument for such behavior is obtained by looking at the integrand of Eq. (5.36) that depends on the overlap of the two Gaussian functions $P_L(E)$ and $P_R(E)$, each one centered at energy positions that depend on $\kappa_L^2 E_C$ and $\kappa_R^2 E_C$. As discussed above, $X_{RL}^{(1)}$ decreases for small enough C, and so does δL.

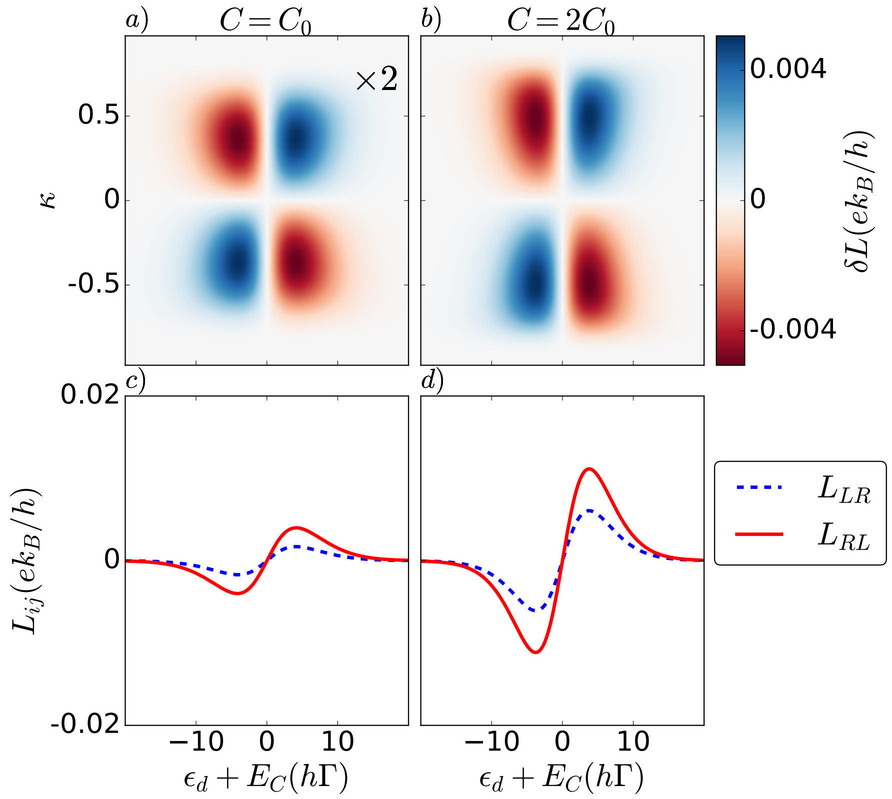

Figure 5.2: Electrothermal asymmetry δL versus dot energy level position $\epsilon_d + E_C$ and capacitance asymmetry κ for different values of the total capacitance a) $C = C_0$, and b) $C = 2C_0$. c) and d) show cuts of L_{LR}, and L_{RL} when $\kappa = 0.5$, for the values of C considered above. We have taken $k_B T_0 = 2h\Gamma$ and $\Gamma_L = \Gamma_R = \Gamma/2$. We take $h\Gamma = 1$ as the energy reference unit. Finite asymmetries $\kappa \neq 0$ give $\delta L \neq 0$.

5.3.2 *Thermal asymmetry*

A similar analysis is performed for the thermal coefficients. We start from the expression for the heat current in the single occupancy case:

$$I_L^h = \frac{\gamma_{L,0}^-(\Gamma_{L,0}^+ + \Gamma_{R,0}^+) - \gamma_{L,0}^+(\Gamma_{L,0}^- + \Gamma_{R,0}^-)}{\Gamma_{L,0}^+ + \Gamma_{R,0}^- + \Gamma_{L,0}^- + \Gamma_{R,0}^+} \tag{5.38}$$

Expanding the heat rates we obtain:

$$\gamma_l^+ = \Gamma_l \left(k_B T g_l^{(1)} + g_l'' k_B \Delta T_l\right) \tag{5.39}$$

$$\gamma_l^- = e^{\mu_0/k_B T} \left(\gamma_l^+ - \Gamma_l g_l^{(2)} k_B \Delta T_l\right). \tag{5.40}$$

With these relations, together with Eq. (5.30), we get the expression for the (diagonal) linear thermal asymmetry, $\delta K = K_{LL} - K_{RR}$. It can be separated in two contributions, $\delta K = \delta K_\Gamma + \delta K_\kappa$, with:

$$\delta K_\Gamma = \frac{k_B f^-(\mu_0)}{\sum_l \Gamma_l g_l^{(0)}} \left(\Gamma_L^2 \Theta_L - \Gamma_R^2 \Theta_R\right) \tag{5.41}$$

$$\delta K_\kappa = \frac{k_B f^-(\mu_0)}{\sum_l \Gamma_l g_l^{(0)}} \Gamma_L \Gamma_R X_{RL}^{(2)}. \tag{5.42}$$

Here we have defined:

$$\begin{aligned}\Theta_l &= \left(g_l^{(1)}\right)^2 - g_l^{(2)} g_l^{(0)} \\ &= \int dE dE'(E-E')(E+\Delta\mu^0)f^+(E+\mu_0)f^+(E'+\Delta\mu^0)P_l(E)P_l(E'),\end{aligned} \tag{5.43}$$

which depends on the tunneling events through a single barrier. This factor is related to the thermal conductance for the energy exchange between a single terminal l and the environment. Note that δK_Γ can be finite in the case where one of the barriers is closed $\Gamma_j = 0$, i.e. when neither charge or energy flows through the quantum dot. This term therefore describes asymmetric energy exchange with the environment. On the other hand, δK_κ depends on tunneling through both barriers.

We can hence distinguish two sources of rectification: δK_Γ becomes non zero when asymmetric tunneling barriers are considered, i.e. $\Gamma_L \neq \Gamma_R$ or when $\kappa \neq 0$. It relates to the different time scales that an electron stays in contact with the environment when tunneling from the left or from the right reservoir, as we discuss below. However, δK_κ is is intrinsically dependent on the dynamic coupling to the environment: it is only non zero when the capacitances for each tunneling barrier are different.

The role of a capacitance asymmetry on the heat rectification δK is plotted in Fig. 5.3. There, we show $\delta K = K_{LL} - K_{RR}$ versus the dot gate potential $\varepsilon_d + E_C$ when the asymmetry in the capacitances κ is tuned. We observe that heat rectification reverses its sign at $\kappa = 0$, as expected since $\kappa \neq 0$ means that more heat is being injected in one of the contacts. Importantly, we find different behaviors depending on the total capacitance C. For large enough C, δK changes sign with the position of the level, cf. Fig. 5.3b). This is due to a change in the relative contribution of the two terms, δK_Γ and δK_κ, as shown in the lower panels in Fig. 5.3. This effect introduces an additional way of controlling the heat flows through the device, depending on the position of the different mean values of the $P_j(E)$ distributions with respect to the Fermi energy.

To assess how much the heat flows can be controlled, we study the relative rectification R_L, see Figs. 5.3(c,d). We observe that it reaches values around $80 - 90\%$ at configurations where δK is maximal (lobes in Fig. 5.3a)). The system then behaves as a thermal diode. Even larger rectifications close to a 100% are reached for extreme values of the asymmetry κ. However, heat currents are almost vanishing there.

For small values of C, the asymmetry of the two $P(E)$ functions is large and therefore we find that δK_Γ is enhanced (and negative for $\kappa > 0$), see Fig. 5.3e). Therefore for $C = C_0$, it dominates over δK_κ, which depends on the overlap $\chi_{LR}^{(2)}$. Instead, for high values of C we showed that $X_{LR}^{(n)}$ increases, and on top of that the contribution of δK_Γ becomes smaller, see Fig. 5.3f). Therefore, the competition between the two terms and its dependence with κ gives a nontrivial dependence of the heat rectification with C.

Asymmetric tunneling amplitudes also lead to a finite rectification. In this case, it only depends on δK_Γ. This is shown in Fig. 5.4 which plots δK for symmetric capacitive couplings ($\kappa = 0$) versus the dot gate potential $\varepsilon_d + E_C$ when the asymmetry in the tunneling rate, parametrized as

$$\lambda = \frac{\Gamma_L - \Gamma_R}{\Gamma_L + \Gamma_R} \tag{5.44}$$

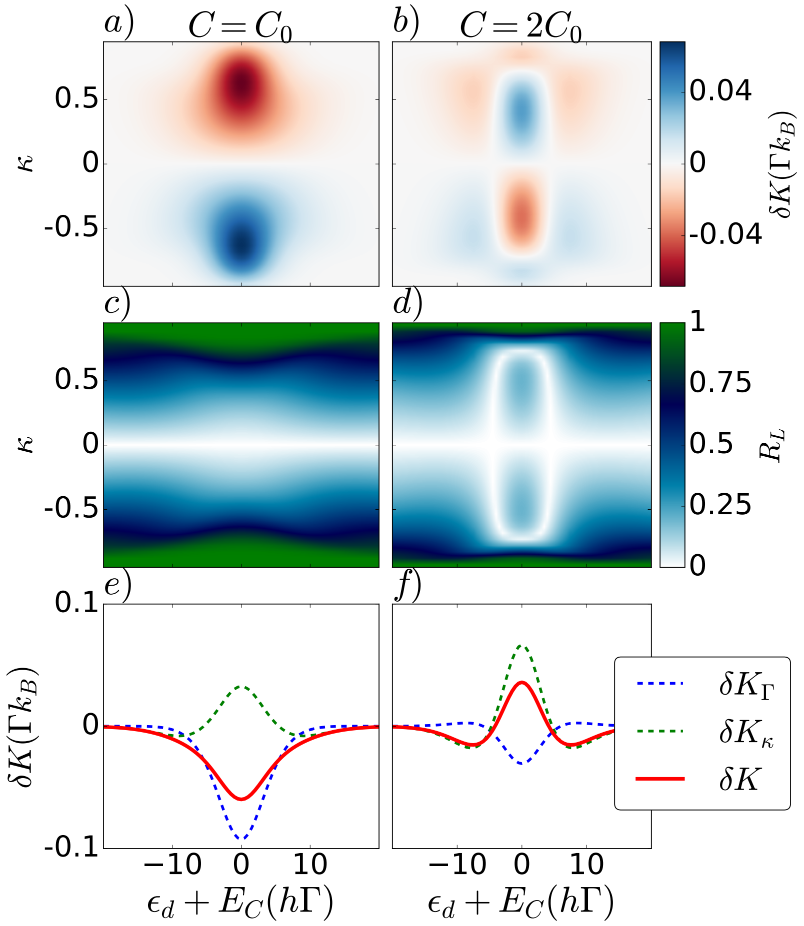

Figure 5.3: a), b) Thermal asymmetry δK versus dot energy level position ϵ_d and capacitance asymmetry κ for different values of the total capacitance $C = C_0, 2C_0$. Thermal rectification occurs for $\kappa \neq 0$, i.e. ($C_L \neq C_R$). c), d) Relative thermal asymmetry R_L for the corresponding configurations a) and b). e), f) Total δK (red line), tunnel δK_Γ (dashed blue line) and capacitance δK_κ (dashed green line) thermal asymmetries evaluated at $\kappa = 0.5$ for two different capacitances $C = C_0 = 2C_0$. The change of sign of δK_Γ which implies the change of sign of the total δK is clearly observed. Same parameters as in Fig. 5.2.

is tuned. Heat rectification stems purely from different kinetic couplings. By allowing, e.g., $\Gamma_L > \Gamma_R$ electrons traversing the left barrier spend shorter times in contact with the environment (and therefore the time where energy-exchange processes are possible is shorter) than electrons at the other barrier. Therefore environmental assisted tunneling transitions are effectively different for both junctions even though they are performed with the same environment, with $P_L(E) = P_R(E)$. Results for δK at $C_L = C_R = C/2$, i.e. $\kappa = 0$, for different values of the barrier asymmetry λ are shown in Fig. 5.4. In this figure we observe that indeed for $\lambda \neq 0$ there is an asymmetry of the thermal coefficients which changes sign with λ. It is also observed that the shape of the asymmetry does not depend strongly on the total capacitance C, as expected, since the source for such heat rectification depends essentially on λ and it does not have an electrostatic origin. Even so, the total value of the rectification decreases with the capacitance.

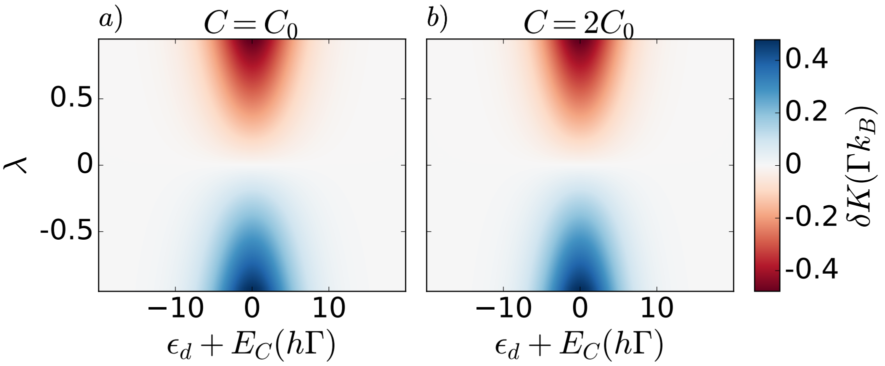

Figure 5.4: Thermal asymmetry δK versus dot energy level position ϵ_d and the barrier asymmetry λ for different values of the total capacitance $C = C_0, 2C_0$. Heat rectification $\delta K \neq 0$ for $\lambda \neq 0$, i.e. ($\Gamma_L \neq \Gamma_R$). Parameters are the same as in Fig. 5.2.

5.3.3 *Thermoelectric performance*

Finally, we focus on how the thermoelectric performance of the device is affected by the environment. Discrete levels in quantum dot systems are known to give a high performance for being ideal energy filters. In terms of efficiency at maximum power, they reach the Curzon-Ahlborn efficiency [186] which in the linear regime is $\eta_{CA} = \eta_C/2$ [216]. As discussed above, energy filtering is harmed by the occurrence of inelastic scattering. Hence, the efficiency is expected to be smaller [217].

This is indeed what we observe in most of the range in Fig. 5.5, which shows the efficiency at maximum power η_{max} [Eq. (5.23)] and the maximum power P_{max} [Eq. (5.22)] as functions of the dot gate position ϵ_d and the asymmetry parameter κ. Even so, we find there that the system reaches efficiencies close to the η_{CA} bound, or even larger, cf. Fig. 5.5f). This happens for large values of the dot level position and at $\kappa > 0$. The efficiency is increased whenever $C_L > C_R$ since this coupling favors the injection of heat from the environment to the right lead effectively helping electrons overcome the bias potential, therefore less heat is needed from the left reservoir to extract the same power. Unfortunately, at these configurations the output power is strongly suppressed, as displayed in Fig. 5.5. Nevertheless, the highest P_{max} can be extracted at reasonably high efficiencies $\eta_{max} \sim \eta_C/3$, see Fig. 5.5f). Therefore, we observed environmental enhanced efficiencies (as compared with a perfect energy filter [186], which are bounded by the Curzon-Ahlborn limit).

We also note that the efficiency is strongly dependent on the details of the coupling to the environment, evidenced by the comparison of Figs. 5.5e) and f). Larger C not only gives larger power, it also generates it at much larger efficiencies, as compared with lower C. Hence, we expect that the engineering of the environmental fluctuations (by considering e.g. non-ohmic impedances) could result in devices with enhanced thermoelectric performances.

5.4 DOUBLE OCCUPANCY

In the light of the results presented in the previous section for the reduced state space with up to one electron, we come back to the general case al-

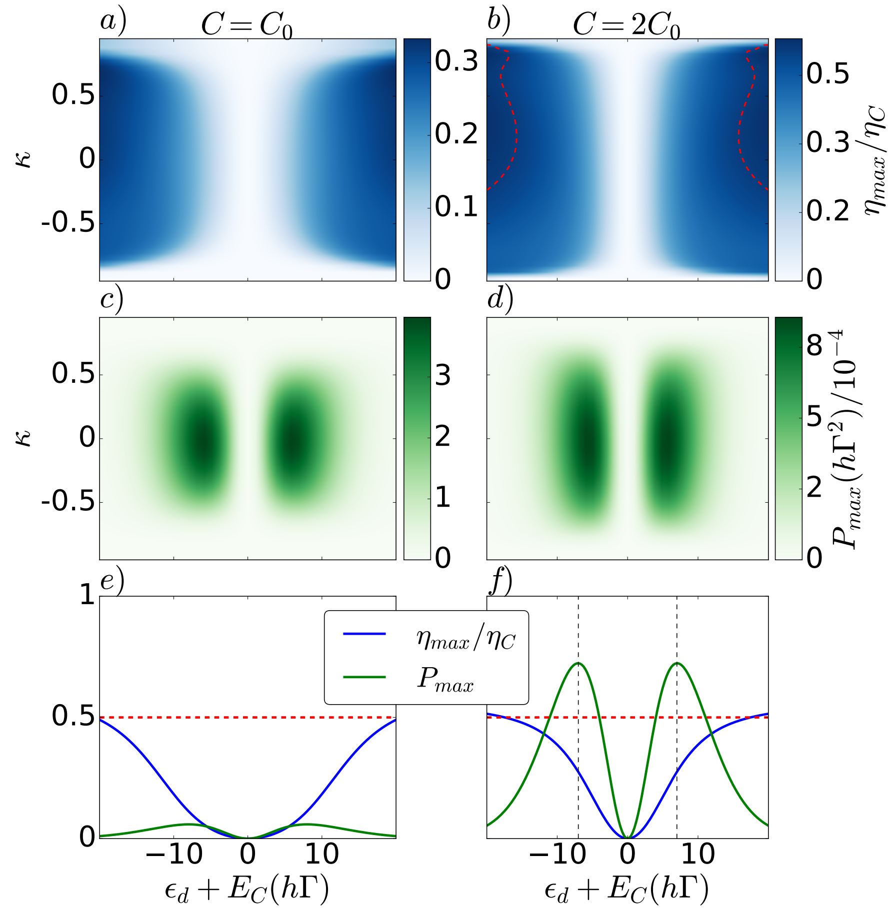

Figure 5.5: Efficiency at maximum power η_{max} in units of the Carnot efficiency η_C versus the dot level position ϵ_d and the asymmetry κ, for different capacitances: a) $C{=}C_0$ and b) $C{=}2C_0$. A red-dashed line marks the Curzon-Ahlborn efficiency, $\eta_{CA} = \eta_C/2$. c), d): Maximum power P_{max} corresponding to the configurations shown in a) and b), respectively. Cuts of the previous curves for $\kappa = 1/2$ are presented in e) and f), for clarity. Same parameters as in Fig. 5.2.

lowing for double occupancy. That is, now we consider $|0\rangle$, $|u\rangle$, $|d\rangle$ and $|2\rangle$. This means that we now need to solve the full master equation, as given in Eq. (5.1). As a consequence now we need to consider not only transitions from or to an empty dot as in

$$\Gamma_{j,0}^{\pm} = \Gamma_j \int dE f^{\pm}(E - eV_j, T_j) P_j(\pm(E - \mu_0)) \tag{5.45}$$

but also transitions to and from an already occupied dot, described by:

$$\Gamma_{j,1}^{\pm} = \Gamma_j \int dE f^{\pm}(E - eV_j, T_j) P_j(\pm(E - \mu_1)). \tag{5.46}$$

Therefore, analytical results for the double occupancy case are cumbersome so we restrict ourselves to present our numerical simulations. The results presented in this section show the two differences: δL and δK.

First, we present the results for δL in Fig. 5.6. As expected, a finite δL arises only with an electrostatic asymmetry coupling, i.e., when $\kappa{\neq}0$. Then, two sawtooth structures for δL appear corresponding to the charging of the

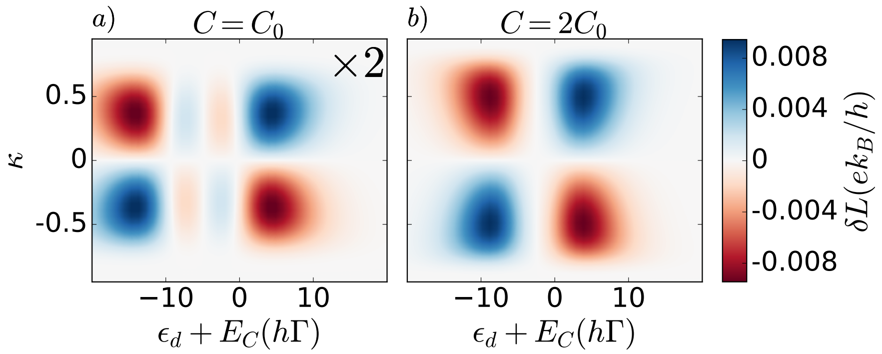

Figure 5.6: Double occupancy electrothermal asymmetry δL versus dot energy level position $\epsilon_d + E_C$ and capacitance asymmetry κ for different values of the total capacitance $C = C_0, 2C_0$. The crossed terms L_{LR}, and L_{RL} are different for $\kappa \neq 0$, i.e. ($C_L \neq C_R$). Parameters are the same as in Fig. 5.2.

system with a second electron. The two sawtooth oscillations are separated by the charging energy $\mu_1 - \mu_0 = 10h\Gamma$, see Fig. 5.6a). Notice that when the charging energy becomes sufficiently small, i.e. for $C = 2C_0$, the two features come closer and the inner oscillations are no longer visible, Fig. 5.6b). The behavior then resembles the one obtained for large charging energy (single occupancy) in Sec. 5.3.

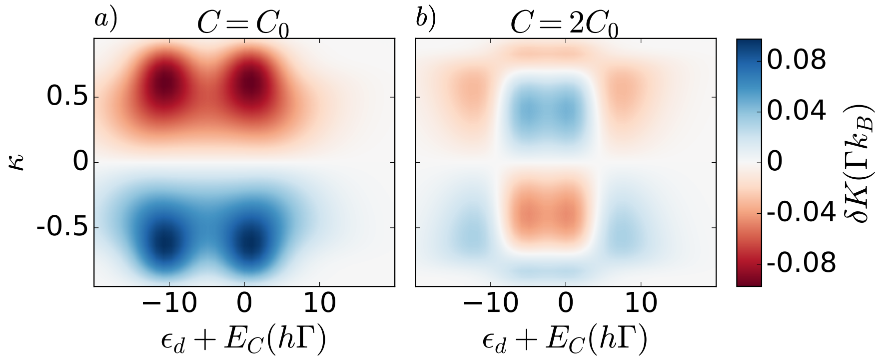

Figure 5.7: Double occupancy thermal asymmetry $K_{LL} - K_{RR}$ versus dot energy level position ϵ_d and capacitance asymmetry κ for different values of the total capacitance $C = C_0$, $2C_0$. Heat rectification $\delta K \neq 0$ for $\kappa \neq 0$, i.e. ($C_L \neq C_R$). Same parameters as in Fig. 5.2.

The heat rectification for the double occupancy case is plotted in Fig. 5.7. We observe the double peak structure for a low capacitance $C = C_0$ due to the two different energy levels available, so we observe a peak for each resonance. As C increases there are two main effects (i) the overall double peak tends to disappear since the charging energy diminishes, and (ii) sign changes appear in the heat rectification (for fixed κ) due a greater weight of δK_κ against δK_Γ when C increases. Therefore the sign of the heat rectification is mainly given by δK_κ for a large capacitance C whereas δK_Γ determines the heat rectification sign when C is small. This behavior is similar to what we observed for the single-occupancy case but with a different strucutre due to the double peak caused by the double occupancy.

5.5 CONCLUSIONS

In closing, we have analyzed the effect of inelasticity introduced by an electromagnetic environment on transport through a conductor (a quantum dot). We have found that even in the absence of a magnetic field, an asymmetric energy exchange with the environment can break symmetries of the transport coefficients, in particular in the thermoelectric and thermal Onsager coefficients. As a consequence an apparent rectification appears in the linear heat currents. Rectification of around $80-90\%$ is found for configurations with significant heat conduction. This rectification due to the environment can be caused both by an asymmetric capacitive coupling or by asymmetric tunnel barriers for the dot. Furthermore, we have shown that heat injected from the environment can either improve or diminish the efficiency at maximum power output of the device when used as an engine. Efficiencies close to the Curzon-Ahlborn (or even larger) are attainable even if at vanishing power output. This improvement in efficiency is attained when the couplings of the system are chosen to promote charge transport in the desired direction, effectively diminishing the required heat from the hot reservoir.

We have considered here the case of a high-impedance environment. Other kind of interactions will have different impact on the performance of the system. The experimental ability to engineer the electromagnetic environment [218] opens the way to improve the control of thermal flows in mesoscopic conductors.

It is clear then that a properly engineered environment can favor transport through a quantum dot and improve its performance as a thermoelectric engine. In an extreme case one could envision this environment to be "intelligent", i.e. it would act on the system according to the state of the system, thus further improving its performance. Such a feedback scheme is equivalent to a Maxwell demon type of feedback which we study in the next chapter.

6

CHIRAL MAXWELL DEMON IN A QUANTUM HALL SYSTEM WITH A LOCALIZED IMPURITY

6.1 INTRODUCTION

As we have seen in Chapter 5 quantum dots are devices suitable for the implementation of quantum engines or refrigerators. Besides, their performance can be externally optimized. More precisely, we have seen that the presence of inelastic effects by the environment helps improve the efficiency and the output power of the quantum-dot-based engine. Quantum dots are a good platform to implement quantum engines not only because of their energy filtering properties but also because of the tunability of their energetic properties. On top of that, we saw that an asymmetry in the system helps further the increase in efficiency of the quantum engine.

The question now comes of how to further improve this increase in efficiency. Since asymmetry plays a crucial role, a natural step is to resort to a system with an intrinsic asymmetry. This is the case for a quantum Hall system characterized by the formation of chiral edge channels [219, 220], as we have seen in Section 1.3 of the introduction and in Chapter 3. Furthermore it has been shown [221] that in such a system, i.e. in a quantum dot embedded in a quantum Hall bar, see Fig. 6.1; the reversal of the magnetic field causes a change in the chirality of the edge states which means that the time-reversal symmetry is broken. As a consequence and due to electronic interactions in the quantum dot, the local detailed balance (LDB), the relation between forward and backward processes, is broken. This means that we can possibly devise a clever way to use this system to act as a very efficient engine since a Maxwell demon mechanism can take advantage of a broken LDB [222].

Since Maxwell envisioned in a *gedankenexperiment* the possibility of an entity, an intelligent agent (a demon to Lord Kelvin) capable of separating warm and cold particles of a gas without performing work apparently violating the second law of thermodynamics, the idea attracted plenty of theoretical attention [223]. The apparent paradox was addressed on a basis in which information and entropy must be related [224]. Information is then, a physical magnitude and it fulfills physical laws [225]. Erasing information implies energy dissipation [226–228] that compensates the entropy reduction suffered by a system in the presence of the demon and ensures the validity of the second thermodynamic law. Such information-to-energy conversion is regarded as the solution of the Maxwell demon paradox [225]. Nowadays Maxwell's demon is interpreted as a feedback control mechanism to convert information into energy. Even though Maxwell's idea was enunciated as a *gedankenexperiment*, present technologies have made possible to build it at small scales, for instance by using Brownian particles [229, 230], single electrons [231], lasers pulses [232] and, most recently in a quantum spin Hall system [233]. However, demons for quantum systems [234] are hard to experimentally design and work and thus show a scarcer experimental activity due to technical difficulty of implementing a truly quantum demon [148, 229] despite the possibility of improved performance [235]. It is worth mentioning that the great progress in the development of stochastic thermodynamics, has resulted in theoretical proposals for stochastic Maxwell demons [222, 236–241] and finally in an experimental implementation of an autonomous Maxwell demon using coupled quantum dots [163] where one of the dots is used to control, through capacitive coupling, the current through the other dot, used as a SET.

A key ingredient for the performance of stochastic Maxwell demons is the breakdown of detailed balance conditions [222] as direct consequence of a clever feedback mechanism. The breakdown of such relations is usually achieved through an asymmetry in the system [222, 238]. This asymmetry is a necessary but not sufficient condition for the breakdown of the local detailed balance (LDB) condition. The breakdown of the local detailed balance requires that forward and backward relations are not related by an exponential Boltzmann factor. Breaking the local detailed balance condition thus creates an imbalance between forward and backward processes from which the demon can profit.

The out-of-equilibrium LDB is broken in quantum Hall (QH) systems with localized impurities due to a non-symmetric electrostatic response of the system when the magnetic field is reversed [221]. Precisely we benefit from this feature to devise a Maxwell demon feedback scheme in a QH bar device with an impurity. We show how the chirality of the edge channels favors the operation of a demon that pushes an electrical current against a bias or that extracts heat from a cold reservoir. The protocol requires two conditions to be satisfied *(i)* electrostatic interactions must be asymmetric when the magnetic field or edge motion is reversed and *(ii)* tunneling events between the edge modes and the localized level must be energy dependent. Under these circumstances the demon is able to convert information into work to drag an electrical current that moves contrary to the applied bias or to extract energy from a cold reservoir. Below we describe the theoretical framework for the chiral demon protocols.

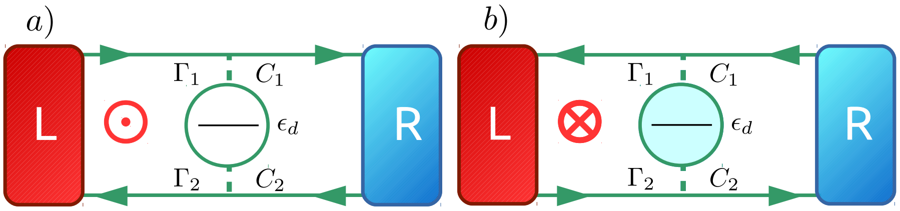

Figure 6.1: The device composed by two electronic reservoirs (Left and Right), the QH bar with edge states represented with lines with arrows (representing direction of transport) and the localized impurity of energy level ϵ_d with tunnel couplings $\Gamma_{1(2)}$ and capacitive couplings $C_{1(2)}$. In a) (for $B > 0$) the upper (lower) edge state travels from L(R) to R(L), instead in b) (for $B < 0$) the upper (lower) edge state travels from R(L) to L(R).

6.2 THEORETICAL APPROACH

As mentioned, our device is a topological setup consisting of a quantum Hall bar defined between two reservoirs (L and R) with an embedded single quasi-localized state of energy ϵ_d and it can only be singly occupied since we restrict ourselves to the Coulomb blockade regime with a sufficiently strong Coulomb energy. Such level is tunnel coupled to chiral edge states of the QH system at filling factor $\nu = 1$, see Fig. 6.1. The applied magnetic field defines the direction of transport (represented by arrows) in each of the chiral modes. Tunneling events between chiral conducting states, $i = 1, 2$, and the quasi-localized state are modeled by the tunneling rates $\Gamma_i^{0(1)}$ that depend on energy. Thus, tunneling rates are different depending on the dot charge state, either empty (0) or filled (1). Electrons in the quasi-localized state are capacitively coupled to those in the edge channels via the capacitances C_i [219, 220, 242]. Due to the chirality of the edges states, the coupling of the quasi-bound state to the left and right reservoirs changes by reversing the magnetic field that exchanges the direction of motion of such modes, see Fig. 6.1. In this manner, for $B > 0$ [Fig. 6.1a)] the level is coupled to the left (L) reservoir through the upper capacitance (C_1) and to the right (R) reservoir through the bottom capacitance (C_2). Under these considerations the quasi-localized level for $B > 0$ has a chemical potential given by

$$\mu_d^+ = \epsilon_d + \frac{e}{C_1 + C_2} \left(C_1 V_L + C_2 V_R \right), \tag{6.1}$$

being $V_{L(R)}$ the voltage in reservoir $L(R)$ and e the electron charge. Changing the field direction ($B < 0$), [Fig. 6.1b)] leads to a reverse motion for the conducting modes, with a chemical potential

$$\mu_d^- = \epsilon_d + \frac{e}{C_1 + C_2} \left(C_2 V_L + C_1 V_R \right). \tag{6.2}$$

Note that the difference between both chemical potentials for $B < 0$, and $B > 0$ becomes

$$\mu_d^- - \mu_d^+ = e\eta(V_R - V_L), \tag{6.3}$$

where $\eta = \frac{C_1 - C_2}{C_1 + C_2}$ measures the asymmetry between capacitances. As a consequence, the difference between chemical potentials is finite only when the setup is under non-equilibrium conditions ($V_L \neq V_R$) and the capacitances are different, meaning $\eta \neq 0$. Then, electrostatic interactions are not symmetric when B is reversed [242].

To describe transport through the interacting level we employ the Master equation framework, see Section 2.4, taking advantage of the fact that in the Coulomb Blockade regime transport happens sequentially. We permit two charge states, namely $|0\rangle$ and $|1\rangle$ whose occupation probabilities are governed by the master equations

$$\begin{aligned} \dot{p}_0 &= -(W_{10}^L + W_{10}^R)p_0 + (W_{01}^L + W_{01}^R)p_1, \\ \dot{p}_1 &= -(W_{01}^L + W_{01}^R)p_1 + (W_{10}^L + W_{10}^R)p_0. \end{aligned} \tag{6.4}$$

The transition rates between those two states are given by W_{mn}^α where m is the final state of the dot, n is the initial state and, α is the reservoir to/from which the electron comes. Due to the demon protocol, described below and which needs to be taken into account in the master equation, the transition rates that fill the dot (W_{10}^α) are always given for a situation in which $B > 0$ and those that empty the dot (W_{01}^α) occur for $B < 0$. This is the basis for our Maxwell demon feedback scheme to work properly since both transitions rates are not related to each other by a LDB condition[221] as we show below. These previous transition rates, in the sequential tunneling regime, are readily obtained from Fermi's golden rule and read:

$$W_{10}^{L(R)} = \Gamma_{1(2)}^0 f_{L(R)} \left(\mu_d^+ - \mu_{L(R)} \right), \tag{6.5}$$

$$W_{01}^{L(R)} = \Gamma_{1(2)}^1 \left[1 - f_{L(R)} \left(\mu_d^- - \mu_{L(R)} \right) \right], \tag{6.6}$$

being $f_{L(R)}(\mu_d^{+/-} - \mu_{L(R)}) = 1/(1 + \exp \beta_{L(R)}[\mu_d^{+/-} - \mu_{L(R)}])$ the Fermi distribution function of the reservoir $L(R)$ with electrochemical potential $\mu_{L(R)}$ and $\beta_{L(R)} = 1/k_B T_{L(R)}$ with $T_{L(R)}$ the temperature of the respective reservoir. As we remarked before, these rates depend on the orientation of the magnetic field through their dependence on the quasi-bound state chemical potential $\mu_d^{+/-}$. Due to the chirality of the system, the inversion of the magnetic field changes the quasi-bound dot energy at which transport is more favored which means that the LDB condition:

$$\frac{W_{10}^L}{W_{01}^L} = e^{-\beta\left(\epsilon_d - \frac{e\Delta V}{2}\right)}, \tag{6.7}$$

is not fulfilled anymore in this system [221] since the relation between rates is modified to:

$$\frac{W_{10}^L}{W_{01}^L} \sim \frac{\Gamma_1^0}{\Gamma_1^1} e^{-\beta\left(\epsilon_d - \frac{e\Delta V}{2}\right)} \left(1 - \left[1 - 2f_L\left(\epsilon_d - \frac{e\Delta V}{2}\right)\right] \beta\eta \frac{e\Delta V}{2}\right), \tag{6.8}$$

with $\Delta V = V_L - V_R$ being the applied bias. We also observe that an energy dependent model for the tunneling rates $\Gamma_1^0 \neq \Gamma_1^1$ breaks the LDB even if capacitances are equal. However, we show here that the demon works properly solely when both requirements are met *(i)* asymmetric capacitances, and *(ii)* energy dependent tunneling rates with asymmetric barriers. It is to be noted that a more complete model for the capacitive coupling, as the one in Ref. [242], could lead to both requirements for the breakdown of the LDB to be fulfilled solely by asymmetric barriers and with symmetric capacitances. We take the tunneling rate energy dependence to be within the WKB approximation. Here, the energy dependence of the tunneling rates is exponential, as shown experimentally [243]

$$\Gamma_\alpha^{0/1} = \Gamma_\alpha e^{k_\alpha(\mu_d^{+/-} - E_\alpha)}, \tag{6.9}$$

where $\alpha = 1, 2$ denotes the barrier, k_α models the energy dependence and E_α is the top energy of the barrier. We profit from the fact that in this approximation barriers are asymmetric whenever $k_1 \neq k_2$.

6.3 PUSHING A CURRENT AGAINST A BIAS

6.3.1 *Demon protocol*

As explained before, LDB is broken, by reversing the magnetic field when the barriers are asymmetric so that they favor certain transitions and restrict others. Under these circumstances we devise a working process for the demon (see Fig. 6.2) and investigate if it would be able to drive a current against a voltage bias ($V_L > V_R$), in other words to drive a current from right to left, in the absence of a temperature gradient $T_L = T_R = T$. Furthermore, we take the demon to be at the same temperature, $T_D = T$. The process is as follows:

Step 1: Starting with $B > 0$ and an empty dot, the process is triggered when an electron enters the dot from the right contact (probability $\propto \Gamma_2^0$). Due to the orientation of the magnetic field, the energy of the electron in the dot is μ_d^+.

Step 2: The demon detects that the dot is singly occupied and accordingly it changes the direction of the magnetic field to $B < 0$, this raises the level energy for the localized state up to μ_d^-.

Step 3: Since now the energy of the electron inside the localized state has augmented it becomes easier to tunnel out through the upper barrier (probability $\propto \Gamma_1^1$) and as a consequence the dot is emptied. This leads to transport of one electron from the right to the left reservoir even though $V_L > V_R$.

Step 4: To finish, the demon detects the change in the localized state occupation and restores the initial magnetic field to $B > 0$.

This process is carried out without a thermal gradient but always at finite temperature. This protocol can not work if any of the reservoirs is at zero temperature since then there are no available electrons in excited states.

Note that the demon pushes electrons against a bias, this operation is optimal as long as the localized state level energy is increased as much as possible therefore helping charges climb against the applied bias. The energy difference after reversing the magnetic field is encountered in Eq. (6.3). Then, we need to take $\eta < 0$, i.e. $C_2 > C_1$, given that $V_L > V_R$. Therefore the feedback scheme is more effective whenever η is close to -1 or at the very nonlinear regime (large $V_L - V_R$).

Although tunneling processes in Steps 1 and 3 are against the bias and thus less likely, this inconvenient can be overcome by cleverly engineering the tunneling rates, see below and Eq. (6.12).

It is clear then that the demon's action is to control the energy level inside the dot through the magnetic field in a clever way. Since this has an effect on the transition rates, the way to theoretically implement the feedback in the transport description is to modify the rates in the master equation Eq. (6.4). Then, the feedback scheme is taken into account by taking the transition rates at the correct magnetic field orientations.

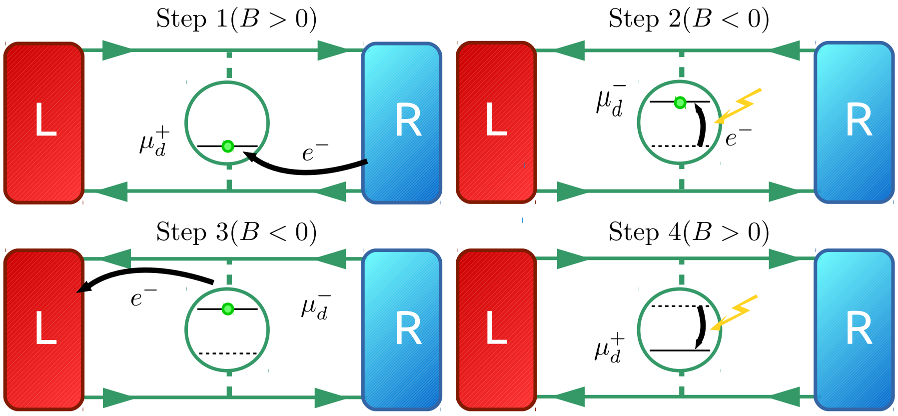

Figure 6.2: Sketch of the performed action by the demon to push electrons against a bias. The demon's action is represented by yellow lightning (steps 2 and 4).

Once the feedback scheme is incorporated to the master equation we are ready to solve it (we restrict to the stationary regime $\dot{p}_{0/1} = 0$) and thus we are able to study the demon protocol and assess whether it works. To this end we characterize the action of the demon through the charge current, the energy current to the demon and the information current that it is able to extract from the system.

6.3.2 *Charge current*

In order to characterize transport and to see whether the demon is able to drive a current against the applied bias or not, we calculate the currents using the probabilities from Eq. (6.4):

$$I_L = e(-W^L_{10}p_0 + W^L_{01}p_1). \tag{6.10}$$

By this definition currents are positive when particles go into a reservoir and negative otherwise and fulfill the particle conservation relation $I_L + I_R = 0$. Then, solving Eq. (6.4) in the steady state regime, the probabilities are easily obtained, yielding

$$I_L = \frac{e(W^L_{01}W^R_{10} - W^L_{10}W^R_{01})}{W^R_{01} + W^L_{01} + W^R_{10} + W^L_{10}}. \tag{6.11}$$

We see from this expression that the first term accounts for particles entering the dot from the right and exiting through the left (positive contribution) and the second term accounts for particles entering the dot from the left and leaving through the right (negative contribution). In order to improve performance of the Maxwell demon we want the first term to be bigger than the second one since we want a current flowing from right to left.

From the expressions of the transition rates and the current, Eqs. (6.5) and (6.11) respectively, we see that to favor the first term of the current we need to enhance $\Gamma^1_1\Gamma^0_2$ with respect to $\Gamma^0_1\Gamma^1_2$. From the expressions of the tunneling rates we obtain their ratio:

$$\frac{\Gamma^1_1\Gamma^0_2}{\Gamma^0_1\Gamma^1_2} = e^{(k_1-k_2)(\mu^-_d-\mu^+_d)}. \tag{6.12}$$

It is observed then that we are able to favor the numerator by taking $k_1 > k_2$, given that $\mu^-_d - \mu^+_d \geqslant 0$.

In Fig. 6.3 we represent the charge current in reservoir L. Current is negative as long as it flows with the bias according to our sign criterion. In Fig. 6.3 a) we observe that symmetric barriers lead to a current that always follows the bias independently of feedback strength η. However, in Fig. 6.3 b) when the tunneling barriers are different and for a sufficiently high η value the current starts to flow opposite to the bias, becoming positive. This notable fact is thanks to the action of the demon.

Noticeably, the ability of the demon to change the energy level is proportional to the applied bias: $\mu^-_d - \mu^+_d \propto \eta\Delta V$. This means that by increasing the applied voltage the current flowing against the bias enhances as well. The bias which in principle is an obstacle that needs to be overcome becomes rather a help because the action of the demon augments with it.

Even so, the fact that the demon is not able to push a current against the bias for small asymmetry implies that this demon can not work in the ideal limit. Indeed, the fact that the demon is not working for $\eta \ll -1$ means that the demon can not operate under ideal conditions, where no heat is injected since this would require symmetric couplings, $\eta = 0$ (see Eq. (6.14)).

6.3.3 *Energy current to the demon*

To fully characterize the demon and since it is not ideal, the energy flow from the system to the demon is evaluated. The energy current is related to

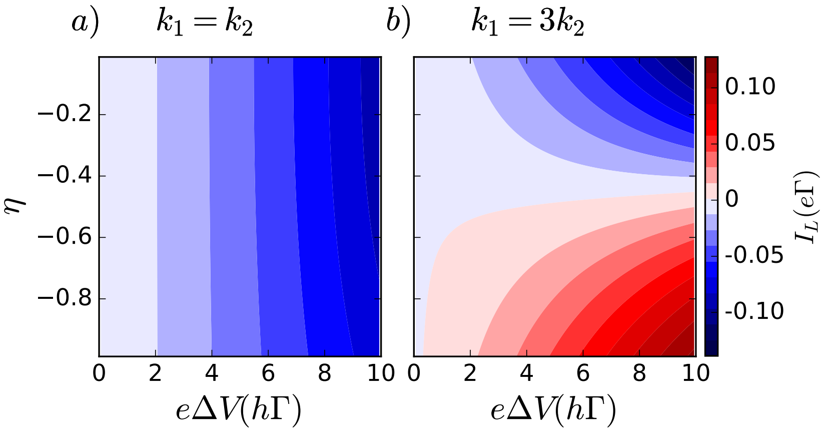

Figure 6.3: Current to (positive) or from (negative) the left reservoir I_L for different values of η as a function of $\Delta V = V_L - V_R$. The current is negative when it flows in the bias voltage direction. The parameters have been chosen so that $k_1 = k_2$ in a) and $k_1 = 3k_2$ in b). We have taken $\Gamma_1 = \Gamma_2 = \Gamma$, $k_1 = 0.1/h\Gamma$ and, $k_B T = 10h\Gamma$.

the energy change that the demon causes on the electrochemical potential of the localized impurity. We calculate this current by measuring the number of electrons going in and out of the dot times their respective energies, yielding

$$J_D = \mu_d^+ (W_{10}^L + W_{10}^R) p_0 - \mu_d^- (W_{01}^L + W_{01}^R) p_1. \tag{6.13}$$

This expression can be simplified, using the solution to the master equation Eq. (6.4) in the stationary regime:

$$J_D = (\mu_d^+ - \mu_d^-) \frac{(W_{10}^L + W_{10}^R)(W_{01}^L + W_{01}^R)}{W_{10}^L + W_{10}^R + W_{01}^L + W_{01}^R}. \tag{6.14}$$

Hence, we see that this energy current is proportional to the energy difference of the electrochemical potentials caused by the demon times the activity current which measures how many particles go in and out of the impurity. Our findings for the energy current carried by the demon are shown in Fig. 6.4. The energy injected by the demon increases with η and with the applied voltage, as expected. Comparing the results for symmetric barriers [Fig. 6.4 a)] and asymmetric ones [Fig. 6.4 b)] we show that the current energy does not change significantly. This indicates that the energy injected by the demon although present and necessary is not the key factor in pushing the current against the bias. Let us now move on to the information entropy.

6.3.4 *Information current*

The final step in the characterization of the demon is the key quantity of an ideal Maxwell demon, i.e. the information that it can extract from the system in order to perform [222]. We start from the system information [236] given by Shannon's entropy $S = -k_B \sum_m p_m \ln p_m$, where p_m are the occupation probabilities given by Eq. (6.4). Then the entropy balance, $\dot{S} = \dot{S}_e + \dot{S}_i$, can be written as an entropy production $\dot{S}_i$ and an entropy flow $\dot{S}_e$ that satisfy $\dot{S}_i = -\dot{S}_e$.

The entropy flow in the system can be separated in the standard form of the entropy flow given by the exchanged heat in each reservoir (ν) over

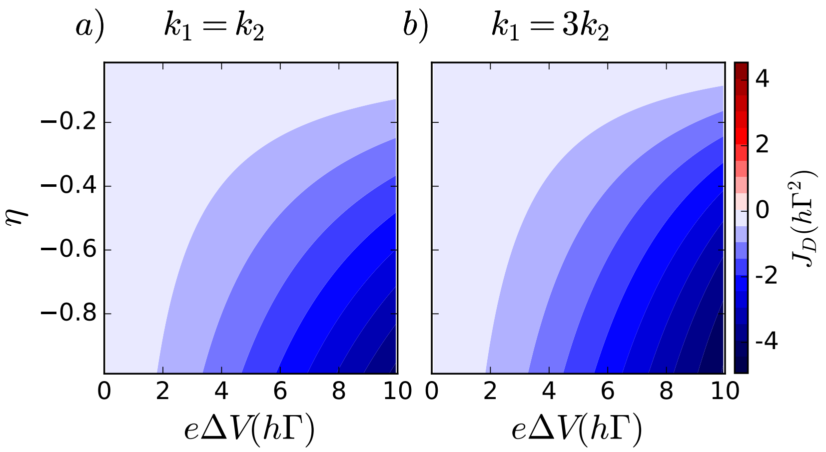

Figure 6.4: Energy current (J_D) injected by the demon for different values of η. The parameters have been chosen so that $k_1 = k_2$ in a) and $k_1 = 3k_2$ in b). Parameters are the same as in Fig. 6.3.

the temperature and an extra term accounting for the entropy flow to the demon $\dot{S}_D$:

$$\dot{S}_e = \sum_{\nu=L,R} \frac{J_\nu}{T_\nu} + \dot{S}_D. \tag{6.15}$$

The heat currents in each reservoir are given by an expression similar to that of the charge with the rates modified to take into account the heat carried in each transition:

$$J_\nu = (\mu_d^- - \mu_\nu) W_{01}^\nu p_1 - (\mu_d^+ - \mu_\nu) W_{10}^\nu p_0. \tag{6.16}$$

The entropy flow to the demon, $\dot{S}_D$, consists of two parts, the entropy flow caused by the energy flux J_D and an information flow I_F that powers the demon. This second term labeled I_F is the information flow extracted by the demon in its application of the feedback protocol:

$$I_F = \dot{S}_D - \frac{J_D}{T_D}. \tag{6.17}$$

This information current is the main characteristic of the Maxwell demon since it measures the information that the demon extracts from the system in order to be able to apply the necessary feedback scheme. Specially in the case of an ideal Maxwell demon ($J_D = 0$), it is the only measurable quantity associated to the Maxwell demon [222].

Fig. 6.5 represents the information current for the demon. In Fig. 6.5 a) we observe that the information current is basically negligible. This corroborates that the demon is acting wrongly, being unable to extract information from the system. However, when barriers depend differently on energy [see Fig. 6.5 b)] the demon starts to be able to extract information from the system. Noticeably, we observe that the cases in which the demon drags an electrical current against the bias system coincide with the cases in which the demon is able to extract information from the system, compare Figs. 6.3 and 6.5. This is the definitive indicator that the extraction of information is the key to our demon's operation.

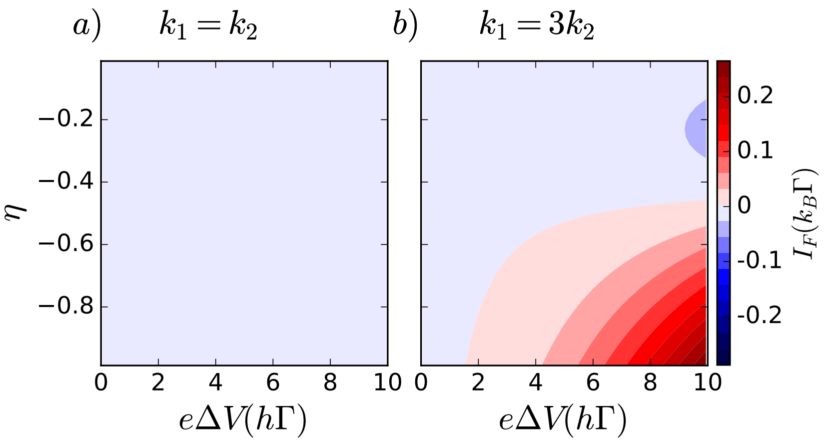

Figure 6.5: Information current (I_F) of the demon for different values of η. The parameters have been chosen so that $k_1 = k_2$ in a) and $k_1 = 3k_2$ in b). Parameters are the same as in Fig. 6.3.

6.4 COOLING A COLD RESERVOIR

Another interesting application of the demon feedback, besides pushing a current against a bias, is using it for cooling purposes. This was shown experimentally in Ref. [163] where cooling was achieved using a double quantum dot setup. They used the setup of Ref.[239], originally thought for pushing a current against a bias.

In this section we investigate the possibility of using our setup for cooling purposes, studying the ability of the demon to extract a heat current from a cold reservoir.

To this end we use a configuration with $T_L > T_R = T_D$ and we aim to extract heat from R. Ideally, the demon should be able to perform this action without the help of a voltage bias but unfortunately this is not possible since, as previously discussed, the demon is not able to perform any action at $\Delta V = 0$. Therefore, we need a finite bias to observe this effect. Given that our aim is to cause an energy flow out of the cold reservoir (R) we choose a bias such that it helps achieve our goal, i.e. $V_R > V_L$.

6.4.1 *Demon protocol*

The working process of the demon is very similar to the one used to push a current against the bias but now instead of increasing the energy of the electrons inside the dot we do the opposite, effectively extracting a hot electron from R and lowering their energy, before injecting it into reservoir L, see Fig. 6.6. In this scenario the demon would work as follows:

Step 1: (Starting with $B > 0$ and an empty dot) An electron enters the dot from the right contact (probability $\propto \Gamma_2^0$). Due to the orientation of the magnetic field, the energy of the electron in the dot is μ_d^+. In order to be able to lower the energy of the electron in the feedback process it is needed that $\eta < 0$ since $V_R > V_L$.

Step 2: The demon detects the occupation of the dot and changes the direction of the magnetic field to $B < 0$, lowering the energy level of the dot to μ_d^-.

Step 3: The dot is emptied, with the electron traveling to the left reservoir (probability $\propto \Gamma_1^1$).

Step 4: The demon detects again the change of state in the dot and restores the initial magnetic field to $B > 0$.

All in all is a very similar procedure to that of pushing a current against a bias and therefore we use the same description as before. In fact, we see that the transition rates that we need to favor are the same as before. Also, since we want the demon to lower the energy level we should take $\eta < 0$ as before given that now we have $V_R > V_L$.

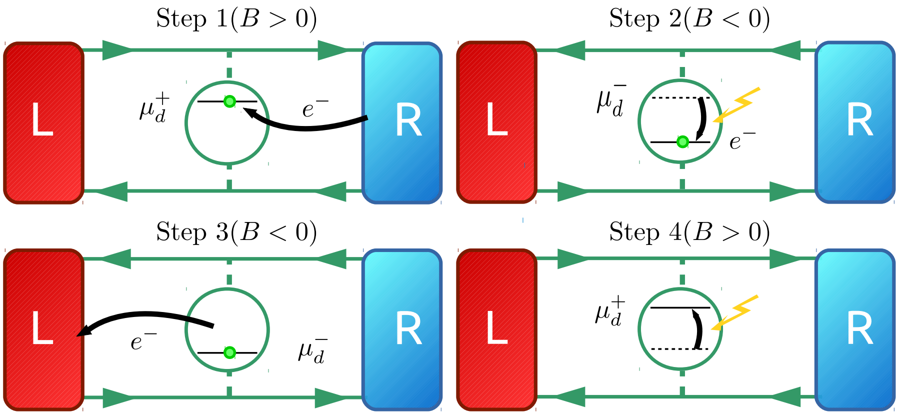

Figure 6.6: Sketch of the performed action by the demon to cool the right reservoir. The demon's action is represented by yellow lightning (steps 2 and 4).

6.4.2 *Heat current*

In this second application of the Maxwell demon feedback we want to see whether it can cool a cold reservoir, in other words if it can carry a heat current against a thermal gradient. To this end we study the heat currents in the system and observe if they flow from hot (L) to cold (R) or otherwise. Therefore we need to calculate the heat currents in each reservoir:

$$J_\nu = (\mu_d^- - \mu_\nu) W_{01}^\nu p_1 - (\mu_d^+ - \mu_\nu) W_{10}^\nu p_0. \tag{6.18}$$

Our main interest is in the heat current in the right reservoir since it is the cold reservoir and is the one that we aim to cool with the action of the demon. In the steady state regime, this current reads as follows:

$$J_R = \frac{(eV_R - \mu_d^+) W_{01}^L W_{10}^R + (\mu_d^- - eV_R) W_{10}^L W_{01}^R + (\mu_d^- - \mu_d^+) W_{10}^R W_{01}^R}{W_{01}^R + W_{01}^L + W_{10}^R + W_{10}^L}. \tag{6.19}$$

We see that the heat current has three different terms. The first two terms describe the movement of an electron from one reservoir to the other whereas the last term describes transitions at different energies (due to the action of the demon) in the same reservoir. The first term is the one described in the explanation of the protocol, so it is the one that the demon should enhance. Even so, all three terms can be negative (meaning that they help cool the cold reservoir). Hence, it is not so clear as it was with the charge current which are the terms that matter the most for the action of cooling.

It is important to note that the energy current is more sensitive to errors than the charge current. Given the probabilistic nature of the events described here, the protocol is not always correctly applied because undesired transitions can happen. Tuning the barriers is the way to ensure that these errors have a low probability of happening but it is not possible to make them completely disappear. In the case of the charge current, the events consisting of one error are not perceived since they involve the transport of one electron in and out of the same reservoir which results in a null charge current. Oppositely, in the heat current these errors are clearly visible and appear as the third term in the energy current J_R. These processes, although they help cool the right reservoir they are not a desired event since the cooling comes purely from extracting energy from the system rather than extracting information (or entropy) and thus are not demon-like processes. As a consequence, it is impossible to have a purely information-powered Maxwell demon in this setup.

This is observed in Fig. 6.7 where we see that indeed there is cooling of the cold reservoir (J_R is negative, thus flowing out of R). Comparing Fig. 6.7 a) and b) we see that the amount of heat extracted from R does not change much when the barriers are asymmetric, unlike what happened for the charge. Therefore we observe that there is cooling in both cases but now we need to clarify the origin of this cooling and investigate if it really comes from the extraction of information by the demon or if it is a direct consequence of the energy extraction by the demon.

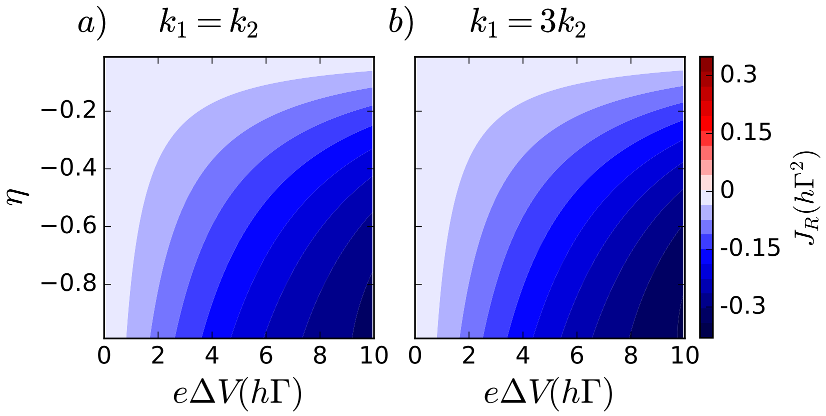

Figure 6.7: Heat current flowing from the cold reservoir J_R, negative when flowing out of the reservoir, positive otherwise. The parameters have been chosen so that $k_1 = k_2$ in a) and $k_1 = 3k_2$ in b). We have taken $\Gamma_1 = \Gamma_2 = \Gamma$, $k_1 = 0.1/h\Gamma$ and, $k_B T = 10h\Gamma$.

6.4.3 *Energy current to demon*

To know the origin of the cooling occurring in the setup we start by studying the energy current to the demon. As we did for the case of the demon acting against a voltage bias, we study the energy flow between demon and system. The energy current to the demon is described by the same equation as before, see Eq. (6.14). As shown in Fig. 6.8, the demon extracts energy from the system when acting as a refrigerator. We observe there that the energy extracted by the demon is bigger when barriers are symmetric [Fig. 6.8a)] than when they are not [Fig. 6.8 b)]. This means that the demon is able to cool by the same amount despite needing to extract less energy from the system which means that the energy extraction is not the only mechanism acting to cool the system.

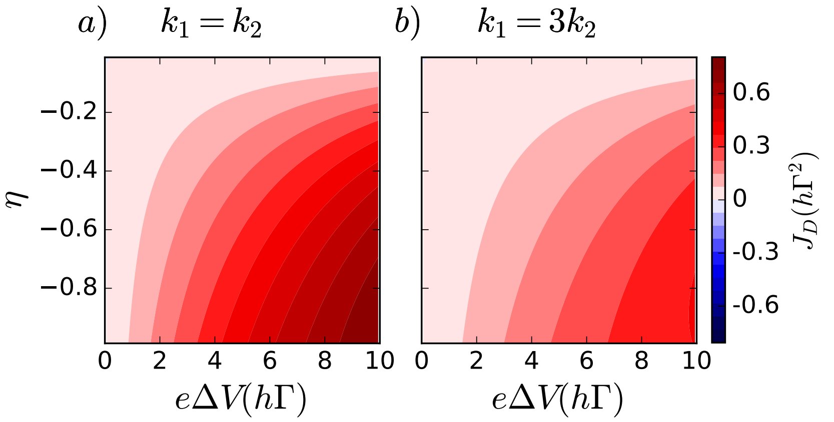

Figure 6.8: Energy current J_D injected by the demon. The parameters have been chosen so that $k_1 = k_2$ in a) and $k_1 = 3k_2$ in b). Parameters are the same as in Fig. 6.3.

6.4.4 *Information current*

Finally we look at the information current of the demon when performing as a refrigerator which is described by the previously derived expression, Eq. (6.17). In Fig. 6.9 a) we see that the demon is not able to extract information when the barriers are symmetric and thus all cooling effects are due to the energy extracted. On the other hand, for asymmetric barriers, see Fig. 6.9 b), information is flowing to the demon, meaning that it is able to cool the R reservoir not only by extracting energy but also by lowering its entropy.

These results explain why there is no change in the cooling power J_R despite a lower extracted heat by the demon J_D, showing that indeed the demon is able to perform some cooling via information extraction.

Oppositely to what was observed for the case of pushing a current against a bias, here the main cause of the cooling effect is not the information but the direct extraction of energy by the demon. So, we conclude that our setup despite being able of cooling is not a good candidate for the implementation of a cooling feedback scheme.

6.5 CONCLUSIONS

We have shown that it is possible to mimic the action of a quantum engine without a thermal gradient thanks to the effect of a non-ideal Maxwell demon feedback on transport through a localized state in a quantum Hall system. We proposed a working principle for a Maxwell demon based on the chirality of the edge states. We showed that it is applicable under the conditions: *(i)* asymmetry of the capacitive interactions as the magnetic field is reversed under non equilibrium conditions, and *(ii)* energy dependence of the tunneling probabilities through the barriers.

We show with a precise feedback protocol how a demon is able to push electrical current against the applied bias voltage by extracting information from the system. We demonstrate that this is effectively the case, the demon

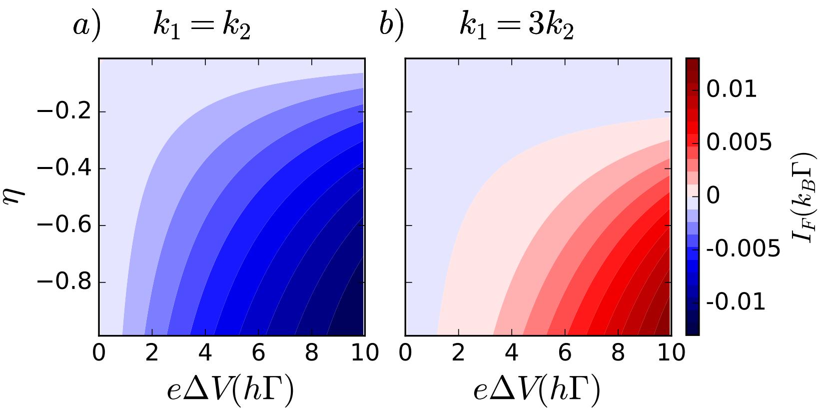

Figure 6.9: Information current I_F to the demon. The parameters have been chosen so that $k_1 = k_2$ in a) and $k_1 = 3k_2$ in b). Parameters are the same as in Fig. 6.3.

works satisfactorily whenever is able to extract information from the system. Our scheme opens an important avenue for the design of Maxwell demons that benefit from the topological properties of quantum matter in interacting systems since any means of switching the chirality would be well described by our theoretical description and would serve the same purpose as the reversal of the magnetic field.

On the other hand, we apply a similar protocol in order to cool a cold reservoir. We find that in this case the demon is not able to properly perform the desired action of cooling by extracting information from the system. Or at least is only partially able to perform such action, being the extraction of energy the main mechanism of cooling.

It is to be noted that although the reversal of such high magnetic fields dissipates a lot of heat and is hard to implement in the desired time scale of few nanoseconds with the experimental techniques available nowadays, this reversal is only meant as a reversal of the chirality of the edge states of the quantum Hall system. This reversal could be achieved for example, using a fixed magnetic field of a few T in one direction and then triggering a pulsed high magnetic field on the opposite direction to achieve the reversal of the magnetic field. These pulsed magnetic fields are triggered over typical time scales of microseconds [244] which is a reasonable operation time for the demon. Another possibility would be to move the sample between two well-localized fixed magnetic fields configured in opposite directions, achieving an effective reversal of the magnetic field. In both of these processes, the QD state could be preserved by lowering its energy and restoring it afterwards.

This work is an attempt to open the path to the creation of Maxwell-demon type of schemes in quantum systems. The discovery of new effects and new systems in the quantum world offer tools to be exploited by Maxwell demon feedbacks. Here we studied the possibility of taking advantage of the topological properties of a system to favor the operation of a demon but many not yet discussed quantum effects could be used to the same end. Demons that could exploit effects such as coherence have not been proposed until very recently [245].

7

CONCLUSIONS AND OUTLOOK

The interplay of energy and charge currents in systems in the nano-scale is the main focus of this thesis. We have shown that the energy and charge flows are fundamentally different despite the fact that some relations among them can be found in nanosystems. We have also investigated the role of external agents in the behavior of these magnitudes and we have studied how the relation between charge and energy can be exploited in order to implement thermoelectric devices. We have also seen the range of applicability of the different formalisms that we used to describe the different systems under study.

In Chapter 3 we have studied interference effects on the charge, energy, and spectral currents as well as on the charge current noise at the output of a MZI fed by one and by two single particle sources.

A dependence on the magnetic flux going through the interferometer, observed as interference effects, has been shown for all studied quantities in the MZI fed only by one source. We have shown that the interference effects are affected by the detuning of the arms of the interferometer due to the energy dependence of the transmission through the MZI. As a consequence, energy and charge currents are out of phase and a finite DC current can be observed at both outputs of the interferometer even if the total injected current is zero. Two interpretations of these results were given, based either on the wave nature of the signal or on the particle properties of electrons.

On a second step, we add a second single-particle source in the middle of the lower arm of the interferometer. Hence, we are able to investigate how the interference in the MZI is affected by two-particle effects. These effects, either collisions or absorptions, stemming from the synchronization of the sources introduce new relevant time scales. These new time-scales lead to a suppression of the interference in the spectral current when the sources are tuned to allow for absorptions of particles, or even to the occurrence of additional energy-dependent oscillations when there is a possibility of collisions of particles of the same type. These new time-scales lead to a suppression of the interference in the spectral current when the sources are tuned to allow for absorptions of particles, or even to the occurrence of additional energy-dependent oscillations when the possibility of collisions of particles of the same type is given.

As a result of the occurrence of these new time-scales, the absorption of particles at $\mathrm{SPS_B}$, as well as the collision of particles at $\mathrm{QPC_R}$ lead to a suppression of interference in the charge current.

We show that two interpretations coexist for this: the averaging of the magnetic-flux dependent oscillations in the spectral current leads to a suppression of the interference in the charge current and, on the other hand, it can be explained by the possibility of extracting which-path information from reduced fluctuations due to two-particle effects. The particle interpretation is corroborated by the behavior of the noise which shows that indeed there is a reduction of fluctuations when the interference is suppressed.

Even so, we also show that when considering the behavior of the energy current in the case of collisions, the particle picture does not hold. Hence, we are able to show that charge and energy currents behave in a fundamentally different way when considering electrons and holes since the energy current exhibits interference effects while the charge current does not.

As a further step in our research, it would be interesting to compute the energy current noise to know how the fluctuations in it are affected by the presence of two-particle effects.

In Chapter 4 we investigated an interacting conductor coupled to a single reservoir and modulated by an electrical AC signal. This circuit corresponds to a quantum capacitor, similar to that used in Chapter 3. We have characterized the energy current spectrum in the linear response regime for arbitrary AC frequencies and we have shown, with symmetry arguments, that one needs to take into account the heat stored or relaxed at the barrier in the expression of the heat currents. We have considered the strong interacting limit, where Coulomb blockade is relevant. We used two prototypical interacting conductors, a single-orbital quantum dot and a multi-orbital conductor– a carbon nanotube quantum dot coupled to a single reservoir–, to illustrate our results for the energy current.

Our results show that photo assisted features appear in the electrical and heat flows, and that the electrothermal admittance can be positive or negative and the sign can be chosen by adjusting properly the AC frequency.

In Chapter 4 we have thus developed a theoretical framework to study interacting conductors coupled to one reservoir under AC-driving and we have shown that photon-assisted events caused by an AC-driving have an impact both on the charge and on the heat currents in an interacting conductor which is an important issue for engineering nanoelectronic circuits with optimal heat dissipation performances.

A natural next step to this work would be the completion of the Onsager matrix for this system, by studying the response of charge and energy currents to a temperature AC driving.

The effect of considering an electromagnetic environment on transport through a conductor (a quantum dot) and its impact in the form of inelasticity was investigated in Chapter 5. The environment, the surrounding circuit, induces a dynamical Coulomb blockade in the transport of electrons through the quantum dot. We have found that the energy exchange between the electrons traversing the dot and the environment can break symmetries of the transport coefficients, even in the absence of a magnetic field. This breakdown of the symmetries happens when the energy exchange is not symmetric in both barriers and is visible in the thermoelectric and thermal Onsager coefficients and thus an apparent heat rectification appears even in the linear regime.

The heat rectification that we found can be of relevance even in configurations with significant heat conduction. We have shown that there are two possible origins for the heat rectification, either an asymmetric capacitive coupling of the electrons in the dot to the electrons in the reservoirs or asymmetric tunnel barriers for the dot. On the other hand, asymmetries on the thermoelectric coefficients are only caused by asymmetric capacitances.

The performance of such a setup as a thermoelectric engine was also investigated and we found that the environment can either improve or diminish the efficiency at maximum power output. Efficiency is improved when the couplings of the system are chosen to promote charge transport in the desired direction which effectively reduces the heat needed for such purpose. In this case, efficiencies close to the Curzon-Ahlborn limit are reachable although at vanishing power output.

The results in Chapter 5 are valid for a high-impedance environment. Hence, a natural way to expand them is to consider other environments which could have different effects on the performance of the system. One could then investigate which properties of the environment are best suited for the performance of the system and try to engineer a proper environment to try and take advantage of it.

In Chapter 6 we propose a working principle for a Maxwell demon that profits from the chirality of the edge states in a quantum Hall system. The proposed device consists of a localized state created by an impurity in a quantum Hall system. We were able to show that the Maxwell demon can reproduce the action of a quantum thermoelectric engine without the need of a thermal gradient thanks to the extraction of information. The conditions required for the demon to work are the asymmetry of the capacitive interactions as the magnetic field is reversed under non-equilibrium conditions, and an asymmetry in the energy dependence of the tunneling probabilities through the barriers.

We proposed a precise feedback protocol that the demon can apply to push an electrical current against an applied bias, therefore extracting work, by extracting information about the state of the system and without the need of a thermal gradient. We checked that the protocol is effective in extracting work from the system whenever the demon is able to extract information.

Similarly, we propose a similar feedback protocol to use the demon as a refrigerator. We find that in this case, although cooling is achieved, the demon is not performing thanks to the extraction of information but rather thanks to an extraction of heat. We showed that in this case the mechanism behind the cooling is the extraction of energy, although improved by a certain amount of extraction of information.

Our scheme opens an important avenue for the design of Maxwell demons that benefit from the topological properties of quantum matter in interacting systems since any means of switching the chirality would be well described by our theoretical description and would serve the same purpose as the reversal of the magnetic field.

Nanoscale systems offer a variety of effects not available in macroscopic systems that could be potentially exploited by a Maxwell demon. The work in Chapter 6 is an attempt to open the path to the creation of Maxwell-demon type of schemes in quantum systems. By trying to exploit the topological properties to operate the demon we took a first step to exploiting quantum effects by a Maxwell demon, but many other effects might be used to favor the operation of the demon.

In closing, we have shown how heat and charge currents behave in fundamentally different ways in the nanoscale. We have shown the interplay of these quantities can be exploited to devise more efficient thermoelectric quantum engines and how the different techniques can be applied to describe systems in the different regimes.

Part III

APPENDIX

A

SYNCHRONIZED TWO-PARTICLE EMISSION - COMPLEMENTARY EXPRESSIONS

This appendix is devoted to present the expressions for the spectral, charge, and energy currents as well as charge-current noise for the cases that were not presented in the main text of Chapter 3. We complement the expressions for the spectral current with the expressions for the cases that were not presented in the main text and give the full expressions for the charge and energy currents. For the charge-current noise we give the full expression when only source A is working and give the expressions for the cases not presented when both sources are working.

A.1 SPECTRAL CURRENT

In Section 3.4.1 we present the spectral currents detected at the output of the MZI when both SPSs are working, leading to the collision of (or the absorption of) electrons. Here, we complement this discussion by presenting the analytic results for the spectral current in the case where a hole emitted from $\mathrm{SPS_A}$ encounters an electron emitted from $\mathrm{SPS_B}$

$$\begin{aligned} i^{he}(E,\Phi) &= R_L R_R i_A^h(E) + R_L T_R i_B^e(E) \\ &+ T_L T_R \left(i_B^e(E) + i_A^h(E)\right)\left(1 - \frac{4\sigma_A\sigma_B}{{\Delta t_d^{he}}^2 + (\sigma_A+\sigma_B)^2}\right) \\ &- 2\gamma i_A^h(E)\mathbb{R}\mathrm{e}\left\{e^{-i\Phi}e^{-iE\Delta\tau/\hbar}\left(1 - \frac{-2i\sigma_B}{\Delta t_d^{he} - i\,(\sigma_A+\sigma_B)}\right)\right\}. \end{aligned} \tag{A.1}$$

Furthermore, we find for the hole part of the spectral current in the case of possible collision of holes

$$\begin{aligned} & i^{hh}(E,\Phi) = R_L R_R i_A^h(E) + T_L T_R i_A^h(E)\times \\ & \mathbb{R}\mathrm{e}\left\{1 + \frac{4\sigma_A\sigma_B}{{\Delta t_d^{hh}}^2 + (\sigma_A-\sigma_B)^2} + 2i\sigma_B\frac{\Delta t_d^{hh} + i(\sigma_A+\sigma_B)}{{\Delta t_d^{hh}}^2 + (\sigma_A-\sigma_B)^2}e^{-iE\left(\Delta t_d^{hh} - i(\sigma_A-\sigma_B)\right)/\hbar}\right\} \\ & + R_L T_R i_B^h(E) + T_L T_R i_B^h(E)\times \\ & \mathbb{R}\mathrm{e}\left\{1 + \frac{4\sigma_A\sigma_B}{{\Delta t_d^{hh}}^2 + (\sigma_A-\sigma_B)^2} + 2i\sigma_A\frac{\Delta t_d^{hh} + i(\sigma_A+\sigma_B)}{{\Delta t_d^{hh}}^2 + (\sigma_A-\sigma_B)^2}e^{-iE\left(\Delta t_d^{hh} - i(\sigma_B-\sigma_A)\right)/\hbar}\right\} \\ & - 2\gamma i_A^h(E)\times \\ & \mathbb{R}\mathrm{e}\left\{e^{-i\Phi}e^{-iE\Delta\tau/\hbar}\left[1 - \frac{2i\sigma_B}{\Delta t_d^{hh} - i\,(\sigma_A-\sigma_B)}\left(1 - e^{-iE\left(\Delta t_d^{hh} - i(\sigma_A-\sigma_B)\right)/\hbar}\right)\right]\right\}. \end{aligned} \tag{A.2}$$

In order to find the limit in which either $\mathrm{SPS_A}$ of $\mathrm{SPS_B}$ is switched off, it is enough to set $\sigma_A \to 0$ (respectively, $\sigma_B \to 0$). The same applies for Eqs. (3.23) and (3.24).

A.2 CHARGE CURRENT

All expressions for the time-averaged charge current given in the main text in the regime where particles of opposite type arrive in the detector from the two SPSs can be obtained from the general expression

$$\begin{aligned}
\frac{\bar{I}^{\mathrm{eh+he}}}{e/\mathcal{T}} &= R_L R_R \left(n_A^h - n_A^e\right) + R_L T_R \left(n_B^h - n_B^e\right) \\
&+ T_L T_R \frac{\Delta t_d^2 + (\sigma_A - \sigma_B)^2}{\Delta t_d^2 + (\sigma_A + \sigma_B)^2} \left(n_A^h - n_A^e + n_B^h - n_B^e\right) \\
&- 2\gamma \mathbb{R}\mathrm{e}\Bigg\{ e^{-i\Phi} \Bigg(n_A^h \frac{2i\sigma_A}{\Delta\tau + 2i\sigma_A} \left(1 - n_B^e \frac{-2i\sigma_B}{\Delta t_d - i(\sigma_A + \sigma_B)}\right) \\
&- n_A^e \frac{-2i\sigma_A}{\Delta\tau - 2i\sigma_A} \left(1 - n_B^h \frac{2i\sigma_B}{\Delta t_d + i(\sigma_A + \sigma_B)}\right) \Bigg) \Bigg\},
\end{aligned} \tag{A.3}$$

by setting the respective particle numbers $n_k^i = 0, 1$. Here, we assume that the time difference $\Delta t_d^{eh} = \Delta t_d^{he} \equiv \Delta t_d$ is equal for electrons and holes. However, different collision conditions Δt_d^{ij} can be obtained straightforwardly by adjusting them for each contribution n_k^i. The result for the MZI with a single SPS_A is found by setting $n_B^e = n_B^h = 0$ and by taking $\sigma_B = 0$ if SPS_B is switched off.

The general expression for the charge current in the regime where particles of the same type arrive in the detector from both SPSs is

$$\begin{aligned}
\frac{\bar{I}^{\mathrm{ee+hh}}}{e/\mathcal{T}} &= R_L R_R \left(n_A^h - n_A^e\right) + R_L T_R \left(n_B^h - n_B^e\right) \\
&+ T_L T_R \frac{\Delta t_d^2 + (\sigma_A + \sigma_B)^2}{\Delta t_d^2 + (\sigma_A - \sigma_B)^2} \left(n_A^h + n_B^h - n_A^e - n_B^e\right) \\
&- 2 T_L T_R \frac{4\sigma_A \sigma_B}{\Delta t_d^2 + (\sigma_A - \sigma_B)^2} \left(n_A^h n_B^h - n_A^e n_B^e\right) \\
&- 2\gamma \mathbb{R}\mathrm{e}\left\{ e^{-i\Phi} \left(n_A^h \frac{2i\sigma_A}{\Delta\tau + 2i\sigma_A} - n_A^e \frac{-2i\sigma_A}{\Delta\tau - 2i\sigma_A} \right) \right\} \\
&+ 2\gamma \mathbb{R}\mathrm{e}\Bigg\{ e^{-i\Phi} \Bigg(n_A^h n_B^h \frac{2i\sigma_A}{\Delta\tau + 2i\sigma_A} \frac{2i\sigma_B}{\Delta t_u + i(\sigma_A + \sigma_B)} \\
&- n_A^e n_B^e \frac{-2i\sigma_A}{\Delta\tau - 2i\sigma_A} \frac{-2i\sigma_B}{\Delta t_u - i(\sigma_A + \sigma_B)} \Bigg) \Bigg\}.
\end{aligned} \tag{A.4}$$

Also here we took $\Delta t_d^{ee} = \Delta t_d^{hh} \equiv \Delta t_d$ and $\Delta t_u^{ee} = \Delta t_u^{hh} \equiv \Delta t_u$ for simplicity.

A.3 ENERGY CURRENT

Similar to the case of the charge current, we only show a part of the different particle contributions to the energy current in the main text. In this appendix we report the full expressions, where the same considerations for the different contributing particles, n_k^e and n_k^h, and the time differences characterising their synchronised emissions, Δt_u^{ij} and Δt_d^{ij}, apply, as it was explained for the charge currents in Appendix A.2.

When the SPSs are tuned such that particles of different type emitted from the two sources arrive at the detector in the same half period and hence absorptions can possibly occur, the general expression for the energy current is

$$\begin{aligned}
J^{eh+he} &= \frac{\hbar}{2\sigma_A\mathcal{T}}\left(n_A^e+n_A^h\right)\left(R_LR_R+T_LT_R\right)+\frac{\hbar}{2\sigma_B\mathcal{T}}\left(n_B^e+n_B^h\right)T_R \\
&-T_LT_R\left(\frac{\hbar}{2\sigma_A\mathcal{T}}+\frac{\hbar}{2\sigma_B\mathcal{T}}\right)\left(n_A^e n_B^h+n_A^h n_B^e\right)\frac{4\sigma_A\sigma_B}{\Delta t_d^2+\left(\sigma_A+\sigma_B\right)^2} \\
&-2\gamma\frac{\hbar}{2\sigma_A\mathcal{T}}\mathbb{R}\mathrm{e}\left\{e^{-i\Phi}\left[n_A^e\left(\frac{-2i\sigma_A}{\Delta\tau-2i\sigma_A}\right)^2\left(1-n_B^h\frac{2i\sigma_B}{\Delta t_d+i\left(\sigma_A+\sigma_B\right)}\right)\right.\right. \\
&\left.\left.+n_A^h\left(\frac{2i\sigma_A}{\Delta\tau+2i\sigma_A}\right)^2\left(1-n_B^e\frac{-2i\sigma_B}{\Delta t_d-i\left(\sigma_A+\sigma_B\right)}\right)\right]\right\}.
\end{aligned}\tag{A.5}$$

For the regime in which collisions between particles can occur, we find

$$\begin{aligned}
J^{ee+hh} &= \frac{\hbar}{2\sigma_A\mathcal{T}}\left(n_A^e+n_A^h\right)\left(R_LR_R+T_LT_R\right)+\frac{\hbar}{2\sigma_B\mathcal{T}}\left(n_B^e+n_B^h\right)T_R \\
&+T_LT_R\left(\frac{\hbar}{2\sigma_A\mathcal{T}}+\frac{\hbar}{2\sigma_B\mathcal{T}}\right)\left(n_A^e n_B^e+n_A^h n_B^h\right)\frac{4\sigma_A\sigma_B}{\Delta t_d^2+\left(\sigma_A+\sigma_B\right)^2} \\
&-2\gamma\frac{\hbar}{2\sigma_A\mathcal{T}}\mathbb{R}\mathrm{e}\left\{e^{-i\Phi}\left[n_A^e\left(\frac{-2i\sigma_A}{\Delta\tau-2i\sigma_A}\right)^2\left(1-n_B^e\frac{-2i\sigma_B}{\Delta t_u-i\left(\sigma_A+\sigma_B\right)}\right)\right.\right. \\
&\left.\left.+n_A^h\left(\frac{2i\sigma_A}{\Delta\tau+2i\sigma_A}\right)^2\left(1-n_B^h\frac{2i\sigma_B}{\Delta t_u+i\left(\sigma_A+\sigma_B\right)}\right)\right]\right\} \\
&+2\gamma\frac{\hbar}{2\sigma_B\mathcal{T}}\mathbb{R}\mathrm{e}\left\{e^{-i\Phi}\left[n_A^e n_B^e\frac{-2i\sigma_A}{\Delta\tau-2i\sigma_A}\left(\frac{-2i\sigma_B}{\Delta t_u-i\left(\sigma_A+\sigma_B\right)}\right)^2\right.\right. \\
&\left.\left.+n_A^h n_B^h\frac{2i\sigma_A}{\Delta\tau+2i\sigma_A}\left(\frac{2i\sigma_B}{\Delta t_u+i\left(\sigma_A+\sigma_B\right)}\right)^2\right]\right\}.
\end{aligned}\tag{A.6}$$

A.4 ANALYTIC EXPRESSIONS FOR THE NOISE

Finally, we consider the charge-current noise, stemming from the current-current correlator of the currents detected in reservoirs 3 and 4. If $\mathrm{SPS_B}$ is switched off and particles are emitted into the MZI only from $\mathrm{SPS_A}$, the total noise stemming from electrons and holes is given by

$$\begin{aligned}
\frac{\mathcal{P}_{MZI,A}}{-e^2/\mathcal{T}} &= \left(T_RR_R+T_LR_L-4\gamma^2\right)\left(n_A^e+n_A^h\right) \\
&+2\gamma\left(T_L-R_L\right)\left(T_R-R_R\right)\mathbb{R}\mathrm{e}\left\{e^{-i\Phi}\left(n_A^e\frac{-2i\sigma_A}{\Delta\tau-2i\sigma_A}+n_A^h\frac{2i\sigma_A}{\Delta\tau+2i\sigma_A}\right)\right\} \\
&-n_A^e\left(2\gamma\mathbb{R}\mathrm{e}\left\{e^{-i\Phi}\frac{-2i\sigma_A}{\Delta\tau-2i\sigma_A}\right\}\right)^2-n_A^h\left(2\gamma\mathbb{R}\mathrm{e}\left\{e^{-i\Phi}\frac{2i\sigma_A}{\Delta\tau+2i\sigma_A}\right\}\right)^2.
\end{aligned}\tag{A.7}$$

The noise for the case of a possible absorption of a hole emitted by $\mathrm{SPS_A}$ by an emission of an electron from $\mathrm{SPS_B}$ is given by

$$\begin{aligned}
\frac{\mathcal{P}^{he}}{-e^2/\mathcal{T}} &= R_LT_L-4\gamma^2+2R_LT_RR_R+2T_LT_RR_R\left(1-\frac{4\sigma_A\sigma_B}{{\Delta t_d^{he}}^2+\left(\sigma_A+\sigma_B\right)^2}\right) \\
&+2\gamma\left(T_L-R_L\right)\left(T_R-R_R\right)\mathbb{R}\mathrm{e}\left\{e^{-i\Phi}\frac{2i\sigma_A}{\Delta\tau+2i\sigma_A}\frac{\Delta t_d^{he}-i\left(\sigma_A-\sigma_B\right)}{\Delta t_d^{he}-i\left(\sigma_A+\sigma_B\right)}\right\} \\
&-\left(2\gamma\mathbb{R}\mathrm{e}\left\{e^{-i\Phi}\frac{2i\sigma_A}{\Delta\tau+2i\sigma_A}\frac{\Delta t_d^{he}-i\left(\sigma_A-\sigma_B\right)}{\Delta t_d^{he}-i\left(\sigma_A+\sigma_B\right)}\right\}\right)^2.
\end{aligned}\tag{A.8}$$

And finally, for the noise in the case of the collision of two holes we find

$$
\begin{aligned}
\frac{\mathcal{P}^{hh}}{-e^2/\mathcal{T}} &= R_L T_L - 4\gamma^2 + 2T_L T_R R_R + 2R_L T_R R_R \left(1 - \frac{4\sigma_A \sigma_B}{\Delta t_u^{hh\,2} + (\sigma_A + \sigma_B)^2}\right) \\
&+ 2\gamma \left(T_L - R_L\right)\left(T_R - R_R\right) \mathbb{R}\mathrm{e}\left\{ e^{-i\Phi} \frac{2i\sigma_A}{\Delta\tau + 2i\sigma_A} \frac{\Delta t_u^{hh} + i\left(\sigma_A - \sigma_B\right)}{\Delta t_u^{hh} + i\left(\sigma_A + \sigma_B\right)} \right\} \\
&- \left(2\gamma \mathbb{R}\mathrm{e}\left\{ e^{-i\Phi} \frac{2i\sigma_A}{\Delta\tau + 2i\sigma_A} \frac{\Delta t_u^{hh} + i\left(\sigma_A - \sigma_B\right)}{\Delta t_u^{hh} + i\left(\sigma_A + \sigma_B\right)} \right\} \right)^2 . \qquad \text{(A.9)}
\end{aligned}
$$

B

OCCUPATION OF AN INTERACTING QUANTUM CAPACITOR

This appendix is devoted to check that the Hartree-Fock approximation realized in Chapter 4 (see Eq. (4.9)) is able to correctly describe Coulomb interactions. To this end we calculate the occupation of the capacitor, N_d, and show that it does not get doubly occupied immediately (as it would happen for a single degenerate energy level) but that it has a plateau for single occupancy $N_d = 1$ caused by Coulomb repulsion between electrons. The occupation is calculated self-consistently from Eq. (4.34).

For illustration, we consider our quantum conductor, as described in Fig. 4.1, and assume that there is only a single orbital ($\epsilon_{m\sigma} = \epsilon_{d\sigma}$). For simplicity we consider the static case, in absence of AC signal. We allow the presence of a small external magnetic field $\epsilon_{d\sigma} = \epsilon_d + \sigma\Delta_Z$ (Δ_Z the Zeeman energy) in order to break explicitly the spin degeneracy, i.e., $N_{d\sigma} \neq N_{d\bar{\sigma}}$. For a single orbital, since the exchange interaction is absent between electrons with same spins the Fock term disappears such that the dot's energy level can be simplified as

$$\widetilde{\epsilon}_{d\sigma} = \epsilon_d + \sigma\Delta_Z + 2E_C\langle d^{\dagger}_{\bar{\sigma}} d_{\bar{\sigma}}\rangle\,. \tag{B.1}$$

We envision the level is occupied by the spin σ electron with energy $\epsilon_{d\sigma}$. When another electron with opposite spin $\bar{\sigma}$ enters the level, its energy is increased by the charging energy $2E_C$. Therefore, as a function of the Fermi energy E_F the dot occupation then does not change continuously, but shows plateaus and discontinuous jumps. These jumps are the clear evidence of Coulomb blockade phenomenon. We illustrate how HF approximation captures charging effects by considering a single orbital quantum dot and plotting its total occupation N_d when the Fermi energy varies in Fig. B.1. The dot occupation shows a plateau of $N_d \approx 1$ in the Coulomb gap region, i.e., $\epsilon_d \lesssim E_F \lesssim \epsilon_d + 2E_C$. This result corroborates the fact that our HF description can reproduce charging effects and thus Coulomb blockade properly.

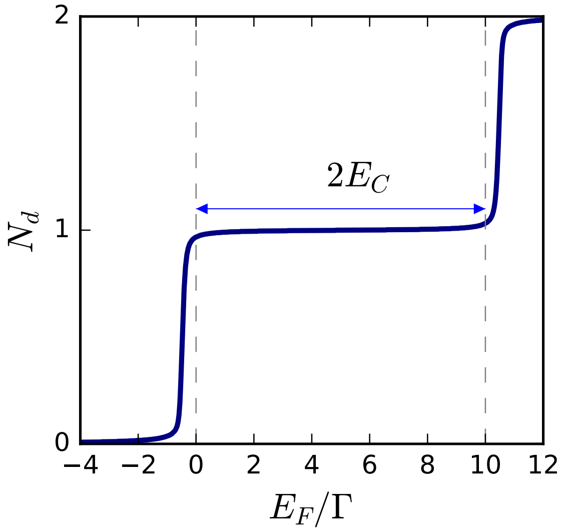

Figure B.1: Quantum dot occupation N_d versus the Fermi energy E_F for a single orbital dot in the Coulomb blockade regime. The dot's energy level is placed at $\epsilon_{d\sigma} = \epsilon_d + \sigma\Delta_Z$ with $\epsilon_d = 0$ and $\Delta_Z = 0.5\Gamma$. Rest of parameters: $2E_C = 10\Gamma$ and $k_B T = 0.04\Gamma$.

C

CAPACITANCES AND RESISTANCES

The complete expressions of the electrical and electrothermal capacitances, and resistances for the quantum capacitor of Chapter 4 are given in this appendix. We also check that the electrical resistance and capacitance are always positive whereas their electrothermal counterparts are not necessarily so.

C.1 ELECTRICAL CONDUCTANCE

The electrical conductance of the capacitor was derived in Ref. [19], see also Eq. (4.41), yielding:

$$g(\omega) = ie^2\omega \mathrm{Tr}\left\{\int \frac{d\epsilon}{2\pi}\mathcal{A}(\epsilon,\hbar\omega)\right\}. \tag{C.1}$$

where $\mathcal{A}(\epsilon,\hbar\omega)$ is defined in the main text, see Eq. (4.30). For low frequency driving we can approximate the conductance in terms of a characteristic capacitance and resistance as

$$g(\omega) = -i\omega C_g + \omega^2 C_g^2 R_g. \tag{C.2}$$

By expanding the expression in terms of the driving frequency ω we find:

$$\begin{aligned} g(\omega) =& -(ie^2)\int \frac{d\epsilon}{2\pi}(-\partial_\epsilon f(\epsilon))\mathrm{Tr}\left[G^{r,eq}_{\sigma,\sigma}(\epsilon)\Gamma G^{a,eq}_{\sigma,\sigma}(\epsilon)\right] \\ &+ \frac{e^2\hbar\omega^2}{2}\int \frac{d\epsilon}{2\pi}(-\partial_\epsilon f(\epsilon))\mathrm{Tr}\left[\left|G^{r,eq}_{\sigma,\sigma}(\epsilon)\Gamma G^{a,eq}_{\sigma,\sigma}(\epsilon)\right|^2\right]. \end{aligned} \tag{C.3}$$

Thus, taking the terms to first order in ω , we obtain the quantum capacitance

$$C_g = e^2\int \frac{d\epsilon}{2\pi}(-\partial_\epsilon f(\epsilon))\mathrm{Tr}\left[G^{r,eq}_{\sigma,\sigma}(\epsilon)\Gamma G^{a,eq}_{\sigma,\sigma}(\epsilon)\right], \tag{C.4}$$

and from the second order in ω terms we obtain the charge relaxation resistance:

$$R_g = \frac{h}{2e^2}\frac{\int d\epsilon(-\partial_\epsilon f(\epsilon))\mathrm{Tr}\left[\left|G^{r,eq}_{\sigma,\sigma}(\epsilon)\Gamma G^{a,eq}_{\sigma,\sigma}(\epsilon)\right|^2\right]}{\left(\int d\epsilon(-\partial_\epsilon f(\epsilon))\mathrm{Tr}\left[G^{r,eq}_{\sigma,\sigma}(\epsilon)\Gamma G^{a,eq}_{\sigma,\sigma}(\epsilon)\right]\right)^2}. \tag{C.5}$$

Both C_g and R_g are always positive, which can be seen from the equations since $(-\partial_\epsilon f(\epsilon)) > 0$ and $G^{r,eq}_{\sigma,\sigma}(\epsilon)\Gamma G^{a,eq}_{\sigma,\sigma}(\epsilon)$ is a density of states and thus positive as well.

C.2 ELECTROTHERMAL ADMITTANCE

Proceeding similarly to the electric case, we are able to obtain the electrothermal capacitance and resistance. We start from the full expression of the electrothermal admittance, as given by Eq. (4.44)

$$m(\omega) = ie\omega \mathrm{Tr}\left\{\int \frac{d\epsilon}{2\pi}\left(\frac{\hbar\omega}{2}+\epsilon\right)\mathcal{A}(\epsilon,\hbar\omega)\right\} \tag{C.6}$$

To obtain the RC electrothermal parameters we use a second order expansion in the AC-frequency on the electrothermal admittance:

$$m(\omega) = -i\omega C_{\mathcal{M}} + \omega^2 C_{\mathcal{M}}^2 R_{\mathcal{M}} \,. \tag{C.7}$$

By performing an expansion up to second order in the electrothermal admittance we obtain

$$\begin{aligned} m(\omega) =& - ie\omega \int \frac{d\epsilon}{2\pi}(\epsilon)(\partial_\epsilon f(\epsilon))\mathrm{Tr}\left[G^{r,eq}_{\sigma,\sigma}(\epsilon)\Gamma G^{a,eq}_{\sigma,\sigma}(\epsilon)\right] \\ &+ \frac{\hbar\omega^2}{2}\int \frac{d\epsilon}{2\pi}(\epsilon)(\partial_\epsilon f(\epsilon))\mathrm{Tr}\left[\left|G^{r,eq}_{\sigma,\sigma}(\epsilon)\Gamma G^{a,eq}_{\sigma,\sigma}(\epsilon)\right|^2\right] . \end{aligned} \tag{C.8}$$

The first order, in ω, term clearly identifies the electrothermal capacitance as

$$C_{\mathcal{M}} = e\int \frac{d\epsilon}{2\pi}(\epsilon)(\partial_\epsilon f(\epsilon))\mathrm{Tr}\left[G^{r,eq}_{\sigma,\sigma}(\epsilon)\Gamma G^{a,eq}_{\sigma,\sigma}(\epsilon)\right] , \tag{C.9}$$

and the second order term leads us to the electrothermal resistance

$$R_{\mathcal{M}} = \frac{h}{2e}\frac{\int d\epsilon(\epsilon)(\partial_\epsilon f(\epsilon))\mathrm{Tr}\left[\left|G^{r,eq}_{\sigma,\sigma}(\epsilon)\Gamma G^{a,eq}_{\sigma,\sigma}(\epsilon)\right|^2\right]}{\left(\int d\epsilon(\epsilon)(\partial_\epsilon f(\epsilon))\mathrm{Tr}\left[G^{r,eq}_{\sigma,\sigma}(\epsilon)\Gamma G^{a,eq}_{\sigma,\sigma}(\epsilon)\right]\right)^2}. \tag{C.10}$$

These two quantities, opposed to what happened for C_g and R_g, are not always positive but instead their sign can change due to the ϵ factor in the integrals. Despite that, since the factor changing their sign is the same for both quantities, they change sign simultaneously which means that their product $C_{\mathcal{M}}R_{\mathcal{M}}$, i.e. the RC time, remains positive.

BIBLIOGRAPHY

[1] G. E. Moore, "Cramming more components onto integrated circuits, Reprinted from Electronics, volume 38, number 8, April 19, 1965, pp.114 ff.," IEEE Solid-State Circuits Society Newsletter **11**, 33–35 (2006).

[2] J. Bardeen and W. H. Brattain, "The Transistor, A Semi-Conductor Triode," Physical Review **74**, 230–231 (1948).

[3] S. B. Desai, S. R. Madhvapathy, A. B. Sachid, J. P. Llinas, Q. Wang, G. H. Ahn, G. Pitner, M. J. Kim, J. Bokor, C. Hu, H.-S. P. Wong, and A. Javey, "MoS2 transistors with 1-nanometer gate lengths," Science **354**, 99–102 (2016).

[4] D. K. Ferry, S. M. Goodnick, and J. Bird, *Transport in Nanostructures* (Cambridge University Press, 2009).

[5] Thomas Ihn, *Semiconductor Nanostructures* (Oxford University Press, 2011).

[6] N. Ofek, A. Bid, M. Heiblum, A. Stern, V. Umansky, and D. Mahalu, "Role of interactions in an electronic Fabry-Perot interferometer operating in the quantum Hall effect regime," Proceedings of the National Academy of Sciences **107**, 5276–5281 (2010).

[7] K. v. Klitzing, G. Dorda, and M. Pepper, "New Method for High-Accuracy Determination of the Fine-Structure Constant Based on Quantized Hall Resistance," Physical Review Letters **45**, 494–497 (1980).

[8] V. Mourik, K. Zuo, S. M. Frolov, S. R. Plissard, E. P.A. M. Bakkers, and L. P. Kouwenhoven, "Signatures of Majorana Fermions in Hybrid Superconductor-Semiconductor Nanowire Devices," Science **336**, 1003–1007 (2012).

[9] M. Kaempgen, C. K. Chan, J. Ma, Y. Cui, and G. Gruner, "Printable Thin Film Supercapacitors Using Single-Walled Carbon Nanotubes," Nano Letters **9**, 1872–1876 (2009).

[10] S. Datta, *Quantum Transport : Atom to Transistor* (2005), p. 419.

[11] Y. V. Nazarov and Y Blanter, "Quantum Transport: Introduction to Nanoscience," Cambridge Univ Pr, 581 (2009).

[12] C. W. J. Beenakker, "Theory of Coulomb-blockade oscillations in the conductance of a quantum dot," Physical Review B **44**, 1646–1656 (1991).

[13] R. C. Ashoori, "Electrons in artificial atoms," Nature **379**, 413–419 (1996).

[14] T. Oosterkamp, *Artificial Atoms and Molecules: on manibody effects and coherence on semiconductor quantum dots*, 1999.

[15] R. Hanson, L. P. Kouwenhoven, J. R. Petta, S. Tarucha, and L. M. K. Vandersypen, "Spins in few-electron quantum dots," Reviews of Modern Physics **79**, 1217–1265 (2007).

[16] D. Goldhaber-Gordon, H. Shtrikman, D. Mahalu, D. Abusch-Magder, U. Meirav, and M. A. Kastner, "Kondo effect in a single-electron transistor," Nature **391**, 156–159 (1998).

[17] J. Gabelli, G. Fève, J.-M. Berroir, B. Plaçais, A. Cavanna, B. Etienne, Y. Jin, and C. Glattli, "Violation of Kirchhoff's Laws for a Coherent RC Circuit," Science **313**, 499–502 (2006).

[18] M. Büttiker, H. Thomas, and A. Prêtre, "Mesoscopic capacitors," Physics Letters A **180**, 364–369 (1993).

[19] S. E. Nigg, R. López, and M. Büttiker, "Mesoscopic Charge Relaxation," Physical Review Letters **97**, 206804 (2006).

[20] G. Fève, A. Mahé, J.-M. Berroir, T. Kontos, B. Plaçais, D. C. Glattli, A. Cavanna, B. Etienne, and Y. Jin, "An On-Demand Coherent Single-Electron Source," Science **316**, 1169–1172 (2007).

[21] T. Jonckheere, J. Rech, C. Wahl, and T. Martin, "Electron and hole Hong-Ou-Mandel interferometry," Physical Review B **86**, 125425 (2012).

[22] E. Bocquillon, F. D. Parmentier, C. Grenier, J.-M. Berroir, P. Degiovanni, D. C. Glattli, B. Plaçais, A. Cavanna, Y. Jin, and G. Fève, "Electron Quantum Optics: Partitioning Electrons One by One," Physical Review Letters **108**, 196803 (2012).

[23] L. P. Kouwenhoven, T. H. Oosterkamp, M. W. Danoesastro, M. Eto, D. G. Austing, T. Honda, and S. Tarucha, "Excitation spectra of circular, few-electron quantum dots," Science **278**, 1788–1792 (1997).

[24] K. I. Bolotin, F. Kuemmeth, A. N. Pasupathy, and D. C. Ralph, "Metal-nanoparticle single-electron transistors fabricated using electromigration," Applied Physics Letters **84**, 3154–3156 (2004).

[25] F. Kuemmeth, K. I. Bolotin, S. F. Shi, and D. C. Ralph, "Measurement of discrete energy-level spectra in individual chemically synthesized gold nanoparticles," Nano Letters **8**, 4506–4512 (2008).

[26] Y. Ji, Y. Chung, D Sprinzak, M. Heiblum, D Mahalu, and H. Shtrikman, "An electronic Mach–Zehnder interferometer," Nature **422**, 415–418 (2003).

[27] P. Roulleau, F. Portier, D. C. Glattli, P. Roche, A. Cavanna, G. Faini, U. Gennser, and D. Mailly, "Finite bias visibility of the electronic Mach-Zehnder interferometer," Physical Review B **76**, 161309 (2007).

[28] L. V. Litvin, H.-P. Tranitz, W. Wegscheider, and C. Strunk, "Decoherence and single electron charging in an electronic Mach-Zehnder interferometer," Physical Review B **75**, 033315 (2007).

[29] L. W. Molenkamp, T. Gravier, H. van Houten, O. J. A. Buijk, M. a. a. Mabesoone, and C. T. Foxon, "Peltier coefficient and thermal conductance of a quantum point contact," Physical Review Letters **68**, 3765–3768 (1992).

[30] A. A. M. Staring, L. W. Molenkamp, B. W. Alphenaar, H. van Houten, O. J. A. Buyk, M. A. A. Mabesoone, C. W. J. Beenakker, and C. T. Foxon, "Coulomb-Blockade Oscillations in the Thermopower of a Quantum Dot," Europhysics Letters (EPL) **22**, 57–62 (1993).

[31] T. Ruokola and T. Ojanen, "Theory of single-electron heat engines coupled to electromagnetic environments," Physical Review B **86**, 035454 (2012).

[32] K. Saito, G. Benenti, G. Casati, and T. Prosen, "Thermopower with broken time-reversal symmetry," Physical Review B **84**, 201306 (2011).

[33] D. Sánchez and L. Serra, "Thermoelectric transport of mesoscopic conductors coupled to voltage and thermal probes," Physical Review B **84**, 201307 (2011).

[34] R. Sánchez and M. Büttiker, "Optimal energy quanta to current conversion," Physical Review B **83**, 085428 (2011).

[35] R. Sánchez and M. Büttiker, "Detection of single-electron heat transfer statistics," EPL (Europhysics Letters) **100**, 47008 (2012).

[36] B. Sothmann, R. Sánchez, and A. N. Jordan, "Thermoelectric energy harvesting with quantum dots," Nanotechnology **26**, 032001 (2015).

[37] H. J. Goldsmid, *Introduction to Thermoelectricity*, Vol. 121, Springer Series in Materials Science (Springer Berlin Heidelberg, Berlin, Heidelberg, 2010).

[38] L. Onsager, "Reciprocal Relations in Irreversible Processes. I.," Physical Review **37**, 405–426 (1931).

[39] H. B. G. Casimir, "On Onsager's Principle of Microscopic Reversibility," Reviews of Modern Physics **17**, 343–350 (1945).

[40] M Buttiker, "Capacitance, admittance, and rectification properties of small conductors," Journal of Physics: Condensed Matter **5**, 9361–9378 (1993).

[41] M. Moskalets, *Scattering matrix approach to non-stationary quantum transport* (2011).

[42] M. Moskalets and M. Büttiker, "Floquet scattering theory of quantum pumps," Physical Review B **66**, 205320 (2002).

[43] M. Moskalets and M. Büttiker, "Dissipation and noise in adiabatic quantum pumps," Physical Review B **66**, 035306 (2002).

[44] C. Altimiras, H. le Sueur, U. Gennser, A. Cavanna, D. Mailly, and F. Pierre, "Non-equilibrium edge-channel spectroscopy in the integer quantum Hall regime," Nature Physics **6**, 34–39 (2010).

[45] M. Büttiker, "Scattering theory of current and intensity noise correlations in conductors and wave guides," Physical Review B **46**, 12485–12507 (1992).

[46] M. Moskalets and M. Büttiker, "Time-resolved noise of adiabatic quantum pumps," Physical Review B **75**, 035315 (2007).

[47] G. D. Mahan, *Many-Particle Physics* (Springer US, Boston, MA, 2000).

[48] A.-P. Jauho, N. S. Wingreen, and Y. Meir, "Time-dependent transport in interacting and noninteracting resonant-tunneling systems," Physical Review B **50**, 5528–5544 (1994).

[49] H. Haug and A.-P. Jauho, *Quantum kinetics in transport and optics of semiconductors* (2008), p. 360.

[50] H. Grabert, G.-L. Ingold, M. H. Devoret, D. Estève, H. Pothier, and C. Urbina, "Single electron tunneling rates in multijunction circuits," Zeitschrift für Physik B Condensed Matter **84**, 143–155 (1991).

[51] G.-L. Ingold and Y. V. Nazarov, "Charge Tunneling Rates in Ultrasmall Junctions," in , edited by H. Grabert and M. H. Devoret (Springer US, Boston, MA, 1992), pp. 21–107.

[52] J. P. Pekola and F. W. J. Hekking, "Normal-Metal-Superconductor Tunnel Junction as a Brownian Refrigerator," Physical Review Letters **98**, 210604 (2007).

[53] J. Splettstoesser, S. Ol'khovskaya, M. Moskalets, and M. Büttiker, "Electron counting with a two-particle emitter," Physical Review B **78**, 205110 (2008).

[54] L. S. Levitov, H. Lee, and G. B. Lesovik, "Electron counting statistics and coherent states of electric current," Journal of Mathematical Physics **37**, 4845–4866 (1996).

[55] D. A. Ivanov, H. W. Lee, and L. S. Levitov, "Coherent states of alternating current," Physical Review B **56**, 6839–6850 (1997).

[56] J. Dubois, T. Jullien, F. Portier, P. Roche, A. Cavanna, Y. Jin, W. Wegscheider, P. Roulleau, and D. C. Glattli, "Minimal-excitation states for electron quantum optics using levitons," Nature **502**, 659–663 (2013).

[57] M. Moskalets and M. Büttiker, "Dynamic scattering channels of a double barrier structure," Physical Review B **78**, 035301 (2008).

[58] R. P. G. McNeil, M. Kataoka, C. J. B. Ford, C. H. W. Barnes, D. Anderson, G. A. C. Jones, I. Farrer, and D. A. Ritchie, "On-demand single-electron transfer between distant quantum dots," Nature **477**, 439–442 (2011).

[59] S. Hermelin, S. Takada, M. Yamamoto, S. Tarucha, A. D. Wieck, L. Saminadayar, C. Bäuerle, and T. Meunier, "Electrons surfing on a sound wave as a platform for quantum optics with flying electrons," Nature **477**, 435–438 (2011).

[60] J. Wanner, C. Gorini, P. Schwab, and U. Eckern, "Driving spin and charge in quantum wells by surface acoustic waves," Advanced Material Interfaces **1**, 1–8 (2014).

[61] M. D. Blumenthal, B. Kaestner, L. Li, S. Giblin, T. J.B. M. Janssen, M. Pepper, D. Anderson, G. Jones, and D. A. Ritchie, "Gigahertz quantized charge pumping," Nature Physics **3**, 343–347 (2007).

[62] B. Kaestner, V. Kashcheyevs, G Hein, K Pierz, U Siegner, and H. W. Schumacher, "Robust single-parameter quantized charge pumping," Applied Physics Letters **192106**, 10–13 (2011).

[63] N. Ubbelohde, F. Hohls, V. Kashcheyevs, T. Wagner, L. Fricke, B. Kästner, K. Pierz, H. W. Schumacher, and R. J. Haug, "Partitioning of on-demand electron pairs," Nature Nanotechnology **10**, 46–49 (2014).

[64] J. Keeling, I. Klich, and L. S. Levitov, "Minimal excitation states of electrons in one-dimensional wires," Physical Review Letters **97**, 116403 (2006).

[65] J. Keeling, A. V. Shytov, and L. S. Levitov, "Coherent particle transfer in an on-demand single-electron source," Physical Review Letters **101**, 196404 (2008).

[66] S. Ol'khovskaya, J. Splettstoesser, M. Moskalets, and M. Büttiker, "Shot Noise of a Mesoscopic Two-Particle Collider," Physical Review Letters **101**, 166802 (2008).

[67] J. Splettstoesser, M. Moskalets, and M. Büttiker, "Two-particle nonlocal Aharonov-Bohm effect from two single-particle emitters," Physical Review Letters **103**, 76804 (2009).

[68] M. Moskalets and M. Büttiker, "Heat production and current noise for single- and double-cavity quantum capacitors," Physical Review B **80**, 081302 (2009).

[69] A. Mahé, F. D. Parmentier, E. Bocquillon, J.-M. Berroir, D. C. Glattli, T. Kontos, B. Plaçais, G. Fève, A. Cavanna, and Y. Jin, "Current correlations of an on-demand single-electron emitter," Physical Review B **82**, 201309 (2010).

[70] S. Juergens, J. Splettstoesser, and M. Moskalets, "Single-particle interference versus two-particle collisions," EPL (Europhysics Letters) **96**, 37011 (2011).

[71] M. Moskalets and M. Büttiker, "Spectroscopy of electron flows with single- and two-particle emitters," Physical Review B **83**, 035316 (2011).

[72] G. Haack, M. Moskalets, J. Splettstoesser, and M. Büttiker, "Coherence of single-electron sources from Mach-Zehnder interferometry," Physical Review B **84**, 081303 (2011).

[73] E. Bocquillon, V. Freulon, J.-M. Berroir, P. Degiovanni, B. Plaçais, A. Cavanna, Y. Jin, and G. Feve, "Coherence and Indistinguishability of Single Electrons Emitted by Independent Sources," Science **339**, 1054–1057 (2013).

[74] G. Haack, M. Moskalets, and M. Büttiker, "Glauber coherence of single-electron sources," Physical Review B **87**, 201302 (2013).

[75] D. Ferraro, A. Feller, A. Ghibaudo, E. Thibierge, E. Bocquillon, G. Fève, C. Grenier, and P. Degiovanni, "Wigner function approach to single electron coherence in quantum Hall edge channels," Physical Review B **88**, 205303 (2013).

[76] P.-A. Huynh, F. Portier, H. le Sueur, G. Faini, U. Gennser, D. Mailly, F Pierre, W. Wegscheider, and P. Roche, "Quantum Coherence Engineering in the Integer Quantum Hall Regime," Physical Review Letters **108**, 256802 (2012).

[77] E. Iyoda, T. Kato, K. Koshino, and T. Martin, "Dephasing in single-electron generation due to environmental noise probed by Hong-Ou-Mandel interferometry," Physical Review B **89**, 205318 (2014).

[78] B. Gaury and X. Waintal, "Dynamical control of interference using voltage pulses in the quantum regime," Nature Communications **5**, 1–11 (2014).

[79] E. Weisz, H. K. Choi, I. Sivan, M. Heiblum, Y. Gefen, D. Mahalu, and V. Umansky, "An electronic quantum eraser," Science **344**, 1363–1366 (2014).

[80] M. Moskalets, "Fermi-sea correlations and a single-electron time-bin qubit," Physical Review B **90**, 155453 (2014).

[81] T. Bautze, C. Süssmeier, S. Takada, C. Groth, T. Meunier, M. Yamamoto, S. Tarucha, X. Waintal, and C. Bäuerle, "Theoretical, numerical, and experimental study of a flying qubit electronic interferometer," Physical Review B **89**, 125432 (2014).

[82] A. A. Vyshnevyy, A. V. Lebedev, G. B. Lesovik, and G. Blatter, "Two-particle entanglement in capacitively coupled Mach-Zehnder interferometers," Physical Review B **87**, 165302 (2013).

[83] A. A. Vyshnevyy, G. B. Lesovik, T. Jonckheere, and T. Martin, "Setup of three Mach-Zehnder interferometers for production and observation of Greenberger-Horne-Zeilinger entanglement of electrons," Physical Review B **87**, 165417 (2013).

[84] P. P. Hofer and C. Flindt, “Mach-Zehnder interferometry with periodic voltage pulses,” Physical Review B **90**, 235416 (2014).

[85] P. N. Butcher, “Thermal and electrical transport formalism for electronic microstructures with many terminals,” Journal of Physics: Condensed Matter **2**, 4869–4878 (1990).

[86] Y. M. Blanter and M. Büttiker, “Shot Noise in Mesoscopic Conductors,” Physics Reports **336**, 1 (1999).

[87] D. Ferraro, B. Roussel, C. Cabart, E. Thibierge, G. Fève, C. Grenier, and P. Degiovanni, “Real-Time Decoherence of Landau and Levitov Quasiparticles in Quantum Hall Edge Channels,” Physical Review Letters **113**, 166403 (2014).

[88] C. Wahl, J. Rech, T. Jonckheere, and T. Martin, “Interactions and charge fractionalization in an electronic Hong-Ou-mandel interferometer,” Physical Review Letters **112**, 46802 (2014).

[89] J. T. Chalker, Y. Gefen, and M. Y. Veillette, “Decoherence and interactions in an electronic Mach-Zehnder interferometer,” Physical Review B **76**, 085320 (2007).

[90] C. Neuenhahn and F. Marquardt, “Dephasing by electron-electron interactions in a ballistic Mach-Zehnder interferometer,” New Journal of Physics **10**, 115018 (2008).

[91] P. Roulleau, F. Portier, P. Roche, A. Cavanna, G. Faini, U. Gennser, and D. Mailly, “Direct measurement of the coherence length of edge states in the integer quantum hall regime,” Physical Review Letters **100**, 126802 (2008).

[92] P. Roulleau, F. Portier, P. Roche, A. Cavanna, G. Faini, U. Gennser, and D. Mailly, “Tuning decoherence with a voltage probe,” Physical Review Letters **102**, 236802 (2009).

[93] E. Bieri, M. Weiss, O. Göktas, M. Hauser, C. Schönenberger, and S. Oberholzer, “Finite-bias visibility dependence in an electronic Mach-Zehnder interferometer,” Physical Review B **79**, 245324 (2009).

[94] D. Sergi, “Energy transport and fluctuations in small conductors,” Physical Review B **83**, 033401 (2011).

[95] F. Battista, M. Moskalets, M Albert, and P Samuelsson, “Quantum Heat Fluctuations of Single-Particle Sources,” Physical Review Letters **110**, 126602 (2013).

[96] M. F. Ludovico, J. S. Lim, M. Moskalets, L. Arrachea, and D. Sánchez, “Dynamical energy transfer in ac-driven quantum systems,” Physical Review B **89**, 161306 (2014).

[97] M. Buttiker, “Symmetry of electrical conduction,” IBM Journal of Research and Development **32**, 317–334 (1988).

[98] F. Marquardt and C. Bruder, “Influence of Dephasing on Shot Noise in an Electronic Mach-Zehnder Interferometer,” Physical Review Letters **92**, 056805 (2004).

[99] F. Marquardt and C. Bruder, “Effects of dephasing on shot noise in an electronic Mach-Zehnder interferometer,” Physical Review B **70**, 125305 (2004).

[100] Y. Aharonov, S. Popescu, D. Rohrlich, and P. Skrzypczyk, “Quantum cheshire cats,” New Journal of Physics **15**, 113015 (2013).

[101] T. Denkmayr, H. Geppert, S. Sponar, H. Lemmel, A. Matzkin, J. Tollaksen, and Y. Hasegawa, “Observation of a quantum Cheshire Cat in a matter-wave interferometer experiment,” Nature Communications **5**, 1–7 (2014).

[102] R. Corrêa, M. F. Santos, C. H. Monken, and P. L. Saldanha, “Quantum Cheshire Cat as simple quantum interference,” New Journal of Physics **17**, 053042 (2015).

[103] W. M. Stuckey, M. Silberstein, and T. McDevitt, “Concerning Quadratic Interaction in the Quantum Cheshire Cat Experiment,” arXiv:1410.1522 (2014).

[104] F. D. Parmentier, E. Bocquillon, J.-M. Berroir, D. C. Glattli, B. Plaçais, G. Fève, M. Albert, C. Flindt, and M. Büttiker, “Current noise spectrum of a single-particle emitter: Theory and experiment,” Physical Review B **85**, 165438 (2012).

[105] F. Giazotto and M. J. Martínez-Pérez, “The Josephson heat interferometer,” Nature **492**, 401–405 (2012).

[106] S. Jezouin, F. D. Parmentier, A. Anthore, U. Gennser, A. Cavanna, Y. Jin, and F. Pierre, “Quantum Limit of Heat Flow Across a Single Electronic Channel,” Science **342**, 601–604 (2013).

[107] C. W. Chang, D. Okawa, A. Majumdar, and A. Zettl, “Solid-State Thermal Rectifier,” Science **314**, 1121–1124 (2006).

[108] W. Lee, K. Kim, W. Jeong, L. A. Zotti, F. Pauly, J. C. Cuevas, and P. Reddy, “Heat dissipation in atomic-scale junctions,” Nature **498**, 209–212 (2013).

[109] R. Maynard and E. Akkermans, “Thermal conductance and giant fluctuations in one-dimensional disordered systems,” Physical Review B **32**, 5440–5442 (1985).

[110] L. D. Hicks and M. S. Dresselhaus, “Thermoelectric figure of merit of a one-dimensional conductor,” Physical Review B **47**, 16631–16634 (1993).

[111] L. E. Bell, “Cooling, heating, generating power, and recovering waste heat with thermoelectric systems.,” Science **321**, 1457–1461 (2008).

[112] Y. Dubi and M. Di Ventra, “Colloquium : Heat flow and thermoelectricity in atomic and molecular junctions,” Reviews of Modern Physics **83**, 131–155 (2011).

[113] P. Rodgers, “Nanomaterials: Silicon goes thermoelectric,” Nature Nanotechnology **3**, 76–76 (2008).

[114] J.-P. Brantut, C. Grenier, J. Meineke, D. Stadler, S. Krinner, C. Kollath, T. Esslinger, and A. Georges, “A Thermoelectric Heat Engine with Ultracold Atoms,” Science **342**, 713–715 (2013).

[115] Y. Kim, W. Jeong, K. Kim, W. Lee, and P. Reddy, “Electrostatic control of thermoelectricity in molecular junctions,” Nature Nanotechnology **9**, 881–885 (2014).

[116] M. Büttiker, A. Prêtre, and H. Thomas, “Dynamic conductance and the scattering matrix of small conductors,” Physical Review Letters **70**, 4114–4117 (1993).

[117] Y. Dovzhenko, J. Stehlik, K. D. Petersson, J. R. Petta, H. Lu, and A. C. Gossard, “Nonadiabatic quantum control of a semiconductor charge qubit,” Physical Review B **84**, 161302 (2011).

[118] G. Cao, H.-O. Li, T. Tu, L. Wang, C. Zhou, M. Xiao, G.-C. Guo, H.-W. Jiang, and G.-P. Guo, "Ultrafast universal quantum control of a quantum-dot charge qubit using Landau–Zener–Stückelberg interference," Nature Communications **4**, 1401 (2013).

[119] W. Lu, Z. Ji, L. Pfeiffer, K. W. West, and A. J. Rimberg, "Real-time detection of electron tunnelling in a quantum dot," Nature **423**, 422–425 (2003).

[120] S. Gustavsson, R. Leturcq, T. Ihn, K. Ensslin, and A. C. Gossard, "Electrons in quantum dots: One by one," Journal of Applied Physics **105**, 122401 (2009).

[121] G. Rosselló, F. Battista, M. Moskalets, and J. Splettstoesser, "Interference and multiparticle effects in a Mach-Zehnder interferometer with single-particle sources," Phys. Rev. B **91**, 115438 (2015).

[122] T. Jullien, P. Roulleau, B. Roche, A. Cavanna, Y. Jin, and D. C. Glattli, "Quantum tomography of an electron," Nature **514**, 603–607 (2014).

[123] J. Gabelli, G. Fève, T. Kontos, J.-M. Berroir, B. Placais, D. C. Glattli, B. Etienne, Y. Jin, and M. Büttiker, "Relaxation Time of a Chiral Quantum R-L Circuit," Physical Review Letters **98**, 166806 (2007).

[124] M. R. Delbecq, V. Schmitt, F. D. Parmentier, N. Roch, J. J. Viennot, G. Fève, B. Huard, C. Mora, A. Cottet, and T. Kontos, "Coupling a Quantum Dot, Fermionic Leads, and a Microwave Cavity on a Chip," Physical Review Letters **107**, 256804 (2011).

[125] Y. Fu and S. C. Dudley, "Quantum inductance within linear response theory," Physical Review Letters **70**, 65–68 (1993).

[126] T. Christen and M. Büttiker, "Low Frequency Admittance of a Quantum Point Contact," Physical Review Letters **77**, 143–146 (1996).

[127] T. Christen and M. Büttiker, "Low-frequency admittance of quantized Hall conductors," Physical Review B **53**, 2064–2072 (1996).

[128] a. Prêtre, H. Thomas, and M. Büttiker, "Dynamic admittance of mesoscopic conductors: Discrete-potential model," Physical Review B **54**, 8130–8143 (1996).

[129] M. Büttiker and T Christen, "Admittance and Nonlinear Transport in Quantum Wires, Point Contacts, and Resonant Tunneling Barriers," in *Mesoscopic electron transport*, edited by L. L. Sohn, L. P. Kouwenhoven, and G. Schön (Springer Netherlands, Dordrecht, 1997), pp. 259–289.

[130] M. Lee, R. López, M.-S. Choi, T. Jonckheere, and T. Martin, "Effect of many-body correlations on mesoscopic charge relaxation," Physical Review B **83**, 201304 (2011).

[131] C. Mora and K. Le Hur, "Universal resistances of the quantum resistance–capacitance circuit," Nature Physics **6**, 697–701 (2010).

[132] J. Gabelli, G. Fève, J.-M. Berroir, and B Plaçais, "A coherent RC circuit," Reports on Progress in Physics **75**, 126504 (2012).

[133] M. Hashisaka, K. Washio, H. Kamata, K. Muraki, and T. Fujisawa, "Distributed electrochemical capacitance evidenced in high-frequency admittance measurements on a quantum Hall device," Physical Review B **85**, 155424 (2012).

[134] S. J. Chorley, J. Wabnig, Z. V. Penfold-Fitch, K. D. Petersson, J. Frake, C. G. Smith, and M. R. Buitelaar, "Measuring the Complex Admittance of a Carbon Nanotube Double Quantum Dot," Physical Review Letters **108**, 036802 (2012).

[135] J. Basset, H. Bouchiat, and R. Deblock, "High-frequency quantum admittance and noise measurement with an on-chip resonant circuit," Physical Review B **85**, 085435 (2012).

[136] T. Frey, P. J. Leek, M. Beck, J. Faist, A. Wallraff, K. Ensslin, T. Ihn, and M. Büttiker, "Quantum dot admittance probed at microwave frequencies with an on-chip resonator," Physical Review B **86**, 115303 (2012).

[137] L. Arrachea, M. Moskalets, and L. Martin-Moreno, "Heat production and energy balance in nanoscale engines driven by time-dependent fields," Physical Review B **75**, 245420 (2007).

[138] J. S. Lim, R. López, and D. Sánchez, "Dynamic thermoelectric and heat transport in mesoscopic capacitors," Physical Review B **88**, 201304 (2013).

[139] B. Sothmann, R. Sánchez, A. N. Jordan, and M. Büttiker, "Powerful energy harvester based on resonant-tunneling quantum wells," New Journal of Physics **15**, 095021 (2013).

[140] J. V. Koski, T. Sagawa, O.-P. Saira, Y. Yoon, A. Kutvonen, P. Solinas, M. Möttönen, T. Ala-Nissilä, and J. P. Pekola, "Distribution of entropy production in a single-electron box," Nature Physics **9**, 644–648 (2013).

[141] M. Bockrath, "Single-Electron Transport in Ropes of Carbon Nanotubes," Science **275**, 1922–1925 (1997).

[142] E. D. Minot, Y. Yaish, V. Sazonova, and P. L. McEuen, "Determination of electron orbital magnetic moments in carbon nanotubes," Nature **428**, 536–539 (2004).

[143] P. Brune, C Bruder, and H Schoeller, "Photon-assisted transport through ultrasmall quantum dots: Influence of intradot transitions," Physical Review B **56**, 4730–4736 (1997).

[144] L.-A. Wu and D. Segal, "Energy flux operator, current conservation and the formal Fourier's law," Journal of Physics A: Mathematical and Theoretical **42**, 025302 (2009).

[145] L. Onsager, "Reciprocal relations in irreversible processes. II.," Physical Review **37**, 405–426 (1931).

[146] F. Giazotto, T. T. Heikkilä, A. Luukanen, A. M. Savin, and J. P. Pekola, "Opportunities for mesoscopics in thermometry and refrigeration: Physics and applications," Reviews of Modern Physics **78**, 217–274 (2006).

[147] G. Benenti, G. Casati, K. Saito, and R. S. Whitney, "Fundamental aspects of steady-state conversion of heat to work at the nanoscale," Physics Reports **694**, 1–124 (2017).

[148] J. P. Pekola, "Towards quantum thermodynamics in electronic circuits," Nature Physics **11**, 118–123 (2015).

[149] R. Sánchez, B. Sothmann, and A. N. Jordan, "Heat diode and engine based on quantum Hall edge states," New Journal of Physics **17**, 075006 (2015).

[150] P. P. Hofer and B. Sothmann, "Quantum heat engines based on electronic Mach-Zehnder interferometers," Physical Review B **91**, 195406 (2015).

[151] P. P. Hofer, J.-R. Souquet, and A. A. Clerk, "Quantum heat engine based on photon-assisted Cooper pair tunneling," Physical Review B **93**, 041418 (2016).

[152] G Marchegiani, P Virtanen, F Giazotto, and M Campisi, "Self-Oscillating Josephson Quantum Heat Engine," Physical Review Applied **6**, 054014 (2016).

[153] J. Rossnagel, S. T. Dawkins, K. N. Tolazzi, O. Abah, E. Lutz, F. Schmidt-Kaler, and K. Singer, "A single-atom heat engine," Science **352**, 325–329 (2016).

[154] B Karimi and J. P. Pekola, "Otto refrigerator based on a superconducting qubit: Classical and quantum performance," Physical Review B **94**, 184503 (2016).

[155] J Meair, J. P. Bergfield, C. A. Stafford, and P. Jacquod, "Local temperature of out-of-equilibrium quantum electron systems," Physical Review B **90**, 035407 (2014).

[156] A. N. Jordan, B. Sothmann, R. Sánchez, and M. Büttiker, "Powerful and efficient energy harvester with resonant-tunneling quantum dots," Physical Review B **87**, 075312 (2013).

[157] S Donsa, S. Andergassen, and K Held, "Double quantum dot as a minimal thermoelectric generator," Physical Review B **89**, 125103 (2014).

[158] B. Roche, P Roulleau, T Jullien, Y Jompol, I Farrer, D. Ritchie, and D. Glattli, "Harvesting dissipated energy with a mesoscopic ratchet," Nature Communications **6**, 6738 (2015).

[159] F. Hartmann, P. Pfeffer, S. Höfling, M. Kamp, and L. Worschech, "Voltage Fluctuation to Current Converter with Coulomb-Coupled Quantum Dots," Physical Review Letters **114**, 146805 (2015).

[160] M Nahum, T. M. Eiles, and J. M. Martinis, "Electronic microrefrigerator based on a normal-insulator-superconductor tunnel junction," Applied Physics Letters **65**, 3123–3125 (1994).

[161] M. M. Leivo, J. P. Pekola, and D. V. Averin, "Efficient Peltier refrigeration by a pair of normal metal/insulator/superconductor junctions," Applied Physics Letters **68**, 1996–1998 (1996).

[162] J. R. Prance, C. G. Smith, J. P. Griffiths, S. J. Chorley, D Anderson, G. A. C. Jones, I Farrer, and D. A. Ritchie, "Electronic Refrigeration of a Two-Dimensional Electron Gas," Physical Review Letters **102**, 146602 (2009).

[163] J. V. Koski, A. Kutvonen, I. M. Khaymovich, T. Ala-Nissila, and J. P. Pekola, "On-Chip Maxwell's Demon as an Information-Powered Refrigerator," Physical Review Letters **115**, 260602 (2015).

[164] S. Kafanov, A. Kemppinen, Y. A. Pashkin, M. Meschke, J. S. Tsai, and J. P. Pekola, "Single-Electronic Radio-Frequency Refrigerator," Physical Review Letters **103**, 120801 (2009).

[165] T. Ruokola and T. Ojanen, "Single-electron heat diode: Asymmetric heat transport between electronic reservoirs through Coulomb islands," Physical Review B **83**, 241404 (2011).

[166] D. Segal, “Single Mode Heat Rectifier: Controlling Energy Flow Between Electronic Conductors,” Physical Review Letters **100**, 105901 (2008).

[167] T. Ruokola, T. Ojanen, and A.-P. Jauho, “Thermal rectification in nonlinear quantum circuits,” Physical Review B **79**, 144306 (2009).

[168] H. Thierschmann, F. Arnold, M Mittermüller, L Maier, C Heyn, W Hansen, H Buhmann, and L. W. Molenkamp, “Thermal gating of charge currents with Coulomb coupled quantum dots,” New Journal of Physics **17**, 113003 (2015).

[169] M. A. Sierra and D. Sánchez, “Nonlinear Heat Conduction in Coulomb-blockaded Quantum Dots,” Materials Today: Proceedings **2**, 483–490 (2015).

[170] K. Joulain, J. Drevillon, Y. Ezzahri, and J. Ordonez-Miranda, “Quantum Thermal Transistor,” Physical Review Letters **116**, 200601 (2016).

[171] R. Sánchez, H. Thierschmann, and L. W. Molenkamp, “All-thermal transistor based on stochastic switching,” Physical Review B **95**, 241401 (2017).

[172] O. Entin-Wohlman, Y. Imry, and A. Aharony, “Three-terminal thermoelectric transport through a molecular junction,” Physical Review B **82**, 115314 (2010).

[173] J Matthews, D. Sánchez, M Larsson, and H Linke, “Thermally driven ballistic rectifier,” Physical Review B **85**, 205309 (2012).

[174] R. Sánchez, B. Sothmann, and A. N. Jordan, “Chiral Thermoelectrics with Quantum Hall Edge States,” Physical Review Letters **114**, 146801 (2015).

[175] A. Dzurak, C. Smith, M Pepper, D. Ritchie, J. Frost, G. Jones, and D. Hasko, “Observation of Coulomb blockade oscillations in the thermopower of a quantum dot,” Solid State Communications **87**, 1145–1149 (1993).

[176] A. S. Dzurak, C. G. Smith, C. H. W. Barnes, M Pepper, L. Martín-Moreno, C. T. Liang, D. A. Ritchie, and G. A. C. Jones, “Thermoelectric signature of the excitation spectrum of a quantum dot,” Physical Review B **55**, R10197–R10200 (1997).

[177] T. E. Humphrey, R Newbury, R. P. Taylor, and H Linke, “Reversible Quantum Brownian Heat Engines for Electrons,” Physical Review Letters **89**, 116801 (2002).

[178] R. Scheibner, E. G. Novik, T. Borzenko, M. König, D. Reuter, A. D. Wieck, H. Buhmann, and L. W. Molenkamp, “Sequential and cotunneling behavior in the temperature-dependent thermopower of few-electron quantum dots,” Physical Review B **75**, 041301 (2007).

[179] R Scheibner, M König, D Reuter, A. D. Wieck, C Gould, H Buhmann, and L. W. Molenkamp, “Quantum dot as thermal rectifier,” New Journal of Physics **10**, 083016 (2008).

[180] S. F. Svensson, A. I. Persson, E. A. Hoffmann, N. Nakpathomkun, H. A. Nilsson, H. Q. Xu, L Samuelson, and H Linke, “Lineshape of the thermopower of quantum dots,” New Journal of Physics **14**, 033041 (2012).

[181] S. F. Svensson, E. A. Hoffmann, N. Nakpathomkun, P. M. Wu, H. Q. Xu, H. A. Nilsson, D. Sánchez, V Kashcheyevs, and H Linke, "Nonlinear thermovoltage and thermocurrent in quantum dots," New Journal of Physics **15**, 105011 (2013).

[182] D. M. Kennes, D Schuricht, and V Meden, "Efficiency and power of a thermoelectric quantum dot device," EPL (Europhysics Letters) **102**, 57003 (2013).

[183] H. Thierschmann, R. Sánchez, B. Sothmann, F. Arnold, C. Heyn, W. Hansen, H. Buhmann, and L. W. Molenkamp, "Three-terminal energy harvester with coupled quantum dots," Nature Nanotechnology **10**, 854–858 (2015).

[184] H. Thierschmann, R. Sánchez, B. Sothmann, H. Buhmann, and L. W. Molenkamp, "Thermoelectrics with Coulomb-coupled quantum dots," Comptes Rendus Physique **17**, 1109–1122 (2016).

[185] G. D. Mahan and J. O. Sofo, "The best thermoelectric.," Proceedings of the National Academy of Sciences **93**, 7436–7439 (1996).

[186] M Esposito, K Lindenberg, and C. Van den Broeck, "Thermoelectric efficiency at maximum power in a quantum dot," EPL (Europhysics Letters) **85**, 60010 (2009).

[187] D. V. Averin and K. K. Likharev, "Coulomb blockade of single-electron tunneling, and coherent oscillations in small tunnel junctions," Journal of Low Temperature Physics **62**, 345–373 (1986).

[188] C. W. J. Beenakker and A. A. M. Staring, "Theory of the thermopower of a quantum dot," Physical Review B **46**, 9667–9676 (1992).

[189] M. Rey, M. Strass, S. Kohler, P. Hänggi, and F. Sols, "Nonadiabatic electron heat pump," Physical Review B **76**, 085337 (2007).

[190] S. Juergens, F. Haupt, M. Moskalets, and J. Splettstoesser, "Thermoelectric performance of a driven double quantum dot," Physical Review B **87**, 245423 (2013).

[191] B. Roche, R.-P. Riwar, B Voisin, E Dupont-Ferrier, R Wacquez, M Vinet, M Sanquer, J Splettstoesser, and X Jehl, "A two-atom electron pump," Nature Communications **4**, 1581 (2013).

[192] R. Sánchez, B. Sothmann, and A. N. Jordan, "Effect of incoherent scattering on three-terminal quantum Hall thermoelectrics," Physica E: Low-dimensional Systems and Nanostructures **75**, 86–92 (2016).

[193] C. H. Schiegg, M. Dzierzawa, and U. Eckern, "Implementation of transmission functions for an optimized three-terminal quantum dot heat engine," Journal of Physics: Condensed Matter **29**, 085303 (2017).

[194] J. Argüello-Luengo, D. Sánchez, and R. López, "Heat asymmetries in nanoscale conductors: The role of decoherence and inelasticity," Physical Review B **91**, 165431 (2015).

[195] J. H. Jiang, M. Kulkarni, D. Segal, and Y. Imry, "Phonon-thermoelectric transistors and rectifiers," Physical Review B **92**, 045309 (2015).

[196] K. Yamamoto, O. Entin-Wohlman, A. Aharony, and N. Hatano, "Efficiency bounds on thermoelectric transport in magnetic fields: The role of inelastic processes," Physical Review B **94**, 121402 (2016).

[197] B. Sothmann, R. Sánchez, A. N. Jordan, and M. Büttiker, "Rectification of thermal fluctuations in a chaotic cavity heat engine," Physical Review B **85**, 205301 (2012).

[198] B. Sothmann and M. Büttiker, “Magnon-driven quantum-dot heat engine,” EPL (Europhysics Letters) **99**, 27001 (2012).

[199] R. Sánchez, R. López, D. Sánchez, and M. Büttiker, “Mesoscopic coulomb drag, broken detailed balance, and fluctuation relations,” Physical Review Letters **104**, 076801 (2010).

[200] D Bischoff, M Eich, O Zilberberg, C Rössler, T Ihn, and K Ensslin, “Measurement Back-Action in Stacked Graphene Quantum Dots,” Nano Letters **15**, 6003–6008 (2015).

[201] G. Bulnes Cuetara, M. Esposito, and P. Gaspard, “Fluctuation theorems for capacitively coupled electronic currents,” Physical Review B **84**, 165114 (2011).

[202] R. Hussein and S. Kohler, “Capacitively coupled nano conductors,” Annalen der Physik **527**, 610–618 (2015).

[203] K. Kaasbjerg and A.-P. Jauho, “Correlated Coulomb Drag in Capacitively Coupled Quantum-Dot Structures,” Physical Review Letters **116**, 196801 (2016).

[204] A. J. Keller, J. S. Lim, D. Sánchez, R. López, S. Amasha, J. A. Katine, H. Shtrikman, and D. Goldhaber-Gordon, “Cotunneling Drag Effect in Coulomb-Coupled Quantum Dots,” Physical Review Letters **117**, 1–5 (2016).

[205] L. Henriet, A. N. Jordan, and K. Le Hur, “Electrical current from quantum vacuum fluctuations in nanoengines,” Physical Review B **92**, 125306 (2015).

[206] P Delsing, K. K. Likharev, L. S. Kuzmin, and T Claeson, “Effect of high-frequency electrodynamic environment on the single-electron tunneling in ultrasmall junctions,” Physical Review Letters **63**, 1180–1183 (1989).

[207] L. J. Geerligs, V. F. Anderegg, C. A. van der Jeugd, J Romijn, and J. E. Mooij, “Influence of Dissipation on the Coulomb Blockade in Small Tunnel Junctions,” Europhysics Letters (EPL) **10**, 79–85 (1989).

[208] M. H. Devoret, D Esteve, H Grabert, G.-L. Ingold, H Pothier, and C Urbina, “Effect of the electromagnetic environment on the Coulomb blockade in ultrasmall tunnel junctions,” Physical Review Letters **64**, 1824–1827 (1990).

[209] S. M. Girvin, L. I. Glazman, M Jonson, D. R. Penn, and M. D. Stiles, “Quantum fluctuations and the single-junction Coulomb blockade,” Physical Review Letters **64**, 3183–3186 (1990).

[210] H. B. Callen and H. L. Scott, “Thermodynamics and an Introduction to Thermostatistics, 2nd ed.,” American Journal of Physics **66**, 164–167 (1998).

[211] P. Jacquod, R. S. Whitney, J. Meair, and M. Büttiker, “Onsager relations in coupled electric, thermoelectric, and spin transport: The tenfold way,” Physical Review B **86**, 155118 (2012).

[212] M. Buttiker, “Coherent and sequential tunneling in series barriers,” IBM Journal of Research and Development **32**, 63–75 (1988).

[213] G.-L. Ingold, P. Wyrowski, and H. Grabert, “Effect of the electromagnetic environment on the single electron transistor,” Zeitschrift für Physik B Condensed Matter **85**, 443–449 (1991).

[214] S. Florens, P. Simon, S. Andergassen, and D. Feinberg, "Interplay of electromagnetic noise and Kondo effect in quantum dots," Physical Review B **75**, 155321 (2007).

[215] G. Benenti, K. Saito, and G. Casati, "Thermodynamic bounds on efficiency for systems with broken time-reversal symmetry," Physical Review Letters **106**, 1–4 (2011).

[216] F. L. Curzon and B. Ahlborn, "Efficiency of a Carnot engine at maximum power output," American Journal of Physics **43**, 22–24 (1975).

[217] N. Nakpathomkun, H. Q. Xu, and H. Linke, "Thermoelectric efficiency at maximum power in low-dimensional systems," Physical Review B **82**, 235428 (2010).

[218] C. Altimiras, O. Parlavecchio, P. Joyez, D. Vion, P. Roche, D. Esteve, and F. Portier, "Dynamical Coulomb Blockade of Shot Noise," Physical Review Letters **112**, 236803 (2014).

[219] D. Sánchez and M. Büttiker, "Chirality in Coulomb-blockaded quantum dots," Physical Review B **72**, 201308 (2005).

[220] D. Sánchez, "Magnetoasymmetric current fluctuations of single-electron tunneling," Physical Review B **79**, 045305 (2009).

[221] R. López, J. S. Lim, and D. Sánchez, "Fluctuation Relations for Spintronics," Physical Review Letters **108**, 246603 (2012).

[222] M. Esposito and G. Schaller, "Stochastic thermodynamics for "Maxwell demon" feedbacks," EPL (Europhysics Letters) **99**, 30003 (2012).

[223] K. Maruyama, F. Nori, and V. Vedral, "Colloquium: The physics of Maxwell's demon and information," Reviews of Modern Physics **81**, 1–23 (2009).

[224] L. Szilard, "Über die Entropieverminderung in einem thermodynamischen System bei Eingriffen intelligenter Wesen," Zeitschrift für Physik **53**, 840–856 (1929).

[225] C. H. Bennet, "The thermodynamics of computation – a review," International Journal of Theoretical Physics **21**, 905 (1982).

[226] R. Landauer, "Irreversibility and Heat Generation in the Computing Process," IBM Journal of Research and Development **5**, 183–191 (1961).

[227] A. Bérut, A. Arakelyan, A. Petrosyan, S. Ciliberto, R. Dillenschneider, and E. Lutz, "Experimental verification of Landauer's principle linking information and thermodynamics," Nature **483**, 187–189 (2012).

[228] Y. Jun, M. Gavrilov, and J. Bechhoefer, "High-precision test of Landauer's principle in a feedback trap," Physical Review Letters **113**, 190601 (2014).

[229] S. Toyabe, T. Sagawa, M. Ueda, E. Muneyuki, and M. Sano, "Experimental demonstration of information-to-energy conversion and validation of the generalized Jarzynski equality," Nature Physics **6**, 988–992 (2010).

[230] É. Roldán, I. A. Martínez, J. M. R. Parrondo, and D Petrov, "Universal features in the energetics of symmetry breaking," Nature Physics **10**, 457–461 (2014).

[231] J. V. Koski, V. F. Maisi, J. P. Pekola, and D. V. Averin, "Experimental realization of a Szilard engine with a single electron," Proceedings of the National Academy of Sciences **111**, 13786–13789 (2014).

[232] M. D. Vidrighin, O. Dahlsten, M. Barbieri, M. S. Kim, V. Vedral, and I. A. Walmsley, "Photonic Maxwell's Demon," Physical Review Letters **116**, 050401 (2016).

[233] A. M. Bozkurt, B. Pekerten, and I. Adagideli, "Work extraction and Landauer's principle in a quantum spin Hall device," Physical Review B **97**, 245414 (2018).

[234] S. Lloyd, "Quantum-mechanical Maxwell's Demon," Physical Review A **56**, 3374–3382 (1997).

[235] J. M. Horowitz and K. Jacobs, "Quantum effects improve the energy efficiency of feedback control," Physical Review E **89**, 042134 (2014).

[236] M. Esposito, R. Kawai, K. Lindenberg, and C. Van den Broeck, "Efficiency at Maximum Power of Low-Dissipation Carnot Engines," Physical Review Letters **105**, 150603 (2010).

[237] G. Schaller, C. Emary, G. Kiesslich, and T. Brandes, "Probing the power of an electronic Maxwell's demon: Single-electron transistor monitored by a quantum point contact," Physical Review B **84**, 085418 (2011).

[238] P. Strasberg, G. Schaller, T. Brandes, and M. Esposito, "Thermodynamics of a physical model implementing a Maxwell demon," Physical Review Letters **110**, 040601 (2013).

[239] P. Strasberg, G. Schaller, T. Brandes, and C. Jarzynski, "Second laws for an information driven current through a spin valve," Physical Review E **90**, 062107 (2014).

[240] A. Kutvonen, J. V. Koski, and T. Ala-Nissilä, "Thermodynamics and efficiency of an autonomous on-chip Maxwell's demon," Scientific Reports **6**, 21126 (2015).

[241] J. P. Pekola, D. S. Golubev, and D. V. Averin, "Maxwell's demon based on a single qubit," Physical Review B **93**, 024501 (2016).

[242] D. Sánchez and M. Büttiker, "Magnetic-field asymmetry of nonlinear mesoscopic transport," Physical Review Letters **93**, 106802 (2004).

[243] K. MacLean, S. Amasha, I. P. Radu, D. M. Zumbühl, M. A. Kastner, M. P. Hanson, and A. C. Gossard, "Energy-Dependent Tunneling in a Quantum Dot," Physical Review Letters **98**, 036802 (2007).

[244] D. Yanuka, S. Efimov, M. Nitishinskiy, A. Rososhek, and Y. E. Krasik, "Generation of strong pulsed magnetic fields using a compact, short pulse generator," Journal of Applied Physics **119**, 144901 (2016).

[245] N. Walldorf, A.-P. Jauho, and K. Kaasbjerg, "Thermoelectrics in Coulomb-coupled quantum dots: Cotunneling and energy-dependent lead couplings," Physical Review B **96**, 115415 (2017).